

Defect-Rich Size-Selected Nanoclusters  
and Nanocrystalline Films of Titanium  
(IV) Oxide and Tantalum (IV) Oxide  
for Efficient Photocatalyst and  
Electroforming-Free Memristor  
Applications

by

Saurabh Srivastava

A thesis

presented to the University Of Waterloo

in fulfilment of the

thesis requirement for the degree of

Doctor of Philosophy

in

Chemistry (Nanotechnology)

Waterloo, Ontario, Canada, 2016

© Saurabh Srivastava (2016)

## **Author's Declaration**

I hereby declare that I am the sole author of this thesis. This is a true copy of the thesis, including any required final revisions, as accepted by my examiners.

I understand that my thesis may be made electronically available to the public.

## Abstract

Transition metal oxides,  $\text{TiO}_2$  and  $\text{Ta}_2\text{O}_5$ , are two of the most extensively studied wide bandgap semiconductor materials (with high work functions). Due to their suitable band edge positions for hydrogen evolution and exceptional stability against photocorrosion upon optical excitation, their application in heterogeneous photocatalysis has attracted a lot of attention. These oxides are also great components in the field of electronic devices such as field effect transistors, solar cells, and more recently advanced memory devices. Here, we focus on ultrasmall nanoclusters ( $< 5$  nm) and nanocrystalline thin films of defect-rich  $\text{TiO}_2$  and  $\text{Ta}_2\text{O}_5$  and their applications as high-performance photocatalysts in photoelectrochemical water splitting reactions and as resistive switching materials in memory applications.

The present work is divided into two main parts. In the first part, ultrasmall nanoclusters (below 10 nm) of defect-rich  $\text{TiO}_2$  and  $\text{Ta}_2\text{O}_5$  are synthesized using a gas phase aggregation technique in a nanocluster generation source based on DC magnetron sputtering. With a careful optimization of the deposition parameters such as aggregation zone length (condensation volume), Ar gas flow rate, deposition temperature and source power, we are able to produce metal/metal oxide nanoclusters with a narrow size distribution. As most of these as-grown nanoclusters are negatively charged, it is possible to conduct size-selection according to their mass-to-charge ratio. Using a quadrupole mass filter (directly coupled to the magnetron source), we achieve precise size-selection of nanoclusters, with the size distribution reduced to below 2% mass resolution. The nearly monosized nanoclusters so produced are deposited onto appropriate substrates to serve as the photoanodes for photoelectrochemical water splitting application.

We demonstrate, for the first time, that the precisely size-selected  $\text{TiO}_2$  nanoclusters can be deposited on H-terminated Si(001) in a soft-landing condition and they can be used as high-performance photocatalysts for solar harvesting, with greater enhancement in the photoconversion efficiency. Three different sizes of  $\text{TiO}_2$  nanoclusters (4, 6 and 8 nm) are synthesized with appropriate combinations of aggregation length and Ar flow rate. Despite the low amount of material loading (of  $\sim 20\%$  of substrate coverage), these supported  $\text{TiO}_2$  nanoclusters exhibit remarkable photocatalytic activities during photoelectrochemical water splitting reaction under simulated sunlight ( $50 \text{ mW/cm}^2$ ). Higher photocurrent densities (up to  $0.8 \text{ mA/cm}^2$ ) and photoconversion efficiencies (up to 1%) with decreasing nanocluster size (at the applied voltage of  $-0.22 \text{ V vs Ag/AgCl}$ ) are observed. We attribute this enhancement to the presence of surface defects, providing a large amount of active surface sites, in the amorphous  $\text{TiO}_2$  nanoclusters as-grown at room temperature. We have further shown that the

incorporation of metallic nanoclusters with the semiconductor photocatalysts can enhance the photoconversion efficiency. In this work, we have co-deposited surface oxygen deficient Ta<sub>2</sub>O<sub>5</sub> or TaO<sub>x</sub> nanoclusters along with Pt nanoclusters of similar nanocluster size (~5 nm), the latter used as a promoter. The electron-hole pairs generated in the water splitting reaction can be effectively separated and stored with the presence of Pt nanoclusters, while the increase in Pt loading as a promoter can enhance the reaction by providing a large number of electrons for H<sub>2</sub> evolution. However, loading too much Pt nanoclusters could actually reduce the photoresponse, which is due to blocking of photosensitive TaO<sub>x</sub> surface by excess Pt nanoclusters. In both cases, the photoconversion efficiency could potentially be enhanced at least 5 times by increasing the amount of nanocluster loading from 20% coverage to a monolayer coverage (e.g., by increasing the amount of deposition time for TiO<sub>2</sub> and TaO<sub>x</sub> nanoclusters). Even higher photoconversion efficiency can be obtained with multiple layers of nanoclusters and by employing nanoclusters with even smaller size and/or with modification by chemical functionalization. These potential improvements could dramatically increase the photoconversion efficiency, making these nanocluster samples to be among the top photoelectrochemical catalysis performers.

In the second part of the present work, we employ defect-rich nanocrystalline TiO<sub>x</sub> and TaO<sub>x</sub> thin films as active materials for resistive switching for memory application. Based on resistive switching principle, memristive devices (or memristors) provide the unique capability of multistep information storage. The development of memristors has often been hailed as the next evolution in non-volatile memories, low-power remote sensing, and adaptive intelligent prototypes including neuromorphic and biological systems. One major obstacle in achieving high switching performance is the irreversible electroforming step that is required to create oxygen vacancies for resistive switching. Using magnetron sputtering film deposition technique, we have fabricated the heterojunction memristor devices based on nanocrystalline TiO<sub>x</sub> and TaO<sub>x</sub> thin films (10-60 nm thick) with a high density of *built-in* oxygen vacancies, sandwiched between a pair of metallic Pt electrodes (30 nm thick). To avoid the destructive electroforming process and to achieve a high switching performance in the memristor device, we carefully manipulate the chamber pressure and ambient in deposition chamber during deposition to generate the required highly oxygen deficient semiconducting films. The films, as-deposited at room temperature, exhibit a crystallite size of 4-5 nm. In the fabricated Pt/TiO<sub>x</sub>/Pt memristors, a high electric field gradient can be generated in the TiO<sub>x</sub> film at a much lower electroforming voltage of +1.5 V, due in part to the nanocrystalline nature, which causes localization of this electric field and consequently enhanced reproducibility and repeatability in the device performance. After the first switching, consecutive 250 switching cycles can be achieved with a low

programming voltage of  $\pm 1.0$  V, along with a high ON/OFF current ratio, and long retention (up to  $10^5$  s).

We further improve this  $\text{TiO}_x$  memristor device by totally removing the electroforming step by fabricating an electroforming-free memristive device based on a heterojunction interface of  $\text{TiO}_x$  and  $\text{TaO}_x$  layers. In the Pt/ $\text{TiO}_x$ / $\text{TaO}_x$ /Pt architecture structure (with Pt serving as the top and bottom electrodes), a high- $\kappa$  dielectric  $\text{TaO}_x$  layer is used to facilitate trapping and release of the electronic carriers, while a  $\text{TiO}_x$  layer provides low-bias rectification as an additional oxygen vacancy source. With the incorporation of  $\text{TaO}_x$  layer, the need for the electroforming step can be eliminated. More importantly, the resistance states of the device can be tuned such that switching between the high resistance state and the low resistance state can be achieved even smaller programming voltage of  $+0.8$  V. With the low leakage current properties of  $\text{TaO}_x$ , the high endurance ( $10^4$  repeated cycles) and high retention capabilities (up to  $10^8$  s) can be enhanced manifold with highly stable ON/OFF current ratio.

In both memristor devices, four different junction sizes ( $5\times 5$ ,  $10\times 10$ ,  $20\times 20$  and  $50\times 50$   $\mu\text{m}^2$ ) have been evaluated according to their ON/OFF current ratio. We observe that the smaller is the junction size is, the higher is the current ratio. For the Pt/ $\text{TiO}_x$ / $\text{TaO}_x$ /Pt memristor, we have also analyzed the thickness dependent effect of the switching behavior of devices with four different  $\text{TaO}_x$  layer thicknesses (10, 20, 40 and 60 nm) and a  $\text{TiO}_x$  layer thickness constant at 10 nm. The device with 10 nm thick  $\text{TaO}_x$  (being amorphous in nature) shows unipolar switching with two SETs and two RESETs in one sweep cycle. This is in contrast to the bipolar resistive switching found in devices with the thicker  $\text{TaO}_x$  films with a SET in the positive sweep and a RESET during the negative sweep. We further demonstrate that resistive switching can also occur at very low programming voltage ( $\sim 50$  mV), thus qualifying it as an ultralow power consumption device ( $\sim \text{nW}$ ). The stable non-volatile bipolar switching characteristics with high ON/OFF current ratio and low power consumption make our devices best suitable for various analog and discrete programmable electric pulses. With the simplicity in the construction, the performance achieved for our memristors represents the best reported to date.

This new class of defect-rich metal oxides nanomaterials with an ultrananocrystalline nature shows solid promises for various catalytic and electronic applications and, also, the simple, scalable room-temperature device fabrication process makes this approach easily migratable further to transparent and/or flexible devices.

## Acknowledgements

I would like to express my deep appreciation to my PhD supervisor Prof. Kam Tong Leung for his continuous encouragement and effective guidance throughout my program. He provided me the opportunity to learn with on-hand experience using different tools, and helpful advice and friendly spirit. He will always be my mentor in all aspects of my life. My special thanks go to my advisory committee members: Prof. Dan Thomas (Department of Chemistry, University of Guelph), Prof. Vassili Karanassios (Department of Chemistry, University of Waterloo), and Prof. Eric Croiset (Department of Chemical Engineering, University of Waterloo), for their constructive feedback and their highly inspiring discussions during our annual meetings.

Distinct recognition is due for our postdoctoral fellows at Waterloo Advanced Technology Laboratory (WATLab): Dr. Nina Heinig and Dr. Joseph P. Thomas for their endless patience and outstanding assistance as well as expert training and continual help with different microscopy and spectroscopy tools. I would also like to express my gratitude to Dr. Lei Zhang, Dr. Shantinarayan Rout for their consistent and enthusiastic cooperation. I am truly thankful to my senior colleagues and group members: Dr. Nafiseh Moghimi, Dr. Marwa Abd-Ellah, Dr. Jung-Soo Kang, Dr. Bahareh Rahsepar, Anisur Rahman, Donald McGillivray, Hanieh Farkhondeh, and Mahdi Beedel, for their sincere friendship and the positive attitude within our group. I will always be proud for being a part of this significant family.

I gratefully acknowledge all members of the University of Waterloo Chemistry Department, the Waterloo Institute for Nanotechnology (WIN), and the Natural Sciences and Engineering Research Council of Canada (NSERC) for their generous funding of my research in Canada.

Last but not least, I express my warm gratefulness to my parents and my younger sister for their endless love and care, which give me the strength to reach my goals. Finally, I would like to give my sincere gratitude to my other family members and close friends, for their enormous support.

## Dedication

To my parents,

To my Sister,

# Table of Contents

Author's Declaration.....	ii
Abstract.....	iii
Acknowledgements.....	vi
Dedication.....	vii
List of Figures.....	xi
List of Tables.....	xxi
Chapter 1 Introduction.....	1
1.1 Nanomaterials and Nanoclusters.....	1
1.2 Transition metal oxides.....	2
1.2.1 Nanostructured titanium dioxide (TiO <sub>2</sub> ).....	4
1.2.2 Nanostructured tantalum oxide (Ta <sub>2</sub> O <sub>5</sub> ).....	5
1.3 Preparation Methods of nanoclusters/nanoparticles.....	6
1.3.1 Chemical solutions based deposition methods.....	6
1.3.2 Physical deposition methods.....	7
1.4 Photoelectrochemical water splitting.....	9
1.5 Photoelectrochemical properties of TiO <sub>2</sub> and Ta <sub>2</sub> O <sub>5</sub> .....	11
1.5.1 TiO <sub>2</sub> .....	11
1.5.2 Ta <sub>2</sub> O <sub>5</sub> .....	15
1.6 Memristors.....	16
1.7 Scope of the Thesis.....	26
Chapter 2 Experimental Details.....	28
2.1 Synthesis and Deposition of Metal/Metal Oxide Nanoclusters (NCs).....	28
2.1.1 Effects of Nanogen parameters on the nanocluster synthesis.....	29
2.2 Deposition of metal or metal oxide thin film.....	31
2.3 Characterization of the synthesized nanostructures using scanning electron microscopy (SEM), transmission electron microscopy (TEM) and atomic force microscopy (AFM).....	32
2.4 Composition Analysis by X-ray Photoelectron Spectroscopy (XPS) and Secondary Ion Mass Spectroscopy (SIMS).....	35
2.4.1 XPS Chemical-State Composition Analysis.....	35
2.4.2 SIMS Chemical Mapping.....	37
2.5 X-ray Diffraction Crystallography and Ultraviolet/Visible (UV/Vis) Spectroscopy.....	38
2.5.1 X-ray Diffraction Crystallography.....	38

2.5.2 Ultraviolet/Visible (UV/Vis) Spectroscopy.....	39
2.6 Photoelectrochemical analysis.....	40
2.7 Micro/Nanodevices fabrication techniques .....	41
2.8 Electrical characterization .....	43
Chapter 3 Size-Selected TiO <sub>2</sub> Nanocluster Catalysts for Efficient Photoelectrochemical Water	
Splitting .....	44
3.1 Introduction .....	44
3.2 Experimental Details .....	45
3.3 Results and Discussion.....	47
3.4 Conclusions .....	59
Chapter 4 Size-selected, Ultra-small, Defect-rich (TaO <sub>x</sub> , Pt) Nanocluster Composite for Promoter-Enhanced Photocatalysis .....	61
4.1 Introduction .....	61
4.2 Experimental Details .....	62
4.3 Results and Discussion.....	63
4.4 Conclusion.....	72
Chapter 5 Bipolar Memristors Based on Defect-Rich Ultra-Nanocrystalline TiO <sub>x</sub> Film.....	74
5.1 Introduction .....	74
5.2 Materials and Methods .....	76
5.2.1 Device fabrication .....	76
5.2.2 Characterization.....	76
5.3 Results and Discussion.....	78
5.3.1 Switching behavior.....	80
5.4 Conclusion.....	89
Chapter 6 Programmable, Electroforming-free TiO <sub>x</sub> /TaO <sub>x</sub> Heterojunction-Based Non-Volatile Memories.....	90
6.1 Introduction .....	90
6.2 Materials and Methods .....	92
6.2.1 Device fabrication: .....	92
6.2.2 Characterization.....	92
6.3 Results and Discussion.....	93
6.3.1 Pt/TiO <sub>x</sub> /TaO <sub>x</sub> /Pt device architecture.....	93
6.3.2 Memristor Performance and Switching Mechanism.....	94
6.4 Conclusion.....	103

Chapter 7 Concluding Remarks and Outlook .....	105
7.1 Summary .....	105
7.2 Future Work.....	107
7.2.1 Nanoclusters.....	107
7.2.2 Nanocrystalline Thin Films.....	109
Bibliography .....	111

## List of Figures

**Figure 1.1** Crystal structures of TiO<sub>2</sub>. (a) Thermodynamic stable bulk Rutile unit cell of TiO<sub>2</sub> and (b) Anatase unit cell.<sup>45</sup> ..... 5

**Figure 1.2** Schematic diagram depicting the photoelectrochemical water splitting mechanism where the oxidation occurs at the working electrode to produce O<sub>2</sub> whereas reduction occurs on counter (Pt) electrode to produce H<sub>2</sub>.<sup>57</sup> ..... 10

**Figure 1.3** Band positions of several semiconductors in contact with an aqueous electrolyte. The valence band (lower edge) and the conduction band (upper edge) are separated with the bandgap (in eV). The energy scale is with respect to the reversible hydrogen electrode (RHE).<sup>57</sup> ..... 11

**Figure 1.4** SEM images of TiO<sub>2</sub> plain nanorods and branched nanorods, along with their photoelectrochemical water splitting properties.<sup>66</sup> ..... 13

**Figure 1.5** Modified TiO<sub>2</sub> nanowire (NW) and nanobelt structures and their photoelectrochemical water splitting performance. (a) Photographs showing different appearance of these one-dimensional nanostructured films, (b) and (c) are photocurrent densities and photoconversion efficiencies of the corresponding nanostructures as a function of applied potential.<sup>40</sup> ..... 14

**Figure 1.6** (a) Schematic block diagram for all four fundamental two-terminal circuit elements: resistor (R), capacitor (C), inductor (L) and memristor (M). Note that R, C, L and M are the functions of the independent variable, yielding nonlinear elements. In the case of a charge controlled memristor, this variable is a single-valued function M(q). (b) Schematic diagrams of a memristor device with two different regions of oxide material (doped and undoped) when operated in the ON and OFF states.  $R_{ON}(w/D)$  and  $R_{OFF}(l-w/D)$  are the resistances in doped and undoped regions, respectively, where  $w$  is the width of doped region and  $D$  is the width of the dielectric.<sup>70</sup> ..... 17

**Figure 1.7** A family of device states exists when two dynamic metal (Pt)/semiconductor (TiO<sub>x</sub>) junctions are operated in series exhibiting four different current-voltage characteristics. The interface with metal and insulating oxide interface led with low oxygen vacancy concentration behaves as the Schottky junction where the device works as open rectifier. The metal and conducting oxide interface behaves as Ohmic junction led by high oxygen vacancy concentration, where the band bending facilitates the drift of charge carriers and the device exhibits shunted rectifier<sup>88</sup> ..... 20

**Figure 1.8** (a) An AFM image of an array of 17 crosspoint nanodevices with a 50 nm half-pitch. The thickness of the insulating TiO<sub>2</sub> layer is 50 nm. (b) The initial  $I$ - $V$  curve of the device in its virgin state (pre-switching state) exhibits a rectifying state. (c) Experimental (solid) and modelled (dotted)  $I$ - $V$  switching curves of the device for 50 cycles showing the pinched hysteresis loop for the ON and

OFF states (bottom inset shows the log-scale switching) with the top inset depicting the equivalent circuit.<sup>87</sup> ..... 21

**Figure 1.9** Schematic diagrams of the internal switching phenomena as governed by the nature of the conduction channel: (a) Electric-field-dominating bipolar nonlinear, (b) electric-field -dominating bipolar linear, (c) Joule-heating-driven nonpolar bi-stable, and (d) Joule-heating-driven nonpolar threshold. Inset of each schematic shows the current-voltage loops corresponding to the switching behavior.<sup>89</sup> ..... 22

**Figure 1.10** Layer by layer conductive AFM tomography to observe the filamentary structure in Al<sub>2</sub>O<sub>3</sub> based memristors. The scale bar in Figure 1.10d is 80 nm and the average space between each slice is ~ 0.5 nm.<sup>91</sup> ..... 23

**Figure 1.11** Resistive switching structure of the Ta<sub>2</sub>O<sub>5-x</sub>/TaO<sub>2-x</sub> device. (a) Schematic representation of the multilayer structure with the movement of internal oxygen vacancies responsible for switching. (b) SEM images of the 30-nm crossbar device array. (c) TEM image of the crossbar device stacking (d) typical bipolar *I-V* switching behavior.<sup>107</sup> ..... 25

**Figure 2.1** Photographs of different parts of Nanogen nanocluster generation source. (a) The bottom chamber (top left) houses the source head (bottom left). (b) The top chamber (top right) contains the quadrupole mass filter (bottom right). The NCs get deposited onto a substrate placed 30 cm in front of the exit (orifice)..... 29

**Figure 2.2** Photograph of the physical vapor deposition system based on the magnetron sputtering technique that is used for both thin film deposition and clusters generation via the Nanogen source (Mantis Deposition Ltd.). (a) Two RF and two DC sputtering sources, along with a quartz crystal monitor (QCM) are installed, along with (b) controlled electronics..... 32

**Figure 2.3** Photograph of the MERLIN field-emission scanning electron microscope (FESEM), equipped with secondary electron in-lens and out-of-lens (SE2) detectors, and backscattered electron detector (BSD) as well as an EDAX energy-dispersive X-ray analysis system. .... 33

**Figure 2.4** Photograph of a Zeiss Libra 200 MC transmission electron microscope. .... 34

**Figure 2.5** Photograph of Digital Instruments Dimension 3100 Scanning Probe Microscope used for atomic force microscopy..... 35

**Figure 2.6** Photograph of the Thermo-VG Scientific ESCALab 250 Microprobe used for chemical-state composition analysis of the nanoclusters and thin films. .... 36

**Figure 2.7** Photograph of ION-TOF SIMS-5 system used for chemical analysis of the metal/metal oxide heterostructures. .... 37

**Figure 2.8** Photograph of the Panalytical X’pert Pro MRD X-ray diffractometer used for crystal structure characterization of thin films. The instrument is set up in the parallel beam geometry with an

X-ray mirror and a parallel plate collimator used for the incident and diffracted beam optics, respectively.....	39
<b>Figure 2.9</b> Photograph of Perkin Elmer Lambda 1050 NIR/UV/Vis Spectrometer used for the transmittance/reflectance measurements for thin films. ....	40
<b>Figure 2.10</b> Photographs of various components of the water splitting experiment including the electrochemical analyzer, illumination station, all the electrodes and combined experimental setup. ....	41
<b>Figure 2.11</b> Photographs of (a) an Intelligent Micro Patterning SF-100 Xpress maskless optical lithography system used to fabricate the memristive devices, and (b) Raith IONLine ion beam lithography system used to fabricate the memristive devices with nano-sized junctions. ....	42
<b>Figure 2.12</b> Photograph of Signatone probe station coupled with an Agilent B1500 semiconductor parameter analyzer used for electrical characterization of the memristor devices. Inset shows the measurement setup where two probes are connected to the two electrodes of the memristor device. .	43
<b>Figure 3.1</b> Schematic diagram of the production of a size-selected cluster beam in the Nanogen cluster source (not drawn to scale), which involves the following steps: (a) generation of $Ti_n$ moieties and their ions by magnetron sputtering, (b) collisional condensation that leads to nucleation and gas aggregation, and eventually to $Ti_n$ and $Ti_n^-$ cluster formation, and (c) size selection of $Ti_n^-$ clusters ions by a quadrupole mass filter. The $Ti_n^-$ cluster ions exiting the aggregation (or Nanogen source) chamber from a 3 mm dia. aperture become oxidized by the ambient in the deposition chamber and the resulting $TiO_2$ cluster ions are then deposited and neutralized on the substrate under soft-landing condition to produce the size-selected $TiO_2$ nanoclusters. The aggregation length (AL), defined as the separation between the front face of the target and the entrance plane of the quadrupole, and the Ar gas flow are the main parameters used to control the overall cluster size distribution before size selection. No bias is applied to the substrate to ensure soft landing of the nanoclusters. ....	47
<b>Figure 3.2</b> (a) Cluster size (left axis) and deposition chamber pressure (right axis) as a function of Ar flow rate for different aggregation length (AL) from 10 to 90 mm, in steps of 10 mm; and (b) typical nanocluster size distributions, as represented by quadrupole collector current (left axis), obtained with three typical combinations of (AL, Ar flow rate) as marked by large open circles in (a): A = (80 mm, 30 sccm), B = (60 mm, 35 sccm) and C (20 mm, 55 sccm). The vertical dashed line marks the respective mode cluster size of each nanocluster distribution, while the corresponding sharpen peak marked by the darken area corresponds to the distribution of nanoclusters mass-selected (within 2% of the mode cluster size) by applying an appropriate set of DC and AC voltages to the quadrupole mass filter. The total mass (right axis) as a function of nanocluster size produced by the Nanogen cluster source is also shown. ....	49

**Figure 3.3** AFM images of size-selected TiO<sub>2</sub> nanoclusters obtained with mode sizes of (a) 3.5 nm, (b) 5 nm and (c) 6.2 nm (deposited with appropriate growth conditions) and with a mode size of 5 nm deposited with three different growth conditions (AL, Ar- flow): (d) (80 mm, 40 sccm), (e) (60 mm, 35 sccm), and (f) (20 mm, 30 sccm), all on H-Si substrates. AFM images of size-selected TiO<sub>2</sub> nanoclusters with a mode size of 6 nm deposited on three different substrates: (g) H-Si, (h) glass, and (i) quartz. All AFM images are obtained for a scanned area of 1×1 μm<sup>2</sup>. Insets show the corresponding histograms for the cluster size distributions of the nanoclusters from 2 to 8 nm obtained under appropriate (AL, Ar-flow) combinations, with the peak marked by the numbers of the clusters with the respective mode sizes..... 51

**Figure 3.4** AFM images of the TiO<sub>2</sub> nanoclusters deposited on H-Si substrates for (a) 15 and (b) 60 minutes. All AFM images are obtained with a scanned area of 1×1 μm<sup>2</sup>. Evidently, no clear increase in the cluster size as a result of cluster agglomeration on the substrate is observed even for the longer deposition time, which confirms the soft-landing deposition condition of nanoclusters with low kinetic energies. .... 52

**Figure 3.5** XPS spectra of Ti 2p region for TiO<sub>2</sub> nanoclusters as-deposited on a H-Si substrate, and as a function of sputtering time. Only the Ti 2p<sub>3/2</sub> region is used here to identify various chemical states of the nanoclusters. .... 54

**Figure 3.6** XPS spectra of Ti 2p region for commercial TiO<sub>2</sub> powder (anatase) as a function of sputtering time. The reduction of Ti<sup>4+</sup> phase is observed in the commercial anatase powder sample after 270 s of Ar-ion bombardment, which corresponds to the emergence of non-stoichiometric Ti oxide phases. Commercial rutile powder is also found to exhibit similar result as anatase powder (data not shown)..... 55

**Figure 3.7** Corresponding XPS spectra of (a) O 1s and (b) Si 2p regions for the as-prepared TiO<sub>2</sub> nanocluster (6 nm) film shown in Figure 3.5..... 55

**Figure 3.8** (a) Schematic diagram of the mechanism of a photoelectrochemical water splitting reaction. An expanded view of a TiO<sub>2</sub> nanocluster (NC, red sphere), consisting of Ti (green spheres), O (pink spheres) and H atoms (brown spheres), is shown as the bottom inset. The top inset shows the electron-hole pair generation in TiO<sub>2</sub> upon UV-vis light illumination, which supplies holes (h<sup>+</sup>) for the oxidation of OH<sup>-</sup> leading to O<sub>2</sub> evolution at the photoanode and electrons (e<sup>-</sup>), upon travelling to the counter electrode through an external circuit, for reduction leading to H<sub>2</sub> generation. (b) Photocurrent densities as a function of applied potential obtained in a photoelectrochemical water splitting reaction in a 5M KOH electrolyte, using TiO<sub>2</sub> nanoclusters of different sizes (4, 6 and 8 nm) and the post-annealed TiO<sub>2</sub> nanoclusters (6 nm), all on H-Si, as the photoanodes, all with an illumination area of 5×5 mm<sup>2</sup> under a 300 W Xe-lamp at a power density of 50 mW/cm<sup>2</sup>. (c) TEM

images of 4 nm (left), 6 nm (center) and 8 nm nanoclusters (right) deposited directly on holey carbon TEM grids, along with high resolution images shown as insets illustrating their respective degrees of crystallinity..... 58

**Figure 3.9** (a) Photoconversion efficiency (PCE) as a function of applied potential,  $E_{app}$ , for TiO<sub>2</sub> nanoclusters with three different sizes as deposited on H-Si under illumination from a Xe lamp with a power density of 50 mW/cm<sup>2</sup>. (b) Photocurrent density,  $J_p$ , as a function of  $E_{app}$  for 6-nm TiO<sub>2</sub> nanocluster in the dark (bottom line) and under illumination by UV light (obtained with a low pass filter, second top line), visible light (obtained with an AM 1.5 filter, third top line), and the full spectrum (without any filter, top line). The photoconversion efficiency of the water splitting reaction in the presence of external applied potential is calculated by using the equation: ..... 59

**Figure 4.1** (a) Schematic diagram of the nanocluster generation source coupled with a quadrupole mass filter for precise size selection (not drawn to scale). Two sources can be ignited simultaneously to create a composite plasma consisting of two materials (Ta and Pt in this work) through magnetron sputtering. The constituent atoms combine together in the aggregation zone to form Ta<sub>n</sub> and Pt<sub>n</sub> clusters, which are transported out of the aggregation chamber through a 3 mm orifice by the Ar gas flow. Generally, a large fraction of the clusters are positively charged (Ta<sub>n</sub><sup>+</sup> and Pt<sub>n</sub><sup>+</sup>) so that a quadrupole mass filter can be used to perform size selection of the nanoclusters (after exiting through the orifice) based on their mass-to-charge ratio. The size-selected nanoclusters then enter into the main chamber where they become partially oxidized and neutralized to form TaO<sub>x</sub>, and deposit onto the substrate under soft-landing condition. The aggregation length (AL) corresponds to the distance between the source and the 3 mm orifice, which can be varied to obtain different nanocluster sizes. (b) Cluster size as a function of Ar-gas flow rate for different aggregation lengths from 10 to 90 mm (in step of 10 mm). (c) Size distribution as represented by the quadrupole collector current as a function of nanocluster diameter for a fixed Ar flow rate of 20 sccm and variable aggregation lengths from 10 to 90 mm (in step of 10 mm). The mode cluster size is defined as the size for the peak maximum of each distribution curve..... 64

**Figure 4.2** Near Gaussian nanocluster size distribution profiles for the Ta and Pt nanoclusters obtained separately at (40 sccm, 60 mm) with the mode size of 4.7 nm each, where the quadrupole collector current (left axis) is proportional to the cluster population of specific cluster size. The total masses of the nanoclusters (right axis) are also shown as functions of their diameters. The vertical shaded area correspond to the segment of the cluster size distribution within 2% mass resolution as selected by applying an appropriate set of AC and DC voltages on the quadrupole mass filter..... 66

**Figure 4.3** Secondary electron SEM images of the co-deposited Ta and Pt nanoclusters with deposition parameters (30 sccm, 60 mm) obtained for Ta deposition for 30 min and Pt deposition for

(a) 15 min, (c) 30 min and (d) 45 min. Inset of (b) shows the corresponding size distribution before size selection, while the shaded area marks the portion of the nanoclusters size-selected by the quadrupole mass filter. (d) AFM image used to estimate the nanocluster size distribution by using the heights of the nanoclusters..... 67

**Figure 4.4** TEM image of the (TaO<sub>x</sub>, Pt) nanoclusters directly co-deposited on lacey carbon coated TEM grid. The corresponding high-resolution TEM images of a Pt and a TaO<sub>x</sub> nanocluster, each of 5 nm dia, are shown in top right and bottom right panels, respectively. The Pt nanocluster depicting the interplanar spacing corresponds to Pt(111) plane, while the TaO<sub>x</sub> nanocluster is found to be amorphous..... 68

**Figure 4.5** XPS spectra of (a) O 1s (b) Pt 4f and (c) Ta 4f regions for the (TaO<sub>x</sub>, Pt) nanoclusters co-deposited on a H-Si substrate as a function of Ar sputtering time..... 69

**Figure 4.6** Schematic diagrams of the mechanism of photoelectrochemical water splitting reactions for TaO<sub>x</sub> NCs (5 nm dia.) (a) without and (b) with Pt NCs (5 nm dia.) co-deposited on H-Si. (c) Photocurrent density and (d) photoconversion efficiency as functions of applied potential obtained for a photoelectrochemical water splitting reaction in a 1 M KOH electrolyte, using the (TaO<sub>x</sub>, Pt) nanoclusters supported on H-Si substrates as the photoanodes, all with an illumination area of 5×5 mm<sup>2</sup> under a 300 W Xe lamp coupled with an AM 1.5 G filter at a power density of 50 mW/cm<sup>2</sup> (half sun)..... 71

**Figure 5.1** Device fabrication and electron microscopic analysis. (a) Schematic representation of device fabrication involving three maskless lithography (ML) steps. In ML1, an I bar pattern for the bottom electrode is exposed to the photoresist. This is then followed by development in MF-24 to remove the photoresist for the pattern, sputter-coating with Pt, and finally the lift-off to remove the remaining photoresist. This process is then repeated in ML2 where a 60 nm TiO<sub>x</sub> junction layer is deposited in the patterned area whereas in ML3 is repeated with the same parameters for the Pt top layer deposition. Once the device stacking structure is fabricated, the electrical characterization is performed by connecting the microprobes to the top and bottom Pt electrodes while the switching process is observed in the TiO<sub>x</sub> layer. (b) SEM image of the array of devices with different junction sizes (5×5 μm<sup>2</sup>, 10×10 μm<sup>2</sup>, 20×20 μm<sup>2</sup> and 50×50 μm<sup>2</sup>) fabricated on the same chip, and (c) selected TiO<sub>x</sub> surface morphology in high magnification. (d) Photograph of the actual device array. .... 77

**Figure 5.2** Physical characterization for TiO<sub>x</sub> based memristor devices. (a) Schematic cross-sectional view of the Pt/TiO<sub>x</sub>/Pt device architecture supported on a SiO<sub>2</sub>/Si substrate. (b) TEM image of a cross section of a typical memristor device, with the corresponding EDX elemental maps (top right) and high-resolution TEM images of selected Pt and TiO<sub>x</sub> regions (bottom right). For each device, the layer thickness of the top Pt electrode is 30 nm, while those for the TiO<sub>x</sub> active layer and the bottom

Pt electrode are 60 nm. A 5 nm thick Ti layer is pre-deposited immediately before depositing the bottom Pt layer electrode on the SiO<sub>2</sub>/Si substrate in order to provide better Pt adhesion to the substrate. (c) XRD profile and (d) depth-profiling XPS spectra of Ti 2p region of a TiO<sub>x</sub> film as-deposited on the Pt bottom electrode pre-deposited with a Ti adhesion layer, all supported on a SiO<sub>2</sub>/Si substrate, shown along with the reference patterns for Pt FCC (PDF# 01-087-0644) and TiO<sub>x</sub> tetragonal phase (PDF# 00-008-0386) in c and with the binding energy locations of relevant Ti ionic states in d. As Ti<sup>nt</sup> (in TiO<sub>x</sub>) could be reduced to metallic Ti by ion sputtering, we limit the sputtering only to no more than 10 s. Precise manipulation of the Ar-gas flow rate provides good control of the oxygen vacancy defect concentration to make the TiO<sub>x</sub> active layer suitable for electronic transport.<sup>79</sup>

**Figure 5.3** (a) SIMS depth profiles for the Pt/TiO<sub>x</sub>/Pt memristor with junction size of 50×50 μm<sup>2</sup>.

Secondary ion mass spectrometry is used to examine the changes in the elemental composition in the multilayered device as a function of sputtering depth. Different colored regions correspond to different layers as mentioned on the top of each colored region. Evidently, there is a uniform distribution of oxygen within the TiO<sub>x</sub> matrix while there is no oxygen diffusion into the Pt layer, which accounts for the stability of the electrode. (b) UV-Vis spectra in transmittance mode for the TiO<sub>x</sub> film as-deposited and annealed on glass substrates. The difference in the transmittance is due to the phase change with oxidation during annealing step. The as-deposited film is semi-transparent with the observed transmittance at ~8%, while annealing causes the sample to become more transparent, with the transmittance increased up to ~30 %. This can be correlated with the phase change from the more conducting TiO<sub>x</sub> to the more insulating TiO<sub>2</sub> due to further oxidation during annealing. .... 80

**Figure 5.4** Memristive switching characteristics and mechanism of a typical Pt/TiO<sub>x</sub>/Pt device with a 5×5 μm<sup>2</sup> junction size. (a) (Upper) Current (I) vs voltage (V) curve for the first positive (activation) sweep involving resistive switching at the electroforming voltage of +1.5 V. In the first negative (initialization) sweep, the voltage-controlled negative differential resistance (NDR) observed at – 0.92–1.08 V is due to inhomogeneity in the electric field caused by vacancy gradient. Inset shows the same I-V curve for the virgin state of the device (prior to electroforming). (Middle) |I| vs V profiles (with |I| in a semilog scale) for the virgin and electroforming states, and (lower) corresponding resistance vs V profile for the high resistance state (HRS) and low resistance state (LRS) in the electroforming step. The resistance is observed to be of the order of MΩ in HRS vs. kΩ in LRS. (b) Schematic representation of the bipolar switching in the memory element. With the device initially stayed in an equipotential state (the virgin state) with uniformly distributed oxygen vacancies prior to any electrical bias, a positive bias (V<sub>Electroforming</sub>) is applied to create an electric potential gradient in order to induce ionic drift of the oxygen vacancies. After this irreversible electroforming process, a

negative bias is applied to return the device from the LRS to HRS. Following the interface-type switching mechanism, the positively charged oxygen vacancies can be pushed towards (SET) and away from (RESET) the interface through a conduit that covers the whole junction size, respectively, by the positive and negative sweep biases. (c) Typical I-V switching loop observed (without any evidence of negative differential resistance) in normal SET (OFF to ON) and RESET (ON to OFF) operations after the first electroforming process..... 83

**Figure 5.5** Virgin and activation states of the memory devices with a  $5 \times 5 \mu\text{m}^2$  junction size. (a) In the virgin state, the I-V curve is obtained with a sweep voltage ( $\pm 1.0$  V) applied on either of the top or bottom electrodes while keeping the respective other electrode grounded. Because of the single-phase  $\text{TiO}_x$  film, this interface-type switching behavior is irrespective of the directional bias, i.e. the I-V curve obtained with the bias applied on the top electrode (TE) [and the bottom electrode (BE) grounded] is a mirror image of that obtained with the bias applied on the bottom electrode (and the top electrode grounded). (b) During the device activation step, resistive switching is obtained at an electroforming voltage of  $+1.5$  V and  $-1.5$  V for the device operated with BE and TE grounded, respectively. The corresponding I-V behavior also exhibits a negative differential resistance region starting at  $-0.92$  V and  $+0.92$  V, respectively. The similar resistive switching behavior of the device found when operated with both directions of the applied bias reveals the similar nature of the top Pt/ $\text{TiO}_x$  and the bottom  $\text{TiO}_x$ /Pt interfaces..... 84

**Figure 5.6** Junction size dependency, resistive switching endurance, and resistance state retention. (a)  $|J|$  vs V profiles of memristor devices with four different junction sizes ( $5 \times 5 \mu\text{m}^2$ ,  $10 \times 10 \mu\text{m}^2$ ,  $20 \times 20 \mu\text{m}^2$  and  $50 \times 50 \mu\text{m}^2$ ) after the electroforming step. The current densities (J) are found to be inversely proportional to the junction size, which supports the interface-type memristive switching mechanism. Among all four junction sizes, the best (i.e. highest) ON-to-OFF current density ratio is obtained with the  $5 \times 5 \mu\text{m}^2$  junction. The lower current obtained for the device with the smaller junction size promises lower power consumption as the device continues to be miniaturized. This is also particularly promising for high density device manufacturing involving discrete SET and RESET processes. The corresponding  $|I|$  vs V profiles in the 0.60-0.95 V region for all four junction sizes (inset) illustrate the lower current but higher ON-to-OFF current ratio found for the smaller junction sizes, thus validating the lower power consumption performance for the device with a smaller junction. (b) I-V curves and corresponding  $|I|$  vs V profiles (inset) within the sweep voltage range of  $\pm 1.0$  V for over 250 consecutive SET/RESET cycles for the memristor device with a  $5 \times 5 \mu\text{m}^2$  junction size. (c) ON and OFF currents obtained at a small READ voltage of  $+0.25$  V for the 250 switching cycles, where the writing is performed at  $V_{\text{SET}}$  ( $+1.0$  V) and erasing at  $V_{\text{RESET}}$  ( $-1.0$  V). The currents for both the LRS and HRS are observed to be very stable throughout the sweep cycles. (d)

Current vs time plots to illustrate the retention characteristics of the memristive device observed at a constant READ voltage of 0.25 V for the virgin state (before activation) and the ON state (after activation). The current obtained after the activation is extremely stable for over  $10^5$  s, with a projected device lifetime to be well over 10 years. .... 86

**Figure 5.7** Memristor response to electric pulses with short and long time widths. (a) Resistive switching of the Pt/TiO<sub>x</sub>/Pt device indicating stable current response upon short-term potentiation obtained with short electric pulses of +0.25 V amplitude (read voltage) applied for 0.5 s in a 5 s interval. (b) The corresponding current response upon long-term potentiation obtained with stable ON and OFF states for read voltages (0.25 V) applied for 300 s in a 300 s interval over a testing period of  $10^5$  s. (c) SET voltages of the Pt/TiO<sub>x</sub>/Pt device obtained at different sweep rates.  $V_{SET}$  tends to become smaller almost linearly with the smaller sweep rate. (d) Binary ON-OFF operation with alternating +1.0 V and -1.0 V pulses at different switching frequencies (30, 8, 1 and 0.1 Hz) and corresponding pulse durations (0.03, 0.125, 1 and 10 s). Switching between the ON and OFF states is highly dependent on the input parameters, where the SET/RESET window is found to be stable for frequencies above a particular value (8 Hz in our case) i.e. for smaller pulse duration (less than 0.125 s). .... 88

**Figure 6.1** Device schematics and physical characterization of the Pt/TiO<sub>x</sub>/TaO<sub>x</sub>/Pt heterojunction. (a) SEM images of the device with  $10 \times 10 \mu\text{m}^2$  junction size along with the corresponding EDX elemental mapping (b) indicating the relative quantities of Pt, Ti, Ta, and O. (c) Schematic diagram of the multilayer architecture of the Pt/TiO<sub>x</sub>/TaO<sub>x</sub>/Pt memristor device with specified thicknesses for each layer. The thickness of the TaO<sub>x</sub> layer is varied from 10-60 nm, while keeping the TiO<sub>x</sub> thickness the same (10 nm), to observe the TaO<sub>x</sub> layer thickness dependency on the electrical behavior of the memristor devices. (d) XRD spectra of unpatterned TaO<sub>x</sub> films with four different thicknesses (10, 20, 40 and 60 nm), as deposited on the Pt coated SiO<sub>2</sub>/Si substrates (peaks are labeled with the ref. 00-015-0244 for TaO<sub>x</sub> and 00-001-1311 for Pt). It is observed that the 10 nm thick film is amorphous in nature while the other films show nanocrystalline behavior, with similar nanocrystallite size (~ 4.5 nm). (e) & (f) Depth profile with respect to Ar-ion sputtering in XPS spectra for Ta 4f and O1s for the larger area of TaO<sub>x</sub>/Pt layer deposited on SiO<sub>2</sub>/Si substrate. .... 95

**Figure 6.2** Schematic diagrams of band structures in various states during the switching mechanism in a Pt/TiO<sub>x</sub>/TaO<sub>x</sub>/Pt heterojunction memristor for (a) Virgin state under zero bias condition: For TiO<sub>x</sub> and TaO<sub>x</sub> (solid line), band bending occurs due to smaller energy gaps of the vacancy defects in the films (Red dotted lines shows the actual band structure of pure TiO<sub>2</sub> and Ta<sub>2</sub>O<sub>5</sub>). (b) & (c) the drift of oxygen vacancies with the applied positive voltage below  $V_{SET}$  at BE. (d) At  $V_{SET}$ , the conduction band edge lowers further where oxygen vacancies may easily migrate to TE via tunneling and the

device switches to LRS. (e) When the voltage is swept back, at  $V_{\text{RESET}}$ , the oxygen vacancies are pushed away from TE and the device switches back to HRS. The role of  $\text{TiO}_x$  layer between TE and  $\text{TaO}_x$  layer is to provide an intermediate bandgap for the vacancies flow at lower energy. During RESET, a trap level is created in the  $\text{TaO}_x$  film which remains afterwards to facilitate the repeated switching cycles by trapping some charge carriers..... 97

**Figure 6.3** Electrical  $I$ - $V$  characteristics of  $\text{TiO}_x/\text{TaO}_x$  based memory cell. (a) Electrical switching characteristics of the  $5 \times 5 \mu\text{m}^2$  cell exhibiting the bipolar resistive switching with four different states, inset shows the semi-log scale. (b) Current density vs. voltage plot for demonstrating the cell-size dependency on the switching (SET) voltage. (c) The device could also be switched at ultimate low programming voltage as low as 50 mV with around 300 nW power consumption. (d) Resistive switching characteristic of the  $\text{Pt}/\text{TaO}_x/\text{Pt}$  memristors for comparison with the  $\text{TiO}_x/\text{TaO}_x$  heterostructure based memristors. It could clearly be noticed that its  $I$ - $V$  characteristic follows the exponential (Schottky) behavior within  $\pm 2.0$  V in case of  $\text{TaO}_x$  based memristors while for  $\text{TiO}_x/\text{TaO}_x$  based memristors, the SET states is achieved at +0.8 V..... 99

**Figure 6.4** SET and RESET states dependency on physical parameters for  $\text{TiO}_x/\text{TaO}_x$  memristors. (a) Two different switching mechanism for two different thicknesses of  $\text{TaO}_x$  layer. (b) HRS and LRS currents vs.  $\text{TaO}_x$  layer thickness for a  $10 \times 10 \mu\text{m}^2$  memory cell at +0.5 V applied bias..... 100

**Figure 6.5** Repeatability, endurance and retention capabilities of the  $\text{TiO}_x/\text{TaO}_x$  memristor. (a) Extremely high switching repeatability of over  $10^4$  cycles for the electroforming-free cell with junction size  $10 \times 10 \mu\text{m}^2$  and  $\text{TaO}_x$  film thickness 60 nm. (b) Plot between current vs switching cycles for HRS and LRS states showing the almost constant ON/OFF current ratio for over 1000 cycles at the applied bias +0.5 V. (c) Remarkable retention capabilities of the  $10 \times 10 \mu\text{m}^2$  cell with 60 nm  $\text{TaO}_x$  layer in HRS and LRS at a small applied voltage (+0.5 V). (d) The highly reproducible electrical behavior of the arrays of cells with same cell size, over the same chip showing the similar switching voltages. .... 102

**Figure 6.6** Programmable switching modes of  $\text{TiO}_x/\text{TaO}_x$  memristors. (a) RESET states of the  $10 \times 10 \mu\text{m}^2$  cell with 60 nm  $\text{TaO}_x$  layer corresponding to different stopping voltages (+0.75-2.5 V). Inset shows the corresponding SET voltages for different stopping voltage. The SET and RESET states can be manually programmed by using different stopping voltages. (b) Binary switching in virgin state and switching state exhibiting short term potentiation at an applied voltage of +0.5 V with 0.5 s interval for  $10 \times 10 \mu\text{m}^2$  cell with 60 nm thick  $\text{TaO}_x$  layer..... 103

**Figure 7.1** (a)  $\text{TiO}_2$  nanowires decorated by 5 nm Pt nanoclusters and (b)  $\text{CuO}$  nanowires decorated by 3 nm Ta nanoclusters. .... 109

## List of Tables

<b>Table 1.1</b> Important physical properties of $\text{TiO}_2$ and $\text{Ta}_2\text{O}_5$ .....	4
<b>Table 1.2</b> $\text{Ta}_2\text{O}_5$ photocatalysts for solar water splitting. <sup>68</sup> .....	15
<b>Table 1.3</b> List of functional oxides used in redox resistive devices suitable for adaptive electronics applications. TE and BE represent top electrode and bottom electrode, respectively.....	18
<b>Table 3.1</b> RMS surface roughness over $1 \times 1 \mu\text{m}^2$ area as a function of deposition time for $\text{TiO}_2$ nanoclusters deposited on H-Si substrates with an Ar flow rate of 20 sccm and aggregation length of 50 mm.....	53



# Chapter 1

## Introduction

Atoms are building blocks for all matters in our universe. Atoms and molecules combine together because of their complementary shapes and charges that attract each another. During the past decade, the reduction in size of functional architectures has been the predominant trend in many fields of science and technology. Structural size down to the nanometer scale leads not only to a miniaturization of functional units but also to the development of new materials and systems with unique physical and chemical properties. It is because at nanoscale, where the dimension regime is as low as a billionth of a meter ( $10^{-9}$  m), the nanomaterials have a much larger surface area to volume ratio (or specific surface area) than their bulk counterpart, which along with the quantum size effect forms the basis of their unique physiochemical properties.<sup>1</sup> Nanotechnology, in traditional sense, involves building materials, devices, and appliances in the 1-100 nm size regimes from bottom up, with atomic precision.<sup>2</sup> Numerous applications particularly in the field of energy and electronics make nanotechnology an important attraction among researchers in various fields. There are whole different classes of nanomaterials but the general categories are divided into zero dimensional (nanoparticles and nanoclusters), one dimensional (nanowires, nanotubes, nanobelts etc.), two dimensional (thin films, nanowalls etc.) and three dimensional (nanoflowers, nanocages etc.) based on their nanostructures. Our work is mostly focused on zero dimensional and two dimensional nanostructures.

### 1.1 Nanomaterials and Nanoclusters

One of the widely accepted unique properties of the metal nanoparticles such as Au and Ag (below 50 nm) is the surface plasmon resonance behavior,<sup>3</sup> where the noble metal nanoparticles on the surface of a dielectric produce collective coherent oscillation of free electrons in the conduction band by the interactive electromagnetic field at a metal/dielectric interface.<sup>4-6</sup> Recently, magnetic nanoparticles have been used as magnetic resonance imaging contrasting agents to study signal amplification in surface plasmon resonance. They can also be used to conveniently conjugate with the desired biomolecules on their surface because of their ability to offer the surface modification chemistry, therefore making these nanoparticles the ideal candidates for chemical (methanol, ethanol and hydrogen) sensors<sup>7,8</sup> and biological (proteins, DNAs, peptides, viruses) sensors.<sup>9</sup> Transition metal nanoparticles can also be used for magnetic separation of water pollutants.

Nanoclusters are collection of atoms (more than one to a few thousands of atoms together), and depending on the atomic sizes the size of the nanoclusters could range from sub-nanometer to 10 nm in the diameter.<sup>10</sup> Nanoclusters provide a direct link between the distinct behavior of atoms and nanoparticles and that of bulk materials. Transition metal and metal oxide nanoclusters (NCs) have attracted a lot of recent attention due to their numerous applications in catalysis,<sup>11,12</sup> information storage,<sup>13</sup> biomedical,<sup>14</sup> sensors,<sup>15</sup> and optoelectronic<sup>16,17</sup> and magnetic devices.<sup>18-20</sup> Nanocluster assemblies can be used to tune the materials properties and lattice parameters through careful selection of the constituent building blocks by coupling physical and chemical properties. Nanoclusters could be categorized, based on their constituents, as single metallic, bimetallic or hybrid nanoclusters. Depending on their synthesis techniques, the nanoclusters may have different shape and crystalline phases. Accordingly, amorphous or crystalline nanoclusters can be created for different application purposes. For example, amorphous NCs with high density of surface defects can be used for defect-driven processes while crystalline surface can be used for processes in which defects would degrade or adversely affect the efficiency. It is also possible to form NCs with a crystalline core covered by an amorphous surface layer of a few nanometers.

Size selectivity is one of the key parameters to study size-dependent functional catalytic properties of these nanoclusters corresponding to their specific surface area.<sup>2,5,21-25</sup> In the early 1980s, the development of precise size-selected nanocluster molecular beam system has enabled cluster formation with a well-defined size distribution, which has opened up new opportunities for understanding gas-phase reaction dynamics and catalysts. More recently, there is a growing interest in the deposition of a three-dimensional array of size-selected nanoclusters (with a nearly monosized distribution) on to different surfaces because of emerging applications in nanotechnology.<sup>26-28</sup> Our work will focus on isolated size-selected nanoclusters (below 10 nm in dia.) and on thin film making up of nanocrystallites (below 10 nm in size) based on transition metal oxides.

## 1.2 Transition metal oxides

Transition metals are the Group 3-12 elements in the periodic table with partially filled *d* sub-shell (often called d-block elements). They have various characteristic properties such as colored compounds due to *d-d* electronic transition (charge transfer), multiple oxidation states due to small energy differences between different metastable ionic states, and high capacity for binding with a variety of ligands to provide transition metal complexes. The transition metal and their oxides, at nanoscale, have been extensively used in the area of homogeneous and heterogeneous catalysis because of their ability to adopt multiple oxidation states and to produce complexes by forming bonds between their surface atoms and the molecular reactants.<sup>9</sup> There is also a variety of other applications

of nanostructured transition metal oxides. TiO<sub>2</sub> nanostructures (nanoparticles and nanowires) and their composites with other metal oxides have been investigated to enhance the conductivity and diffusion coefficient of the Li-ion in lithium ion batteries.<sup>29</sup> It was observed that the diffusion length of the Li-ion is strongly dependent on the size of the nanoparticles because of the increasing specific surface area with decreasing particle size and thus with improving capacity and conductivity. Nanoporous TiO<sub>2</sub> was found to improve the diffusion length of Li ions, leading to a higher capacity. Various chemical sensors have been fabricated using ZnO,<sup>30</sup> CuO<sup>31</sup> and SnO<sub>2</sub><sup>32</sup> nanostructures (nanowires, nanobelts, nanotubes) due to their easy synthesis, high sensitivity and good stability compared to other metal oxide nanomaterials. CuO and ZnO nanostructures have also been studied for their photovoltaic application, in which dye sensitized solar cells (DSSCs) were fabricated using the CuO/ZnO heterojunctions on ITO. SnO<sub>2</sub> is also well known for its low UV degradation and high thermal stability, which is strongly preferred in photovoltaic applications.<sup>33</sup> Initially, Ta<sub>2</sub>O<sub>5</sub> nanomaterials were used as an antireflective layer in optical and photovoltaic devices, but in the last decade its high dielectric constant made it a well-known dielectric material in the electronic industry.<sup>34</sup> Transition metal oxides have also been widely investigated in solar cell applications for their tunable electrode work functions in maximizing the open circuit voltage. For example, TiO<sub>2</sub>, ZnO, Ta<sub>2</sub>O<sub>5</sub> and ZrO<sub>2</sub> can be used as cathode buffer layer because of their low work functions while MoO<sub>3</sub>, NiO, CuO and V<sub>2</sub>O<sub>5</sub> can be used as anode buffer layers due to their high work functions. Transition metal oxides are given more importance over metals in the electronic applications because their work functions are higher than those of metals and they are considerably less expensive than metals such as gold (Au) and platinum (Pt). Among all the metals, Pt has the highest work function (5.3 eV), while V<sub>2</sub>O<sub>5</sub> has a work function of ~7.0 eV.

The present work is based on two of the most popular transition metal oxides: TiO<sub>2</sub> and Ta<sub>2</sub>O<sub>5</sub>. Some of the physical and chemical properties of TiO<sub>2</sub> and Ta<sub>2</sub>O<sub>5</sub> are listed in Table 1.1.

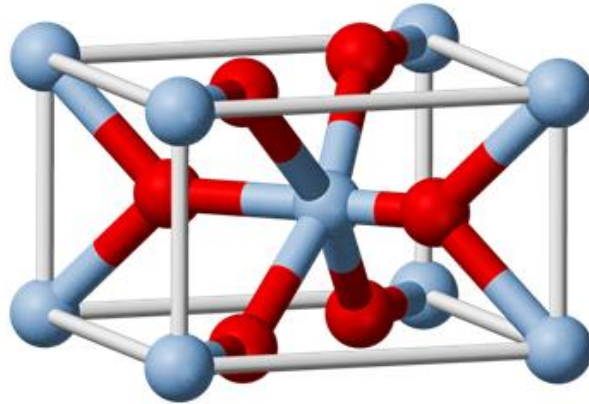
**Table 1.1** Important physical properties of TiO<sub>2</sub> and Ta<sub>2</sub>O<sub>5</sub>.

Properties	TiO <sub>2</sub>	Ta <sub>2</sub> O <sub>5</sub>
Molar mass (amu)	79.866	441.893
Density	4.23 g/cm <sup>3</sup>	8.37 g/cm <sup>3</sup>
Band gap	3.05 eV (Rutile)	3.9 eV
Crystal structure	Tetragonal	Orthorhombic
Dielectric constant	83-100	90-110
Refractive index (n)	2.488 (Anatase)	2.275

### 1.2.1 Nanostructured titanium dioxide (TiO<sub>2</sub>)

TiO<sub>2</sub> is a well-known binary compound semiconductor that can form three different phases: rutile, anatase and brookite. Most of the TiO<sub>2</sub> physical and chemical properties are obtained in either the rutile or anatase phase (Figure 1.1a&b) with the respective indirect bandgaps of 3.05 eV and 3.12 eV. Due to its compatible band-edge positions, high photocatalytic activity, high resistance to photocorrosion, low cost, and lack of toxicity (high biocompatibility), TiO<sub>2</sub> is also one of the most studied transparent conductive oxides.<sup>35</sup> Synthesis of TiO<sub>2</sub> nanostructures has been conducted on different substrates, including silicon, glass, sapphire, diamond and graphene by using either wet chemistry methods including sol-gel,<sup>36</sup> hydrothermal<sup>37</sup> and electrochemical methods, or dry synthesis techniques such as sputter coating<sup>38</sup> chemical vapor deposition,<sup>39</sup> pulsed laser deposition<sup>40</sup> and metal organic chemical vapor deposition.<sup>41</sup> A variety of TiO<sub>2</sub> nanostructures, including nanowires, nanoparticles, nanotubes, and nanowalls have been used in various applications such as cosmetics, food industry, catalysis, hydrogen production by photoelectrochemical water splitting, chemical and biosensors, and field effect transistors.<sup>42-44</sup>

## a Rutile



## b Anatase

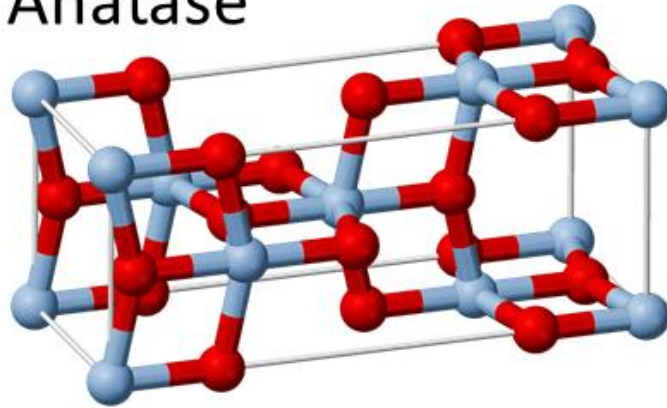


**Figure 1.1** Crystal structures of  $\text{TiO}_2$ . (a) Thermodynamic stable bulk Rutile unit cell of  $\text{TiO}_2$  and (b) Anatase unit cell.<sup>45\*</sup>

### 1.2.2 Nanostructured tantalum oxide ( $\text{Ta}_2\text{O}_5$ )

In recent years,  $\text{Ta}_2\text{O}_5$  has emerged as an interesting semiconducting material for various applications in different fields of research. Its higher chemical stability than other transition metal oxides and its high dielectric constant make  $\text{Ta}_2\text{O}_5$  a great candidate for use as a photocatalyst and as an electronic component in thin film transistors and field effect transistors. Different deposition methods, such as sputtering and physical/chemical vapor deposition, have been used to prepare various  $\text{Ta}_2\text{O}_5$  nanostructures such as nanowires, nanobelts and many other hierarchical structures which have been employed in sensing and lithium battery storage applications.<sup>46</sup>

---

\* Reproduced with permission from: Austin et.al. PNAS **2008**, *105*, 17217-17221. Copyright (2008) by The National Academy of Sciences of the USA.

### **1.3 Preparation Methods of nanoclusters/nanoparticles**

A wide variety of techniques have been used for the synthesis of metal and metal oxide nanoclusters and nanoparticles. They can be generally divided into chemical solution based deposition and physical vapor deposition methods.

#### **1.3.1 Chemical solutions based deposition methods**

Colloidal based wet-chemistry methods, sol-gel method and electrodeposition methods are some of the more commonly used techniques to prepare metal and metal oxide nanoclusters in solutions. Colloidal based methods (first proposed by Faraday in 1857)<sup>47</sup> are based on the synthesis of nanoclusters in the size range of 1-30 nm, and they involve reduction of metal ions in solution in the presence of polymeric ligands or surfactants. The resulting colloidal metal particles (produced by chemical reduction of metal salt) generally consist of a metallic core surrounded by a ligand shell, protecting the particle from coalescence. The method was further modified by Turkevich<sup>48</sup> in 1950, who proposed that the mechanism involves stepwise nucleation, growth and agglomeration under suitable conditions. Bimetallic and hybrid nanoclusters can also be prepared using this technique in two different ways as follows. During the growth of bimetallic nanoparticles, the second step of growth takes place by using the first metal seed layer as the nuclei for further growth while the hybrid nanoparticles can be synthesized by performing co-reduction in the solution containing both types of colloidal metal particles. This process comes with an unavoidable drawback that the remaining residue inside the nanoparticle film could affect the purity of the product and therefore material-sensitive applications.

Another common preparation method for metal and metal oxide nanoparticles is the sol-gel method (initially developed in 1960s), in which the material of interest is dissolved in a liquid in order to bring the product back as a solid in a controlled manner.<sup>36</sup> The process begins with sol formation of the sol, a liquid with insoluble colloidal nanoparticles, followed by development of the nanoparticles based gel induced by aggregation of the these nanoparticles. Various semiconductor nanostructures with different morphologies have been prepared using the sol-gel synthesis.<sup>12,49</sup> However, the main disadvantage of this method is the use of a large quantity of organic solvent, which becomes impractical for large-scale production in the industry.

Electrochemical method is a cost-effective method for preparing different types of metal and metal oxide nanomaterials that are found in many applications.<sup>50</sup> The relatively low-temperature synthesis process offers potential for large-scale production. This process is based on anodic electrodeposition in an electrolyte medium using a conventional three-electrode electrochemical cell that consists of a

working electrode (the substrate), a reference electrode (generally Ag/AgCl (3M KCl)) and a counter electrode (typically a platinum wire). The one-step process follows the reaction:



Different deposition parameters, including the electrolyte concentration, deposition temperature, deposition time, and pH of the solution, can be optimized to achieve different sizes, shapes and morphologies. This process could be time-consuming because of the slow deposition rate, and depending on the electrolyte the final product could also come with unavoidable reaction residues that may affect the properties.

### 1.3.2 Physical deposition methods

The wet-chemistry methods do not always provide the best reproducibility and consistency and the resulting products are highly sensitive to the deposition parameters. Synthesis of nanoclusters (1-10 nm) and nanoparticles (10-100 nm) using the physical vapor deposition techniques has gained immense interest because of its reproducible outcome. In physical vapor deposition, the source material is promoted (atom by atom) into the vapor phase followed by their deposition onto the substrates. Metal oxide nanoclusters can be created by the reaction between the vapor phases of these desired metal and the oxygen gas during the deposition. Parameters such as the type of substrate, deposition (or substrate) temperature, and the chamber pressure, flow rates and nature of the reactive gases can all be used to control the morphology, dimension and crystallinity of the resulting metal oxide nanoclusters.

Among the common physical deposition techniques for preparing nanostructured materials are pulsed laser deposition, supersonic expansion through a pulsed valve, thermal and e-beam evaporation, and magnetron sputtering. In the pulsed laser deposition technique, the source material is struck and ejected by the application of a powerful pulsed laser beam, and with the help of argon (Ar) as a carrier gas the source atoms get deposited on the substrates.<sup>40</sup> The laser-driven metal vaporization occurs within a supersonic nozzle and the ejected metal vapor is carried out with a high-density helium (He) carrier gas prior to the full expansion of the vapor further downstream.<sup>51</sup> Thermal evaporation and e-beam evaporation techniques also work on the same principle where the source is irradiated with heat and electron beam, respectively, and the metal particles are ejected and deposited on the substrates.<sup>52,53</sup>

Magnetron sputtering is a well-known technique used for large-scale production in industry, An inert gas such as Ar is used as the medium to create a self-sustaining plasma (energetic neutrals, ions and electrons) by a high-voltage power supply, and the energetic particles in the plasma are used to

bombard a solid target to eject the source atoms into the gas phase. The source atoms collide with one another in the gas phase because of their short mean free path and they tend to agglomerate and form clusters around the nucleation point created by some of the Ar ions. A large fraction of the Ar gas is non-ionized and they further help in carrying the generated clusters towards the substrate. There are two different types of sputtering methods: direct current (DC) sputtering and radio frequency (RF) sputtering. DC sputtering is only used for conducting sources such as metals, while RF sputtering is useful for sputtering materials from the conducting, insulating, and semiconducting targets such as metal oxides. Physical vapor deposition techniques, such as magnetron sputtering, are relatively expensive as compared to solutions-based techniques but they have great advantages in terms of purity, selectivity and reproducibility, in addition to the easy control of the deposition parameters.

Among all the physical deposition techniques, the magnetron sputtering technique is the most commonly used thin film deposition method, because it can sputter materials with high melting point even at room temperature and it offers high yield. A large variety of materials can be easily deposited using this technique and a high purity film can be achieved due to the required high vacuum environment. Another advantage of this technique is that it preserves the composition close to that of source material during the sputtering process because different elements spread differently (according to their masses) but difference is constant. Once the source material arrives at the substrate, different nanostructures can be synthesized depending on the substrate morphology and geometry. This technique has enabled creation of one-dimensional nanostructures by catalyst assisted vapor-liquid-solid (VLS) and vapor-solid (VS) growth on various substrates by controlling such parameters as target-to-substrate separation, carrier gas flow rate, nature of the catalysts, deposition temperature and chamber pressure, and the magnetron input power.<sup>54-56</sup>

A novel nanocluster generation instrument (Nanogen 500) developed by Mantis Deposition Ltd. is based on the magnetron sputtering process in which an aggregation zone (condensation zone) is coupled with the source. The ejected particles from the source material (usually a metal) travel in the long aggregation zone filled with Ar-gas where they collide with one another and agglomerate to form the nanoclusters. These clusters exit the aggregation zone through a 5 mm nozzle and pass through a quadrupole mass filter before they are deposited onto the substrates. The mass filter can be used to allow only clusters with a particular size to pass through it and to filter out the other clusters, therefore enabling a precisely size-selected monosized cluster film to be deposited on a variety of substrates. The size and shape of the nanoclusters are dependent on such factors as Ar-gas flow rate in the aggregation zone, aggregation zone length (condensation volume), magnetron input power, and

the AC/DC pole voltage ratio of the quadrupole mass filter. Details of the synthesis processes and effects of various physical parameters are discussed in the experimental chapter.

#### **1.4 Photoelectrochemical water splitting**

Efficient utilization of solar energy is one of the primary goals in green energy technology and in the quest for reducing the consumption of fossil fuels and the harmful effects of global warming. While semiconductor materials employed in a photovoltaic device are used for solar light to electricity generation, semiconductor materials can also be used to convert solar energy directly to chemical energy for hydrogen production and such a process is known as the photoelectrochemical water splitting reaction. Unlike photovoltaics, this is a water-based process, in which the semiconductor material, used as an electrode, is immersed in an aqueous electrolyte, and sunlight is used to illuminate the entire photoelectrochemical cell to supply energy for the water-splitting reaction. When the semiconductor absorbs photons with energies greater than its bandgap energy, electrons in the valence band are excited to the conduction band. As a result, excited electrons and holes are generated in the conduction and valence bands, respectively. These photogenerated charge carriers then undergo the appropriate redox reactions. The semiconductor material, to be used as the photocatalyst for the photoelectrochemical water splitting reaction, must have a bandgap that overlaps the reduction and oxidation potentials  $\text{H}^+/\text{H}_2$  (0 V vs. RHE) and  $\text{O}_2/\text{H}_2\text{O}$  (+1.23 V vs. RHE), respectively. When a semiconductor electrode is immersed in an electrolyte solution (such as water), electron transfer takes place between the semiconductor and the electrolyte solution so that the Fermi level is equilibrated with the redox potential of the electrolyte solution. Figure 1.2 shows a schematic diagram of the water splitting mechanism. Grätzel<sup>57</sup> has summarized the effect of different metal oxide systems on the photoelectrochemical water splitting reactions, as presented in the Figure 1.3.

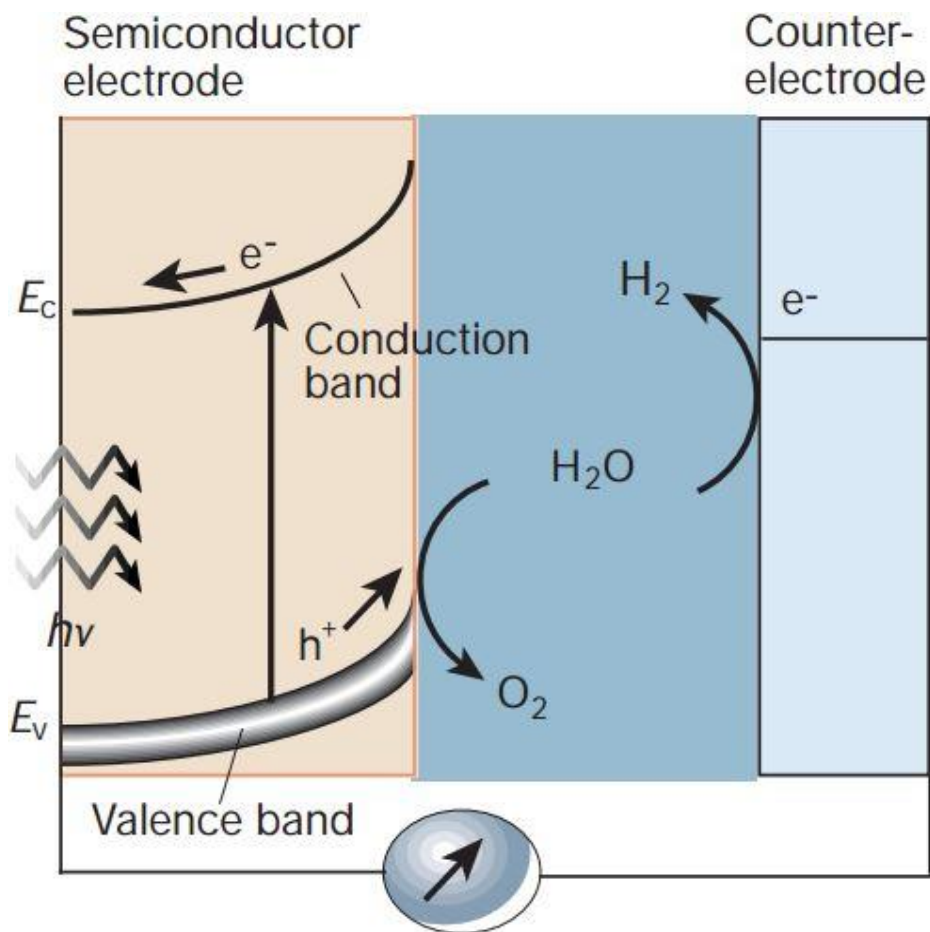


**Figure 1.2** Schematic diagram depicting the photoelectrochemical water splitting mechanism where the oxidation occurs at the working electrode to produce  $O_2$  whereas reduction occurs on counter (Pt) electrode to produce  $H_2$ .<sup>57†</sup>

<sup>†</sup> Reproduced with permission from: Grätzel M., Nature **2001**, 414, 338-344. Copyright (2001) by Nature Publishing Group.

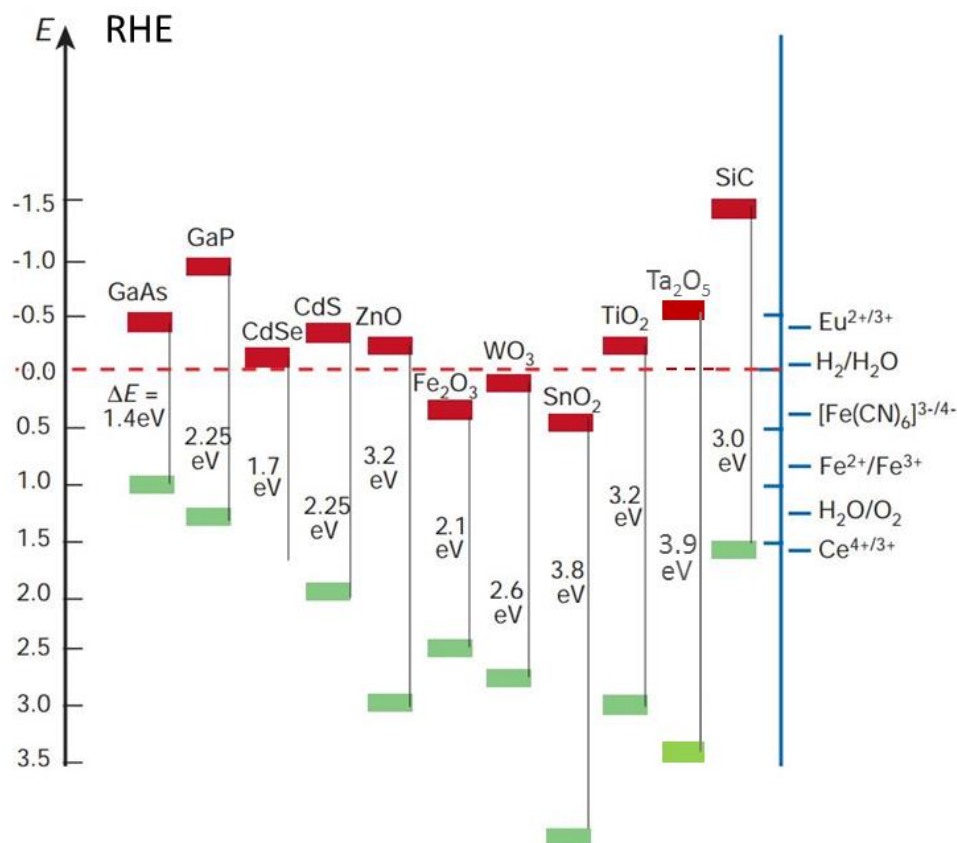


**Figure 1.3** Band positions of several semiconductors in contact with an aqueous electrolyte. The valence band (lower edge) and the conduction band (upper edge) are separated with the bandgap (in eV). The energy scale is with respect to the reversible hydrogen electrode (RHE).<sup>57‡</sup>

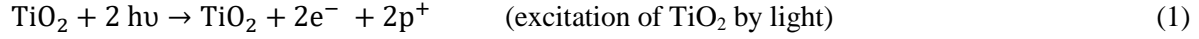
## 1.5 Photoelectrochemical properties of TiO<sub>2</sub> and Ta<sub>2</sub>O<sub>5</sub>

### 1.5.1 TiO<sub>2</sub>

Among all the photocatalyst materials developed to date, TiO<sub>2</sub> remains the most promising material for use as a photoanode for photoelectrochemical water splitting reaction because of its high chemical stability and low-cost production.<sup>58</sup> In the 1970s, Fujishima and Honda investigated the water photolysis, for the first time, by electrochemical decomposition of water using an electrochemical cell with TiO<sub>2</sub> as the photoanode and platinum (Pt) as the photocathode.<sup>59</sup> Their success has motivated researchers to study the photoelectrochemical properties of TiO<sub>2</sub> nanostructures for solar light

<sup>‡</sup> Reproduced with permission from: Grätzel M., Nature **2001**, *414*, 338-344. Copyright (2001) by Nature publishing Group.

harvesting for green energy application. They suggested that water can be decomposed into hydrogen and oxygen by visible light without any external applied voltage following the scheme:



In the past three decades, researchers have given enormous efforts on advancing the photoelectrochemical water splitting properties of TiO<sub>2</sub> nanostructures (nanotubes, nanowires and other hierarchical nanostructures) by developing various techniques. Khan et al. reported that chemically modified TiO<sub>2</sub> nanoparticles, employing as the photocathode, exhibit higher photoconversion efficiency as compared to the as-prepared TiO<sub>2</sub> nanoparticles.<sup>60,61</sup> Park et al. studied the doping effect on the photoelectrochemical water splitting properties of TiO<sub>2</sub> nanotubes and they observed that carbon-doped TiO<sub>2</sub> nanotubes array can significantly enhance the photoconversion efficiency.<sup>62</sup> Kitano et al. investigated the effect of Pt nanoparticles deposited on TiO<sub>2</sub> thin film for photoconversion enhancement and they observed that with the Pt-loading, the water can be decomposed under visible light.<sup>63</sup> Lin et al. created a TiO<sub>2</sub>/TiSi<sub>2</sub> heterostructure system for high-efficiency photoelectrochemical water splitting process.<sup>64</sup> Hartmann et al. conducted a comparative study of the photolysis reactions by using TiO<sub>2</sub> thin film photocathodes prepared by two different mechanisms (nanoparticle based and sol-gel based) and they observed that the sol-gel based mesoporous TiO<sub>2</sub> electrode provides 10 times higher photoconversion efficiency than their counterpart, crystalline nanoparticles based photoelectrode. Several studies reported the active surface dependency of the photoelectrochemical properties of TiO<sub>2</sub> nanomaterials, where different surfaces were observed to exhibit different activities towards the water photolysis reaction.<sup>37</sup> Allam and coworkers performed the nitrogen doping and palladium (Pd) alloying study on TiO<sub>2</sub> nanotube film and attributed that the better enhancement in the photoelectrochemical water splitting properties is achieved combinatorially.<sup>65</sup> Cho et al. have compared the performance of plain TiO<sub>2</sub> nanorods with branched TiO<sub>2</sub> nanorods for hydrogen production during water splitting.<sup>66</sup> They observed that the branched TiO<sub>2</sub> nanorods exhibit manifold increase in the photoconversion efficiency as a result of the four times increase in their specific surface area of the branching, as shown in Figure 1.4.

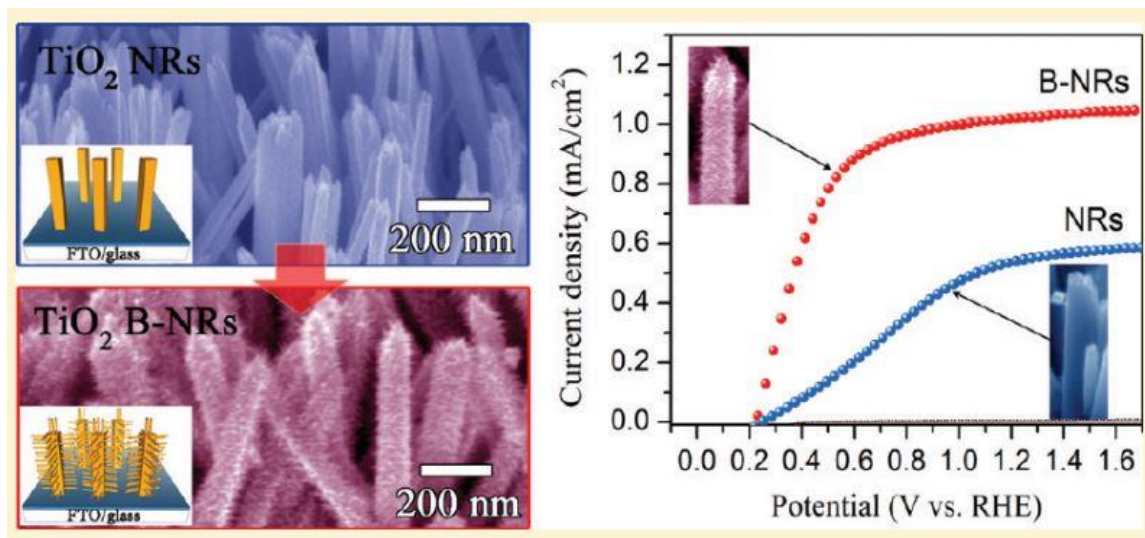


**Figure 1.4** SEM images of TiO<sub>2</sub> plain nanorods and branched nanorods, along with their photoelectrochemical water splitting properties.<sup>66§</sup>

Wang and coworkers have shown the enhancement in water splitting properties of TiO<sub>2</sub> nanowires upon annealing in hydrogen environment at different temperatures.<sup>67</sup> Recently, our group has compared the photoelectrochemical water splitting properties of different TiO<sub>2</sub> nanostructures and demonstrated that the photoelectrochemical water splitting properties can be greatly enhanced in the visible solar spectrum by synthesizing and using defect-rich nanoparticle-decorated TiO<sub>2</sub> nanowires as the photoanode, as shown in Figure 1.5.<sup>40</sup> To date, there has been no study on water photolysis based on ultra-small TiO<sub>2</sub> nanostructures and their size-dependent behavior in the water splitting mechanism. Our work in the water splitting reaction is based on TiO<sub>2</sub> nanoclusters in the size range of 4-10 nm, which we will present detailed size-dependent photolysis study for the first time.

<sup>§</sup> Reproduced with permission from: Cho, I. S. et al., *Nano Lett.* **2011**, *11*, 4978-4984. Copyright (2011) by American Chemical Society.

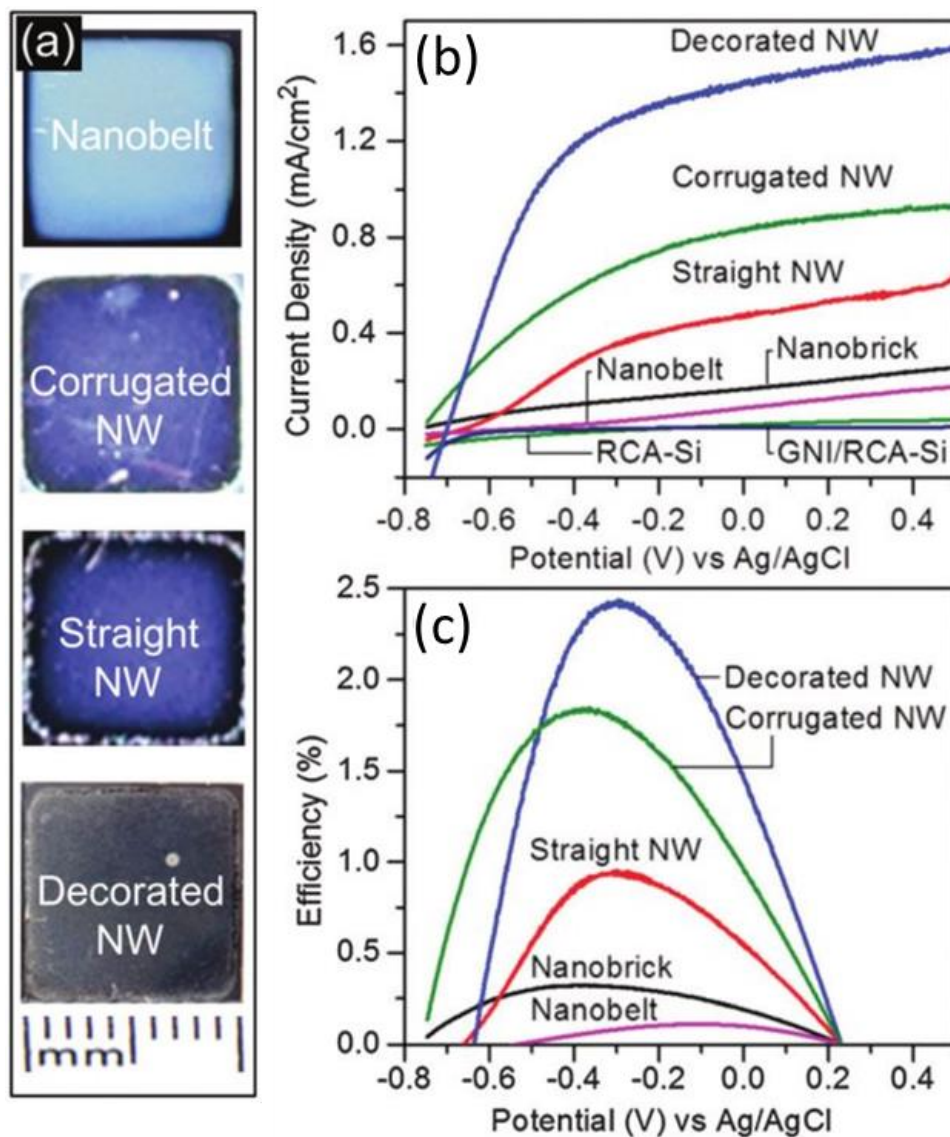


**Figure 1.5** Modified TiO<sub>2</sub> nanowire (NW) and nanobelt structures and their photoelectrochemical water splitting performance. (a) Photographs showing different appearance of these one-dimensional nanostructured films, (b) and (c) are photocurrent densities and photoconversion efficiencies of the corresponding nanostructures as a function of applied potential.<sup>40\*\*</sup>

\*\* Reproduced with permission from: Rahman et al., Energy Environ. Sci. **2015**, 8, 3363-3373, Copyright (2015) by Royal Society of Chemistry.

## 1.5.2 Ta<sub>2</sub>O<sub>5</sub>

On the other hand, Ta<sub>2</sub>O<sub>5</sub>, with a bandgap of ~3.9 eV, has attracted much recent interest as an alternative semiconductor material for photocatalytic reactions. As the redox potentials of H<sup>+</sup>/H<sub>2</sub> and O<sub>2</sub>/H<sub>2</sub>O are well within the valence band maximum and conduction band minimum of Ta<sub>2</sub>O<sub>5</sub>, Ta<sub>2</sub>O<sub>5</sub> promises to be an high-performance catalyst material for solar water splitting.<sup>68</sup> Many different approaches have been extensively investigated in order to achieve efficient photocatalysis with Ta<sub>2</sub>O<sub>5</sub>, and these include developing nanostructures with different morphologies exhibiting large specific surface area with small dimension and bandgap engineering by doping to harvest the visible part of the solar spectrum. The photocatalytic activities of different material forms of Ta<sub>2</sub>O<sub>5</sub> are shown in Table 1.2. Zhou et al. have studied water splitting properties assisted by visible light for an Indium (In) doped Ta<sub>2</sub>O<sub>5</sub> thin film.<sup>69</sup> In our work, we synthesize Ta<sub>2</sub>O<sub>5</sub> nanoclusters using the Nanogen and deposit them on a H-terminated Si (H-Si) substrate. The resulting photocathode has been found to show enhanced photoelectrochemical water splitting efficiency with extremely small amount of material.

**Table 1.2** Ta<sub>2</sub>O<sub>5</sub> photocatalysts for solar water splitting.<sup>68††</sup>

Catalysts	Synthesis method	Cocatalyst (loading amount)	Light source	Reaction solution	Activity (μmol h <sup>-1</sup> g <sup>-1</sup> )	
					H <sub>2</sub>	O <sub>2</sub>
Ta <sub>2</sub> O <sub>5</sub> powder	Commercial	NiO <sub>x</sub> (1 wt%)	400 W Hg	Na <sub>2</sub> CO <sub>3</sub>	153	79
Ta <sub>2</sub> O <sub>5</sub> powder	Commercial	NiO <sub>x</sub> (1 wt%)	400 W Hg	Pure water	190	99
Ta <sub>2</sub> O <sub>5</sub> powder	Solvothermal	None	400 W Hg	2-Propanol	610	NA
Mesoporous Ta <sub>2</sub> O <sub>5</sub>	Ligand-assisted templating	NiO (4 wt%)	450 W Hg	Pure water	1030	544
Mesoporous Ta <sub>2</sub> O <sub>5</sub>	Ligand-assisted templating and sol-gel	NiO (5 wt%)	300 W Hg	Methanol	914.65	NA
Mesoporous Ta <sub>2</sub> O <sub>5</sub>	Ligand-assisted templating	NiO <sub>x</sub> (3 wt%)	450 W Hg	Pure water	112 00 <sup>a</sup>	5433 <sup>a</sup>
Ta <sub>2</sub> O <sub>5</sub> powder	Commercial	NiO (1 wt%)	300 W Hg	Methanol	588	NA
Ta <sub>2</sub> O <sub>5</sub> powder	Commercial	NiO (1 wt%)	300 W Hg	AgNO <sub>3</sub>	NA	48
F doped Ta <sub>2</sub> O <sub>5</sub> spheres	Co-precipitation and hydrothermal	None	NA	Methanol	52.4	NA
Fe doped Ta <sub>2</sub> O <sub>5</sub>	Sol-gel	Pt (1 wt%)	350 W Xe	Methanol	700	NA
In <sub>2</sub> O <sub>3</sub> /Ta <sub>2</sub> O <sub>5</sub>	Sol-gel	Pt (1 wt%)	300 W Xe	Methanol	3780	NA
CdS/Ta <sub>2</sub> O <sub>5</sub>	Evaporation-induced self-assembly and ion-exchange	None	300 W Xe	Methyl blue	10 814	NA
Ta <sub>2</sub> O <sub>5</sub> nanotubes	Anodization	None	240 W Hg-Xe	Ethanol	4900 ± 320	NA
Ta <sub>2</sub> O <sub>5</sub> hollow spheres	Layer-by-layer assembly	None	500 W Xe	Methanol	7100	NA
Ta <sub>2</sub> O <sub>5</sub> hollow spheres	Templating	Ni/NiO	300 W Xe	Methanol	980	NA

<sup>a</sup> Activity of the 1st hour.

†† Reproduced with permission from: Zhang et al., Chem. Soc. Rev. **2014**, *43*, 4395-4422. Copyright (2014) by Royal Society of Chemistry.

## 1.6 Memristors

In addition to the aforementioned remarkable photocatalytic properties, TiO<sub>2</sub> nanostructures also exhibit novel nanoelectronics properties. Until 2005, there has been little interest on their electronic properties, especially the applications of TiO<sub>2</sub> nanostructures as a memory material. After the first ever demonstration of a memory device based on TiO<sub>2</sub> thin film by Strukov et al.,<sup>70</sup> there has been an explosive interest in developing similar memory devices based on the nanostructures of TiO<sub>2</sub>.

Memristors, a concatenation of “memory resistors”, are two-terminal devices categorized as a type of passive circuit elements that maintain a relationship between the time integrals of current and voltage across the terminals. First postulated by Leon Chua<sup>71</sup> in 1971, memristors are the fourth basic circuit elements in the group of other three classical circuit elements, i.e., resistors, inductors and capacitors. From the circuit point of view, three basic two-terminal circuit elements are defined in terms of an interrelationship between two of the four fundamental circuit variables such as the current ( $i$ ), the voltage ( $V$ ), the charge ( $q$ ) and the electronic flux ( $\varphi$ ). Out of the six possible combinations of these four variables, five have been well-known for their interrelationships as represented below and schematically shown in Figure 1.6a:

Resistor between  $V$  and  $i$  ( $dV = Rdi$ )

Inductor between  $\varphi$  and  $i$  ( $d\varphi = Ldi$ )

Capacitor between  $q$  and  $V$  ( $dq = CdV$ )

Only one relationship between  $\varphi$  and  $q$  is undefined. Like the other three, the memristor also exhibits the impedance in the circuit but it is not constant as R, L and C. The memristance, M, is defined by:

$$d\varphi = Mdq$$

where M is a function of  $q$  and therefore the circuit shows a nonlinear behavior.

The hallmark of all memristors is that when a sweep voltage cycle is applied to one of the terminals while keeping the other one grounded, the device shows a pinched hysteresis loop.<sup>‡‡</sup> The most basic mathematical definition of a current-controlled memristor for circuit analysis is the differential form with respect to time:

$$V = R(q) i$$

---

<sup>‡‡</sup> Pinched hysteresis loop is a hysteresis loop where the  $I$ - $V$  curves never intersect the x and y-axes except the origin, i.e. the current waveform should show zero when the applied sweep voltage is set to zero.

$$dq/dt = i$$

where  $q$  is the state variable of the device and  $R$  is the generalized resistance that depends upon the internal state of the device.

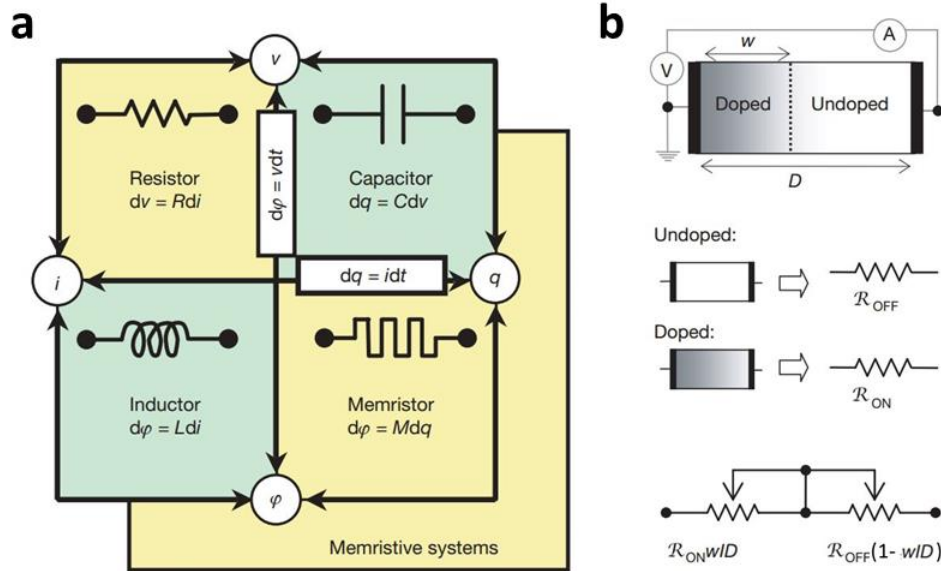


**Figure 1.6** (a) Schematic block diagram for all four fundamental two-terminal circuit elements: resistor ( $R$ ), capacitor ( $C$ ), inductor ( $L$ ) and memristor ( $M$ ). Note that  $R$ ,  $C$ ,  $L$  and  $M$  are the functions of the independent variable, yielding nonlinear elements. In the case of a charge controlled memristor, this variable is a single-valued function  $M(q)$ . (b) Schematic diagrams of a memristor device with two different regions of oxide material (doped and undoped) when operated in the ON and OFF states.  $R_{ON}(w/D)$  and  $R_{OFF}(1-w/D)$  are the resistances in doped and undoped regions, respectively, where  $w$  is the width of doped region and  $D$  is the width of the dielectric.<sup>70§§</sup>

Electrical switching in thin-film devices (especially metal oxide semiconductors) has recently attracted a lot of attention because of its functional scaling capabilities. Memristors are basically the electrical switches that provide two different resistance states with respect to the voltage applied to the circuit. Based on the switching mechanism, the memristors can be largely divided into two categories. Anion-based devices include the oxide insulators, such as transition metal oxides, complex oxides, large bandgap dielectrics and some non-oxides such as nitrides and chalcogenides.<sup>72-74</sup> In this category, the oxygen vacancies are the mobile species and the switching mechanism is therefore based on the resistance change in the oxide material where changes in the valence states in electrode

§§ Reproduced with permission from: Strukov et al., Nature **2008**, 453, 80-83. Copyright (2008) by Nature Publishing Group.

metal occur as a result of the motion of these vacancies. We have listed various functional metal oxides and categorized them according to their unipolar or bipolar switching<sup>\*\*\*</sup> characteristics along with their performance data, as shown in Table 1.3. Our motivation behind fabricating bipolar memristive devices based on  $\text{TiO}_x$  and  $\text{TaO}_x$  is the resistance ratios between high resistance state and low resistance state ( $\Delta R$ ) and the retention time along with endurance which are enhanced multifold in our experiments. For example,  $\Delta R$  in our devices is 260, the retention times are  $10^8$  s whereas the endurance are over  $10^5$ .

In cation-based devices, one of the electrodes is made of an electrochemically active material and the mobile species in this case are metallic cations. The insulating materials in this category are electrolytes such as sulphides, iodides, and selenides.<sup>75-77</sup>

**Table 1.3** List of functional oxides used in redox resistive devices suitable for adaptive electronics applications. TE and BE represent top electrode and bottom electrode, respectively.

Oxide	TE-BE	$\Delta R = R_{\text{ON}}/R_{\text{OFF}}$	Switching Speed	Retention Time (s)	Endurance	Ref.
<b>Binary, Bipolar</b>						
CoO	Ta-Pt	$10^3$	20 ns	-	100	78
HfO <sub>x</sub> / TiO <sub>x</sub>	TiN-TiN	$10^3$	5 ns	$10^5$ @ 27 °C	$10^5$	79
TiO <sub>2</sub>	Pt-TiN	$10^3$	5 ns	$10^5$ @ 85 °C	$10^6$	80
ZrO <sub>2</sub>	TiN-Pt	10	1 μs	$10^5$ @ 27 °C	$10^3$	81
<b>Binary, Unipolar</b>						
HfO <sub>2</sub>	Pt-Pt	$10^2$	-	$10^6$ @ 27 °C	140	82
NiO	Pt-Pt	$10^2$	5 μs	$10^7$ @ 90 °C	$10^6$	72
TaO <sub>x</sub>	Cu-Pt	$10^2$	80 ns	$10^6$ @ 90 °C	100	83
TiO <sub>x</sub>	Pt-Pt	$10^4$	-	-	25	84
WO <sub>x</sub>	TiN-W	4	300 ns	$10^4$ @ 100 °C	$10^7$	85
ZnO	Pt-Pt	$10^4$	-	-	100	86

A typical memristor device consists of an electrochemically active metal oxide thin film sandwiched between a pair of top and bottom metal electrodes, where the sandwiched layer is responsible for switching. After three decades of theorizing the existence of the memristors, Strukov et al. in 2008 were able to produce, for the first time, a working model of memristor device based on a sandwiched  $\text{TiO}_2$  thin film between a pair of Pt layers. They found that the switching mechanism in

<sup>\*\*\*</sup> In unipolar switching, the device switches to ON and OFF with the same voltage polarity while in bipolar switching, an opposite voltage polarity is required to switch the device ON and OFF.

the device between the ON and OFF states are due to the flow of oxygen vacancies within the TiO<sub>2</sub> matrix between the top and bottom Pt layers.<sup>70</sup> As the oxygen vacancies are positively charged, they act like n-type dopants. The area with the higher density of vacancies behaves as a doped region and is conducting in nature, while the counterpart is undoped and is therefore insulating. Figure 1.6b shows the behavior of the switching matrix with the flow of oxygen vacancies with the voltage applied at one electrode with the respective electrode grounded, which lead to two resistance variables,  $R_{ON}$  and  $R_{OFF}$ . As the doped region increases or decreases with the applied voltage sweep, the device is in the ON state when the full length,  $D$  (corresponding to the film thickness of the sandwiched layer) has a high concentration of dopants, and vice versa for the OFF state. The total resistance of the device can be calculated using  $R_{ON}$  and  $R_{OFF}$  and the thickness of the doped region,  $w(t)$ .

$$v(t) = \left( R_{ON} \frac{w(t)}{D} + R_{OFF} \left( 1 - \frac{w(t)}{D} \right) \right) i(t) \quad (1)$$

$$\frac{dw(t)}{dt} = \mu_V \frac{R_{ON}}{D} i(t) \quad (2)$$

which yields the following formula for  $w(t)$

$$w(t) = \mu_v \frac{R_{ON}}{D} q(t) \quad (3)$$

where  $\mu_v$  is the dopant mobility. By combining Equations 1 and 3, the memristance  $M(q)$  of the device can be obtained. Since  $R_{OFF} \gg R_{ON}$ , the equation simplifies to:

$$M(q) = R_{OFF} \left( 1 - \frac{\mu_v R_{ON}}{D^2} q(t) \right) \quad (4)$$

$M(q)$  becomes very large and significant when the thickness of the film scales down. It therefore becomes very important for understanding the electronic characteristics of the devices in the nanoscale.<sup>††</sup>

Yang et al.<sup>87</sup> performed a set of experiments on a single-crystalline rutile TiO<sub>2</sub> bulk crystal with the bandgap of 3.0 eV in a Pt/TiO<sub>2</sub>/Pt memristor. They first created an oxygen-deficient TiO<sub>2</sub> layer near the surface by annealing the crystal in a reducing environment. These oxygen vacancies then transformed the wide bandgap insulating oxide into an electrically conductive doped semiconductor. After the deposition of Pt pads on the top and bottom surfaces, the electrical characterization was

---

<sup>†††</sup> Equations are reproduced with permission form: Strukov et al., Nature **2008**, 453, 80-83. Copyright (2008) by Nature Publishing Group.

performed by applying the voltage on one Pt electrode with the other Pt electrode grounded. All four possible combinations were tried and the resulting four different quasi-static electrical end-states of the devices are shown in Figure 1.7.

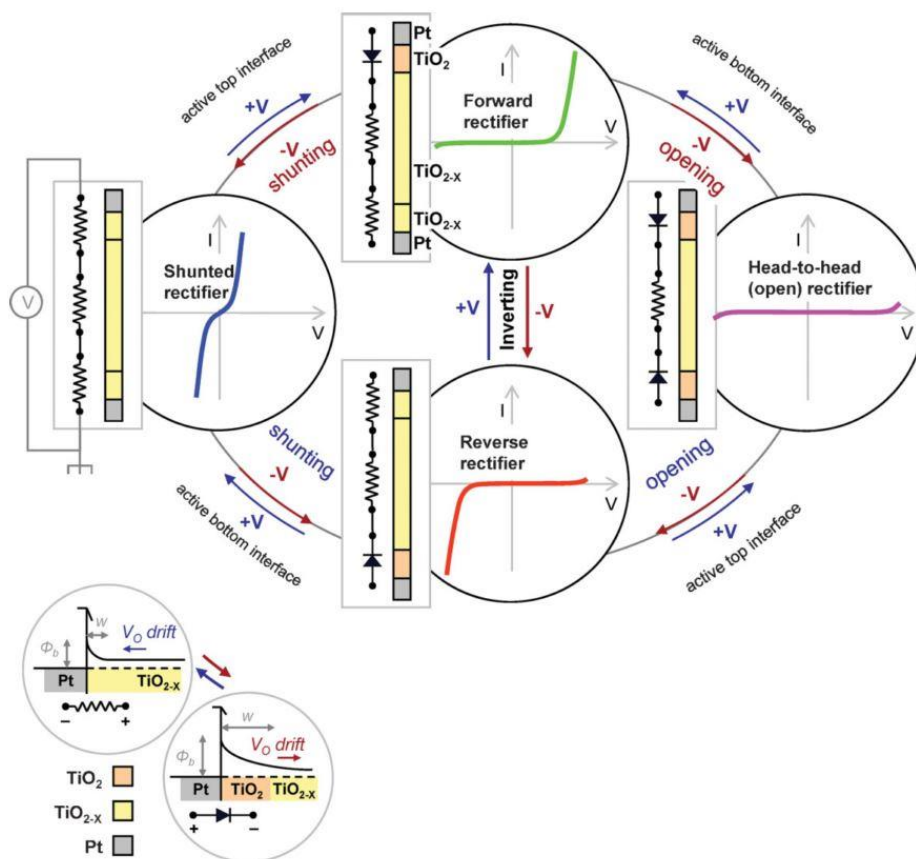


**Figure 1.7** A family of device states exists when two dynamic metal (Pt)/semiconductor ( $\text{TiO}_x$ ) junctions are operated in series exhibiting four different current-voltage characteristics. The interface with metal and insulating oxide interface led with low oxygen vacancy concentration behaves as the Schottky junction where the device works as open rectifier. The metal and conducting oxide interface behaves as Ohmic junction led by high oxygen vacancy concentration, where the band bending facilitates the drift of charge carriers and the device exhibits shunted rectifier<sup>88†††</sup>

The same group later expanded on the concept and fabricated a  $1 \times 17$  array of crosspoint nanodevices with a 30 nm thick Pt film and 120 nm thick  $\text{TiO}_2$  film and showed that the nonlinear electronic transport is controlled by the oxygen vacancy doped metal/oxide interfaces (Figure 1.8).

††† Reproduced with permission from: Yang et al., Adv. Mat. **2009**, *21*, 3754-3758. Copyright (2009) by Wiley Publications.

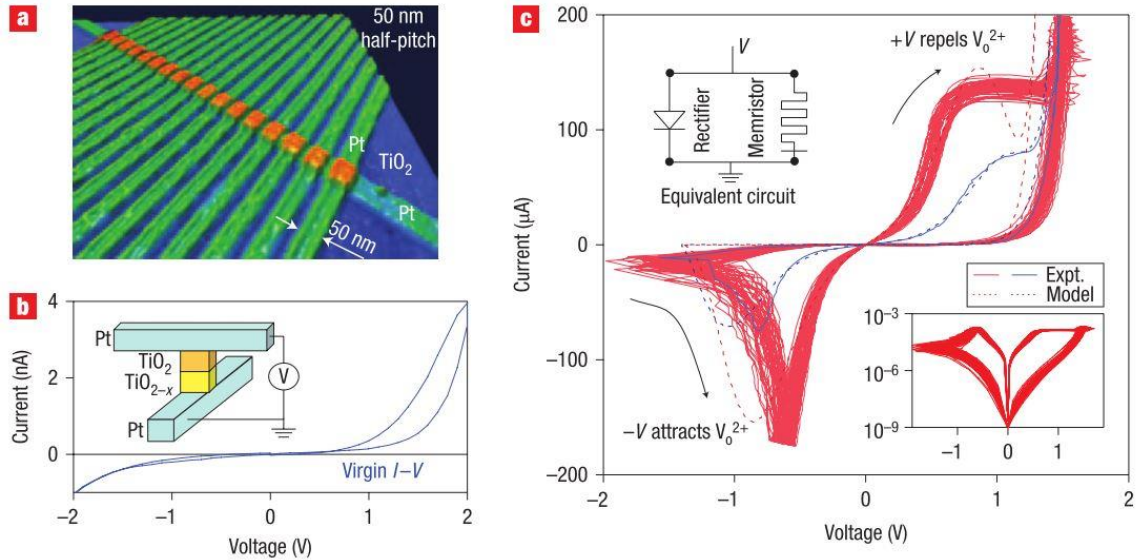


**Figure 1.8** (a) An AFM image of an array of 17 crosspoint nanodevices with a 50 nm half-pitch. The thickness of the insulating TiO<sub>2</sub> layer is 50 nm. (b) The initial *I-V* curve of the device in its virgin state (pre-switching state) exhibits a rectifying state. (c) Experimental (solid) and modelled (dotted) *I-V* switching curves of the device for 50 cycles showing the pinched hysteresis loop for the ON and OFF states (bottom inset shows the log-scale switching) with the top inset depicting the equivalent circuit.<sup>87§§§</sup>

There are various reports describing the switching mechanism based on different types of sandwiched thin films. Generally, there are two types of switching mechanisms in the memristor devices. One is based on drift and diffusion of the oxygen vacancies, which are thermally created by Joule heating. The other mechanism involves the formation and rupture of a conducting filament (a small vertical column between the top and bottom Pt electrodes) of the oxygen-deficient phase. It is possible that both mechanisms could co-exist and different mechanisms could become the predominant one in different material systems. Transition metal oxide films have proven to be the best materials for the memristive applications as they possess many thermodynamically metastable intermediate oxide phases which are conducting in nature, and the resistance state of the oxides can therefore be tuned by creating and manipulating these phases.

According to the driving forces during the memristive switching, the switching behavior of memristors can be divided into four categories as described by Yang et al. in their review article.<sup>89</sup> Depending on whether the switching is thermal dominated or electric-field dominated, the respective

§§§ Reproduced with permission from: Yang et al., Nature Nanotechnology **2008**, 3, 429-433. Copyright (2008) by Nature Publishing Group.

switching behavior could become unipolar/non-polar or bipolar. Schematic diagrams of these switching scenarios are shown in Figure 1.9. Generally speaking, the switching tends to be bipolar if the electric field plays a significant role and nonpolar if the thermal effects are dominant.

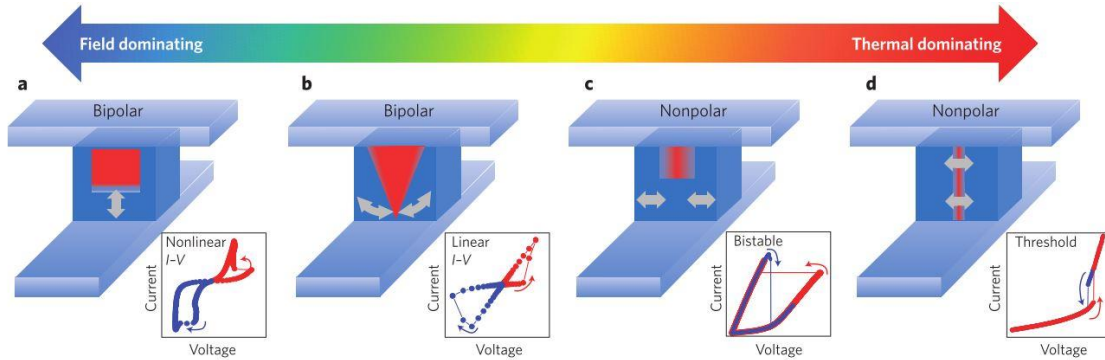


**Figure 1.9** Schematic diagrams of the internal switching phenomena as governed by the nature of the conduction channel: (a) Electric-field-dominating bipolar nonlinear, (b) electric-field -dominating bipolar linear, (c) Joule-heating-driven nonpolar bi-stable, and (d) Joule-heating-driven nonpolar threshold. Inset of each schematic shows the current-voltage loops corresponding to the switching behavior.<sup>89\*\*\*\*</sup>

An essential feature of the memristive switching device is the electroforming step, in which a relatively high voltage (6-10 V) is applied to the device in its virgin state to create the oxygen vacancies as a result of Joule heating in the perfect crystal. Once the electroforming step is over, the device is activated and stable switching between the ON and OFF states is enabled with appropriate applied sweep voltage.

Recently, there has been an increasing interest towards the advancement in the memristive switching properties of the metal oxide films sandwiched between a pair of metal electrodes. As stated above, the  $\text{TiO}_2$  based memristors show nonpolar/unipolar resistive switching dominated by the Joule heating at a high applied bias. Using high resolution transmission electron microscope, Kwon et al. observed that due to Joule heating at high temperature, a small vertical column of the  $\text{TiO}_2$  film is converted to a conducting oxygen-deficient  $\text{Ti}_n\text{O}_{2n-1}$  phase (often known as the Magnèli phase), which is responsible for the device transitioning from the high resistance state (HRS) to the low resistance state (LRS) i.e. the device switches from the OFF to ON state.<sup>90</sup> They concluded that the Magnèli phase is a thermodynamically stable phase with a uniform distribution of oxygen vacancies,

\*\*\*\* Reprinted with permission from: Yang et al., Nature Nanotechnology **2013**, 8, 13-24. Copyright (2013) by Nature Publishing Group.

and therefore with increasing oxygen vacancies the formation of Magnèli phase will be thermodynamically favorable. Celano et al. used conducting AFM tomography to image the surface upon slicing the metal oxide film ( $\text{Al}_2\text{O}_3$ ) layer by layer, in order to identify the region of the conductive filament, as shown in Figure 1.10.<sup>91</sup>

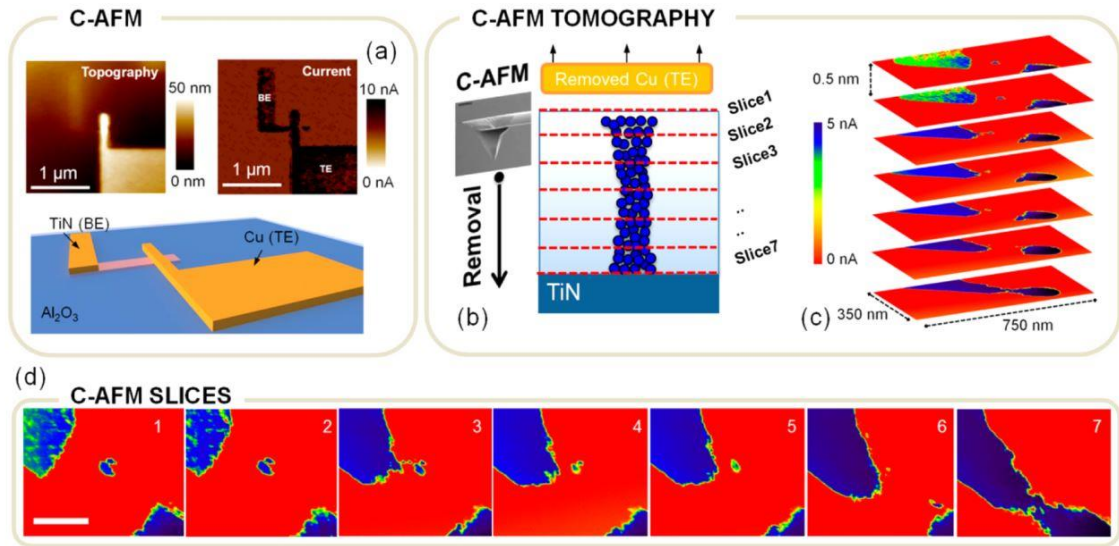


**Figure 1.10** Layer by layer conductive AFM tomography to observe the filamentary structure in  $\text{Al}_2\text{O}_3$  based memristors. The scale bar in Figure 1.10d is 80 nm and the average space between each slice is  $\sim 0.5$  nm.<sup>91††††</sup>

Many reports have discussed the presence of a negative differential resistance during the resistive switching due to the metal-insulator phase transition. Pickett et al. and Alexandrov et al. proposed a model for the coexistence of memristance and current-controlled negative differential resistance in the metal/oxide metal system, and further suggested that the evolution of the negative differential resistance is a thermodynamic process from the locally conductive filaments parallel to the current flow.<sup>92,93</sup>

The thermal dominating electroforming process for the conductive filament formation is less desirable in the switching mechanism due to the asymmetric distribution of temperature during Joule heating. The subsequent device behavior may completely change with the repeated cycles and the device performance could degrade faster.<sup>90,94</sup> The result is that in effect each and every device has to

†††† Reprinted with permission from: Celano et al., Nano Lett. **2014**, *14*, 2401-2406. Copyright (2014) by American Chemical Society.

go through the electroforming step in order to perform the switching afterwards, which is a high-power consumption process. Since high-temperature electroforming is basically uncontrollable and it varies significantly from sample to sample or even within devices on the same chip, there are intense efforts to reduce the electroforming voltage in order to fabricate a long lasting memristive device with low power consumption and stable performance.<sup>95,96</sup> In an effort to increase the stability and performance of the memristors, nanoparticles such as ZnO nanocrystals<sup>13</sup>, Pt nanocrystals<sup>97,98</sup>, and iron oxide (Fe<sub>2</sub>O<sub>3</sub>) nanoparticles<sup>99</sup> have been used as the sandwiched materials or used for embedding into metal oxide thin film.

Though, TiO<sub>2</sub> based memristors have been proven to be excellent memory devices in terms of ON/OFF resistance ratio and switching speed,<sup>80</sup> they lag behind in terms of the lifetime and endurance because of leakage current in every repeated cycle due to oxygen evolution. As a result, the performance degrades in successive cycles due to this corrosion effect. Recently, many groups have attempted to incorporate high-k dielectric materials such as Ta<sub>2</sub>O<sub>5</sub>, V<sub>2</sub>O<sub>3</sub>, and HfO<sub>2</sub> to overcome the issue with the leakage current and thus to improve the endurance of the devices.<sup>100-102</sup> Miao et al. have shown a high repeatability in the switching behavior by using a TaO<sub>x</sub> layer as the switching material that contains a high density of built-in oxygen vacancies but each device has to go through the high-bias electroforming process.<sup>103</sup> Kim et al. have reported the near-electroforming-free switching behavior by doping Si into the Ta<sub>2</sub>O<sub>5</sub> based memristors.<sup>104</sup> Other groups have also been trying to create an electroforming-free memristor device to avoid the high-bias electroforming step and to lower the power consumption. However, these efforts could only lead to operating voltage range of still up to a few volts, which remain too high<sup>105,106</sup> Several of the key steps towards making the electroforming-free memristors involve creating built-in oxygen vacancies, doping and multilayer stacking (Figure 1.11).<sup>102,107</sup> The present work will address the challenges towards fabricating the low power consumption electroforming-free memristive devices based on TiO<sub>x</sub> and TiO<sub>x</sub>/TaO<sub>x</sub> heterojunction multilayer structures with high repeatability and lifetime.

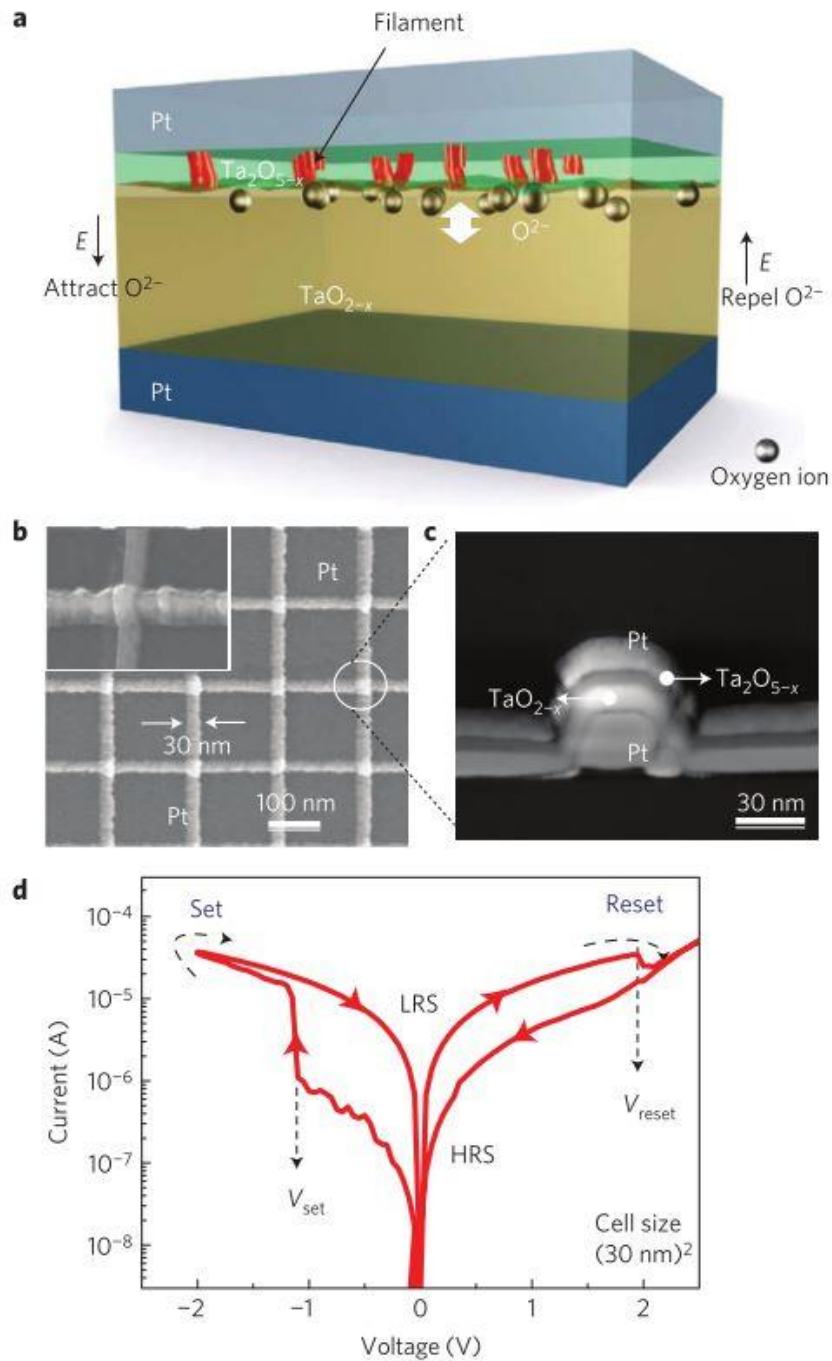


**Figure 1.11** Resistive switching structure of the Ta<sub>2</sub>O<sub>5-x</sub>/TaO<sub>2-x</sub> device. (a) Schematic representation of the multilayer structure with the movement of internal oxygen vacancies responsible for switching. (b) SEM images of the 30-nm crossbar device array. (c) TEM image of the crossbar device stacking (d) typical bipolar *I-V* switching behavior.<sup>107\*\*\*\*</sup>

\*\*\*\* Reproduced with permission from: Lee et al., Nature Materials **2011**, *10*, 625-630. Copyright (2011) Nature Publication Group.

## 1.7 Scope of the Thesis

The general objective of the present work is to develop novel nanoarchitectures based on transition metal and metal oxide materials, particularly  $\text{TiO}_2$  and  $\text{Ta}_2\text{O}_5$ , and to develop their applications as photocatalysts and memristor components. The common goals for these materials are to create defect-rich crystal structures with controlled oxygen-vacancy concentration and hybrid materials to be used in various applications. In the first part, we prepare ultra-small nanoclusters of  $\text{TiO}_2$ , with different morphologies and nanocrystalline behaviors, and investigate their application as photocatalysts for photoelectrochemical water splitting. In the second part, we fabricate memristor devices based on metal/metal oxide/metal device structure and evaluate their current-voltage behavior based on the transition metal oxides as the switching material sandwiched between two metal electrodes. In this chapter (Chapter 1), we present a short introduction to transition metal oxides and their unique properties, along with a brief literature review focusing on the common physical and chemical synthesis methods to produce metal and metal oxide nanoclusters. After a brief introduction to the photoelectrochemical water splitting process and the key parameters, we then reviewed recent important studies of  $\text{TiO}_2$  and  $\text{Ta}_2\text{O}_5$  nanostructures used for photoelectrochemical water splitting reaction. In the latter half of Chapter 1, we discussed the memristors and their material-based switching mechanisms, along with a review of recent studies on achievable device performance. In Chapter 2, we briefly describe the experimental procedure used to synthesize the metal/metal oxide nanoclusters and thin films, along with a more detailed discussion about the deposition parameters. We briefly outline the working principle of the characterization techniques used to study their morphologies, crystal structures, and chemical-state composition properties. Characterization techniques for investigating the optical, electrical and photoelectrochemical properties are also given. We have also described the micro/nanodevices fabrication techniques and the process parameters relevant for memristor device work.

We present our data in the next four chapters. We describe the synthesis and characterization of precisely size-selected  $\text{TiO}_2$  nanoclusters (Chapter 3),  $\text{Ta}_2\text{O}_5$  nanoclusters and co-deposited ( $\text{TaO}_x$ , Pt) nanoclusters (Chapter 4) deposited on various substrates using the gas-condensation technique via DC magnetron sputtering. Detailed studies of the resulting morphology, crystal structure and chemical-state composition properties of these nanoclusters obtained by manipulating key growth parameters, including Ar-gas flow, condensation zone length (aggregation length), deposition time, input power and AC/DC voltage sets on the quadrupole mass filter, are given. We then investigate and evaluate the size-dependent photoelectrochemical water splitting properties of  $\text{TiO}_2$ , and  $\text{TaO}_x$  and ( $\text{TaO}_x$ , Pt) nanoclusters. The density of Pt nanoclusters has also been varied in the latter case in order to examine

their effect on water splitting. Our results show one of the highest photoconversion efficiencies for such nanocluster systems with a very low amount of material loading which is also well comparable to the other photocatalytic materials without any post modification. The performances could easily be improved by increasing the nanocluster loading onto the substrate or chemically modifying the nanocluster surface or both.

Chapter 5 presents the study of non-volatile memristor devices based on nanocrystalline  $\text{TiO}_x$  thin film as the switching material in the Pt/ $\text{TiO}_x$ /Pt system. After detailed discussion of the fabrication process and the parameters used for the multilayer stacking, we present the underlying mechanism of resistive switching with high ON/OFF current ratios. A special interest is the dependence of switching behavior on the junction size and this aspect will be investigated with devices with appropriately fabricated junction sizes. Our result shows the lowest electroforming voltage (1.5 V) ever reported for the  $\text{TiO}_x$  based system, with remarkably high retention capabilities ( $10^8$  s). The high repeatability, high endurance and very high retention qualities are attributed to the low electroforming voltage because of the nanocrystalline nature of the  $\text{TiO}_x$  film.

In Chapter 6, we present the further studies on the enhancement of the memristive switching properties by incorporating a highly oxygen deficient  $\text{TaO}_x$  layer as a source of oxygen vacancies. The current-voltage characteristics of the devices exhibit an electroforming-free nature, where a high bias is not required to perform the high power consumption, irreversible electroforming step to turn the device ON for the first time. This is a significant result where the combine effect of  $\text{TiO}_x$  and  $\text{TaO}_x$  layers are stacked together to form the electroforming-free memristive devices for the first time. The high repeatability, very high endurance and ultra-high retention capabilities of the Pt/ $\text{TiO}_x$ / $\text{TaO}_x$ /Pt device is attributed to the nanocrystalline nature of all the films and to the high dielectric constant of  $\text{TaO}_x$  film, which significantly reduces the leakage current and thus enhancing the performance stability. The similar SET voltages for hundreds of devices fabricated on the same chip describe the reproducibility of the memristors. In addition, the thickness variation of the  $\text{TaO}_x$  layer, while keeping the  $\text{TiO}_x$  layer thickness same, leads to two different switching mechanisms, which are elaborated further in this chapter.

Finally, we summarize, in Chapter 7, our conclusions and comments on future work.

## Chapter 2

### Experimental Details

This chapter summarizes the experimental techniques that are used for synthesis and characterization of metal/metal oxide nanoclusters and thin films, and the fabrication techniques used to fabricate micro/nanodevices.

#### 2.1 Synthesis and Deposition of Metal/Metal Oxide Nanoclusters (NCs)

The metal/metal oxide nanoclusters are deposited by using a novel NC generation source based on a gas-phase aggregation technique, in which the source atoms are sputtered off the source target by DC magnetron sputtering into an aggregation zone where they condense and aggregate to form clusters in nanoscale range.<sup>108</sup> There are many parameters that can be optimized to achieve the selectivity in terms of size, shape and properties of these NCs. A high-resolution quadrupole mass filter is coupled with the system to perform the size selection on the nanoclusters in the gas phase before depositing onto the substrate. Depending on the material, the range of the NC size (diameter) can be varied from as small as 1 nm to 15 nm by varying the deposition parameters. These parameters are carrier gas flow, aggregation (condensation) zone length, source current supply, deposition or sample temperature, pressure and AC/DC voltage ratio (U/V ratio) on the quadrupole mass filter. The working principle and effect of each parameter will be explained in the following sections. Figure 2.1 shows the photographs of the nanocluster generation source (Nanogen 500, Mantis Deposition Ltd.)<sup>109</sup> used in the present work. Housed in the bottom chamber of the Nanogen system (Figure 2.1a) is the NC generation source that consists of a trio head where three different metallic sources (each 5 mm dia., 3 mm thick) can be installed and they can be ignited one by one for multilayer deposition or simultaneously for co-deposition. The quadrupole mass filter is housed in the top chamber of the Nanogen system (Figure 2.1b) and is used for the precise size-selection of the NCs.

Gas-phase aggregation technique is based on the principle of emission of source atoms under plasma sputtering. A plasma is generated when the molecules of an inert gas, such as Argon (Ar), are field ionized with the applied bias. Guided by a DC magnetic field, the  $\text{Ar}^+$  ions strike the source material and sputter off the source atoms. These source atoms then travel through the aggregation zone where they collide with one another and agglomerate together to form the nanoclusters, which then leave the aggregation zone through a 5 mm orifice. Precise size selection of the nanoclusters is achieved just before exiting from the orifice by applying a set of appropriate AC and DC voltages on

the diagonal pole pairs of the quadrupole mass filter. The size distribution curve corresponds to the collector current collected as a function of the nanocluster size on the quadrupole mass filter. A particular set of AC-DC voltages allow clusters of a particular size to follow an appropriate oscillatory path to pass through the quadrupole, exit the orifice, and deposit on the substrate placed at 30 cm above the quadrupole mass filter. Clusters of all other sizes follow different oscillating paths that do not lead to the orifice and these clusters are lost inside the Nanogen chamber.

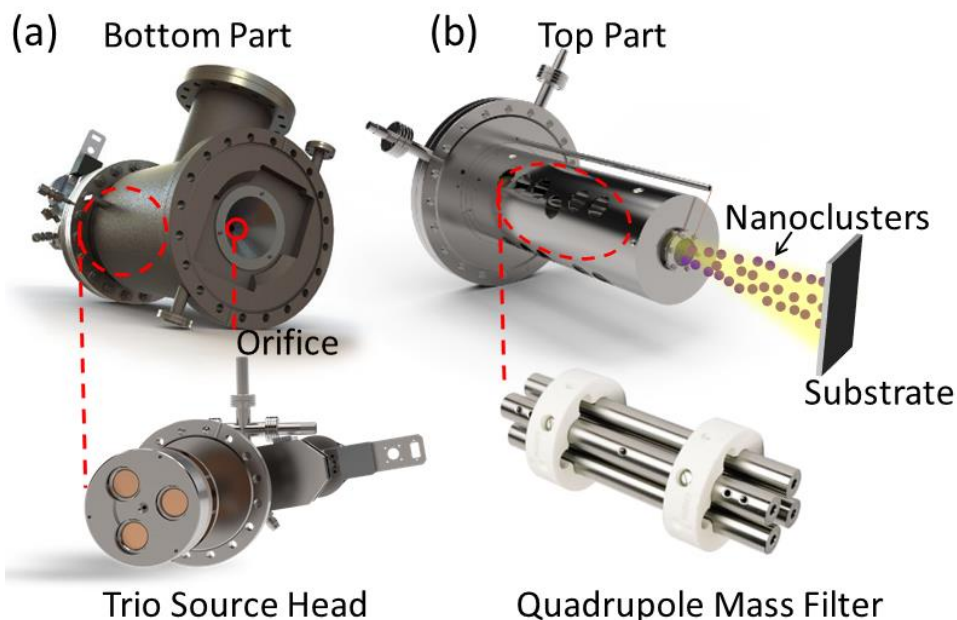


**Figure 2.1** Photographs of different parts of Nanogen nanocluster generation source. (a) The bottom chamber (top left) houses the source head (bottom left). (b) The top chamber (top right) contains the quadrupole mass filter (bottom right). The NCs get deposited onto a substrate placed 30 cm in front of the exit (orifice).<sup>§§§§</sup>

## 2.1.1 Effects of Nanogen parameters on the nanocluster synthesis

### 2.1.1.1 Gas flow:

Argon flow plays an important role during the growth of NCs in three ways. A certain amount of the Ar atoms, depending on the applied bias, undergo field ionization to generate the plasma for sputtering the source material, while some act as the nucleation seeds in the gas phase for the nanoclusters to grow and the majority of the atoms work as the carriers to transport the nanoclusters towards the orifice. Low Ar gas flow rate provides less seeds for NCs to grow while at the same time

<sup>§§§§</sup> [www.mantisdeposition.com/](http://www.mantisdeposition.com/).

the kinetic energy of the as-grown NCs becomes smaller inside the aggregation zone. Consequently, the clusters stay in the aggregation chamber for a longer time and become bigger, which leads to a larger cluster size. On the other hand, high Ar-flow rate causes the as-grown clusters to sweep away quickly through the orifice and they do not have sufficient time to agglomerate further, which leads to a smaller NC size.

#### 2.1.1.2 Aggregation zone length:

Aggregation zone length is the second most important parameter that controls the NC size. Large aggregation zone facilitates a greater number of collisions among the NCs before they exit from the orifice, which results in the larger size of the NCs so produced due to agglomeration. A smaller aggregation zone length does not provide enough time for a high number of collisions and therefore the size of the NCs becomes smaller.

#### 2.1.1.3 Source current supply:

Source bias also plays a decisive role for the size and shape of the as-grown nanoclusters. A lower applied bias creates a lower intensity plasma and therefore a smaller amount of sputtered source material, which leads to a lower number of atoms available for collisions and agglomeration to form bigger NCs. A low bias therefore generally produces smaller NCs and conversely a high bias creates larger NCs. In terms of cluster density, a high bias generates a higher cluster density because of the higher sputtering rate.

#### 2.1.1.4 Deposition temperature:

Nanocluster agglomeration rate during deposition on a substrate depends upon the deposition temperature (i.e., substrate temperature). A higher substrate temperature provides more energy to the NCs impinging at the substrate surface, enabling the NCs to more efficiently self-organize on the substrate. On the other hand, at low temperature or room temperature, the as-grown nanoclusters undergo soft landing on the substrate with minimal further movement.

#### 2.1.1.5 AC/DC voltage ratio of quadrupole mass filter:

A quadrupole mass filter is used to perform size selection of NCs obtained by gas-phase aggregation according to their mass-to-charge ratio. The quadrupole mass filter consists of four cylindrical metallic poles of equal length and diameter appropriately placed to create an oscillating field. A set of AC and DC voltages can be applied to diagonal pole pairs to create the electrostatic field that facilitates a charge particle with a specific charge-to-mass ratio to follow a well-defined oscillating path. As the as-grown NCs leave the aggregation zone and enter the mass filter region, only NCs of a

particular charge-to-mass ratio (preselected by the appropriate AC and DC voltages) are allowed to pass through the mass filter following the appropriate oscillating path, while others would impinge into the mass filter and other parts of the chamber and would therefore be blocked from reaching the substrate. Only the nanoclusters with the correct charge-to-mass ratio could reach the substrate and the resulting NCs so deposited are essentially mono-sized within  $\pm 0.2$  nm. The size distribution of the NCs corresponds to the collector current measured on the mass filter. By monitoring the collector current, size selection can be performed in real time by applying AC and DC voltages with the appropriate ratio that corresponds to the mode cluster size during deposition.

Once the nanoclusters pass through the mass filter, they are collected on the substrate positioned in front of the quadrupole mass filter. Different physical parameters can also be varied on the substrates to control how the nanoclusters arrange themselves upon landing. These parameters are deposition time, substrate temperature, bias and conductivity.

## **2.2 Deposition of metal or metal oxide thin film**

The main vacuum system connected to the Nanogen source used for depositing nanoclusters also houses two RF and two DC magnetron sputtering sources that are used for ultrathin film deposition. Due to the availability of the RF bias (and the RF sputtering sources), even metal oxide targets can easily be sputtered, allowing metal oxides (and dielectrics and insulator materials) to be deposited. Four different source targets can be sputtered in various combinations simultaneously or all together to achieve controlled intermixing and/or sequentially one by one to create multilayer heterojunctions. Multiple mass flow controllers are connected to the sputtering sources in order to control the various gas flow rates and ratios in the chamber during deposition. Some gases (such as  $N_2$  or He) can be used for doping purposes as well. Figure 2.2 shows the physical vapor deposition system (Mantis Deposition Ltd.) that contains the four magnetron sputtering sources and the Nanogen source. The physical properties of the deposited films depend on a few important parameters such as Ar gas flow, Ar/ $O_2$  ratio, substrate temperature and deposition time, which can be chosen appropriately to achieve the desired quality and properties. A quartz crystal monitor, attached just below the substrate holder, is used to measure the deposition rate of the growing film.

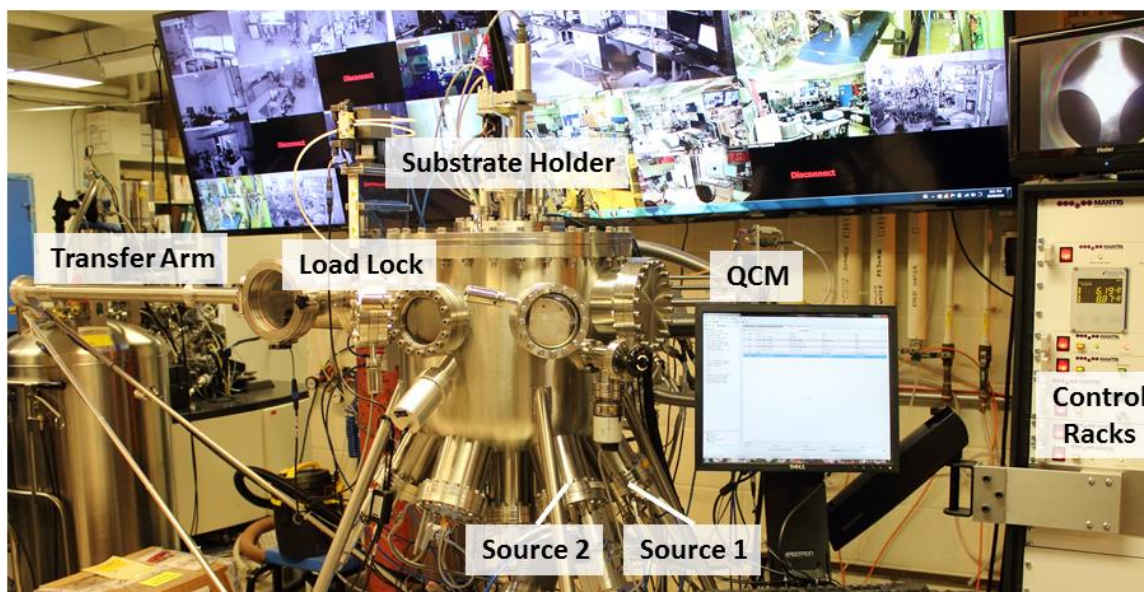


**Figure 2.2** Photograph of the physical vapor deposition system based on the magnetron sputtering technique that is used for both thin film deposition and clusters generation via the Nanogen source (Mantis Deposition Ltd.). (a) Two RF and two DC sputtering sources, along with a quartz crystal monitor (QCM) are installed, along with (b) controlled electronics.

### **2.3 Characterization of the synthesized nanostructures using scanning electron microscopy (SEM), transmission electron microscopy (TEM) and atomic force microscopy (AFM)**

The structure-property relations and shape/size-dependent properties of the samples are investigated by using different electron microscopic techniques to image the surface and structure of metal/metal-oxide nanoclusters, thin films and nanowires.<sup>110</sup> Field-emission Scanning Electron Microscopy (SEM) is always the first tool to be used to examine the surface morphology of the samples. Figure 2.3 shows the Merlin SEM microscope, which is equipped with a field-emission source and the Gemini-II advanced electron optics column capable of an acceleration voltage up to 30 kV. The Merlin has been used to examine the nanocluster size distribution on the substrate and their surface morphology at high magnification, and also the surface morphologies of thin films and nanowires in the present work. In SEM, a high-energy electron beam is focused on the sample with a typical spot size of 1 nm. The electron beam interacts with the sample, creating secondary electrons (with kinetic energy less than 50 eV). The secondary electrons emitted near the surface are then collected by using an appropriate detector upon scanning this fast incident electron beam across selected area of the sample. Various detectors are employed in the microscope and they include Everhart-Thornley type in-lens

and out-of-lens detectors for secondary electron imaging and energy-selective and angle-selective detectors (AMETEK) for backscattered electron imaging.

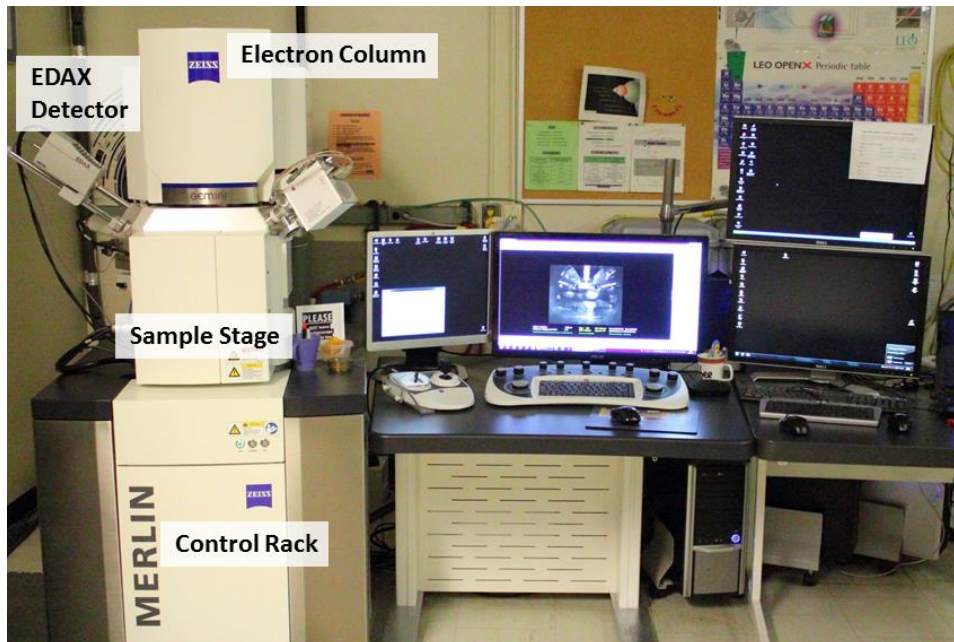


**Figure 2.3** Photograph of the MERLIN field-emission scanning electron microscope (FESEM), equipped with secondary electron in-lens and out-of-lens (SE2) detectors, and backscattered electron detector (BSD) as well as an EDAX energy-dispersive X-ray analysis system.

The system is also equipped with an EDAX energy-dispersive X-ray (EDX) analysis system, which provides elemental composition characterization of the sample based on detection of element-specific X-ray emission from the sample, upon excitation by the high-energy electron beam. The X-ray emission spectra can be used for quantification of the composition of the elements in the sample through the intensities of their characteristic X-ray emission lines.<sup>111</sup>

Transmission electron microscopy (TEM) measurements<sup>112,113</sup> have been performed by using a JOEL 2010F microscope at McMaster University and more recently a Zeiss Libra 200 MC microscope at the University of Waterloo, both operated at 200 kV (Figure 2.4). The nature of the crystalline structure and identification of the crystal planes of the individual nanostructures are investigated by using TEM. The samples for TEM analysis are generally prepared by either directly depositing the material onto the lacey carbon coated copper grid (in case of thin film and nanoclusters) or by scrapping with a sharp blade the nanowires off the substrate and transferring them on the TEM grid.

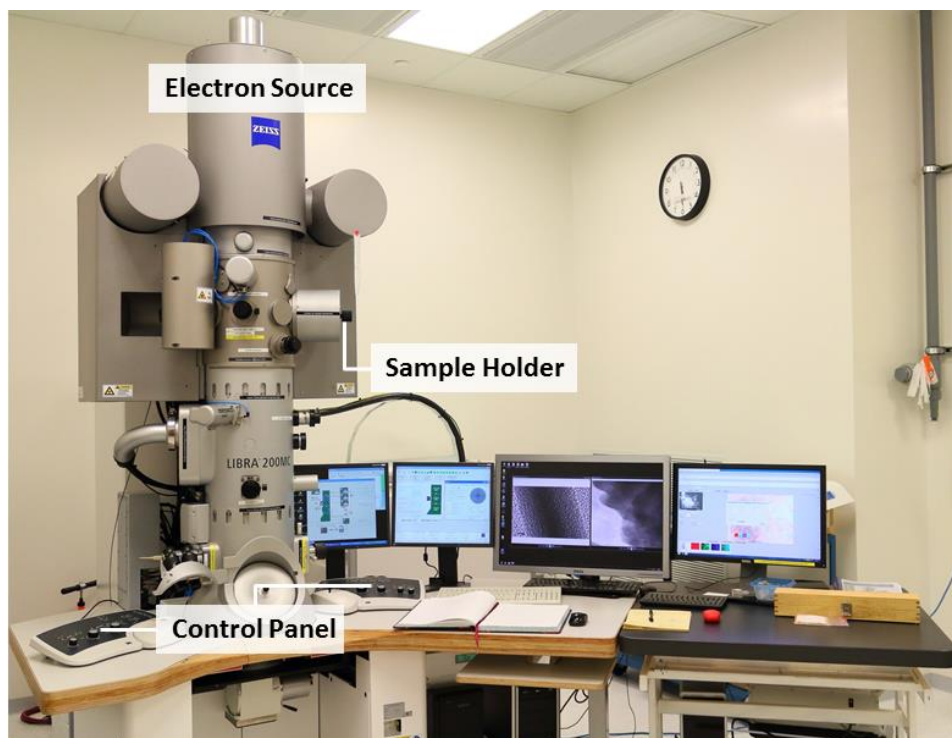


**Figure 2.4** Photograph of a Zeiss Libra 200 MC transmission electron microscope.

Atomic force microscopy (AFM)<sup>114</sup> is conducted in a Digital Instruments Dimension 3100 Nanoman Nanoscope IV (Figure 2.5). AFM is used to characterize the nanocluster size distribution on the substrate and the surface roughness of the nanocluster film and thin films. The samples are scanned in tapping mode using a silicon nitride ( $\text{Si}_3\text{N}_4$ ) tip. Since AFM has a lateral resolution limit of  $>10$  nm and is usually too large for the nanoclusters (with diameters less than 8 nm), the vertical height profile is used to measure the size distribution of the nanoclusters due to much higher height resolution (few Å) in AFM.

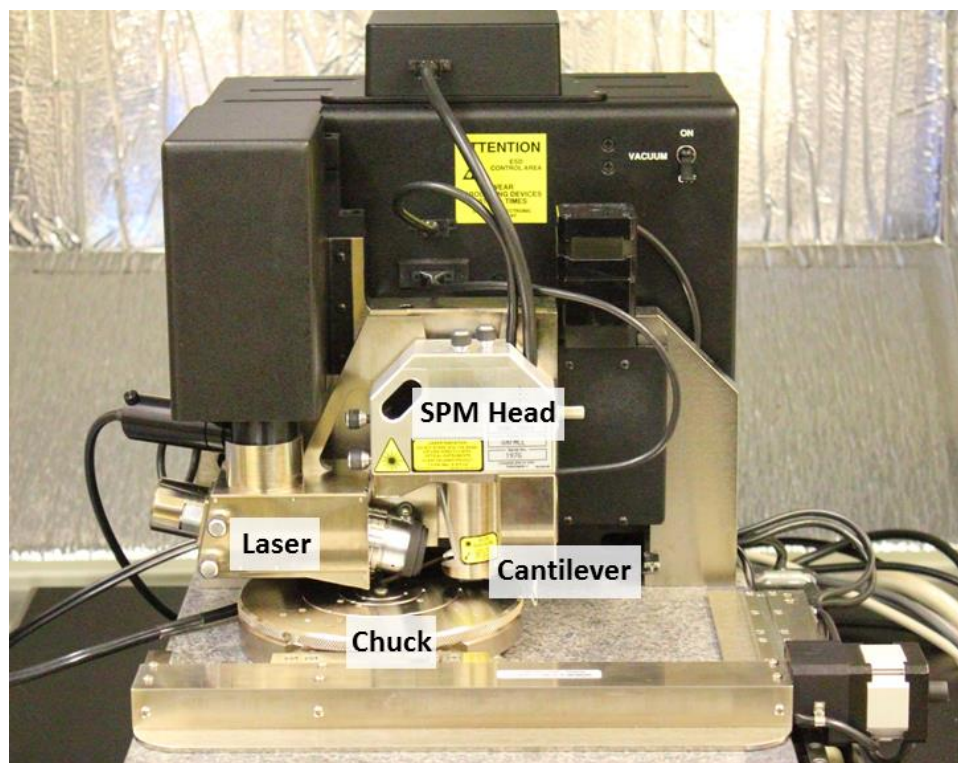


**Figure 2.5** Photograph of Digital Instruments Dimension 3100 Scanning Probe Microscope used for atomic force microscopy.

## **2.4 Composition Analysis by X-ray Photoelectron Spectroscopy (XPS) and Secondary Ion Mass Spectroscopy (SIMS)**

### **2.4.1 XPS Chemical-State Composition Analysis**

In order to examine the chemical-state composition of the as-prepared metal and metal oxide nanoclusters and thin films, X-ray photoelectron spectroscopy is used.<sup>115</sup> XPS spectra have also been collected in the depth-profiling mode to understand the chemical-state compositional changes in the near-surface region as a function of sputtering depth using an Argon ion source to sputter away materials interleavingly between XPS spectral measurements. The XPS system used in this project is Thermo-VG Scientific ESCALab 250 Microprobe (Figure 2.6), which is equipped with an Al K $\alpha$  monochromatic X-ray source (1486.6 eV) and is capable of a typical energy resolution of 0.4-0.5 eV full width half maximum (FWHM). When the incident X-ray impacts the sample, the subsequent de-excitation by emission of an electron from either the core or valence levels of the sample produces the photoelectron. The kinetic energy of these photoelectrons is analyzed by using a hemispherical

energy analyzer and can be used to determine the corresponding binding energy by the Einstein equation:

$$E_{\text{binding}} = E_{\text{hv}} - (E_{\text{kinetic}} + \phi)$$

where  $E_{\text{binding}}$  is the binding energy of the electron,  $h\nu$  is the photon energy (i.e. 1486.6 eV for Al  $K\alpha$ ;  $h$  is the Planck constant and  $\nu$  is the light frequency),  $E_{\text{kinetic}}$  is the kinetic energy of the photoelectron as measured by the analyzer, and  $\phi$  is the work function dependent on both the spectrometer and the material.

The electrons photo-ejected from the atomic core-levels or from the valence band of the material when illuminated with the monochromatic X-rays have typical kinetic energies that correspond to an inelastic mean free path (i.e., escape depth) of less than 10 nm, making XPS an extremely surface-sensitive technique. By comparing the binding energy of specific chemical states with the corresponding references, we can infer information about the local chemical environment by determining the chemical shifts.

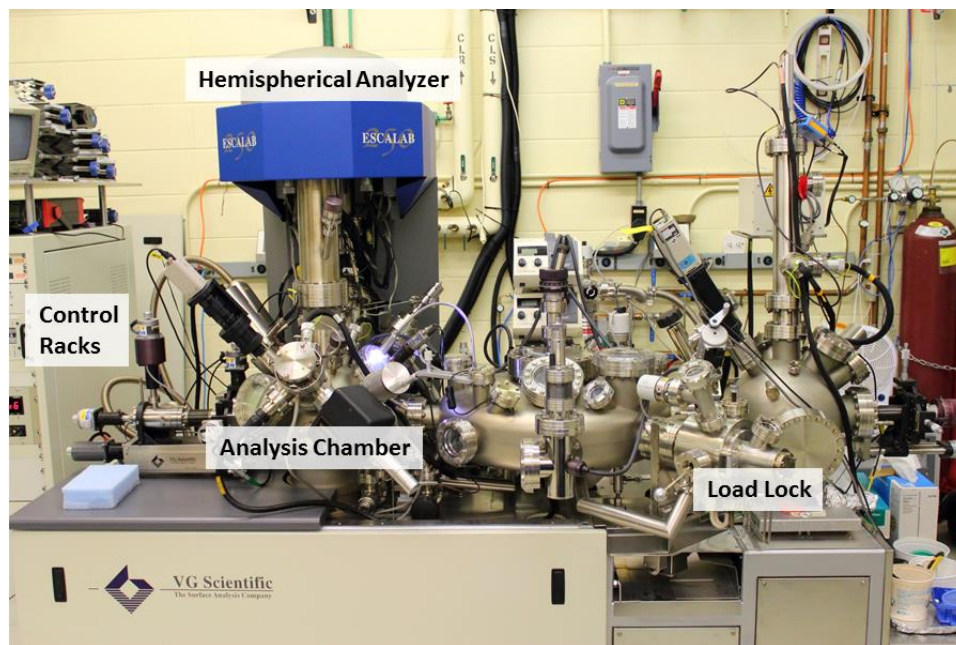


**Figure 2.6** Photograph of the Thermo-VG Scientific ESCALab 250 Microprobe used for chemical-state composition analysis of the nanoclusters and thin films.

## 2.4.2 SIMS Chemical Mapping

Time of flight secondary ion mass spectrometry (ION-TOF-SIMS 5) is a surface analysis technique that can produce three-dimensional high-resolution chemical images.<sup>116</sup> SIMS can also be used for analyzing soft materials and biomaterials nowadays because of the recently introduced Argon cluster sputtering ion source technology. SIMS works on the principle of ion-based imaging where emission of secondary ions is triggered by bombarding the sample surface with a focused high-energy primary ion beam (1-40 keV). Based on the time-of-flight of secondary ions travelled in the TOF analyzer, the nature of the secondary ions can be identified.<sup>117</sup> Selected peaks in the resulting mass spectra collected point by point on the surface by rastering the primary ion beam across the surface can be used to construct the chemical maps of specific ions (chemical species) of interest.

In the ION-TOF SIMS 5 system (Figure 2.7), the  $\text{Bi}^{3+}$  primary ion source (analysis beam) positioned at  $45^\circ$  to the sample is operated at 30 keV beam energy with a 0.4 pA beam current and a 100  $\mu\text{s}$  pulse width. Secondary ions are electrostatically directed to the TOF analyzer by biasing the sample stage at 2.5 kV with the extraction lens set at 4.5 kV at an opposite polarity. Appropriate secondary ions are collected over a rastered sampling area usually of  $100 \times 100 \mu\text{m}^2$  to obtain a 2D map. The sample could also be sputtered with a  $\text{Cs}^+$  ion beam or an Argon cluster ion beam (each generated from a separate sputtering ion source) alternating with the  $\text{Bi}^{3+}$  primary ion beam to remove the sample layer by layer at a well-defined sputtering rate.

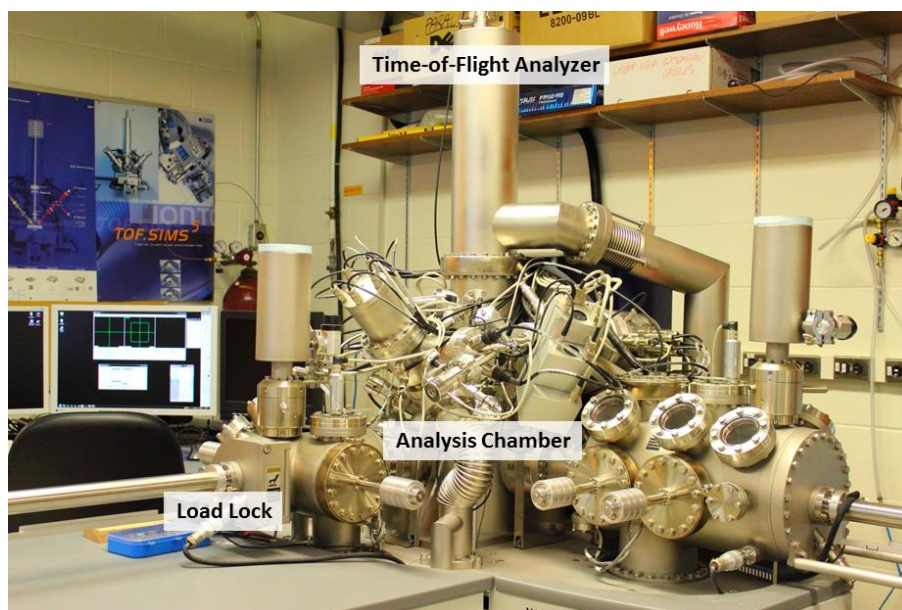


**Figure 2.7** Photograph of ION-TOF SIMS-5 system used for chemical analysis of the metal/metal oxide heterostructures.

## 2.5 X-ray Diffraction Crystallography and Ultraviolet/Visible (UV/Vis) Spectroscopy

### 2.5.1 X-ray Diffraction Crystallography

X-ray diffraction (XRD) is a powerful tool for determining the crystallography of the bulk as a hard X-ray beam (e.g. Cu K $\alpha$ ) could penetrate deep into the materials in order of micrometers.<sup>118</sup> Crystal structures of metal or metal oxide nanomaterials are analyzed by using a Panalytical X'pert Pro MRD X-ray diffractometer, capable of various optics and diffraction geometries (Figure 2.8). Since the amount of nanomaterial on the substrate surface is mostly very small, the intensity from the nanomaterial is low and is overwhelmed by the substrate signal (Si in our case). In this case, glancing incidence X-ray diffraction (GIXRD) technique is used to capture more signal from the nanomaterials and less from the substrate. In GIXRD, the detector is moved from 0 to 2 $\theta$  angle while the incidence angle of the X-ray beam is maintained at a very shallow angle (close to the critical angle of the sample). As the incidence angle is below the critical angle, an evanescent wave is formed, and it penetrates less than 100 nm of the surface and therefore produces enhanced signal from the very thin top layer of the nanomaterial, overcoming the substrate signal. For this purpose, a parallel beam geometry with an X-ray mirror on the incident beam side and a parallel-plate collimator on the diffracted beam side is used. This configuration allows GIXRD measurements at a typical incidence angle of 0.4° for most samples.

To analyze the grain size, we perform the Scherrer analysis. The Scherrer formula used for calculating the average crystallite size is given by:

$$\text{Crystallite Size} = \frac{K \times \lambda}{(B_{\text{Observed}} - B_{\text{Instrument}}) \times \cos \theta}$$

where K is the shape factor of the nanocrystallites (typical value close to 1),  $\lambda$  is the wavelength of the X-ray used for obtaining the diffraction pattern,  $\theta$  is the peak position,  $B_{\text{Observed}}$  is the peak width (or FWHM) of the most intense XRD peak of the sample, and  $B_{\text{Instrument}}$  is the peak width observed for the standard stress-free sample, which arises due to instrumental effects. For the X-ray optics used in our GIXRD system, the observed  $B_{\text{Instrument}}$  is 0.40° (or 0.0022 rad).

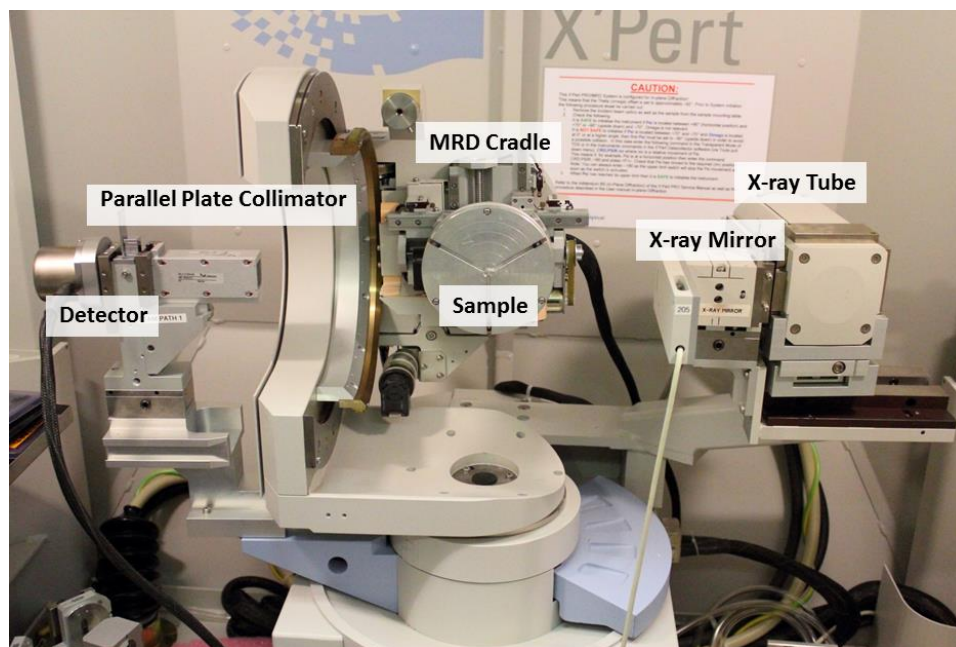


**Figure 2.8** Photograph of the Panalytical X'pert Pro MRD X-ray diffractometer used for crystal structure characterization of thin films. The instrument is set up in the parallel beam geometry with an X-ray mirror and a parallel plate collimator used for the incident and diffracted beam optics, respectively.

## 2.5.2 Ultraviolet/Visible (UV/Vis) Spectroscopy

Spectroscopic techniques are commonly used to analyze the optical behavior of the metal and metal oxide nanocluster film and thin films.<sup>119</sup> The optical properties of the metal and metal oxide nanocluster film (deposited by using the Nanogen source) and thin films (deposited by using RF magnetron sputtering sources) as-deposited and annealed on glass substrates are investigated by using a UV/Vis spectrophotometer (Perkin-Elmer Lambda 1050) with a wavelength range of 175-3300 nm and a bandwidth of 2 nm, and with a monochromator for reducing stray light and also for enhancing the resolution (Figure 2.9). The system has high sensitivity photomultiplier, peltier-controlled InGaS and PbS detectors to provide the full UV/Vis/NIR range. All the measurements are performed in transmittance mode within the wavelength range 200-600 nm. The transmittance (T) can be converted to absorbance A by using the formula,  $A = -\log T$ . The band gap of the material can be calculated using the formula  $E_g = 1240/\lambda_{\max}$ , where  $\lambda_{\max}$  (in nm) is the wavelength of maximum absorption and  $E_g$  (in eV) is the band gap.

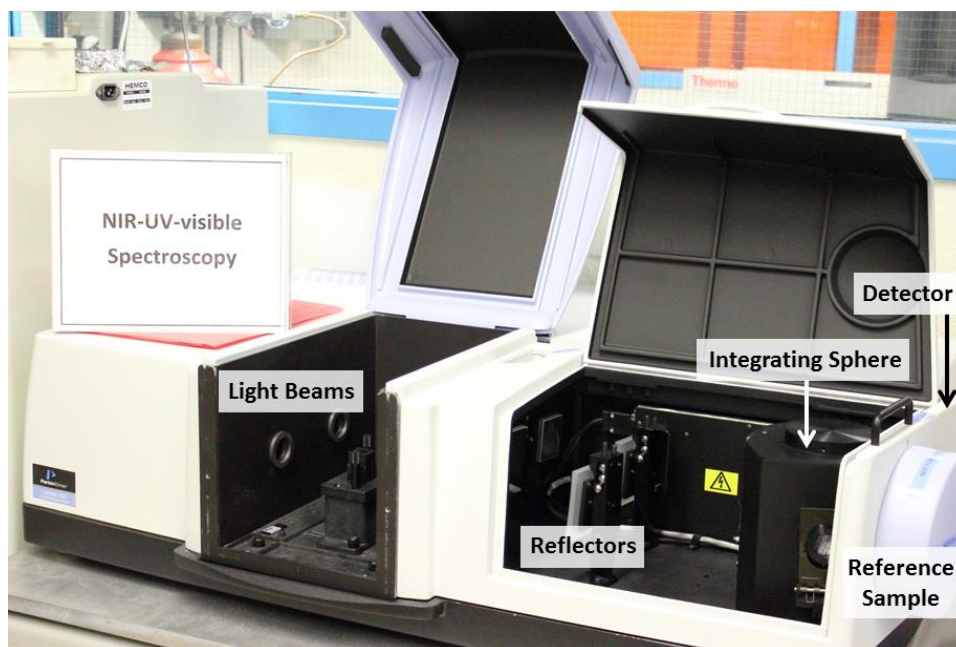


**Figure 2.9** Photograph of Perkin Elmer Lambda 1050 NIR/UV/Vis Spectrometer used for the transmittance/reflectance measurements for thin films.

## 2.6 Photoelectrochemical analysis

In this work, linear sweep voltammetry is used to investigate the photoelectrochemical water splitting behavior of the nanomaterials deposited on the substrates by using a CH Instruments 660A electrochemical station (Figure 2.10).<sup>40</sup> A three-electrode system is used in this process, in which an Ag/AgCl (3M KCl) electrode is used as the reference electrode (RE), a Pt wire is used as the counter electrode (CE) and the sample is used as the working electrode (WE). The experiment is performed in an aqueous electrolyte solution (KOH in this project) in a quartz beaker. A 300 W Xenon lamp (300-1000 nm, Oriel Instruments 6258) with different optical filters (low-pass, high-pass and AM 1.5G) is used to deliver UV and visible light onto the sample during the photocurrent measurements with a power density of 50 mA/cm<sup>2</sup>. More details about the experimental technique are described in forthcoming chapters.

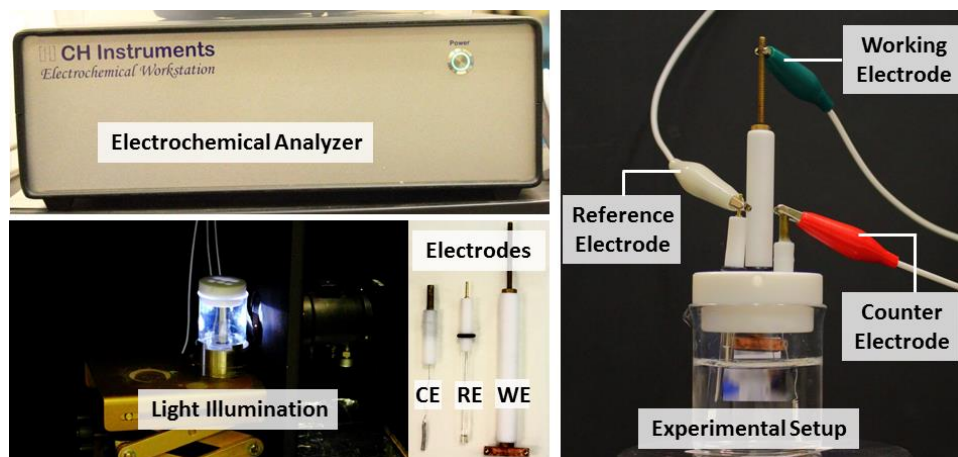


**Figure 2.10** Photographs of various components of the water splitting experiment including the electrochemical analyzer, illumination station, all the electrodes and combined experimental setup.

## 2.7 Micro/Nanodevices fabrication techniques

Different micro/nanodevices are fabricated in this work for different application purposes. A novel maskless photolithography system from Intelligent Micro Patterning Ltd.<sup>120</sup> is used to pattern microscale devices (Figure 2.11a). The patterns are created in bitmap (.bmp) format using paint. A 20× optics is used to provide the magnification to achieve the smallest minimal feature size (1 μm). A high-performance photoresist Shipley S 1827, along with MCC primer (both purchased from Microchem), is used. Since the photoresist layer is quite thin (~500 nm), the MCC primer serves as an adhesive layer for the photoresist. The coating of the primer and photoresist is performed in a spin coater (Laurell Tech. Corp.) at 4500 rpm for 40 s consecutively to achieve a coating thickness of 500 nm each. The sample is baked at 120 °C on a hot plate after each of the spin coating steps. Once the pattern writing is completed, the sample is developed in the MF-24 developer for 30 s to dissolve the UV exposed area. After development, the sample is then deposited with different materials accordingly by using RF or DC magnetron sputtering in a physical vapor deposition system (Mantis Deposition Ltd.) or/and tabletop sputter coater (EMS). The last step in the device fabrication process is the lift-off, which is performed by dipping the coated samples in HPLC-grade acetone (Sigma Aldrich) for 1-5 min to remove the undeveloped area of the sample, leaving only the desired device pattern behind. For multilayer device fabrication, the same procedure is repeated for as many layer as necessary, while proper alignments by means of appropriately placed alignment marks is performed in between in order to achieve the precise stacking (and overlaying) of the multilayers. For nano-sized junctions, a novel ion beam lithography system (Raith IONLine) is used (Figure 2.11b).<sup>121</sup>

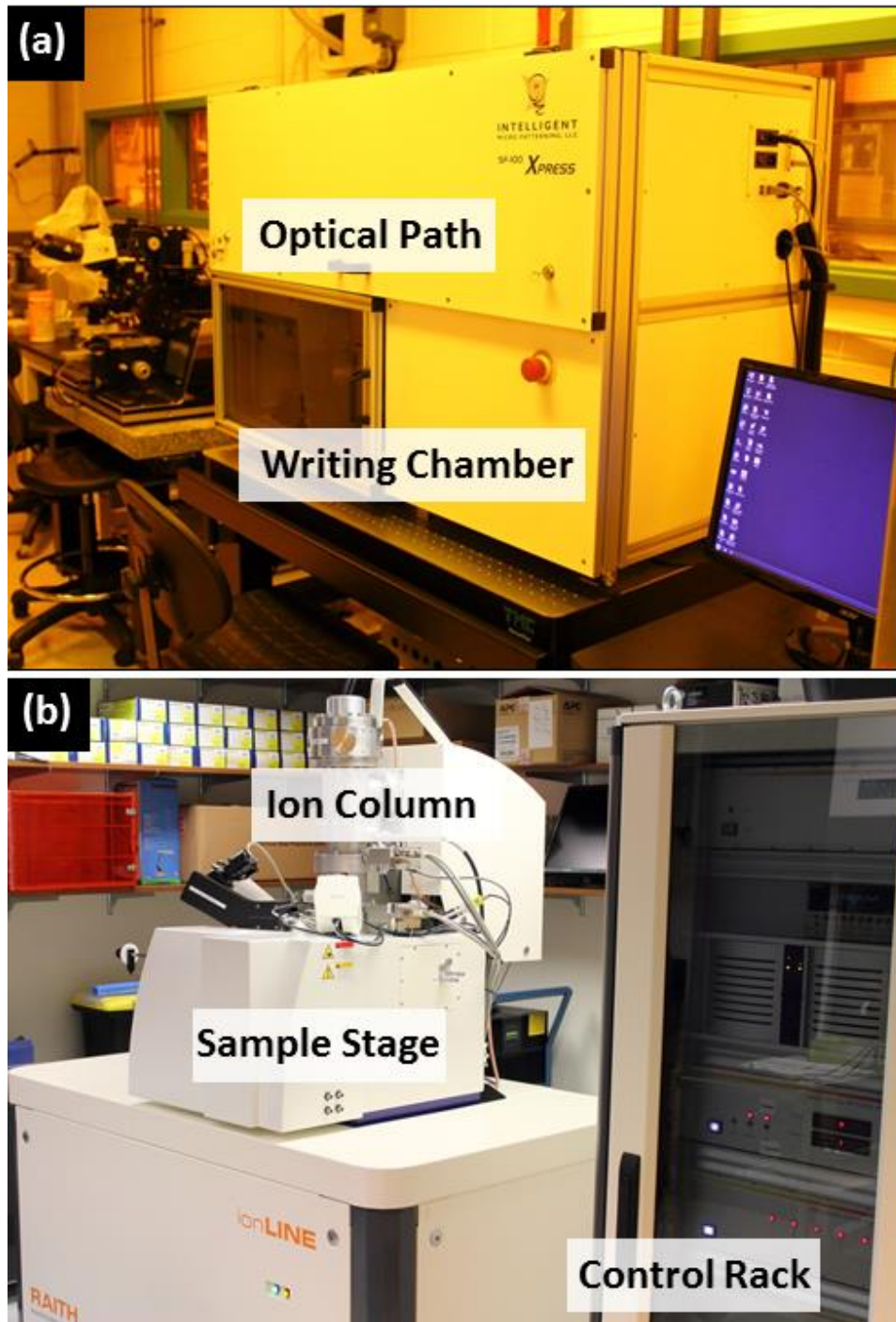


**Figure 2.11** Photographs of (a) an Intelligent Micro Patterning SF-100 Xpress maskless optical lithography system used to fabricate the memristive devices, and (b) Raith IONLine ion beam lithography system used to fabricate the memristive devices with nano-sized junctions.

## 2.8 Electrical characterization

All of the fabricated devices are tested using a semiconductor device analyzer (Agilent Technologies B1500) coupled with a probe station (Signatone, S1160A) (Figure 2.12).<sup>122</sup> Tungsten probes with 10  $\mu\text{m}$  tip width are used for making the contact with the device and all the measurements are taken at room temperature. In most of the cases, a two-probe testing scheme is employed, where voltage is applied on one probe while the other probe is kept grounded and the current is measured between the electrodes.

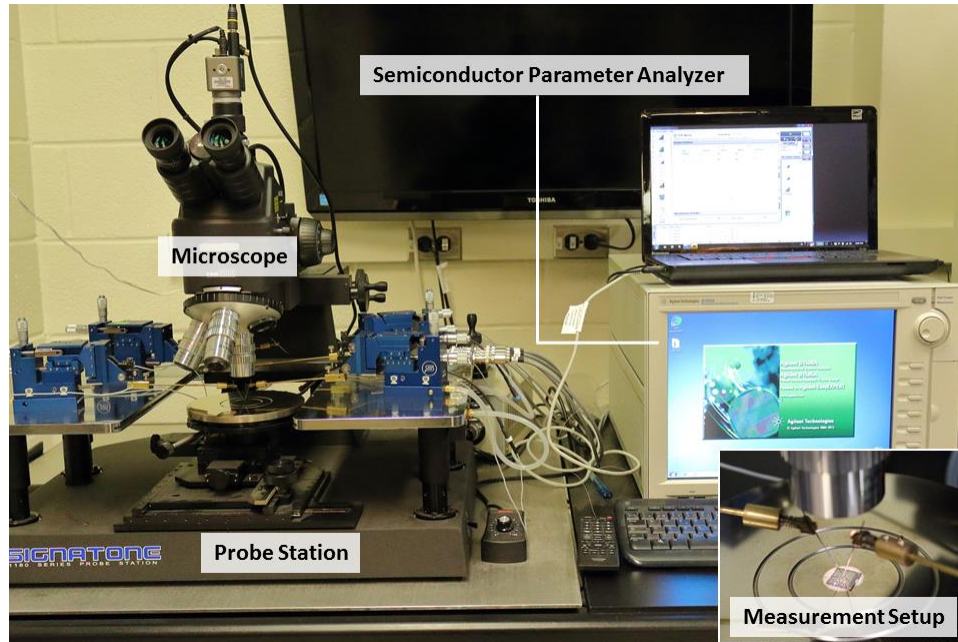


**Figure 2.12** Photograph of Signatone probe station coupled with an Agilent B1500 semiconductor parameter analyzer used for electrical characterization of the memristor devices. Inset shows the measurement setup where two probes are connected to the two electrodes of the memristor device.

## Chapter 3

# Size-Selected TiO<sub>2</sub> Nanocluster Catalysts for Efficient Photoelectrochemical Water Splitting<sup>\*\*\*\*\*</sup>

### 3.1 Introduction

Transition metal and metal oxide nanoclusters (NCs) have attracted a lot of recent attention due to their numerous applications in catalysis, sensors, optoelectronic and magnetic devices.<sup>7,10,20,123–127</sup> In the early 1980s, the development of precise mass (or size) selected nanocluster molecular beam systems has enabled cluster formation with a well-defined size distribution, which has opened up new opportunities for understanding gas-phase reaction dynamics and catalysts.<sup>51,128,129</sup> More recently, there has been renewed interest in the deposition of transition metal NCs and the assembly of three-dimensional arrays of discrete size-selected NCs or nanoparticles onto surfaces.<sup>9,26–28,130–132</sup> These NC assemblies (i.e. nanosystems) allow the chemical properties of these materials to be tuned by controlling their nanoscale cluster/particle size and structure, with further optimization made possible by modifying the nature of nanoconstituents often combinatorially. Since molecular beam technique has enabled the study of free, unsupported NCs in the gas phase,<sup>133,134</sup> various procedures have been developed to deposit transition metal NCs onto substrates (or supports) by gas phase aggregation technique.<sup>9,27,28,132</sup> The objective of this deposition approach is to preserve the size of the as-formed NCs on the surfaces. However, acquiring nearly monosized NCs at a few nanometer scale remains a difficult task. Size-tuning of supported transition metal NCs can be used to enhance the catalytic activity at the NC surface and interfacial regions.<sup>135</sup> A major challenge in the synthesis of stable and well-controlled arrays of size-specific NCs is the inhibition of aggregation on the surface. Early studies have largely focused on metal NCs, including Ag,<sup>9,26</sup> Au,<sup>130</sup> Cu,<sup>27</sup> Pd<sup>28</sup> and Zn<sup>136</sup> NCs. In contrast, there are considerably fewer studies on metal oxide NCs, particularly titanium dioxide (TiO<sub>2</sub>) NCs, and on their size tuning with a narrow size distribution produced by using the general technique of gas-phase aggregation.<sup>38,137–139</sup> Lambert's group deposited doped TiO<sub>2</sub> NCs using a gas condensation technique in an oxygen and methane ambient.<sup>132</sup> Using a gas-aggregation source, Drabik *et al.* produced Ti NCs in lower vacuum condition, which then became oxidized in ambient.<sup>137</sup>

High chemical stability and low-cost production have made TiO<sub>2</sub> one of the most widely used photocatalytic materials since the first report of water splitting using TiO<sub>2</sub> by Fujishima and Honda

---

\*\*\*\*\* This section is made from one of my publications: Srivastava et al., ACS Nano **2014**, 8, 11891-11898. Copyright (2014) by the American Chemical Society.

over 30 years ago.<sup>140</sup> TiO<sub>2</sub> is also one of the most studied transparent conductive oxides, with band gaps of 3.02 eV for rutile and 3.2 eV for anatase structures.<sup>141</sup> With the bottom of the conduction band more negative than the redox potential of H<sub>2</sub>/H<sub>2</sub>O (0 V) and the top of the valence band more positive than the redox potential of H<sub>2</sub>O/O<sub>2</sub> (-1.23 V),<sup>60,140-142</sup> TiO<sub>2</sub> is possibly the “ideal” photocatalyst for the photoelectrochemical water splitting reaction. Different types of TiO<sub>2</sub> nanostructures, including nanoparticles and nanowires, and thin films have been tested for the water splitting reaction but found to produce a photocurrent density no greater than 0.1 mA/cm<sup>2</sup>.<sup>142-144</sup> An assembly of discrete NCs would be of great interest because of its high specific surface area that provides a large number of reaction sites (per volume) for electron-hole pair generation for water splitting reaction upon light illumination.

As Ti and its oxides are of great importance to catalysis and nanoelectronics, the synthesis of stable, size-selected Ti and TiO<sub>2</sub> NCs in a controlled way could offer new prospect for creating novel cluster-assembled materials with desirable properties for electronic and optoelectronic applications, including memory devices, fuel cells and solar cells. Here, we present a new fabrication process to produce well-ordered, precisely size-selected, monosized NCs with excellent uniformity over a large area using a novel NC magnetron sputter source with a quadrupole mass filter built-in. We further demonstrate the exceptional photoelectrochemical catalytic performance of these high quality TiO<sub>2</sub> NCs as photoanodes in a water splitting reaction.

### 3.2 Experimental Details

Size-selected TiO<sub>2</sub> NCs are produced using a gas condensation technique with a gas-aggregation cluster source based on DC magnetron sputtering (Nanogen 500, Mantis Deposition Ltd.),<sup>145</sup> which employs the Haberland concept of cluster formation.<sup>133,134</sup> A schematic diagram of the Nanogen source is shown in Figure 3.1. A titanium target (99.95% purity, ACI Alloys) is mounted in the cluster source chamber with a base pressure of  $1 \times 10^{-8}$  mbar. A broad beam of Ti atoms is generated by DC magnetron sputtering (at 55 mA) in Ar and these sputtered atoms condense into clusters under high collision-prone ambient condition. The cluster growth involves two basic steps: (a) generation of Ti atoms, particle fragments and ions by magnetron sputtering, which then undergo (b) collisional condensation, involving nucleation and gas-phase aggregation leading to cluster formation.<sup>134</sup> Cluster growth can be controlled by varying the Ar gas pressure and the aggregation length in the condensation zone of the aggregation chamber (where cluster formation occurs as a result of collisions of atoms with one another). Since a large fraction of the NCs so generated by the Nanogen source is negatively charged, it is possible to provide precise mass selection of NCs of a particular size based on their mass-to-charge ratios by using a quadrupole mass filter in the NC source. A set of

AC and DC voltages is applied to the quadrupole filter, with 2% mass resolution and throughput up to  $10^6$  amu, to facilitate an oscillating path that allows passage of cluster ions of the selected size. After exiting the aggregation chamber through an orifice (3 mm dia.), the cluster ions are neutralized and collected on the substrate positioned 70 mm in front of the orifice in the deposition chamber. The input flow rate of the Ar gas in the Nanogen source is used to control the (deposition) chamber pressure ( $10^{-4} - 10^{-3}$  mbar) at which the deposition process occurs. In particular, the input Ar flow rate directly affects the processes in the condensation zone and the efficiency of the clusters emerging from the aggregation chamber.<sup>28</sup> Cluster sizes of 2-15 nm (dia.) can be produced using the Nanogen source, and monosized clusters smaller than 8 nm are the focus of the present work. The substrates used for the present work are H-terminated Si(100) (denoted as H-Si), quartz and float glass. All the substrates are cleaned ultrasonically in acetone and isopropanol before use, while the Si substrate is also rinsed in 2% HF for 10 min to remove the native oxide layer and to produce H-termination on the Si substrate (H-Si).

The surface morphology and the size of the NCs are characterized *ex-situ* by atomic force microscopy (AFM) operated in tapping mode in a Digital Instruments Dimension 3100 Nanoman Nanoscope IV microscope, while the crystallinity of the NCs is determined by transmission electron microscopy (TEM) in a JEOL 2010F microscope operated at 200 kV. TEM samples are prepared by directly depositing the NCs onto a holey carbon TEM grid. Chemical-state composition is analyzed by X-ray photoelectron spectroscopy (XPS) as a function of Ar ion sputtering time in a Thermo-VG Scientific ESCALab 250 Microprobe, equipped with a monochromatic Al K $\alpha$  X-ray source (1486.6 eV). Ar ion sputtering is performed over a raster area of  $3 \times 3$  mm<sup>2</sup> at an ion beam energy of 3 keV and a typical sample current density of 110 nA/mm<sup>2</sup>. The XPS data is fitted by using Casa XPS software with a Shirley background. The photoelectrochemical water splitting experiments are performed by using a CH Instruments 660A electrochemical station in a three-electrode quartz cell with an electrolyte solution of 5 M KOH (prepared from analytical grade KOH and Millipore water at room temperature). Photocurrents are measured with the size-selected NCs deposited on a substrate as the working electrode (i.e., the photoanode), both in the dark and under the illumination of a 300 W Xenon lamp (300-1000 nm, Oriel Instruments 6258) with an AM 1.5 filter. A minimum power density of 50 mA/cm<sup>2</sup> is delivered to the sample. Ag/AgCl (3M KCl) and Pt are used as the reference and counter electrodes, respectively.

## Nanogen Cluster Source

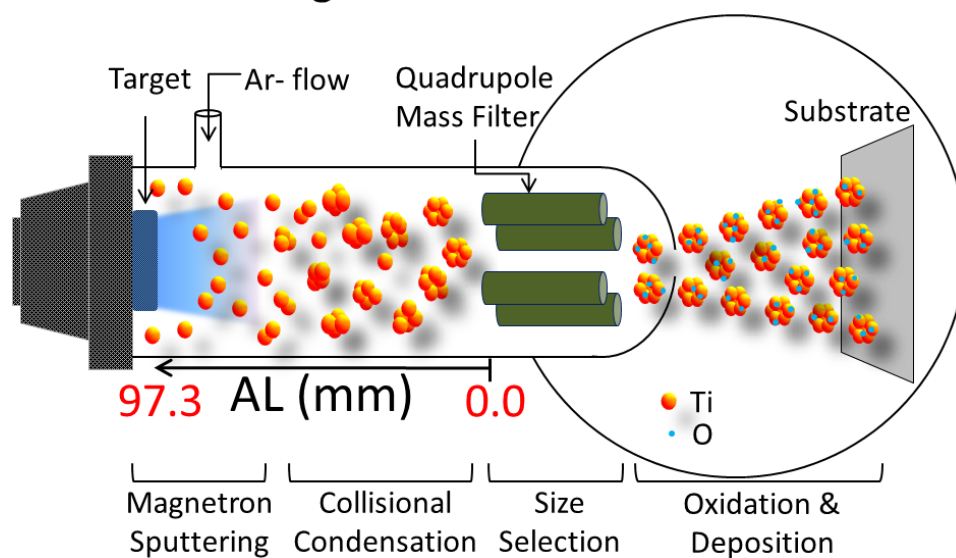


**Figure 3.1** Schematic diagram of the production of a size-selected cluster beam in the Nanogen cluster source (not drawn to scale), which involves the following steps: (a) generation of  $Ti_n$  moieties and their ions by magnetron sputtering, (b) collisional condensation that leads to nucleation and gas aggregation, and eventually to  $Ti_n$  and  $Ti_n^-$  cluster formation, and (c) size selection of  $Ti_n^-$  clusters by a quadrupole mass filter. The  $Ti_n^-$  cluster ions exiting the aggregation (or Nanogen source) chamber from a 3 mm dia. aperture become oxidized by the ambient in the deposition chamber and the resulting  $TiO_2$  cluster ions are then deposited and neutralized on the substrate under soft-landing condition to produce the size-selected  $TiO_2$  nanoclusters. The aggregation length (AL), defined as the separation between the front face of the target and the entrance plane of the quadrupole, and the Ar gas flow are the main parameters used to control the overall cluster size distribution before size selection. No bias is applied to the substrate to ensure soft landing of the nanoclusters.

### 3.3 Results and Discussion

In our experiment, size-selected NCs with specified mass-to-charge ratios are successfully synthesized by using the Nanogen source (shown schematically in Figure 3.1). Figure 3.2a shows the average NC size (diameter) as a function of the Ar gas flow for different aggregation lengths (ALs). In spite of the small exit aperture (3 mm dia) of the Nanogen source, the pressure at which the NCs are deposited on the substrate (in the deposition chamber) depends linearly on the Ar gas flow during growth (Figure 3.2a). The Ar gas pressure is found to have the largest effect on the growth kinetics of the NCs. The system can therefore be optimized to provide the desired cluster size by controlling the Ar flow rate in the aggregation chamber. Not only does the Ar gas flow help to initiate the plasma for sputtering to occur, Ar also works as a carrier gas to support the growth of the NCs by providing them nucleation centers in the gas phase and to carry them towards the substrate. The aggregation chamber provides the important space needed for the target source atoms to undergo collisional

condensation.<sup>145</sup> This space can be physically adjusted by changing the AL, which corresponds to the target-to-quadrupole separation (Figure 3.1). As a general rule, an increase in the Ar flow causes a decrease in the NC size because the clusters are swept out of the aggregation chamber faster before the clusters have sufficient time to self-condense to a larger size. Figure 3.2a shows an almost linear decrease in cluster size with increasing Ar flow rate for all ALs from 10 to 90 mm. We observe that AL also affects the size distribution of resulting NCs. For a fixed Ar flow rate, the cluster size increases with increasing AL (Figure 3.2a). This is consistent with our expectation that a bigger aggregation volume provided by a larger AL allows the Ti atoms in transit to reside in the aggregation chamber longer, thereby facilitating more collisional encounters to form larger clusters. Our present study, therefore, shows that the smallest cluster size can be achieved by maintaining a high Ar-flow for a short AL. Conversely, the larger cluster size can be obtained by employing a lower carrier gas flow for a longer AL. As illustrated in Figure 3.2a, the cluster size can be tuned in the range below 10 nm and a cluster size as small as 3 nm can be easily obtained. This size regime is smaller than the TiO<sub>2</sub> NCs reported earlier.<sup>9,23,27,28,132,138</sup>

Figure 3.2b shows the relative populations of NCs as-formed in the gas phase as a function of NC size for three typical (AL, Ar-flow) combinations: A = (80 mm, 30 sccm), B = (60 mm, 35 sccm) and C = (20 mm, 55 sccm). The relative population of the NCs is indicated by the quadrupole collector current. A near-Gaussian size distribution is clearly observed for all (AL, Ar-flow) sets. As the mode cluster size (marked by the peak maximum) increases, the peak collector current decreases with concomitant increase in the width of its distribution, from set C to set B to set A. Upon applying an appropriate set of voltages to the quadrupole mass filter, the cluster size distribution can be dramatically narrowed to a sharp profile as defined by the mass resolution of the quadrupole, which demonstrates the effectiveness of mass selection by the quadrupole mass filter. Figure 3.2b also shows that the cluster mass increases quadratically with increasing cluster size.

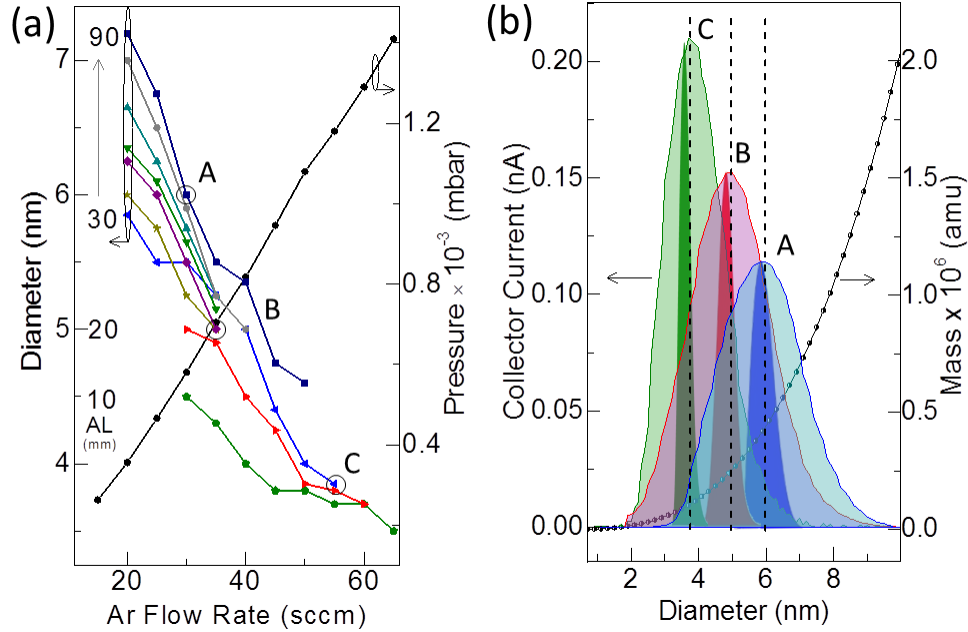


**Figure 3.2** (a) Cluster size (left axis) and deposition chamber pressure (right axis) as a function of Ar flow rate for different aggregation length (AL) from 10 to 90 mm, in steps of 10 mm; and (b) typical nanocluster size distributions, as represented by quadrupole collector current (left axis), obtained with three typical combinations of (AL, Ar flow rate) as marked by large open circles in (a): A = (80 mm, 30 sccm), B = (60 mm, 35 sccm) and C (20 mm, 55 sccm). The vertical dashed line marks the respective mode cluster size of each nanocluster distribution, while the corresponding sharpen peak marked by the darken area corresponds to the distribution of nanoclusters mass-selected (within 2% of the mode cluster size) by applying an appropriate set of DC and AC voltages to the quadrupole mass filter. The total mass (right axis) as a function of nanocluster size produced by the Nanogen cluster source is also shown.

Figure 3.3a-c shows tapping-mode AFM images of  $\text{TiO}_2$  NCs deposited on H-Si substrates along with their size distributions at mode cluster sizes of 3.5, 5.0 and 6.2 nm, respectively, obtained with appropriate (AL, Ar flow rate) settings. With the spatial resolution of AFM generally larger than 10 nm, we estimate the size (diameter) of the as-deposited NCs from their respective height profiles, assuming a spherical shape for these NCs. A near-Gaussian size distribution (obtained without the use of the quadrupole mass filter) is clearly observed for all three mode sizes. The size distributions obtained from our AFM measurements for the as-deposited NCs are also found to be in good accord with and therefore validate those as reflected by the collector current profiles of the quadrupole mass filter (Figure 3.2b).

The impact energy of the NCs is one of the key parameters in cluster-surface collisions. Given the kinematics of the system, the  $\text{TiO}_2$  NCs should undergo soft-landing onto the substrate because the NCs impinging onto the substrate are very small in size and their kinetic energy at room temperature

is less than 0.1 eV.<sup>134,146</sup> The NCs so deposited should therefore have their stoichiometry preserved, without any change to their chemical or physical properties, and they are not expected to undergo further diffusion into the bulk upon physisorption. In the present work, no bias is applied on the substrate to maintain low impinging energy of the NCs to the substrate, thereby ensuring soft-landing condition. Furthermore, it should be possible to produce TiO<sub>2</sub> NCs of the same cluster size but with different areal density by simply manipulating different (AL, Ar-flow) combinations for the same deposition time. To demonstrate this unique control provided by the present technique of NC generation, we show, in Figure 3.3d-f, three different densities obtained for NCs with essentially the same mode cluster size of 5 nm. The variation in the densities of these NCs with the same mode size can be understood in terms of the kinematics of the NCs produced under different conditions. In particular, the kinetic energy of the impinging NCs could significantly affect the nature/type of the event that follows. For a high Ar flow rate and a larger AL, less energetic NCs will be produced. This is because of the resulting larger number of collisions among clusters themselves and/or with the wall of the aggregation chamber over a longer period of time. This low kinetic energy regime ensures soft landing without any subsequent diffusion on the surface and/or into the bulk. On the other hand, in the other limit of a low Ar flow rate and a smaller AL, more energetic NCs will be generated because of less resulting collisional encounters. Some of the NCs could also bounce backward due to head-on collisions with the surface, thereby reducing the cluster density on the surface. The areal density can also be controlled by the amount of deposition time, while keeping other preparation conditions the same to ensure that the clusters physisorb under soft-landing condition and without any cluster aggregation (Figure 3.4) and also without any deformation from spherical shape (as observed by TEM, Figure 3.8d) on the surface. The present technique of NC generation therefore provides a sensitive control of the relative kinetic energy of NCs in the gas phase in the soft-landing regime.

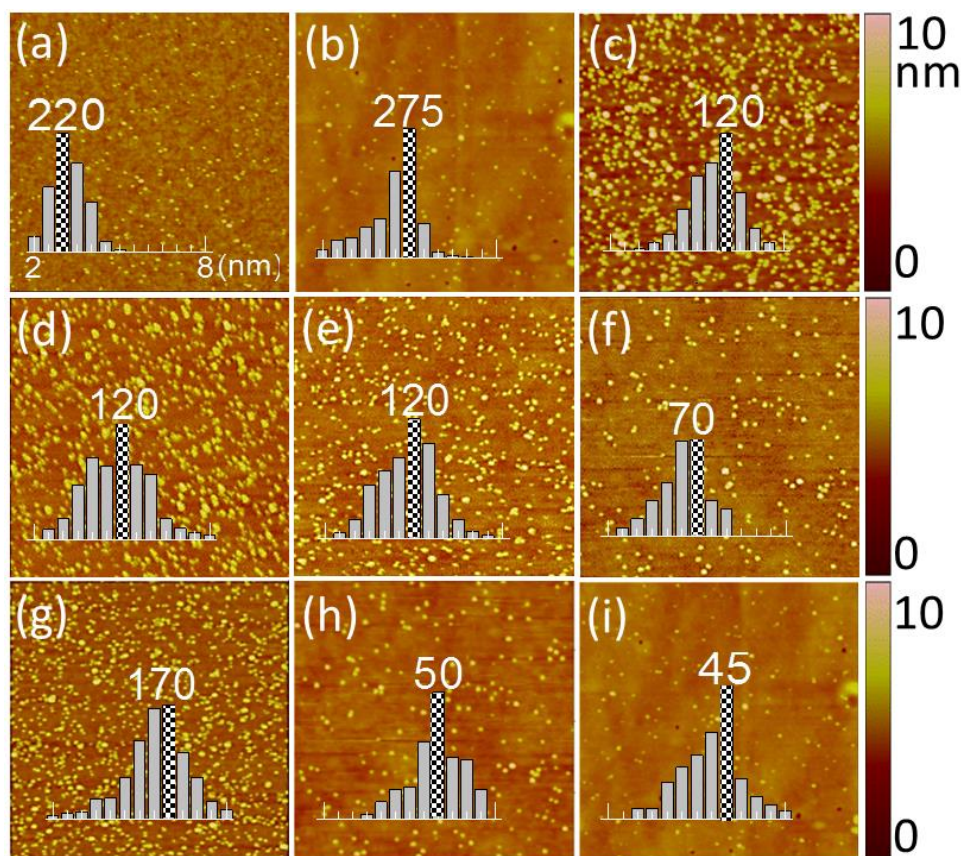


**Figure 3.3** AFM images of size-selected  $\text{TiO}_2$  nanoclusters obtained with mode sizes of (a) 3.5 nm, (b) 5 nm and (c) 6.2 nm (deposited with appropriate growth conditions) and with a mode size of 5 nm deposited with three different growth conditions (AL, Ar-flow): (d) (80 mm, 40 sccm), (e) (60 mm, 35 sccm), and (f) (20 mm, 30 sccm), all on H-Si substrates. AFM images of size-selected  $\text{TiO}_2$  nanoclusters with a mode size of 6 nm deposited on three different substrates: (g) H-Si, (h) glass, and (i) quartz. All AFM images are obtained for a scanned area of  $1 \times 1 \mu\text{m}^2$ . Insets show the corresponding histograms for the cluster size distributions of the nanoclusters from 2 to 8 nm obtained under appropriate (AL, Ar-flow) combinations, with the peak marked by the numbers of the clusters with the respective mode sizes.

The adhesion properties of  $\text{TiO}_2$  towards different types of substrate surfaces are further investigated by depositing  $\text{TiO}_2$  NCs on three different substrates simultaneously under the same deposition condition. Figure 3.3g-i compares the areal densities of  $\text{TiO}_2$  NCs deposited on H-Si, glass, and quartz substrates. The sizes of NCs on all three substrates are found to be similar (6 nm), consistent with the mode size as selected by the appropriate (AL, Ar-flow) combination of (80 mm, 30 sccm). Interestingly, the areal density of the NCs on H-Si ( $\sim 750/\mu\text{m}^2$ ) is considerably higher than those on glass ( $\sim 180/\mu\text{m}^2$ ) and quartz substrates ( $\sim 170/\mu\text{m}^2$ ). This is consistent with the higher sticking coefficient of  $\text{TiO}_2$  thin film on H-Si when compared to those on the other two oxide surfaces. The NC densities for glass and quartz are similar because of the similar chemical nature of

these oxide surfaces. Despite the expected high propensity of  $\text{TiO}_2$  on the oxide surface to aggregate due to its higher enthalpy than those of the oxide surfaces,<sup>133</sup> we see no evidence of cluster aggregation on the surface even after deposition for a longer time (Figure 3.4a&b), with individual NCs remaining uniformly distributed over the entire surface. This further confirms the soft-landing condition provided by the Nanogen cluster source. The deposition time can therefore be used to control the surface coverage, i.e. the areal density of the NCs (which is important to their application as catalysts), and therefore the resulting surface roughness. The RMS surface roughness is estimated from AFM measurement for samples obtained with different deposition times (Table 3.1), and found to increase with increasing deposition time from 15 to 20 to 30 min, followed by a decrease after 60 min of deposition. The latter reduction in RMS roughness could be due to increase in the packing efficiency.

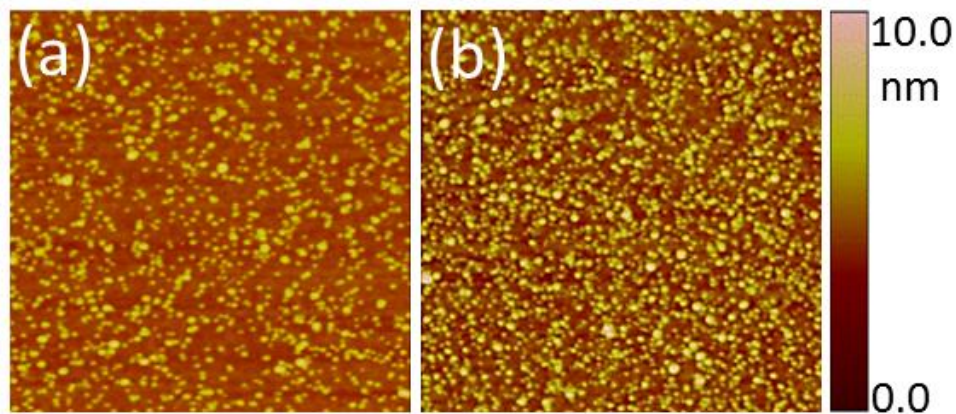


**Figure 3.4** AFM images of the  $\text{TiO}_2$  nanoclusters deposited on H-Si substrates for (a) 15 and (b) 60 minutes. All AFM images are obtained with a scanned area of  $1 \times 1 \mu\text{m}^2$ . Evidently, no clear increase in the cluster size as a result of cluster agglomeration on the substrate is observed even for the longer deposition time, which confirms the soft-landing deposition condition of nanoclusters with low kinetic energies.

**Table 3.1** RMS surface roughness over  $1 \times 1 \mu\text{m}^2$  area as a function of deposition time for  $\text{TiO}_2$  nanoclusters deposited on H-Si substrates with an Ar flow rate of 20 sccm and aggregation length of 50 mm.

Deposition Time (min)	RMS Surface Roughness (nm)
15	1.220
20	1.250
30	1.713
60	1.344

To characterize the chemical nature of the nanoclusters, we show, in Figure 3.5, the XPS spectra of the Ti 2p region collected as a function of sputtering time for a typical  $\text{TiO}_2$  NC film deposited with a mode size of 6 nm on H-Si for 60 min. The prominent Ti 2p<sub>3/2</sub> peak at 459.2 eV corresponds to the  $\text{Ti}^{4+}$  state attributable to  $\text{TiO}_2$  in good accord with an earlier report.<sup>147</sup> The minor shift in the spectrum to a higher binding energy after a brief 5 s of sputtering is due to the removal of surface hydrocarbons commonly present as a result of ambient handling. Upon sputtering for a total of 20 s, a weak Ti 2p<sub>3/2</sub> feature emerges at 457.5 eV and becomes more intense while the  $\text{Ti}^{4+}$  feature is weakened upon sputtering for 90 s. This intermediate feature at 457.5 eV, tentatively assigned to  $\text{Ti}^{3+}$ , becomes reduced in intensity and appears to shift toward a lower binding energy (454.3 eV) upon further sputtering for 270 s. Continued sputtering for 450 s and 650 s causes emergence of a well-defined Ti 2p<sub>3/2</sub> feature at 454.3 eV, which could be assigned to TiO. The Ti 2p<sub>3/2</sub> features located at the intermediate peak position (between  $\text{Ti}^{4+}$  and  $\text{Ti}^{2+}$  states) could therefore be attributed to  $\text{TiO}_x$  ( $2 \geq x \geq 1$ ), which corresponds to non-stoichiometric Ti oxide phases due to the reduction of  $\text{Ti}^{4+}$  to  $\text{Ti}^{3+}$  and  $\text{Ti}^{2+}$  by Ar-ion bombardment.<sup>147</sup> This ion-induced reduction is also confirmed, in our separate experiment, by depth-profiling XPS analysis of commercial  $\text{TiO}_2$  powders (Aldrich, 99.99% purity) (Figure 3.6). The corresponding XPS spectrum of the O 1s region Figure 3.7a for the NC sample (after removing the surface carbonaceous layer by sputtering for 5s) exhibits two peaks at 530.6 eV and 532.8 eV, which are consistent with the assignment to  $\text{TiO}_2$  and  $\text{TiO}_x$ , respectively. The corresponding Si 2p spectrum is found to be dominated by a major Si peak at 99.3 eV and a minor  $\text{SiO}_x$  peak at 103.2 eV due to native oxide Figure 3.7b.

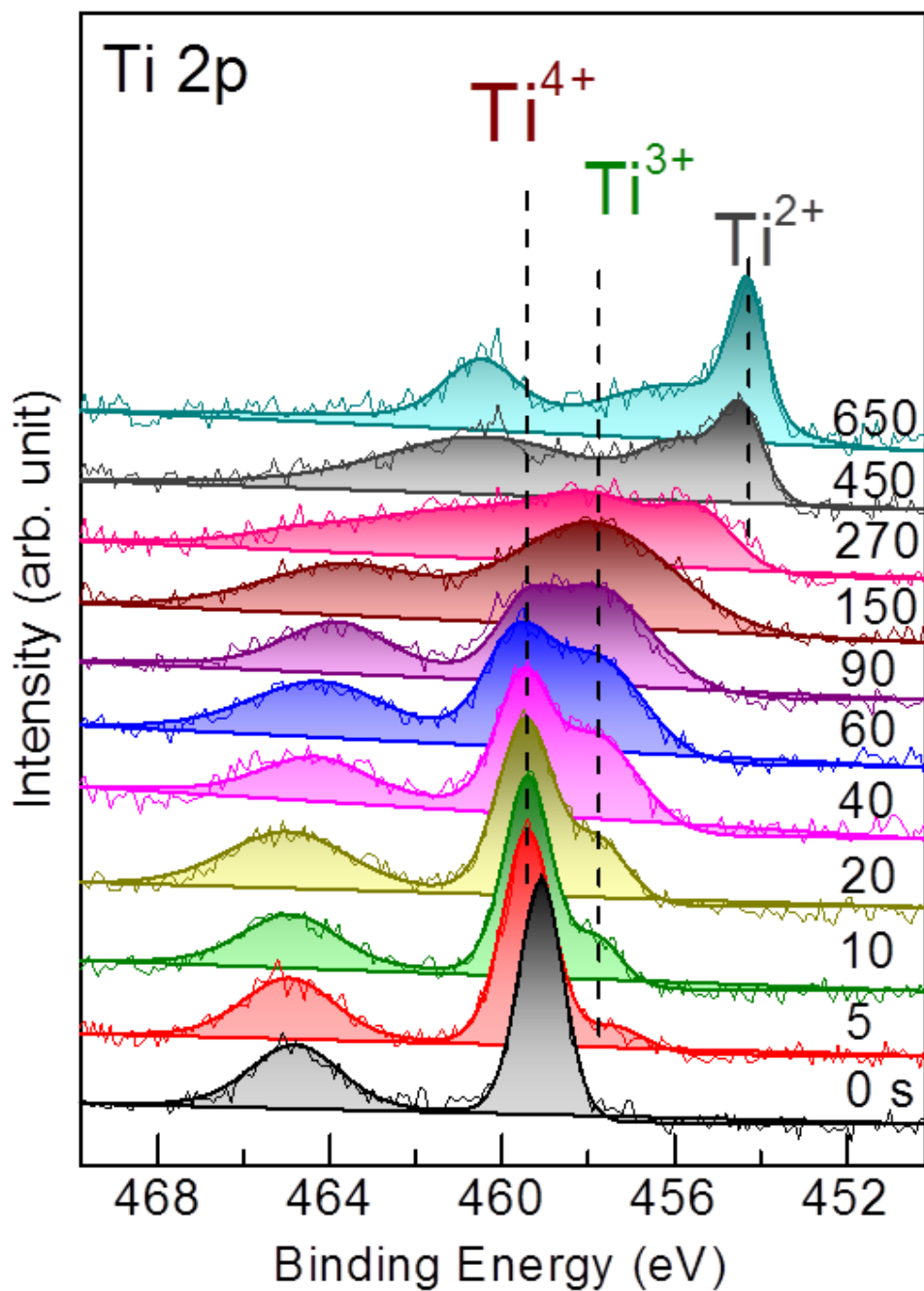


**Figure 3.5** XPS spectra of Ti 2p region for TiO<sub>2</sub> nanoclusters as-deposited on a H-Si substrate, and as a function of sputtering time. Only the Ti 2p<sub>3/2</sub> region is used here to identify various chemical states of the nanoclusters.

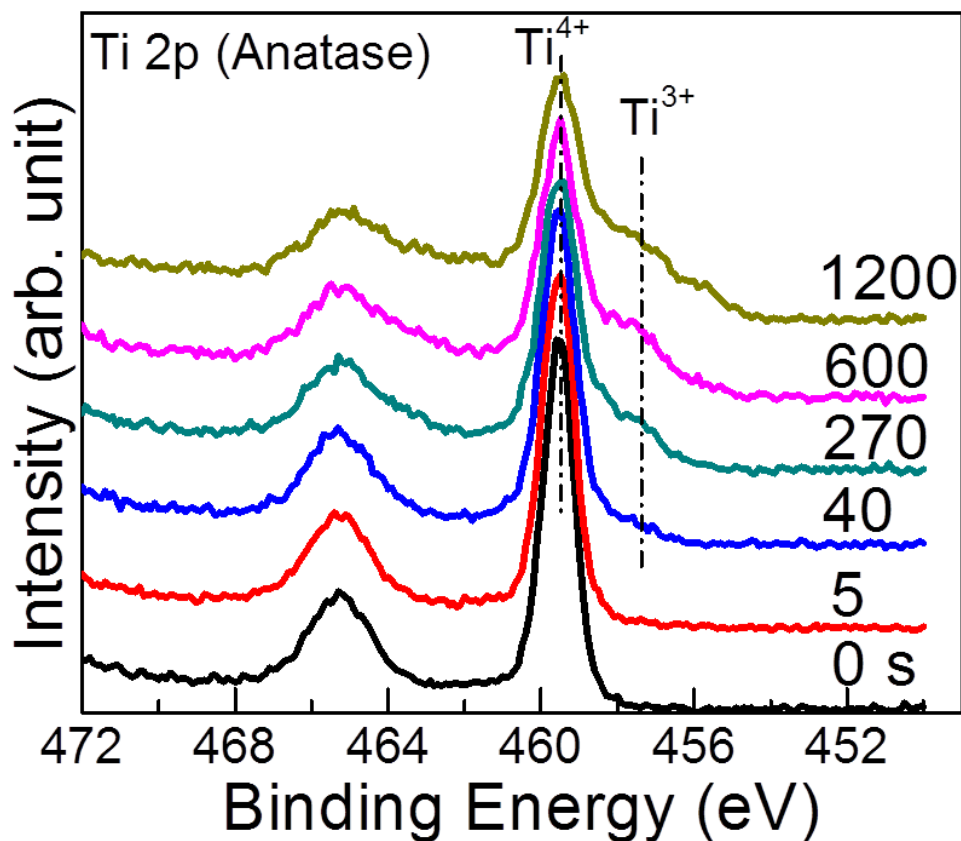


**Figure 3.6** XPS spectra of Ti 2p region for commercial  $\text{TiO}_2$  powder (anatase) as a function of sputtering time. The reduction of  $\text{Ti}^{4+}$  phase is observed in the commercial anatase powder sample after 270 s of Ar-ion bombardment, which corresponds to the emergence of non-stoichiometric Ti oxide phases. Commercial rutile powder is also found to exhibit similar result as anatase powder (data not shown).

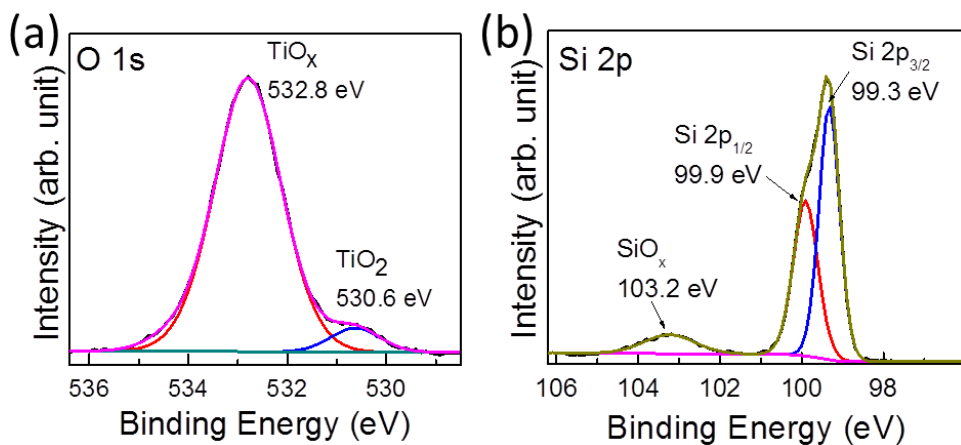


**Figure 3.7** Corresponding XPS spectra of (a) O 1s and (b) Si 2p regions for the as-prepared  $\text{TiO}_2$  nanocluster (6 nm) film shown in Figure 3.5.

To demonstrate the photoelectrochemical catalytic properties, we employ the TiO<sub>2</sub> NCs deposited with different mode sizes on H-Si as the photoanode in a water splitting reaction. All the photocurrent measurements are conducted for an illumination area of 5×5 mm<sup>2</sup> with a power density of 50 mW/cm<sup>2</sup>. The photoelectrochemical water splitting mechanism is described schematically in Figure 3.8a. In a water splitting reaction, photoexcitation occurs at the TiO<sub>2</sub> NC photoanode, which is immersed in an aqueous electrolyte along with the Pt counter-electrode (and an Ag/AgCl reference electrode). Electrons and holes are generated when TiO<sub>2</sub> NC is illuminated with UV-vis light, which facilitates redox reactions (oxidation at the photoanode and reduction at the counter electrode) at the NC-water interface in the electrolyte and leads to hydrogen (H<sub>2</sub>) evolution. Figure 3.8b shows the photocurrent density as a function of applied potential for the TiO<sub>2</sub> NC/H-Si working electrode in 5M KOH in the dark and under illumination of a Xenon lamp. Nanoclusters with three different NC sizes (4, 6 and 8 nm), preselected by using the quadrupole mass filter, are chosen to illustrate the cluster size effect on the photoelectrochemical performance. Evidently, a significant enhancement in the photocurrent density with decreasing NC size is observed. We attribute this to the interplay between the effect of the increase in the specific surface area and that of the increase in the amount of active sites due to the increased amorphicity of the NCs with decreasing size. The TEM images shown in Figure 3.8c illustrates the remarkable homogeneity of the NCs, all with nearly identical size, which further verifies the precise size-selection achieved by using the quadrupole mass filter. Furthermore, the larger NC (8 nm) is found to consist of a crystalline core surrounded by an amorphous shell, while the smaller NCs (6 and 4 nm) below a critical size appear to be completely amorphous. The amorphous nature of the smaller NCs gives rise to a higher density of defects, which work as trapping and recombination centers for the photogenerated electron-hole pairs. To confirm that amorphous TiO<sub>2</sub> NCs are better suited for water splitting reaction, we prepare, in a separate experiment, a “post-annealed” TiO<sub>2</sub> NC sample by annealing the as-deposited 6-nm NCs at 800 °C for 90 min in air. A substantial drop in the photocurrent density is observed for the post-annealed sample (Figure 3.8b). This is due to the reduction in the defect density as a result of improved crystallinity caused by annealing at a high temperature. The increase in the photocurrent density of the totally amorphous 6-nm NCs with respect to that of the crystalline-core amorphous-shell 8-nm NCs is attributed to both of the aforementioned effects, while the further enhancement found for the 4-nm NCs with respect to the 6-nm NCs, both of which are totally amorphous, is due to the effect arising from increase in the specific surface area. Since the surface area plays an important role in photoelectrochemical catalysis, substrate coverages (i.e. the amount of NC loading on the substrate) by TiO<sub>2</sub> nanoclusters for all three samples deposited for 15 min on H-Si substrates are calculated by using the Image J software.

Approximately 20% coverage is observed for all three samples, which suggests that there is a lot of room for potential improvement in the photoelectrochemical performance.

The saturation voltage for the 4-nm NCs is observed to be  $-0.22$  V vs Ag/AgCl (or  $0.78$  V vs RHE), which is well within the range of the typical values of  $0.5$ - $0.8$  V vs RHE found for other  $\text{TiO}_2$  nanomaterials.<sup>62,67,142,148</sup> We obtain a photoconversion efficiency (PCE) of  $\sim 0.43\%$  (Figure 3.9a) and a total PCE, as-estimated according to earlier reports,<sup>60,149</sup> of  $\sim 1.0\%$ , at an applied potential of  $0.78$  V vs RHE. For  $\text{TiO}_2$  nanotubes and other nanostructures, their corresponding total PCEs are in the range of  $0.2 - 3.0\%$ . For  $\text{TiO}_2$  NCs, the present PCE of  $1.0\%$  is the highest ever observed for this type of nanoclusters and it is comparable to the most of these nanomaterials reported in the literature.<sup>36,64,65,67,150,151</sup> This performance is especially remarkable when considering the very tiny amount of  $\text{TiO}_2$  NCs on the substrate, all of which are prepared without any post-synthesis modification or treatment (as often required in earlier work). It should be noted that most of the samples reported in the literature<sup>36,64,65,67,150,151</sup> are based on  $\text{TiO}_2$  or other metal oxide nanowires or nanotubes with post modification and these samples contain a significant (large) amount of materials, which provide a large number of active sites for the photoelectrochemical reaction. In our case, the PCE could potentially be enhanced at least 5 times by increasing the amount of cluster loading from 20% coverage to a monolayer coverage (e.g., by increasing the amount of deposition time). Indeed, a theoretical PCE of 5% would put our NC samples (with just one monolayer of coverage) to be among the top photoelectrochemical catalysis performers based on  $\text{TiO}_2$  nanomaterials for the water-splitting reaction. Even higher PCE can be obtained with multiple layers of  $\text{TiO}_2$  NCs (as was commonly employed for other  $\text{TiO}_2$  nanomaterials in earlier reports). Figure 3.9b shows a comparison between the photocurrent densities for different range of solar spectrum, using different filters. Furthermore, we can also potentially increase the PCE further by employing nanoclusters with even smaller size, and by modifying the clusters with chemical functionalization. Fabricating hybrid and/or core-shell NCs and synthesizing binary or tertiary NC systems could also enhance the PCE, and can be easily realized using the present Nanogen cluster source (equipped with the triple target capability).

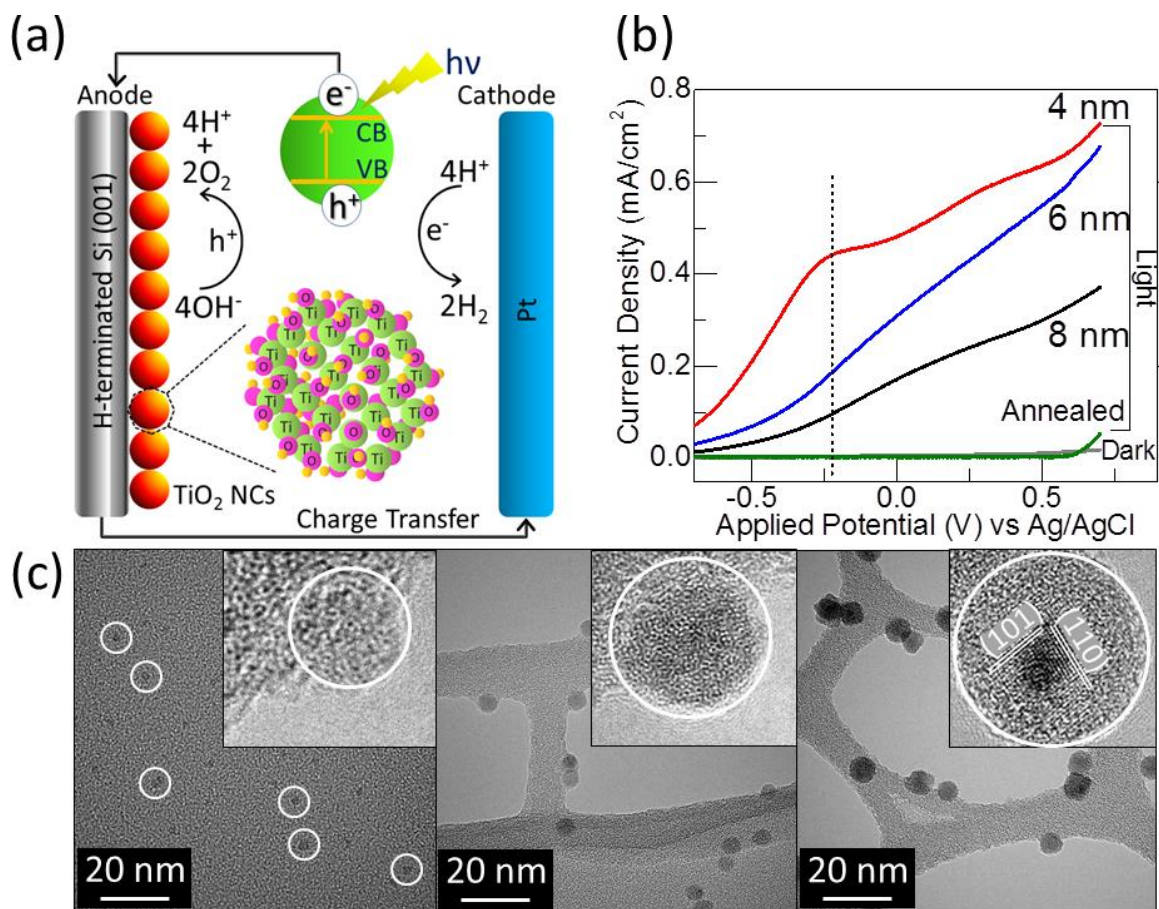


**Figure 3.8** (a) Schematic diagram of the mechanism of a photoelectrochemical water splitting reaction. An expanded view of a  $\text{TiO}_2$  nanocluster (NC, red sphere), consisting of Ti (green spheres), O (pink spheres) and H atoms (brown spheres), is shown as the bottom inset. The top inset shows the electron-hole pair generation in  $\text{TiO}_2$  upon UV-vis light illumination, which supplies holes ( $h^+$ ) for the oxidation of  $\text{OH}^-$  leading to  $\text{O}_2$  evolution at the photoanode and electrons ( $e^-$ ), upon travelling to the counter electrode through an external circuit, for reduction leading to  $\text{H}_2$  generation. (b) Photocurrent densities as a function of applied potential obtained in a photoelectrochemical water splitting reaction in a 5M KOH electrolyte, using  $\text{TiO}_2$  nanoclusters of different sizes (4, 6 and 8 nm) and the post-annealed  $\text{TiO}_2$  nanoclusters (6 nm), all on H-Si, as the photoanodes, all with an illumination area of  $5 \times 5 \text{ mm}^2$  under a 300 W Xe-lamp at a power density of  $50 \text{ mW}/\text{cm}^2$ . (c) TEM images of 4 nm (left), 6 nm (center) and 8 nm nanoclusters (right) deposited directly on holey carbon TEM grids, along with high resolution images shown as insets illustrating their respective degrees of crystallinity.

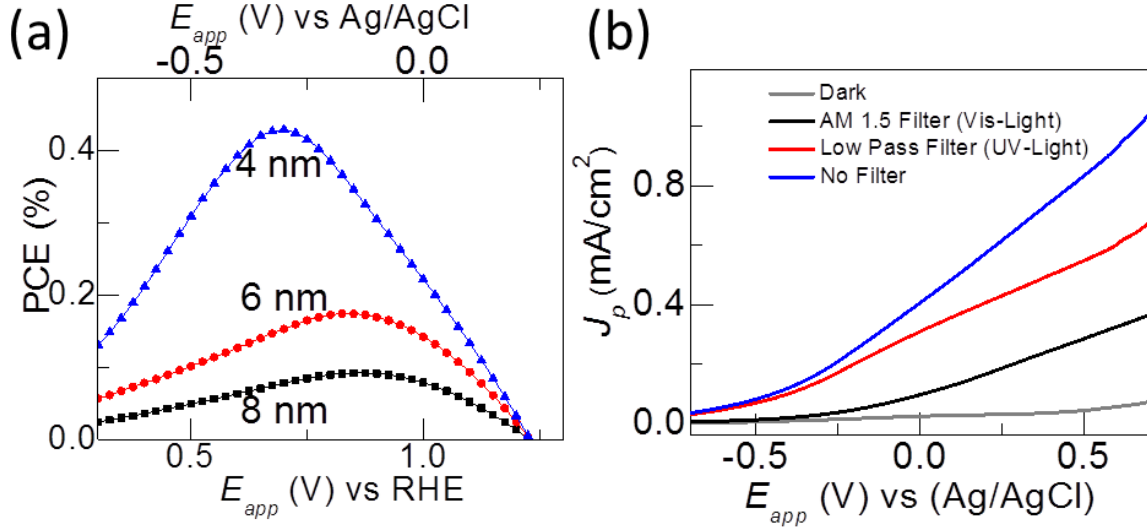


**Figure 3.9** (a) Photoconversion efficiency (PCE) as a function of applied potential,  $E_{app}$ , for TiO<sub>2</sub> nanoclusters with three different sizes as deposited on H-Si under illumination from a Xe lamp with a power density of 50 mW/cm<sup>2</sup>. (b) Photocurrent density,  $J_p$ , as a function of  $E_{app}$  for 6-nm TiO<sub>2</sub> nanocluster in the dark (bottom line) and under illumination by UV light (obtained with a low pass filter, second top line), visible light (obtained with an AM 1.5 filter, third top line), and the full spectrum (without any filter, top line). The photoconversion efficiency of the water splitting reaction in the presence of external applied potential is calculated by using the equation:

$$PCE = \frac{J_p(E_{rev}^o - E_{app})}{I_0}$$

where  $J_p$  is the observed photocurrent density,  $E_{rev}^o$  is the standard reversible potential, which is 1.23 V vs RHE for the water splitting reaction,  $E_{app}$  is the applied potential (vs RHE), and  $I_0$  is the power density of the incident light. Total photoconversion efficiency is calculated by setting  $E_{app}$  to zero in the above equation. For efficiency calculation,  $E_{app}$  vs Ag/AgCl can be converted to  $E_{app}$  vs RHE by using Nernst equation ( $E_{RHE} = E_{Ag/AgCl} + 0.059 \text{ pH} + E_{Ag/AgCl}^o$ ), where  $E_{Ag/AgCl}$  is the applied potential vs Ag/AgCl, pH for 5M KOH is 13.8 and  $E_{Ag/AgCl}^o$  is standard Ag/AgCl electrode potential (0.197 V).

### 3.4 Conclusions

We have successfully fabricated and deposited size-selected TiO<sub>2</sub> NCs on three different substrates (H-Si, glass, and quartz) at room temperature under soft-landing condition using a magnetron-based nanocluster source equipped with a quadrupole mass filter. The growth process of the NCs is studied by depositing the nanoclusters under different growth conditions and by studying their growth environment. On all the substrates employed in the present work, the TiO<sub>2</sub> NCs are found to be essentially monosized and uniformly distributed over the entire surface (without agglomeration), and no surface diffusion of the NCs is observed. The use of a high vacuum system and the precise control over aggregation length and Ar-flow have enabled us to produce TiO<sub>2</sub> NCs with unprecedented high

degree of purity (as verified by XPS) and excellent uniformity in size and distribution (as demonstrated by AFM and TEM). Size-tuning experiments on H-Si substrates indicate that we also have excellent control and reproducibility for the desired NC size. A higher photoelectrochemical catalytic activity for the water splitting reaction is obtained when the NC size is below 6 nm. As the NC size is reduced, the increase in specific surface area and the greater amorphicity of the NCs both contribute to the enhanced photoelectrochemical performance. The Nanogen magnetron cluster source coupled with a quadrupole mass filter is therefore a promising versatile tool for producing high-purity, size-selected, ultra-small TiO<sub>2</sub> NCs (below 10 nm) for application in catalysis, nanoelectronics and nanobiosensors.

## Chapter 4

# Size-selected, Ultra-small, Defect-rich (TaO<sub>x</sub>, Pt) Nanocluster Composite for Promoter-Enhanced Photocatalysis

### 4.1 Introduction

Nanoscience deals with the generation and investigation of nanosized materials.<sup>2</sup> The term “nanocluster” (more than one to a few thousands of atoms) is used for a particle with size greater than individual atoms and molecules but not sufficiently large to exhibit the characteristic properties of bulk matter.<sup>10</sup> They are a direct link between the distinct behaviors of isolated atoms and molecules on the one hand and their bulk counterparts on the other. Nanoclusters have much larger surface area to volume ratio (specific surface area) than bulk matter. In the past decade, transition metal oxide nanoclusters (NCs) have been used in numerous applications in catalysis, sensors, optoelectronic and magnetic devices.<sup>11,13,17,123,124,127</sup> These applications all require the creation of stable arrays of nanoclusters that could maintain their properties with respect to the relevant operating environment. While most of the transition metal and metal oxides have exhibited these properties separately on their own, combination of two or more types of NCs on a single substrate could lead to cooperative, parallel or sequential catalytic processes, which may open up new opportunities of novel cluster applications.<sup>37,63</sup> With the development of nanocluster molecular beam systems, which has been providing fundamental understanding of gas-phase reaction dynamics and catalysts in the past several decades,<sup>51,128</sup> there has been a recent surge in interest in producing three-dimensional arrays of discrete size-selected NCs onto different surfaces.<sup>9,137,152,153</sup> Among the various techniques used for depositing transition metal NCs onto surfaces, gas-phase aggregation technique has shown the most promise in the synthesis of isolated and supported NCs.<sup>27,132,154</sup> There are many studies focused on the nanoclusters of transition metals (Cu<sup>27</sup>, Ag<sup>26</sup>, Au<sup>135</sup>, Pd<sup>28</sup>), metal alloys (Au/Pd<sup>155</sup>, Cu/Au<sup>156</sup>) and metal oxides (TiO<sub>2</sub><sup>38</sup>, ZnO<sup>136</sup>).

In recent years, Ta<sub>2</sub>O<sub>5</sub> (with a band gap of 3.9 eV) has emerged as an important new material for various applications. Its higher chemical stability than other transition metal oxides (e.g. TiO<sub>2</sub>, Fe<sub>2</sub>O<sub>3</sub>, CuO) and its high dielectric constant make Ta<sub>2</sub>O<sub>5</sub> an alternative candidate for photocatalytic reactions. The redox potentials of H<sup>+</sup>/H<sub>2</sub> (0 V vs. RHE) and O<sub>2</sub>/H<sub>2</sub>O (+1.23 V vs. RHE) are well within the valence band maximum and conduction band minimum of Ta<sub>2</sub>O<sub>5</sub>, which makes Ta<sub>2</sub>O<sub>5</sub> a promising high-performance catalyst material for solar water splitting, while Ta<sub>2</sub>O<sub>5</sub> rich with surface and bulk defects (often termed as TaO<sub>x</sub>) offers potential enhancement in the photocatalytic performance particularly in the visible light region. An assembly of discrete TaO<sub>x</sub> NCs would be of

great interest because of its high specific surface area, which provides a large number of reaction sites (per volume) for electron-hole ( $e^-h^+$ ) pair generation for photoelectrochemical water splitting reaction. All the studies have thus far been limited to structural modification of  $Ta_2O_5$  nanostructures to increase the solar harvesting.<sup>68</sup> However, one potential limit on the performance is the high recombination rate of photogenerated electron-hole pairs. We have described a new approach here to further enhance the photocatalytic performance of the semiconductor-based photocatalysts by introducing a reaction promoter. The high recombination rate problem can be alleviated with the deposition of noble metals by taking advantage of their plasmonic properties. Metallic NCs (Pt in our case) support collective electron oscillations, known as surface plasmons, which help in concentrating and scattering the light near the semiconductor/liquid interface that leads to more effective light trapping inside the semiconductor and therefore better solar light harvesting.

In the present work, we focus on size-selected ultrasmall  $TaO_x$  and Pt nanoclusters (both ~5 nm in dia), created and deposited or co-deposited using a unique gas-phase aggregation technique, coupled with a *built-in* quadrupole mass filter for precise size-selection (Ta,  $Z = 73$ , 180.945 amu & Pt,  $Z = 78$ , 195.078 amu). A major challenge in depositing monosized NCs on substrates is the tendency of the NCs to agglomerate on the surface, which is alleviated by ensuring soft-landing of NCs onto the substrates. We further demonstrate the photoelectrochemical catalytic performance of the ( $TaO_x$ , Pt) NC composite film deposited on silicon substrates. As a high density of surface defects is inherently beneficial to potential applications in surface-dependent catalysis and nanoelectronics, the synthesis of stable, precisely size-selected  $TaO_x$  and Pt NC composite promises novel nanocluster composite systems with desirable synergetic physiochemical properties for emerging photoelectrochemical, electronic and optoelectronic applications.

## 4.2 Experimental Details

Size-selected  $TaO_x$  and co-deposited ( $TaO_x$ , Pt) nanoclusters have been produced by using a novel nanocluster generation system (Nanogen 500, Mantis Deposition Ltd.). A DC magnetron sputtering process coupled with gas-phase aggregation, based on Haberland<sup>133,134</sup> concept of cluster formation, is used to deposit the source materials from the metallic Ta and Pt targets (99.95% purity, ACS alloy). Plasmas containing Ta and Pt atoms and ions are generated upon magnetron sputtering in Ar (at 60 mA), and the sputtered atoms condense into clusters under high collision-prone ambient. Details of the cluster growth mechanism have been given in our previous work.<sup>153</sup> Briefly, the cluster growth involves two basic steps: (i) generation of source atoms and ions by sputtering, which then undergo (ii) collisional condensation, involving nucleation and gas-phase aggregation leading to cluster formation.<sup>134</sup> Based on their mass-to-charge ratio, precise mass selection of NCs with a particular size

is achieved by using a quadrupole mass filter with 2% mass resolution before their landing onto the substrate. H-terminated Si(100) (H-Si) substrates are used for the present work. Prior to nanocluster deposition, all the substrates are cleaned ultrasonically in acetone and isopropanol and also rinsed in 2% HF for 10 minutes to remove the native oxide layer and to produce H-termination on the Si substrate. After the deposition, the Ta NCs undergo oxidization in ambient (when the sample is brought out from the deposition chamber), producing TaO<sub>x</sub>. The Pt NCs, on the other hand, remain metallic and stable in air.

The surface morphology, size and crystalline structure of the NCs are characterized by atomic force microscopy (AFM) operated in tapping mode in a Digital Instruments Dimension 3100 Nanoman Nanoscope IV microscope, field-emission scanning electron microscopy (SEM) in a Zeiss Merlin microscope, and transmission electron microscopy (TEM) in a Zeiss Libra 200 MC microscope. TEM samples are prepared by directly depositing the NCs onto a lacey carbon coated TEM copper grid. The chemical-state composition is analyzed by X-ray photoelectron spectroscopy (XPS) in a Thermo-VG Scientific ESCALab 250 Microprobe, equipped with a monochromatic Al K $\alpha$  X-ray source (1486.6 eV). The XPS data is fitted by using the CasaXPS software with a Shirley background. The photoelectrochemical water splitting measurements are performed in a three-electrode system in a quartz cell, where the nanocluster film supported on H-Si is used as the photoanode, and Ag/AgCl (3 M KCl) and Pt are used as the reference and counter electrodes, respectively. The experiments are carried out in an electrolyte solution of 1 M KOH (Sigma Aldrich), prepared in Millipore water at room temperature. The photocurrents are measured with a CH Instruments 660A electrochemical workstation, both in the dark and under illumination of a 300 W Xenon lamp (300-1000 nm, Oriol Instruments 6258) coupled with an AM 1.5 G filter that delivers simulated sunlight with a power density of 50 mW/cm<sup>2</sup>.

### 4.3 Results and Discussion

Size-selected Ta (TaO<sub>x</sub> after oxidization) and Pt NCs with specific mass-to-charge ratios are successfully synthesized using the nanocluster generation source (Nanogen), shown schematically in Figure 4.1a. Figure 4.1b shows the average cluster size (diameter) of Ta NCs as functions of Ar-gas flow rate (15-50 sccm) and aggregation length (10-90 mm). Evidently, the longer the aggregation length in the gas-condensation zone, the larger is the NC size. Depending on the aggregation length (AL), increasing the Ar-gas flow rate could decrease (for AL = 90 mm), decrease and then increase (for AL = 20-80 mm) and have minor effect on (for AL = 10 mm) the NC size, which suggests that both the Ar-gas flow rate and the AL could affect the growth kinetics. Ar flow could affect the NC growth not just by initiating the plasma that sputters the source to remove the source atoms into the

condensation zone (aggregation zone), and also by providing nucleation seeds for NC growth and serving as a carrier gas for transporting the as-grown NCs towards the substrate. Figure 4.1c shows the size distributions as represented by the collector currents as functions of NC size in diameter for the Ta NCs. The collector current peak maximum is found to decrease with increasing aggregation length, while at the same time its peak width (corresponding to the size distribution) broadens. After size selection, the broad NC size distribution (Figure 4.1c) can be typically restricted to within 2% mass resolution (i.e. 2% of the full width of the distribution, Figure 4.2) by applying an appropriate set of AC and DC voltages to the quadrupole mass filter. Further details about parameter optimization and size selection have been discussed elsewhere.<sup>153</sup>

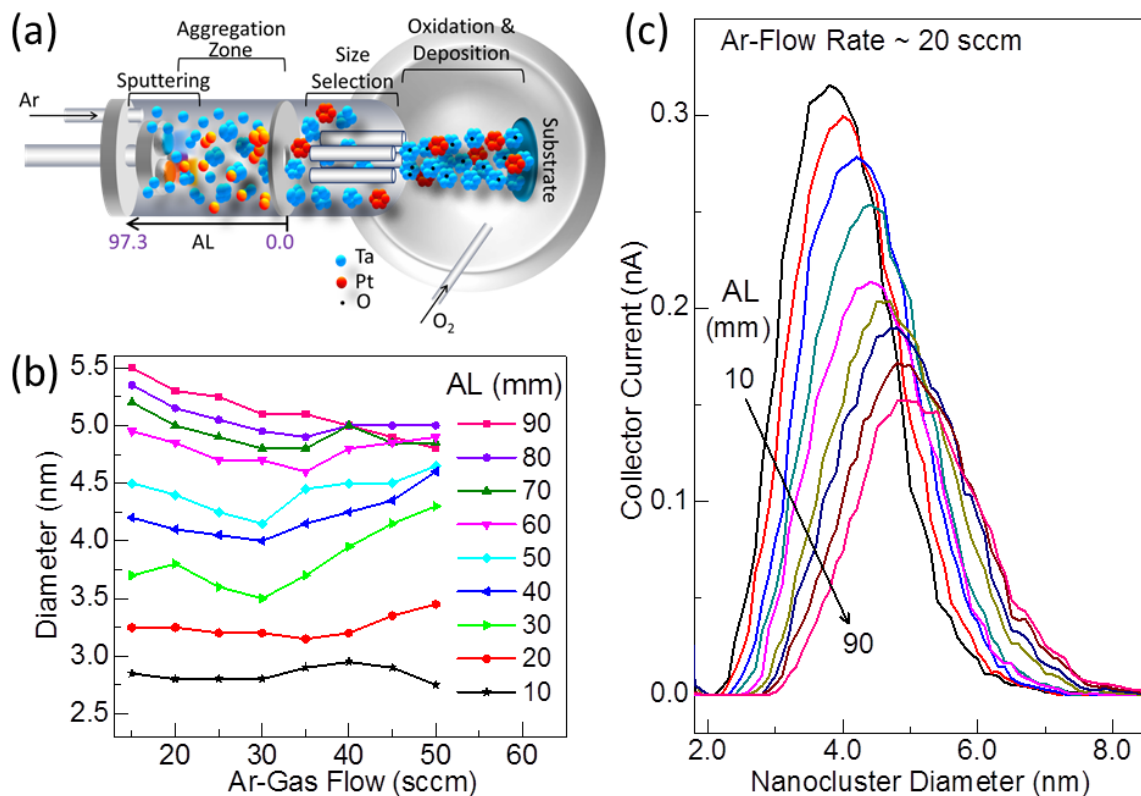


**Figure 4.1** (a) Schematic diagram of the nanocluster generation source coupled with a quadrupole mass filter for precise size selection (not drawn to scale). Two sources can be ignited simultaneously to create a composite plasma consisting of two materials (Ta and Pt in this work) through magnetron sputtering. The constituent atoms combine together in the aggregation zone to form  $Ta_n$  and  $Pt_n$  clusters, which are transported out of the aggregation chamber through a 3 mm orifice by the Ar gas flow. Generally, a large fraction of the clusters are positively charged ( $Ta_n^+$  and  $Pt_n^+$ ) so that a quadrupole mass filter can be used to perform size selection of the nanoclusters (after exiting through the orifice) based on their mass-to-charge ratio. The size-selected nanoclusters then enter into the

main chamber where they become partially oxidized and neutralized to form  $\text{TaO}_x$ , and deposit onto the substrate under soft-landing condition. The aggregation length (AL) corresponds to the distance between the source and the 3 mm orifice, which can be varied to obtain different nanocluster sizes. (b) Cluster size as a function of Ar-gas flow rate for different aggregation lengths from 10 to 90 mm (in step of 10 mm). (c) Size distribution as represented by the quadrupole collector current as a function of nanocluster diameter for a fixed Ar flow rate of 20 sccm and variable aggregation lengths from 10 to 90 mm (in step of 10 mm). The mode cluster size is defined as the size for the peak maximum of each distribution curve.

Co-deposition is started by igniting the plasma to sputter both Ta and Pt targets simultaneously and then collecting the resulting NCs onto the substrate. The sizes of both Ta and Pt NCs are kept fixed at 5 nm (dia) with appropriate setting of the quadrupole mass filter. Figure 4.2 compares the near Gaussian size distribution profiles of Ta and Pt NCs obtained separately for the same (Ar flow rate, AL) combination of (40 sccm, 60 mm). At this combination, both NCs have approximately the same mode size (4.7 nm), because of their similar atomic masses. It is therefore possible to conduct size selection for both Ta and Pt NCs of 4.7 nm by using the same appropriate set of AC and DC voltages on the diagonal poles of the quadrupole mass filter. The vertical shaded region in Figure 4.2 corresponds to parts of the nanocluster distributions that are mass-selected within 2% of the respective mode cluster sizes. The respective total mass profiles (right axis) as a function of nanocluster size for Ta and Pt NCs produced by Nanogen cluster source are also shown in Figure 4.2.

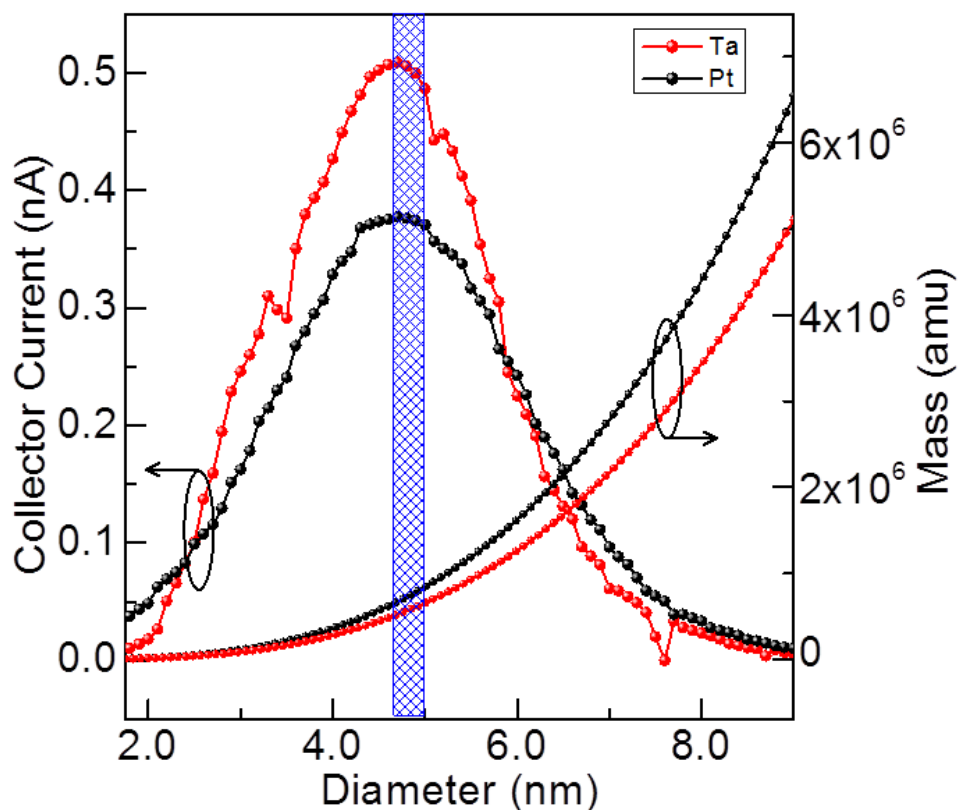


**Figure 4.2** Near Gaussian nanocluster size distribution profiles for the Ta and Pt nanoclusters obtained separately at (40 sccm, 60 mm) with the mode size of 4.7 nm each, where the quadrupole collector current (left axis) is proportional to the cluster population of specific cluster size. The total masses of the nanoclusters (right axis) are also shown as functions of their diameters. The vertical shaded area correspond to the segment of the cluster size distribution within 2% mass resolution as selected by applying an appropriate set of AC and DC voltages on the quadrupole mass filter.

Figure 4.3a shows the secondary electron SEM image of co-deposited TaO<sub>x</sub> and Pt NCs, with respective total deposition times of 30 min and 15 min, on a H-Si substrate. We then increase the Pt deposition time to 30 min (Figure 4.3b) and 45 min (Figure 4.3c) while keeping the Ta deposition time fixed at 30 min during the (TaO<sub>x</sub>, Pt) co-deposition. As expected, the population of Pt clusters (brighter spots) increases with increasing Pt deposition time. The near Gaussian size distribution with a mode size of 5 nm is illustrated for the Ta (30 min) and Pt (30 min) co-deposition in Figure 4.3b, inset. Figure 4.3d shows the tapping-mode AFM image of the (TaO<sub>x</sub>, Pt) NCs co-deposited for 30 min on a H-Si substrate. With the spatial resolution of AFM generally larger than 10 nm, the size of the as-deposited NCs can be estimated from their respective height profile, assuming a spherical shape for the NCs. The size distributions obtained from our *ex-situ* SEM and AFM measurements for the as-

deposited NCs are found to be in good accord with the collector current profiles of the quadrupole mass filter (Figure 4.2).

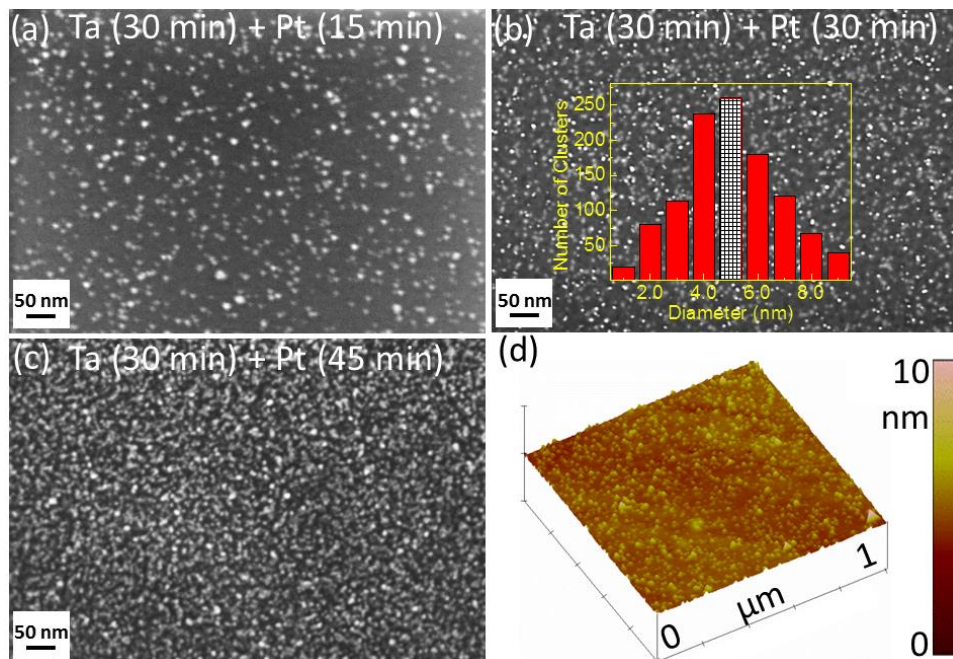


**Figure 4.3** Secondary electron SEM images of the co-deposited Ta and Pt nanoclusters with deposition parameters (30 sccm, 60 mm) obtained for Ta deposition for 30 min and Pt deposition for (a) 15 min, (c) 30 min and (d) 45 min. Inset of (b) shows the corresponding size distribution before size selection, while the shaded area marks the portion of the nanoclusters size-selected by the quadrupole mass filter. (d) AFM image used to estimate the nanocluster size distribution by using the heights of the nanoclusters.

The TEM image of the size-selected ( $\text{TaO}_x$ , Pt) NCs co-deposited for 30 min directly on a TEM grid is shown in Figure 4.4. Evidently, the size of both  $\text{TaO}_x$  and Pt NCs are found to be quite similar ( $\sim 5$  nm), and the excellent uniformity of the nanocluster size is clearly evident. High-resolution TEM images of typical nanoclusters reveal the crystalline nature of Pt NCs (top inset) and amorphous nature of the  $\text{TaO}_x$  NCs (bottom inset). The interplanar spacing of the (111) planes in the Pt NC as determined from the high-resolution image is  $2.27 \text{ \AA}$ , which is in good accord with the FCC Pt crystal.<sup>157</sup>

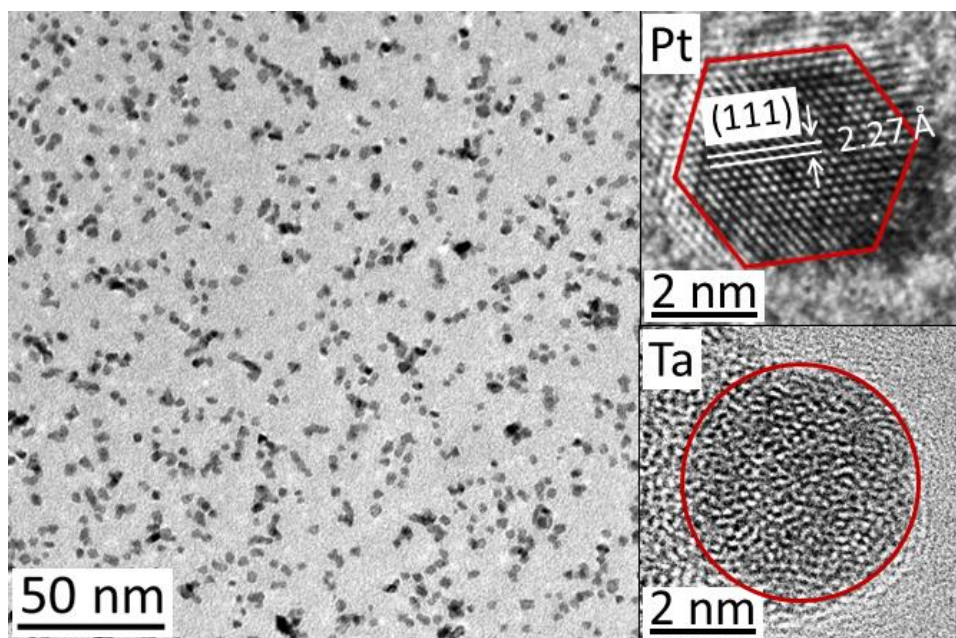


**Figure 4.4** TEM image of the (TaO<sub>x</sub>, Pt) nanoclusters directly co-deposited on lacey carbon coated TEM grid. The corresponding high-resolution TEM images of a Pt and a TaO<sub>x</sub> nanocluster, each of 5 nm dia, are shown in top right and bottom right panels, respectively. The Pt nanocluster depicting the interplanar spacing corresponds to Pt(111) plane, while the TaO<sub>x</sub> nanocluster is found to be amorphous.

Figure 4.5 shows the depth-profiling XPS spectra of the O 1s, Ta 4f and Pt 4f regions of a typical (TaO<sub>x</sub>, Pt) co-deposited NC film (Figure 4.3c) with a common mode size of 5 nm on H-Si. Before sputtering, the O 1s spectrum (Figure 4.5a) exhibits an intense SiO<sub>2</sub> peak at 532.8 eV, with a rather weak shoulder at 530.8 eV consistent with the assignment to Ta<sub>2</sub>O<sub>5</sub>.<sup>158</sup> Upon sputtering, the maximum of the strong O 1s feature appears to shift to a lower binding energy as the peak becomes less intense and broader, which suggests the emergence of other oxygen-deficient TaO<sub>x</sub> phase at a lower binding energy. The prominent Pt 4f<sub>7/2</sub> (4f<sub>5/2</sub>) peak at 71.2 (74.5) eV in Figure 4.5b is attributed to metallic Pt. After 15 s of Ar sputtering, a weak 4f<sub>7/2</sub> (4f<sub>5/2</sub>) peak appears at 72.6 (75.9) eV, which becomes more prominent upon further sputtering. This feature can be assigned as Pt<sub>2</sub>Si, i.e. Pt silicide appearing at the interface between the Pt NCs and Si. In contrast, no Ta silicide feature is observed. The prominent Ta 4f<sub>7/2</sub> (4f<sub>5/2</sub>) peak at 26.9 (28.8) eV corresponds to the Ta<sub>2</sub>O<sub>5</sub> (Figure 4.5c), in good accord with the earlier report.<sup>159</sup> The presence of the strong Ta<sub>2</sub>O<sub>5</sub> feature and the absence of metal silicide feature confirm that the as-grown Ta NCs have been completely oxidized at least in the near-surface region of the NCs. The minor shift in the spectrum towards the lower binding energy is due to the removal of surface hydrocarbons commonly present as a result of ambient handling. A well-defined Ta 4f<sub>7/2</sub> (4f<sub>5/2</sub>) peak begins to emerge at 22.6 (24.5) eV after 30 s of sputtering, and it can be attributed to the

TaO<sub>x</sub> phase ( $1 < x < 2.5$ ). Upon further sputtering to 60 sec, sharper and more intense Ta 4f<sub>7/2</sub> (4f<sub>5/2</sub>) peak appears at 22.4 (24.4) eV, which corresponds to the emergence of the metallic Ta phase. This peak migration is similar to that found for the O 1s feature in Figure 4.5a, indicating the transformation of Ta<sub>2</sub>O<sub>5</sub> to oxygen-deficient TaO<sub>x</sub> ( $1 < x < 2.5$ ) and to metallic Ta as a result of ion-induced reduction of Ta<sub>2</sub>O<sub>5</sub> due to Ar-ion bombardment.<sup>158</sup>

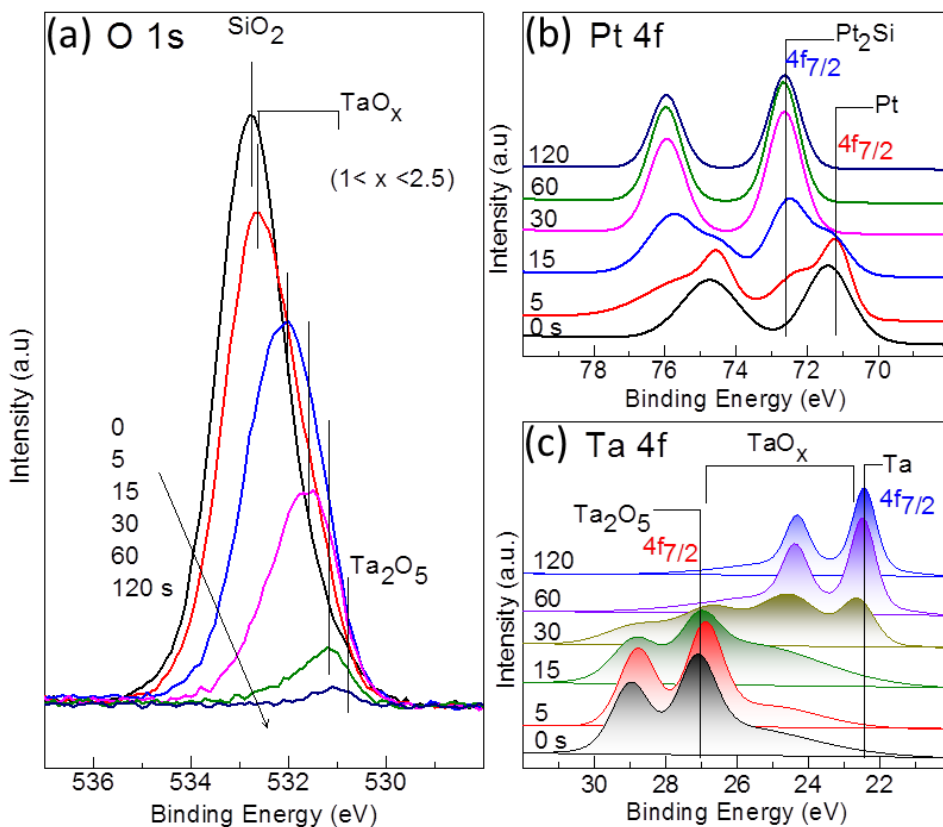


**Figure 4.5** XPS spectra of (a) O 1s (b) Pt 4f and (c) Ta 4f regions for the (TaO<sub>x</sub>, Pt) nanoclusters co-deposited on a H-Si substrate as a function of Ar sputtering time.

The photoelectrochemical water splitting properties of the co-deposited (TaO<sub>x</sub>, Pt) NC samples are studied under simulated sunlight (with an AM 1.5 G filter) using a three-electrode system connected to an electrochemical workstation. H-Si substrates coated with a fixed TaO<sub>x</sub> NC amount and three different Pt NC loading amounts (as shown in Figure 4.3), with a mode size of ~5 nm for both TaO<sub>x</sub> and Pt NCs, are used as the photoanodes, while a Pt wire and Ag/AgCl (3M KCl) solution are used as the counter and reference electrodes, respectively. All the photocurrent measurements are conducted for an illumination area of 5×5 mm<sup>2</sup> with a power density of 50 mW/cm<sup>2</sup> (half a sun), in accord to our

previous work.<sup>153</sup> 1 M KOH is used as the aqueous electrolyte and the light is flashed on the sample immersed in the electrolyte. Before discussing the photocatalytic reactions of the NCs, it is important to emphasize that the substrate (H-Si) shows no photoresponse in dark or upon illumination with the simulated sunlight (data not shown). Figure 4.6a and 6b show the schematic diagrams for the transfer and separation of photogenerated electrons and holes on the TaO<sub>x</sub> NC semiconductor surface, respectively, with and without the presence of metallic Pt NCs. The presence of Pt NCs in the system promotes the water splitting reaction by efficiently concentrating and scattering the intense light near the semiconductor surface. In effect, it increases the number of photogenerated carriers that can reach the semiconductor/electrolyte interface and participate in the desired photoelectrochemical water splitting reaction to produce O<sub>2</sub> and H<sub>2</sub>. With the absence of Pt NCs (Figure 4.6a), the actual amount of separated electrons and holes are less because of their fast recombination and therefore the photocatalytic activity is limited. In contrast, with the presence of Pt NCs (Figure 4.6b), the electron-hole pairs are separated efficiently with the transfer of electrons to the nearby Pt NC surface (before recombination could occur), leading to H<sub>2</sub> production, while the holes remaining onto the semiconducting TaO<sub>x</sub> surface promote the production of O<sub>2</sub>. The Pt NCs in effect serve as the promoters to the TaO<sub>x</sub> photocatalysts by providing temporary charge holding tanks to arrest the quick recombination process at the semiconductor surface. Figure 4.6c compares the photoresponse profiles observed for the three different (TaO<sub>x</sub>, Pt) NC composite samples, consisting of a fixed amount of TaO<sub>x</sub> NCs and different amount of co-deposited Pt NCs (Figure 4.3). Evidently, increasing the relative amount of the Pt NC promoters from 0 to 15 to 30 min deposition has increased the photocurrent density from 0.24 to 0.33 to 0.46 mA/cm<sup>2</sup> at 0.4 V vs Ag/AgCl. For Pt loading with 45 min deposition, however, the photocurrent density has discernibly decreased. This reduction could likely be due to overload of the Pt NCs in the composite system, the excess of which starts to physically block the photosensitive TaO<sub>x</sub> surface, consequently reducing the surface concentration of electrons and holes available for the reaction.

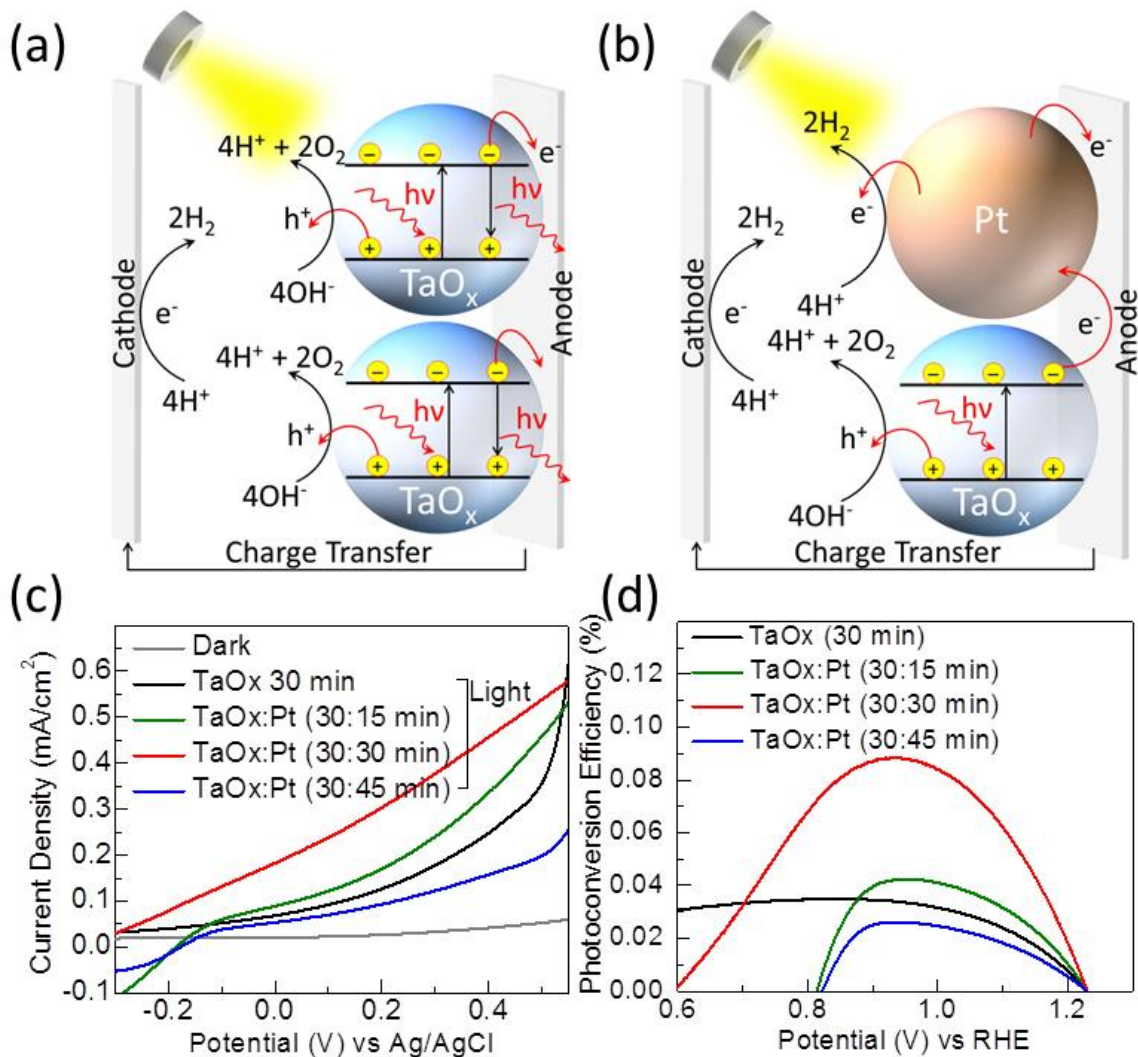


**Figure 4.6** Schematic diagrams of the mechanism of photoelectrochemical water splitting reactions for TaO<sub>x</sub> NCs (5 nm dia.) (a) without and (b) with Pt NCs (5 nm dia.) co-deposited on H-Si. (c) Photocurrent density and (d) photoconversion efficiency as functions of applied potential obtained for a photoelectrochemical water splitting reaction in a 1 M KOH electrolyte, using the (TaO<sub>x</sub>, Pt) nanoclusters supported on H-Si substrates as the photoanodes, all with an illumination area of 5×5 mm<sup>2</sup> under a 300 W Xe lamp coupled with an AM 1.5 G filter at a power density of 50 mW/cm<sup>2</sup> (half sun).

The photoconversion efficiency is dependent on the amount of material loading on the substrate because of the availability of active surface sites. For the (TaO<sub>x</sub>, Pt) NC composite with co-deposition for 30 min, we obtain the highest photoconversion efficiency of ~0.1% (Figure 4.6d), and correspondingly a total photoconversion efficiency of ~0.4%, as estimated based on earlier reports,<sup>153</sup> at an applied potential of 0.92 V vs RHE. This corresponds to the highest ever photoconversion efficiency observed for such a nanocluster system, and it is also comparable to that observed other

types of Ta<sub>2</sub>O<sub>5</sub> nanostructures (with the photoconversion efficiency in the range of 0.01-2.0%).<sup>160,161</sup> This performance is especially remarkable because the NCs have less than a monolayer and only ~20% coverage on the substrate, in marked contrast to all other reported cases which employ a significantly larger amount of materials and therefore provides a potentially much larger number of active sites for the same reaction.<sup>68,161</sup> The most significant result in the present work is that the performance can be enhanced multifold by incorporating a promoter such as Pt NCs in the semiconducting photocatalytic system. Furthermore, no post-synthesis modification is necessary for the present photocatalyst system, in marked contrast to other reported catalysts, where different chemical treatments of the materials have been used to modify the morphology and/or structure of the active surfaces in order to enhance the water splitting reaction and to achieve better solar harvesting.<sup>162,163</sup> Using a linear extrapolation of the coverage of these defect-rich TaO<sub>x</sub> NCs to a monolayer, we estimate our photoconversion efficiency to be 2% (5 times higher than what we observe in this work), which will make our co-deposited nanocluster system a top photoelectrochemical performer in tantalum oxide based photocatalysis. As the amount of active surface sites increases with increasing TaO<sub>x</sub> NC coverage, more Pt NC promoters can also be loaded to further enhance the photocatalytic performance. Furthermore, we could also potentially extend the work to nanoclusters with even smaller size and to clusters appropriately chemically functionalized, also suggested our previous work,<sup>153</sup> both of which promise new opportunities for other nanosize-dependent emerging applications such as nanoelectronics and solar cells.

#### 4.4 Conclusion

We have successfully synthesized and co-deposited size-selected TaO<sub>x</sub> and Pt NCs on H-Si substrates at room temperature under soft landing conditions using a magnetron-based nanocluster source equipped with a quadrupole mass filter. The as-grown NCs are found to be nearly monosized and uniformly distributed over the entire surface (without surface agglomeration), where defect-rich, amorphous TaO<sub>x</sub> NCs (with a typical mode size of 5 nm) are well mixed with nanocrystalline Pt NCs (also with a mode size of 5 nm). Using a different amount of deposition time for each sputtering target, the amount of material loading can be effectively controlled and their effects are studied in a photoelectrochemical water splitting reaction. In the present work, we have described a new approach of introducing a promoter in the photoelectrochemical water splitting reaction to reduce the higher recombination rates of electron-hole pairs generated in the semiconductor photocatalysts and thus enhancing the water splitting performance. The defect-rich TaO<sub>x</sub> NC photocatalysts with high specific surface area, along with the crystalline metallic Pt NC promoters, contribute to the observed enhanced photoelectrochemical performance. The highest photocatalytic activity for the water splitting reaction

is observed when the amount of Pt NCs is almost the same as TaO<sub>x</sub> NCs, while a higher Pt NC loading leads to blockage of photoelectrochemically active surface of TaO<sub>x</sub>, thereby reducing the observed photocatalytic activity. Along with the concept of reaction promoters, the use of size-selected, ultrasmall metal/metal oxide nanoclusters below 10 nm (as produced by the novel Nanogen nanocluster source coupled with the quadrupole mass filter) can be extended to other applications in catalysis, chemical sensing, and nanoelectronics.

# Chapter 5

## Bipolar Memristors Based on Defect-Rich Ultra-Nanocrystalline $\text{TiO}_x$ Film

### 5.1 Introduction

Resistive random access memory (ReRAM), or memristor, based on transition metal oxides has been demonstrated as the fourth passive circuit element with potential application as the next-generation non-volatile memory devices.<sup>70,71,87,90,91,164–168</sup> Properties such as low power consumption, sub-nanosecond switching speed and high switching endurance<sup>87,90</sup> make the memristor an attractive candidate for such adaptive systems as logic circuits, neuromorphic devices and artificial biological systems. With a simple metal/semiconductor-oxide/metal multilayer architecture that is independent of the substrate material, the memristor operates on the principle of binary resistive switching<sup>169</sup> between two discrete resistance states, mediated by an ionic transport process. Inspired by the first successful synthesis of  $\text{TiO}_2$  based memristor by Strukov et al. in 2008,<sup>70</sup> a large class of transition metal oxides<sup>87,88,90,93,95,170–174</sup> along with chalcogenides<sup>175</sup> and organic polymers<sup>176</sup> have been widely studied as the switching materials. Depending on the layered structures and the physical and chemical properties of these materials, there have been several proposed switching mechanisms, such as charge trapping,<sup>95</sup> formation/dissolution of one or more conducting filaments,<sup>91</sup> and electromigration of oxygen vacancies driven by an applied field.<sup>87,88,172</sup> The charge trapping mechanism involves the change in the Schottky barrier height (or width) by the presence of trapped charge carriers (holes or electrons or both) at the metal/oxide interface introduced by the metallic dopants in the switching material.<sup>177–179</sup> Filament-type switching is a widely accepted mechanism for the transition-metal oxide based switches, which are based on the emergence of one or more a few nanometer-wide vertical columns (filaments) of either the electrode metal or oxygen vacancies transported through the insulating oxide layer.<sup>88,90,100</sup> A filamentary system based on an insulating oxide switching layer generally exhibits unipolar (i.e. nonpolar) switching dominated by the Joule heating effect,<sup>93,180</sup> in which an irreversible electroforming process induced by a high bias (generally greater than  $\pm 10$  V) is required to soft-break the metal-oxide electrolyte in order to create a temperature-dependent, oxygen-vacancy-defect-rich conducting phase for resistive tuning.

Alternatively, resistive switching can also be achieved by ionic drift of the electronically charged oxygen vacancies between the two metal-insulator (oxide) interfaces induced by an electric field gradient, thereby tuning the resistance states of the device. This so-called interface-type switching is usually bipolar in nature, where the oxygen vacancies migrate towards or away from the interface

(depending on the voltage polarity) through an oxygen vacancy defect rich conducting conduit with the size of the entire device junction. While a very high electric field ( $10^6 \text{ V cm}^{-1}$ )<sup>181</sup> is generally required to move these vacancies in bulk material, such a field can be easily created by applying a few volts (6-10 V) across a film of a few nanometer thick. Depending on the nature of the switching and electrode materials and the layer stacking arrangement, the switching mechanism could be thermal dominating (filament type) or electric-field dominating (interface type). Of the various obstacles to fabricating a low power consumption memristor device, the high-bias electroforming step is recognized as the root cause behind the poor reproducibility and short life-time of the memristor.<sup>87,88,106,165</sup> While Joule heating cannot be avoided completely during resistive switching, it is the least desirable in terms of electronic stability of the device, because it could change the device behavior completely with time and could potentially damage or even destroy the device due to internal heating.<sup>90</sup> Furthermore, the formation and dissolution of the filamentary channel could vary from sample to sample in an unpredictable fashion, which leads to unreliable performance and low reproducibility and production yield. This remains to be a major challenge and there is therefore an urgent need for a new strategy that could mitigate the adverse Joule heating effect and enable the device to electroform at a much lower applied bias while reducing power consumption.

Here, we report a novel interface-type memristive device comprised of an oxygen-vacancy-defect-rich  $\text{TiO}_x$  ( $1 \leq x < 2$ ) ultrananocrystalline film with nanocrystallite size of 4-5 nm, stacked between a top and a bottom Pt electrodes. Unlike the earlier studies, all of which have focused on starting with a “perfect” material (mostly single-crystalline) and then followed by manipulating the defects such as oxygen vacancies or dopants, our approach is to introduce defects directly from the beginning. We have shown that by creating a defect-rich nanocrystalline  $\text{TiO}_x$  film grown at room temperature, the built-in defects at the edges and along structural dislocations could produce highly active non-stoichiometric regions. This enables localization of the electric field to smaller footprints that not only store the carrier charges in discrete locations but also, more importantly, create a constricted, high electric field gradient with just a small electroforming voltage. We demonstrate, for the first time, dynamic resistive switching of a high-performance  $\text{TiO}_x$ -based memristor that electroforms at a bias as low as +1.5 V (which is the lowest ever reported). Not only does this device provide greater control and reliability but also higher reproducibility in its endurance and retention capacities. With the nonlinear (Schottky) OFF state and linear (Ohmic) ON state, this device also shows stable non-volatile bipolar switching characteristics with a high ON-to-OFF current ratio and low power consumption within  $\pm 1.0 \text{ V}$ , where the device can be accessed with various analog and discrete programmable READ voltages. Together with the simplicity in the device construction, the performance achieved for our memristor promises a new generation of ReRAM device applications.

## 5.2 Materials and Methods

### 5.2.1 Device fabrication

The memristor devices were fabricated as a crossbar structure on a SiO<sub>2</sub>/Si substrate by using a three-layer photolithographical procedure with a maskless photolithography system (SF-100 Xpress, Intelligent Micropatterning Inc.). The device fabrication steps are schematically shown in Figure 5.1a. Shipley 1805 photoresist (MicroChem) was spin-coated on the substrate and the pattern was written under the exposure of UV light (434 nm). The thickness of the photoresist layer was kept at 500 nm in order to achieve high-resolution lithographical features. A 500 nm thick layer of MCC primer (MicroChem) was spin-coated on the substrate before depositing the photoresist. Spin-coating parameters for the primer and photoresist layers were set to 4500 rpm for 40 s, and both layers were baked after the deposition on a hot plate set at 90 °C for 90 s. After the UV lithographical step with a 1.10 s exposure time, the written pattern was developed in a MF-24 developer (MicroChem) for 30 s and then rinsed with Millipore water. For the bottom electrode, a 5 nm thick Ti layer was pre-deposited as an adhesion layer before sputter-deposited a 60 nm thick Pt layer at room temperature, followed by the lift-off process. For the middle active layer, a high-purity TiO<sub>x</sub> layer (60 nm thick) was produced at room temperature by in-situ oxidation of Ti deposited by using a magnetron sputtering source from a Ti metal target (99.95 % purity, ACI Alloys) in a high vacuum physical vapor deposition system (Mantis Deposition Ltd.), followed by the lift-off process. The Ar-flow was kept at 20 sccm to maintain the pressure of the deposition chamber (with a base pressure of 1×10<sup>-8</sup> mbar) at 7.5×10<sup>-3</sup> mbar. A quartz crystal microbalance was used to monitor the thickness of the TiO<sub>x</sub> film. Finally, a 30 nm thick Pt layer was deposited as the top electrode, following the same procedure used for the bottom electrode but for a shorter deposition time. All the layer thicknesses were confirmed by using a profilometer (KLA Tencor P6). For physical characterization, we deposited, in separate experiments, TiO<sub>x</sub> films on SiO<sub>2</sub>/Si, Pt-coated SiO<sub>2</sub>/Si and glass substrates using the same parameters as those used for the actual devices. All the substrates used in this work were cleaned ultrasonically in HPLC grade acetone, isopropyl alcohol and Millipore water (~18.2 MΩ). The SiO<sub>2</sub> layers (50 nm thick) were grown on Si substrates by annealing in an oxygen atmosphere in a quartz tube furnace, with oxygen flow rate set to 50 sccm and the temperature set to 900 °C for 90 min.

### 5.2.2 Characterization

The device morphology was characterized by field emission scanning electron microscopy (SEM) in a Zeiss Merlin electron microscope. Secondary ion mass spectroscopy (SIMS) was used to analyze the elemental composition of the fabricated devices in depth-profiling mode in an ION-TOF SIMS 5

system. The crystalline structures of the as-deposited and annealed  $\text{TiO}_x$  films were determined by using a PANalytical MRD X'pert Pro X-ray diffractometer with a  $\text{Cu K}\alpha$  X-ray source. UV-Visible spectroscopy on the as-deposited and annealed  $\text{TiO}_x$  film was performed in a Perkin-Elmer Lambda 1050 spectrophotometer. For the electrical characterization studies, the resistive switching behavior of the fabricated devices was measured in I-V sweep mode with a two-probe DC measurement configuration by using an Agilent B1500 semiconductor analyzer coupled with an electrical probing station (Signatone Series 1160). Tungsten probe tips with a  $10\ \mu\text{m}$  tip size were used for connecting to the electrodes.

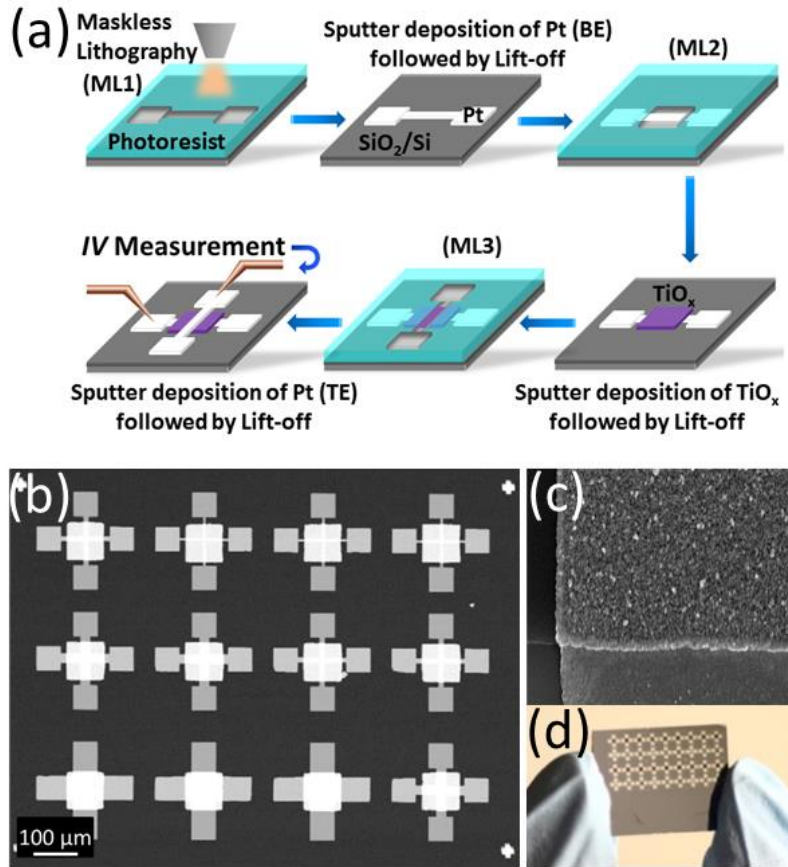


**Figure 5.1** Device fabrication and electron microscopic analysis. (a) Schematic representation of device fabrication involving three maskless lithography (ML) steps. In ML1, an I bar pattern for the bottom electrode is exposed to the photoresist. This is then followed by development in MF-24 to remove the photoresist for the pattern, sputter-coating with Pt, and finally the lift-off to remove the remaining photoresist. This process is then repeated in ML2 where a  $60\ \text{nm}$   $\text{TiO}_x$  junction layer is deposited in the patterned area whereas in ML3 is repeated with the same parameters for the Pt top layer deposition. Once the device stacking structure is fabricated, the electrical characterization is performed by connecting the microprobes to the top and bottom Pt electrodes while the switching process is observed in the  $\text{TiO}_x$  layer. (b) SEM image of the array of devices with different junction sizes ( $5\times 5\ \mu\text{m}^2$ ,  $10\times 10\ \mu\text{m}^2$ ,  $20\times 20\ \mu\text{m}^2$  and  $50\times 50\ \mu\text{m}^2$ ) fabricated on the same chip, and (c) selected  $\text{TiO}_x$  surface morphology in high magnification. (d) Photograph of the actual device array.

### 5.3 Results and Discussion

A high-resolution maskless photolithography technique is used to fabricate the three-layer Pt/TiO<sub>x</sub>/Pt memristor device on a SiO<sub>2</sub>/Si substrate (Figure 5.1a). Magnetron sputtering is used to deposit each layer at room temperature. An array of memristor devices with four typical junction sizes (5×5 μm<sup>2</sup>, 10×10 μm<sup>2</sup>, 20×20 μm<sup>2</sup> and 50×50 μm<sup>2</sup>, Figure 5.1b) is constructed on a 10×10 mm<sup>2</sup> substrate (Figure 5.1d). For each device, the layer thickness of the top Pt electrode is 30 nm, while those for the TiO<sub>x</sub> active layer and the bottom Pt electrode are 60 nm (Figure 5.2a). A 5 nm thick Ti layer is pre-deposited immediately before depositing the bottom Pt layer electrode on the SiO<sub>2</sub>/Si substrate in order to provide better Pt adhesion to the substrate, as suggested in earlier reports.<sup>87,182</sup> The cross-sectional TEM image and the corresponding EDX elemental map of the multilayer device structure (Figure 1b) validate the layer thickness dimensions, while the high-resolution TEM images of selected Pt and TiO<sub>x</sub> areas depict the nanocrystalline nature of both films (Figure 5.2b), which is also confirmed by X-ray diffraction (XRD) analysis (Figure 5.2c). Using the Scherrer analysis and the linewidths of the most intense Pt(111) and TiO<sub>x</sub>(103) features, we estimate the crystallite sizes of the Pt and TiO<sub>x</sub> films to be both 4.5 nm. In contrast, the TiO<sub>x</sub> film deposited directly on a SiO<sub>2</sub>/Si substrate (in a separate experiment) does not exhibit any well-defined peaks and is therefore amorphous. As the deposited Pt layer is ultrananocrystalline, it evidently provides a natural template to facilitate the growth of the defect-rich ultrananocrystalline TiO<sub>x</sub> layer. Precise manipulation of the Ar-gas flow rate provides good control of the oxygen vacancy defect concentration to make the TiO<sub>x</sub> active layer suitable for electronic transport. The weak feature at 77.95° in the XRD profile corresponds to the metallic Ti adhesion layer, which is also confirmed by depth-profiling X-ray photoelectron spectroscopy (XPS, Figure 5.2d).

As Ti<sup>n+</sup> (in TiO<sub>x</sub>) could be reduced to metallic Ti by ion sputtering, we limit the sputtering only to no more than 10 s (Figure 5.2d). The broad Ti 2p<sub>3/2</sub> band between the intense Ti<sup>4+</sup> feature at 459.3 eV and the weak metallic feature at 454.3 eV, emerged after very brief sputtering, could be attributed to the presence of Ti<sup>3+</sup> (at 457.6 eV) and Ti<sup>2+</sup> (at 455.3 eV). The increasing strengths of these latter features with sputtering confirm the presence of highly oxygen-deficient TiO<sub>x</sub> in the near surface, which tends to further reduce to Ti<sup>2+</sup> after 10 s of sputtering. The well distinguished Pt/TiO<sub>x</sub>/Pt structure with a 50×50 μm<sup>2</sup> junction size is also confirmed by secondary ion mass spectrometry (Figure 5.3a). The minor reduction in TiO<sup>-</sup> with increasing depth (i.e. from the top electrode to the bottom electrode) suggests minor intermixing at the interface. UV-Vis transmission spectroscopy (Figure 5.3b) conducted on the larger-area films, deposited on 10×10 mm<sup>2</sup> glass substrates under the same deposition conditions in separate experiments, shows that the transmittance of the as-deposited

film has increased from 8% to 30% in the 400-600 nm region upon annealing, which supports that the as-deposited oxygen-deficient  $\text{TiO}_x$  film has become more stoichiometric  $\text{TiO}_2$  upon annealing in air at 600 °C.

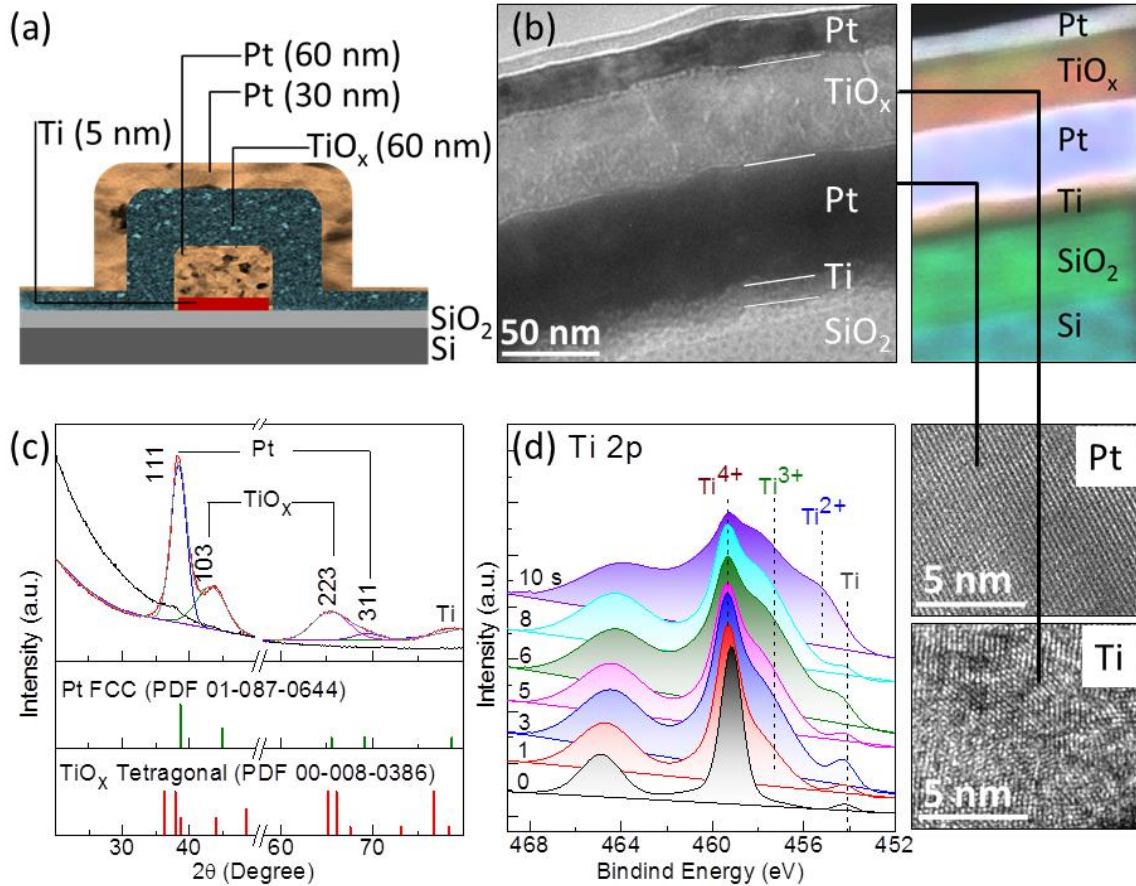


**Figure 5.2** Physical characterization for  $\text{TiO}_x$  based memristor devices. (a) Schematic cross-sectional view of the Pt/ $\text{TiO}_x$ /Pt device architecture supported on a  $\text{SiO}_2/\text{Si}$  substrate. (b) TEM image of a cross section of a typical memristor device, with the corresponding EDX elemental maps (top right) and high-resolution TEM images of selected Pt and  $\text{TiO}_x$  regions (bottom right). For each device, the layer thickness of the top Pt electrode is 30 nm, while those for the  $\text{TiO}_x$  active layer and the bottom Pt electrode are 60 nm. A 5 nm thick Ti layer is pre-deposited immediately before depositing the bottom Pt layer electrode on the  $\text{SiO}_2/\text{Si}$  substrate in order to provide better Pt adhesion to the substrate. (c) XRD profile and (d) depth-profiling XPS spectra of Ti 2p region of a  $\text{TiO}_x$  film as-deposited on the Pt bottom electrode pre-deposited with a Ti adhesion layer, all supported on a  $\text{SiO}_2/\text{Si}$  substrate, shown along with the reference patterns for Pt FCC (PDF# 01-087-0644) and  $\text{TiO}_x$  tetragonal phase (PDF# 00-008-0386) in c and with the binding energy locations of relevant Ti ionic states in d. As  $\text{Ti}^{4+}$  (in  $\text{TiO}_x$ ) could be reduced to metallic Ti by ion sputtering, we limit the sputtering only to no more than 10 s. Precise manipulation of the Ar-gas flow rate provides good control of the oxygen vacancy defect concentration to make the  $\text{TiO}_x$  active layer suitable for electronic transport.

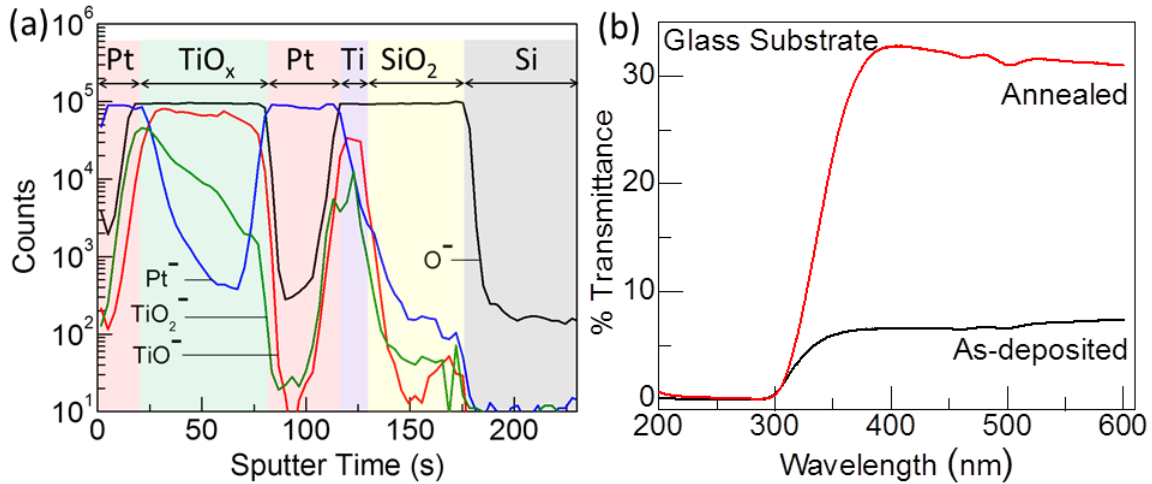


**Figure 5.3** (a) SIMS depth profiles for the Pt/TiO<sub>x</sub>/Pt memristor with junction size of 50×50 μm<sup>2</sup>. Secondary ion mass spectrometry is used to examine the changes in the elemental composition in the multilayered device as a function of sputtering depth. Different colored regions correspond to different layers as mentioned on the top of each colored region. Evidently, there is a uniform distribution of oxygen within the TiO<sub>x</sub> matrix while there is no oxygen diffusion into the Pt layer, which accounts for the stability of the electrode. (b) UV-Vis spectra in transmittance mode for the TiO<sub>x</sub> film as-deposited and annealed on glass substrates. The difference in the transmittance is due to the phase change with oxidation during annealing step. The as-deposited film is semi-transparent with the observed transmittance at ~8%, while annealing causes the sample to become more transparent, with the transmittance increased up to ~30%. This can be correlated with the phase change from the more conducting TiO<sub>x</sub> to the more insulating TiO<sub>2</sub> due to further oxidation during annealing.

### 5.3.1 Switching behavior

Prior to any applied bias, the TiO<sub>x</sub> film stays in the virgin state, exhibiting very high resistance of ~MΩ, with oxygen vacancies distributed uniformly throughout the film thickness. The conduction mechanism of the device in the virgin state is therefore governed by the low oxygen vacancy concentration at the Pt/TiO<sub>x</sub> interface, which leads to Schottky-like rectifying behavior in the current-voltage (I-V) curve over the ±1.0 V range (Figure 5.4a, inset). To “activate” the device for the first time from its virgin state to the ON state, the device must undergo an irreversible electroforming process, in which the applied bias is increased in small increments to generate an electric field gradient just sufficient to enable ionic drift (electromigration of oxygen vacancies in our case) between the electrodes (Figure 5.4b). In the positive sweep (starting from zero applied voltage), the I-V characteristic changes dramatically from the exponential behavior (of the virgin state, Figure 5.4a, inset) at +1.5 V. At this so-called electroforming voltage, the device, for the first time, undergoes a sharp transition from the high resistance state (HRS) to the low resistance state (LRS) with a

significant increase in the corresponding current (Figure 5.4a, top panel). To ensure the safe operation of the device, a compliance current is set to 10 mA. Once activated, the corresponding I-V profile of the device shows a symmetrical Ohmic behavior until  $-0.92$  V, during negative sweep. At  $-0.92$  V, the device exhibits a voltage-controlled negative differential resistance over a small range (from  $-0.92$  V to  $-1.08$  V) before it returns to the OFF state (i.e. the device undergoes a reverse transition from LRS to HRS) at the negative threshold ( $-1.5$  V). This corresponds to the inhomogeneity in the electric field arising from scattered oxygen vacancies during the negative sweep. Due to this inhomogeneity, the interface could provide oxygen vacancy trapping sites created by electric field localization in the ultrananocrystalline film, which causes the difference in oxygen vacancy diffusion capacity and leads to the self-organized spatial pattern formation of the electric field domains<sup>171</sup> and interface-type (isothermal) switching.<sup>172</sup> In a schematic representation of the complete switching mechanism (Figure 5.4b), the activation of the virgin state is followed by initialization in the electroforming (first) cycle, after which the device can be used in subsequent SET/RESET cycles during normal operation. During activation (the first positive sweep), a conduit made up of oxygen vacancies within the  $\text{TiO}_x$  matrix is formed to enable the ionic drift, and at this stage some oxygen vacancies are permanently trapped at the bottom  $\text{TiO}_x/\text{Pt}$  interface. In the first negative sweep (the initialization step), the oxygen vacancies are driven away from the bottom electrode, which opens up a small gap between the trapped vacancies at the bottom electrode and the vacancies attracted towards the top electrode in the conduit (referred here as the conduit gap, Figure 5.4b). Because of the single-phase  $\text{TiO}_x$  film, this switching behavior is irrespective of the directional bias, i.e. the I-V curve obtained with bias applied on the top electrode (and the bottom electrode grounded) is a mirror image of that obtained with the bias applied on the bottom electrode (and the top electrode grounded) (Figure 5.5). This is an important result because almost all of the memristor devices reported to date are unidirectional,<sup>88,166</sup> where one of the interfaces is Ohmic with the other Schottky by default. This unidirectional switching characteristic is due to the presence of an additional  $\text{TiO}_2$  layer in their device architecture,<sup>102,107</sup> which imposes the filament-type switching mechanism based on Joule heating. As the oxygen vacancies have to cross the insulating  $\text{TiO}_2$  barrier by forming a filament (or filaments) via a tunneling process, a significantly higher applied bias is required. In our case, the Schottky and Ohmic interfaces are created with the ionic drift in the single-phase oxygen-deficient  $\text{TiO}_x$  layer, which removes the need of tunneling. This in turn enables the activation of the device at a much lower voltage and the device to be operated in a bi-directional fashion.

The corresponding  $|I|$  vs  $V$  profiles (Figure 5.4a, middle panel) demonstrate the two orders of magnitude difference between the current obtained in the virgin state (over the sweep voltage range of  $\pm 1.0$  V) and that in the electroforming step (sweep voltage range of  $\pm 1.5$  V), while the resistance

profile (obtained based on Ohm's law) for the electroforming step (Figure 5.4a, bottom panel) illustrates the significant resistance difference between HRS ( $\sim\text{M}\Omega$ ) and LRS ( $\sim\text{k}\Omega$ ). The latter also confirms the Schottky to Ohmic Pt/TiO<sub>x</sub> interface exchange during the electric field induced ionic drift in the electroforming process. In contrast to the thermal dominated Chua's memristor,<sup>71</sup> where a critical temperature (induced by Joule heating) is required for filament formation, our memristor shows an extremely sharp transition between the HRS and LRS. This is because the low electroforming voltage (1.5 V) achieved in our case minimizes any excess heat such that the vacancy drift could occur at temperature much lower than the critical temperature. This lower temperature freezes the resistance state, which induces a sharp transition between the HRS and LRS, illustrating the ultrafast switching capability. This is a significant result because the electroforming voltage in our case is much smaller than those in previous reports (6-10 V).<sup>91,94,102,183,184</sup> Even with the so-called electroforming-free devices, their switching (SET) voltages are reported to be 5 V<sup>106</sup> and 10 V,<sup>102</sup> which are at least 5 times the SET voltage of our present device (1 V). Further, the strongly nonlinear and linear I-V curves for the respective OFF and ON states provide much better sensitivity during the READ operation, where an almost constant ON-to-OFF current ratio can be achieved irrespective of the READ voltage. We attribute this to the increase of localized electric field density as a result of the ultrananocrystalline nature of our TiO<sub>x</sub> film, and to the inherently high concentration of built-in oxygen vacancies, which reduces the need for further oxygen vacancy evolution at high bias through Joule heating.

After the first sweep cycle, the device does not require the electroforming voltage to tune its resistance anymore because the device never returns to its virgin state after this irreversible electroforming step. The device switching (Figure 5.4c) can then be described as transitions between two dynamic states (the ON and OFF states) enabled by two processes (SET and RESET). Starting with the OFF state, the device encounters high resistance and therefore provides a very small rectifying current. During the SET process, the device undergoes transition from the HRS (i.e. the OFF state) to LRS (i.e. the ON state), at which the device enters a conducting state that follows the Ohmic behavior. During RESET, the memristor device switches back from the LRS (ON state) to HRS (OFF state), and the device does not return its virgin state ever again. Carrier transport is disturbed only up to a small extent by creating a conduit gap (Figure 5.4b). In the next SET/RESET cycle, it only requires +1.0 V ( $V_{\text{SET}}$ ) to extend the conduit again for switching to the ON state and -1.0 V ( $V_{\text{RESET}}$ ) to retract the conduit for switching back to the OFF state. The SET and RESET can therefore be repeated within  $\pm 1.0$  V in the subsequent sweep cycles.

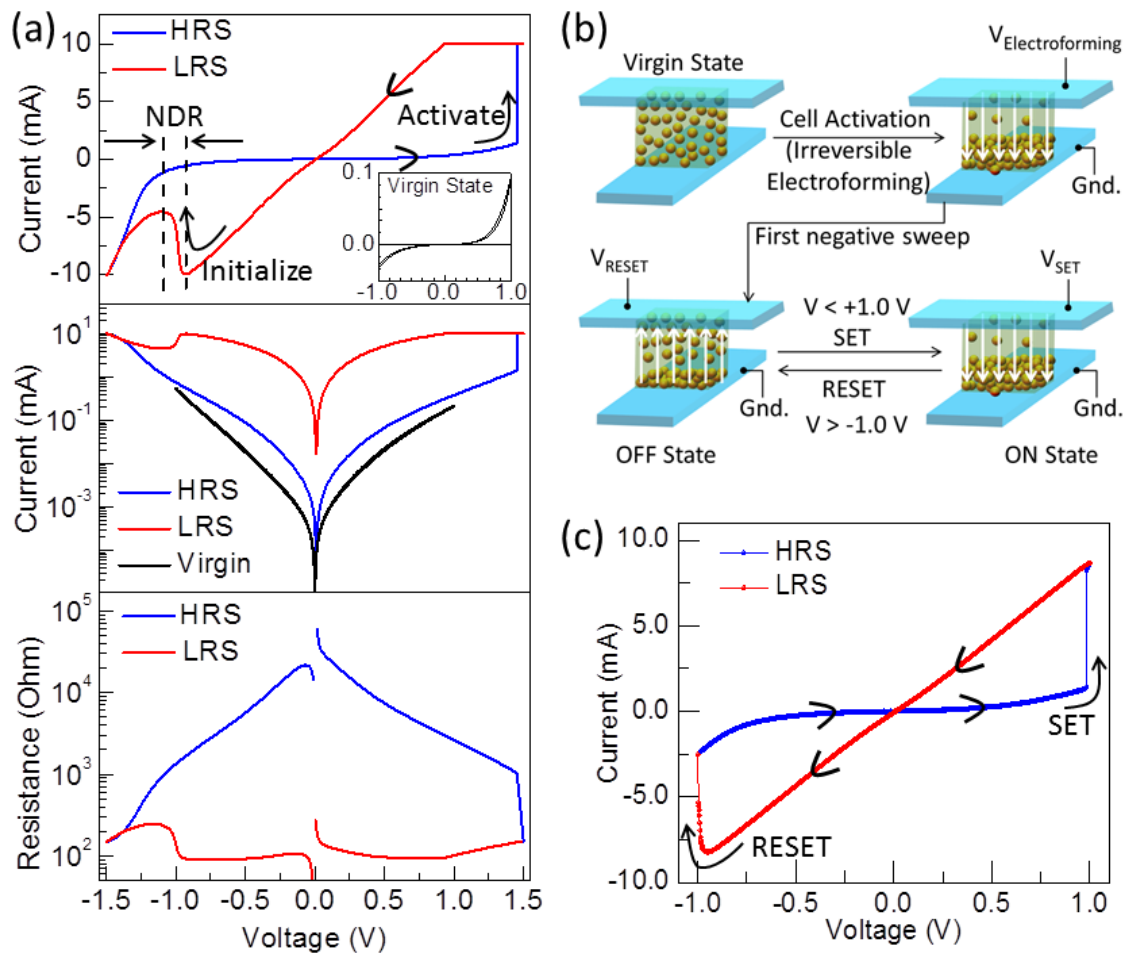


**Figure 5.4** Memristive switching characteristics and mechanism of a typical Pt/TiO<sub>x</sub>/Pt device with a 5×5 μm<sup>2</sup> junction size. (a) (Upper) Current (I) vs voltage (V) curve for the first positive (activation) sweep involving resistive switching at the electroforming voltage of +1.5 V. In the first negative (initialization) sweep, the voltage-controlled negative differential resistance (NDR) observed at −0.92–1.08 V is due to inhomogeneity in the electric field caused by vacancy gradient. Inset shows the same I-V curve for the virgin state of the device (prior to electroforming). (Middle) |I| vs V profiles (with |I| in a semilog scale) for the virgin and electroforming states, and (lower) corresponding resistance vs V profile for the high resistance state (HRS) and low resistance state (LRS) in the electroforming step. The resistance is observed to be of the order of MΩ in HRS vs. kΩ in LRS. (b) Schematic representation of the bipolar switching in the memory element. With the device initially stayed in an equipotential state (the virgin state) with uniformly distributed oxygen vacancies prior to any electrical bias, a positive bias (V<sub>Electroforming</sub>) is applied to create an electric potential gradient in order to induce ionic drift of the oxygen vacancies. After this irreversible electroforming process, a negative bias is applied to return the device from the LRS to HRS. Following the interface-type switching mechanism, the positively charged oxygen vacancies can be pushed towards (SET) and away from (RESET) the interface through a conduit that covers the whole junction size, respectively, by the positive and negative sweep biases. (c) Typical I-V switching loop observed (without any evidence of negative differential resistance) in normal SET (OFF to ON) and RESET (ON to OFF) operations after the first electroforming process.

During the negative sweep, the corresponding  $I$ - $V$  profile of the device shows a symmetrical Ohmic behavior until  $-0.92$  V where the memristive device exhibits voltage-controlled negative differential resistance over a small range, from  $-0.92$  V to  $-1.08$  V, before it returns to an OFF state (i.e. the device undergoes into a reverse transition from LRS to HRS) at the negative threshold ( $-1.5$  V). This corresponds to the inhomogeneity in the electric field arising from scattered oxygen vacancies within the conduit gap. Due to this inhomogeneity, the interface could provide oxygen trapping sites, causing the difference in oxygen diffusion capacity, which leads to the self-organized spatial pattern formation of electric field domains<sup>171</sup> and isothermal switching.<sup>172</sup> It should be noted that because of the single phase  $\text{TiO}_x$  film, this switching behavior is irrespective of the directional bias, i.e. the  $I$ - $V$  profile obtained with bias applied on the top electrode (and the bottom electrode grounded) is a mirror image of that obtained with the bias applied on the bottom electrode (and the top electrode grounded) (Figure 5.5a&b).

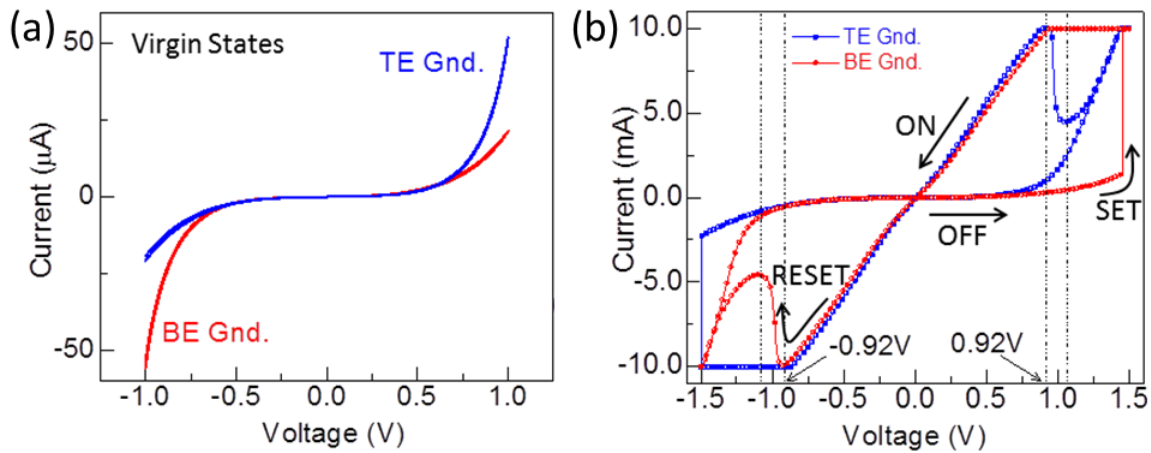


**Figure 5.5** Virgin and activation states of the memory devices with a  $5 \times 5 \mu\text{m}^2$  junction size. (a) In the virgin state, the  $I$ - $V$  curve is obtained with a sweep voltage ( $\pm 1.0$  V) applied on either of the top or bottom electrodes while keeping the respective other electrode grounded. Because of the single-phase  $\text{TiO}_x$  film, this interface-type switching behavior is irrespective of the directional bias, i.e. the  $I$ - $V$  curve obtained with the bias applied on the top electrode (TE) [and the bottom electrode (BE) grounded] is a mirror image of that obtained with the bias applied on the bottom electrode (and the top electrode grounded). (b) During the device activation step, resistive switching is obtained at an electroforming voltage of  $+1.5$  V and  $-1.5$  V for the device operated with BE and TE grounded, respectively. The corresponding  $I$ - $V$  behavior also exhibits a negative differential resistance region starting at  $-0.92$  V and  $+0.92$  V, respectively. The similar resistive switching behavior of the device found when operated with both directions of the applied bias reveals the similar nature of the top Pt/ $\text{TiO}_x$  and the bottom  $\text{TiO}_x$ /Pt interfaces.

The bipolar resistive behavior observed for our memristive devices, with oxygen-vacancy-defect-rich ultrananocrystalline  $\text{TiO}_x$  as the switching matrix, indicates the switching mechanism to be the interface-type, in which ionic drift is driven by electric field through the spatially-formed conduit.<sup>87–89</sup> This is contrary to the popular belief that the switching mechanism in  $\text{TiO}_x$  based memristor devices involves conducting filament formation within the oxide matrix along with a unipolar characteristics (unlike bipolar switching that usually occurs in asymmetric devices).<sup>84,90,185</sup> The thermally driven filament-type and bias-driven interface-type resistive switching mechanisms can be differentiated by considering the area dependence of the current density for four different junction sizes ( $5 \times 5 \mu\text{m}^2$ ,  $10 \times 10 \mu\text{m}^2$ ,  $20 \times 20 \mu\text{m}^2$  and  $50 \times 50 \mu\text{m}^2$ ). While the  $V_{\text{SET}}$  (+1.0 V) and  $V_{\text{RESET}}$  (–1.0 V) are found to be independent of the junction size, the ON-to-OFF current density ratio is inversely proportional to the junction size (Figure 5.6a). These results indicate that resistive switching in the Pt/ $\text{TiO}_x$ /Pt devices involves the entire junction area of the cell, i.e. the entire interface. As the typical filament size is a few tens of nanometer,<sup>186,187</sup> filament formation does not depend on the junction size and conducting-filament-based switching is therefore junction-size independent. This is clearly not the case for our devices here. The smaller current and higher ON-to-OFF current density ratio for smaller junction size suggests lower power consumption and an even higher ON-to-OFF current density ratio can be achieved with a nanoscale junction size. As shown by the nearly overlapping I-V profiles of over 250 consecutive switching cycles (Figure 5.6b), our Pt/ $\text{TiO}_x$ /Pt memristor devices also exhibit a high level of durability in term of its switching repeatability. Each switching cycle is clearly marked by its sharp transition between the HRS and LRS and the process is extremely reversible. The resistance of the HRS and LRS can be READ at a small voltage, which does not affect the resistance state. For the corresponding ON and OFF currents obtained at a small READ voltage of +0.25 V for the aforementioned 250 switching cycles (Figure 5.6c), the small variation (0.25 mA) found for the ON current (~2.0 mA) and the OFF current (~0.1 mA) over the 250 cycles clearly demonstrates the remarkable stability of our memristor devices. It is important to that due to Ohmic (linear) behavior of the ON state, the resistance remains the same in LRS (throughout the bias range), which enables the use of a READ voltage (as small as 10 mV, data is not shown) with less than 10 % error. The minimal power requirement for switching and reading operations makes the device highly desirable for building environment-friendly ultralow power consumption systems. The retention characteristic of a memristive device can be evaluated by monitoring the degradation in the current at a particular applied READ voltage for an extended period of time (Figure 5.6d). At a READ voltage of 0.25 V, the current obtained for the ON state is remarkably stable for at least  $10^5$  s (with less than 1% variation of the average current of 2.0 mA), especially when compared to that in OFF state (with

more than 10% variation) which can be extrapolated to an estimated device lifetime of well over 10 years.

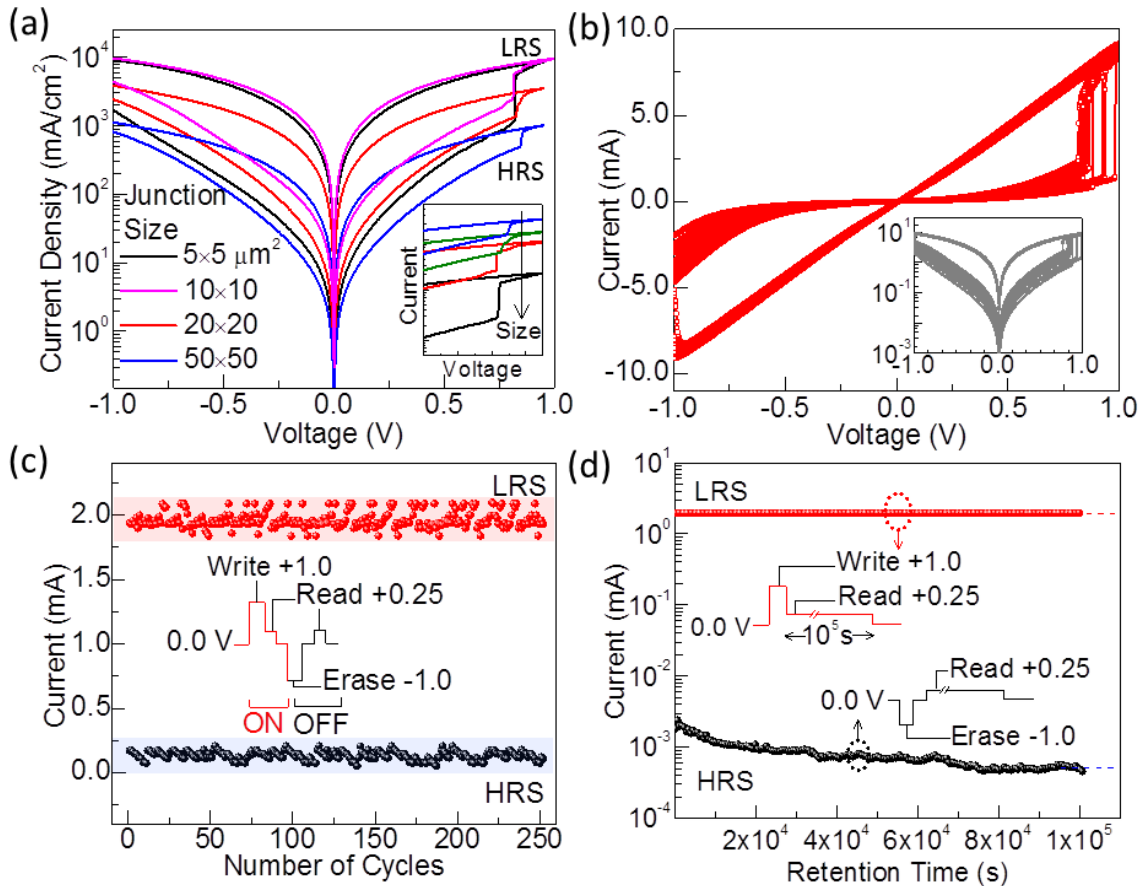


**Figure 5.6** Junction size dependency, resistive switching endurance, and resistance state retention. (a)  $|J|$  vs  $V$  profiles of memristor devices with four different junction sizes ( $5 \times 5 \mu\text{m}^2$ ,  $10 \times 10 \mu\text{m}^2$ ,  $20 \times 20 \mu\text{m}^2$  and  $50 \times 50 \mu\text{m}^2$ ) after the electroforming step. The current densities ( $J$ ) are found to be inversely proportional to the junction size, which supports the interface-type memristive switching mechanism. Among all four junction sizes, the best (i.e. highest) ON-to-OFF current density ratio is obtained with the  $5 \times 5 \mu\text{m}^2$  junction. The lower current obtained for the device with the smaller junction size promises lower power consumption as the device continues to be miniaturized. This is also particularly promising for high density device manufacturing involving discrete SET and RESET processes. The corresponding  $|I|$  vs  $V$  profiles in the 0.60-0.95 V region for all four junction sizes (inset) illustrate the lower current but higher ON-to-OFF current ratio found for the smaller junction sizes, thus validating the lower power consumption performance for the device with a smaller junction. (b) I-V curves and corresponding  $|I|$  vs  $V$  profiles (inset) within the sweep voltage range of  $\pm 1.0$  V for over 250 consecutive SET/RESET cycles for the memristor device with a  $5 \times 5 \mu\text{m}^2$  junction size. (c) ON and OFF currents obtained at a small READ voltage of +0.25 V for the 250 switching cycles, where the writing is performed at  $V_{\text{SET}}$  (+1.0 V) and erasing at  $V_{\text{RESET}}$  (-1.0 V). The currents for both the LRS and HRS are observed to be very stable throughout the sweep cycles. (d) Current vs time plots to illustrate the retention characteristics of the memristive device observed at a constant READ voltage of 0.25 V for the virgin state (before activation) and the ON state (after activation). The current obtained after the activation is extremely stable for over  $10^5$  s, with a projected device lifetime to be well over 10 years.

In analogy to the biological synapse, the device also shows very quick response between the ON and OFF states when triggered with the READ voltage pulses applied for 0.5 s with a repetition interval of 5 s (Figure 5.7a). The ON current is observed to maintain a constant value for the duration and then rapidly returns to its OFF-state value. Such very short response time and very high switching speed are characteristic of excellent short-term potentiation (that can potentially be reduced to the nanosecond or shorter regime), the device could serve as a key building block in advanced computer logic and neuromorphic circuits. Further, the device is also capable of maintaining its ON-state and OFF-state current values for an overall testing period of over  $10^5$  s, with repeated cycles of respective ON-state and OFF-state voltages when applied with a longer interval duration of 300 s (Figure 5.7b), which demonstrates the outstanding long-term potentiation of the device. This dual potentiation behavior of the device facilitates greater flexibility in achieving quick ON/OFF switching response at sequential  $V_{\text{SET}}$  and  $V_{\text{RESET}}$  cycles and small READ voltage. Upon further analysis of the switching behavior of this memristor device based on different sweep rates,  $V_{\text{SET}}$  is found to be highly dependent on and nearly proportional to the sweep rate, with smaller  $V_{\text{SET}}$  obtained for smaller sweep rates and vice versa (Figure 5.7c). When the alternating electrical pulses of +1.0 V and -1.0 V are applied for different time periods (i.e. at different frequencies), the SET/RESET window (corresponding to the difference in current between the ON and OFF states) changes with frequencies during the binary switching (Figure 5.7d). The ON-state and OFF-state currents are found to be extremely stable at and above 8 Hz but become dramatically disrupted for the lower frequencies (i.e. for 1 Hz and 0.1 Hz). This indicates that our memristor device is inherently more compatible with voltage switching at high frequency but not low frequency.

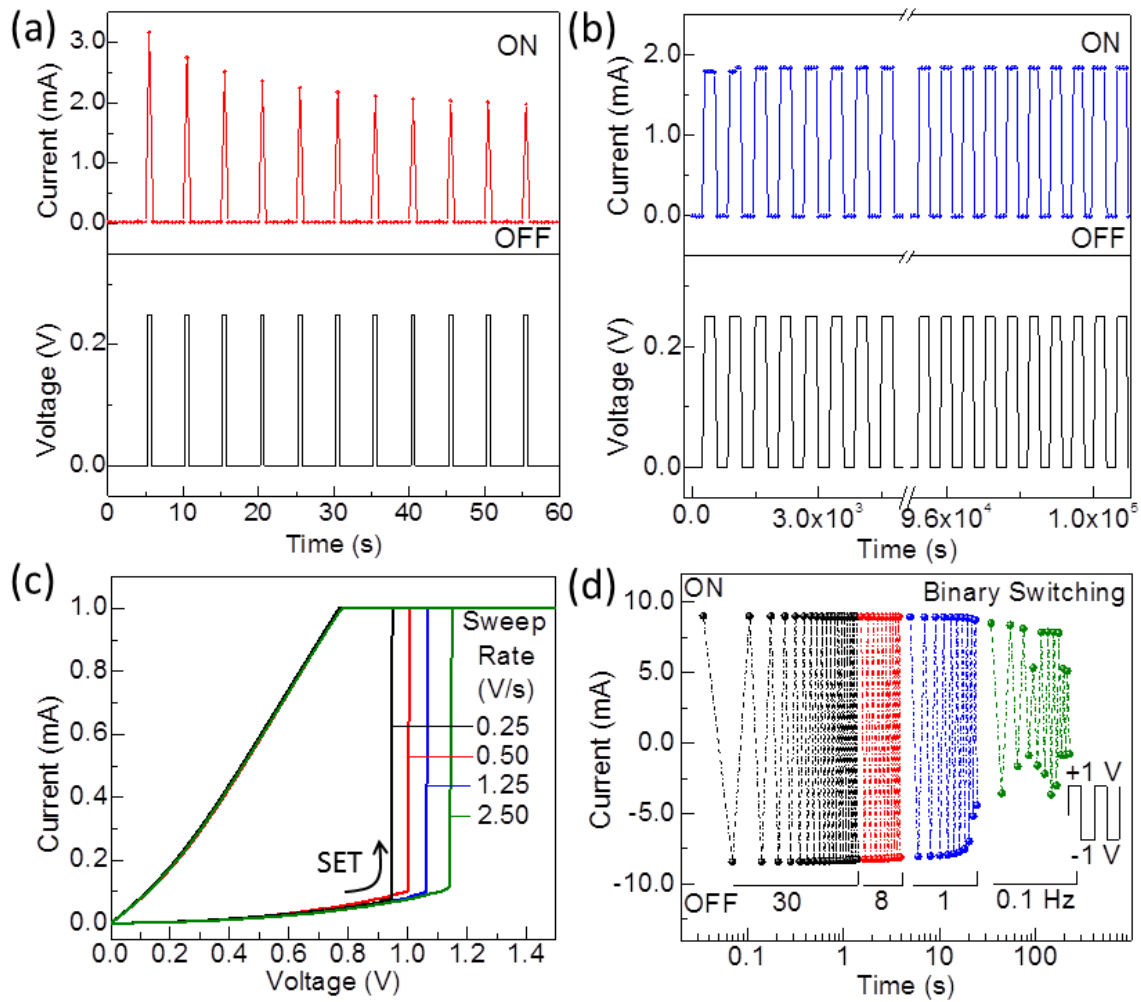


**Figure 5.7** Memristor response to electric pulses with short and long time widths. (a) Resistive switching of the Pt/TiO<sub>x</sub>/Pt device indicating stable current response upon short-term potentiation obtained with short electric pulses of +0.25 V amplitude (read voltage) applied for 0.5 s in a 5 s interval. (b) The corresponding current response upon long-term potentiation obtained with stable ON and OFF states for read voltages (0.25 V) applied for 300 s in a 300 s interval over a testing period of 10<sup>5</sup> s. (c) SET voltages of the Pt/TiO<sub>x</sub>/Pt device obtained at different sweep rates. V<sub>SET</sub> tends to become smaller almost linearly with the smaller sweep rate. (d) Binary ON-OFF operation with alternating +1.0 V and -1.0 V pulses at different switching frequencies (30, 8, 1 and 0.1 Hz) and corresponding pulse durations (0.03, 0.125, 1 and 10 s). Switching between the ON and OFF states is highly dependent on the input parameters, where the SET/RESET window is found to be stable for frequencies above a particular value (8 Hz in our case) i.e. for smaller pulse duration (less than 0.125 s).

## 5.4 Conclusion

In conclusion, we have successfully introduced a new ultrananocrystalline  $\text{TiO}_x$  material for fabricating low-bias electroformed Pt/ $\text{TiO}_x$ /Pt memristor devices. Combined with the ultrananocrystalline nature (with an average crystallite size below 5 nm), the built-in oxygen vacancies in the defect-rich  $\text{TiO}_x$  matrix are found to be responsible for the electric field localization that enables oxygen vacancy trapping at discrete grain locations. This makes possible activation of the memory element at a much lower electroforming voltage (1.5 V) than those reported in the literature. Our devices follow the interface-type switching mechanism, consistent with the observed inverse current density dependency on the junction size. High endurance for large number of repeated cycles and high retention capacity of the device provides an estimated device lifetime of well over 10 years. Along with the operating voltages and the resulting low power consumption advantage, the short-term and long-term potentiation at much smaller READ voltages makes these devices highly suitable for neuromorphic systems. The simple, completely room-temperature fabrication procedure for such high-quality, high-performance memristor devices promises scalable manufacturing of the next-generation ReRAM devices that are easily integrable into a 3D stacking device architecture.

## Chapter 6

# Programmable, Electroforming-free $\text{TiO}_x/\text{TaO}_x$ Heterojunction-Based Non-Volatile Memories

### 6.1 Introduction

Memristors are the pillars of the aspiring futuristic electronic industry, which will soon be used as a fundamentally new class of non-volatile memories in adaptive circuits such as neuromorphic circuits and artificial biological systems. Ultrafast switching, along with low power consumption and very high endurance/retention performance, are the most basic requirements of any future non-volatile memories (memristors).<sup>70,71,103,107,185,188–190</sup> In the past decade, the commonly used memristors were based on valence change memories, where resistive switching is believed to involve mechanisms such as electromigration of oxygen vacancies,<sup>87,88</sup> charge trapping<sup>100</sup> and conducting filaments<sup>90,91,191</sup> depending on electric-field or thermal dominating effects. Currently, the remaining obstacles that need to be overcome in these memory devices include the large variability in electrical performance, the requirement of an electroforming step, and high density integration of the memory cells with lower power consumption. In large part, these obstacles are inter-related, and they come from the of Fowler-Nordheim tunneling,<sup>97,175,184</sup> where a high voltage ( $\pm 6\text{--}10\text{ V}$ ) is required to create a sufficient electric field for soft breakdown of the dielectric material in the metal-insulator-metal three-dimensional stacking structures.<sup>102</sup> The Fowler-Nordheim tunneling is closely related to the formation and rupture of a conducting filaments within the switching matrix between two metal electrodes, and is usually initiated by an irreversible electroforming step, in which a single material phase in the oxide semiconductor is converted into two phases: a conducting oxygen-deficient phase in an insulating matrix.

After the electroforming step, the device shows a pinched hysteresis loop in its current-voltage characteristics, where the device shows a distinct current level shift from a high resistance state (HRS) to a low resistance state (LRS). The major disadvantages of the electroforming process are: (a) time-consuming as each device must go through the electroforming step before commencing normal operation, (b) high variance between the devices, even on the same wafer, and (c) unreliable endurance of the device. These drawbacks are primarily caused by excessive Joule heating,<sup>90,94</sup> and therefore the electroforming voltage can vary uncontrollably from sample to sample. Also, with the further oxygen evolution in each cycle, the conducting channel can become damaged in each write-erase cycle resulting in low reproducibility over a large number of devices on the same chip. Electroforming-free switching behavior is therefore important to facilitate high density device

integration and non-destructive reliable operation at low power with long retention time and high switching speed.<sup>105</sup> The search for a material system that does not require electroforming, and therefore the need for the local conducting filament mechanism, is a crucial next step for further advancement of the memristors. Recently, a few research groups have focused on the use of doping<sup>104</sup>, nanostructure formation<sup>106</sup> and multilayer stacking<sup>166,192–195</sup> in the switching matrix to create an electroforming-free memristor, but the efforts remain limited by the high switching voltages and by the short lifetime (endurance) and retention capabilities caused by non-uniformity of these processes. Here, we demonstrate the exceptional performance of a memristor device based on a novel, hybrid  $\text{TiO}_x/\text{TaO}_x$  switching matrix.

$\text{Ta}_2\text{O}_5$  is a well-known high- $\kappa$  dielectric material commonly used in field-effect transistors,<sup>196–198</sup> but it is attracting a lot of interest for its use in memristor technology.<sup>103,188,190,199–201</sup> While single  $\text{Ta}_2\text{O}_5$  layer based devices have exhibited the characteristic memristive switching (especially in its oxygen deficient phase, often referred as  $\text{TaO}_x$ ), their performance is limited by the need for a high voltage electroforming process (prior to the switching), in which the device in its virgin state must be subjected to a high irreversible electroforming voltage. The electroforming voltage is always much higher than the SET and RESET voltages required for the repeated switching cycles.<sup>107</sup> As each layer could play a significant role in the switching mechanism, heterojunction devices have become very important device architecture for the memristors. For the first time, we present a memristive switching device based on the  $\text{TiO}_x/\text{TaO}_x$  heterojunction, with Pt serving as the top and bottom electrode material. In its metastable state,  $\text{TaO}_x$  serves as the reservoir for the oxygen vacancies, while the switching occurs in the  $\text{TiO}_x$  layer. By varying the  $\text{TaO}_x$  thickness while keeping the  $\text{TiO}_x$  film thickness constant at 10 nm, we could control the switching behavior and optimize the device to achieve electroforming-free switching operation with high reproducibility. The first switching occurs at a much smaller voltage of +0.8 V than previously reported devices,<sup>107,194</sup> with the subsequent  $10^4$  switching cycles at similarly low voltages, yielding a high performance device that is significantly better than others. We further demonstrate that the resistive switching can also occur at very programming voltage ( $\sim 50$  mV), which makes it an ultralow power consumption device ( $\sim$ nW).

## 6.2 Materials and Methods

### 6.2.1 Device fabrication:

The memristor devices are fabricated in a crossbar structure on SiO<sub>2</sub>/Si substrates in three layer photolithographical steps by using a maskless lithography system (Intelligent Micropatterning Inc.). Shipley 1827 photoresist (MicroChem) was spin-coated on the substrate to perform photolithography under the exposure of the UV-light (434 nm). The thickness of the photoresist layer was maintained at 2.5 μm in order to achieve high resolution lithographical features. Spin-coating parameters for the photoresist layer were set to 3500 rpm for 40 s, and the coated film was subsequently baked on a hot plate set at 90 °C for 60 s. After the UV lithographical step, the written pattern was developed in a MF-24 developer (MicroChem) for 60 s and then rinsed with Millipore water. For the bottom electrode, a 30 nm thick Pt layer was sputter-deposited on SiO<sub>2</sub>/Si substrate at room temperature followed by lift-off process. For the middle active layer, a high purity TaO<sub>x</sub> (60 nm thick) layer was deposited at room temperature using a radio frequency (RF) magnetron sputtering source from a Ta metal target (99.95 % purity, ACI Alloy) in a physical vapor deposition system (Mantis Deposition Ltd.) with a base pressure of 1×10<sup>-8</sup> mbar, followed by lift-off process. The Ar-flow was kept at 20 sccm to maintain the chamber pressure at 7.45×10<sup>-3</sup> mbar. A quartz crystal microbalance was used to monitor the thickness of the films. Finally, the top Pt electrode (oriented at 90° with respect to the bottom electrode) was deposited using the same procedure as the bottom electrode. A high purity TiO<sub>x</sub> (10 nm thick) layer is deposited during the top Pt layer deposition. The film thicknesses of all the layers were determined by using a profilometer (KLA Tencor P6). For the physical characterization, the TaO<sub>x</sub> films were deposited on Pt-coated SiO<sub>2</sub>/Si substrates using the same parameters as those used for the actual devices. All the substrates used in this work were cleaned ultrasonically in HPLC grade acetone, isopropyl alcohol and Millipore water (~18.2 MΩ). The native oxide layer (~100 nm) was grown on Si substrates by annealing in an oxygen atmosphere in a quartz tube furnace, with oxygen flow rate set to 50 sccm and the temperature set to 900 °C for 90 min.

### 6.2.2 Characterization

The device morphology is characterized by transmission electron microscopy (TEM) in a Zeiss Libra 200MC microscope and field-emission scanning electron microscopy (SEM) in a Zeiss Merlin electron microscope coupled with an EDAX energy-dispersive X-ray (EDX) analysis system for elemental mapping. X-ray photoelectron spectroscopy (XPS) is conducted in depth-profiling mode in order to characterize the chemical-state composition of the fabricated devices, in a Thermo-VG Scientific ESCALab 250 microprobe equipped with a monochromatic Al Kα X-ray source (1486.6

eV). Argon ion sputtering is performed over a raster area of  $3 \times 3 \text{ mm}^2$  at an ion beam energy of 3 keV and a typical sample current density of  $110 \text{ nA/mm}^2$ . The XPS data are fitted by using the CasaXPS software after removing the Shirley background. The crystalline structures of the as-deposited  $\text{TaO}_x$  films with different film thicknesses are determined by glancing-incidence X-ray diffraction in a PANalytical X'pert Pro MRD diffractometer using a  $\text{Cu K}\alpha$  X-ray source. For the electrical characterization studies, the resistive switching behavior of the fabricated devices was measured in  $I$ - $V$  sweep mode using two probes with a Signatone Series 1160 four-probe dc measurement system coupled to an Agilent B1500 semiconductor analyzer. Tungsten probe tips with a  $10 \text{ }\mu\text{m}$  tip size were used for connecting to the electrodes.

## 6.3 Results and Discussion

### 6.3.1 Pt/TiO<sub>x</sub>/TaO<sub>x</sub>/Pt device architecture

The device structure of a typical multilayer memristor has been fabricated on  $\text{SiO}_2/\text{Si}$  substrates by using a high resolution maskless lithography. The area of  $\text{TiO}_x/\text{TaO}_x$  layer sandwiched between top and bottom Pt electrodes defines the junction size or cell size. The  $\text{TiO}_x$  and  $\text{TaO}_x$  layer are deposited by RF magnetron sputtering of the respective Ti and Ta metal targets. The  $\text{TiO}_x$  film thickness is kept constant at 10 nm while four different  $\text{TaO}_x$  film thicknesses (10, 20, 40 and 60 nm) are used by appropriate deposition times. Figure 6.1a&b show the SEM images and the corresponding EDX elemental maps of the memristor device with a junction size of  $10 \times 10 \text{ }\mu\text{m}^2$  where the EDAX mapping verifies that the oxygen is confined only within the sandwiched layers between the top and bottom Pt layers (that do not get oxidized). The three dimensional device structure is schematically represented in Figure 6.1c.

To examine the  $\text{TaO}_x$  film on the Pt electrode (i.e. without the  $\text{TiO}_x$  layer and the top Pt electrode), we deposit, in separate experiments, individual  $\text{TaO}_x$  films, each with a different film thickness, over a large area on Pt-coated  $\text{SiO}_2/\text{Si}$  substrates. The corresponding glancing-incidence X-ray diffraction patterns for  $\text{TaO}_x$  films with different film thicknesses are shown in Figure 6.1d. For the 10 nm thick  $\text{TaO}_x$  film, its XRD pattern only shows features corresponding to the underlying nanocrystalline Pt film (with a crystallite size of  $\sim 5 \text{ nm}$ , as estimated by the Scherrer analysis, See Supporting Information for calculations), which indicates that the 10 nm thick  $\text{TaO}_x$  film is largely amorphous. All other thicker  $\text{TaO}_x$  films exhibit a nanocrystalline nature with the crystallite size less than 5 nm. The nanocrystalline structure in thicker  $\text{TaO}_x$  film is likely to be induced by the underlying Pt layer, which provides the template for the nanocrystalline growth with longer deposition time. Depth-profiling XPS analysis has been performed on the 60 nm thick  $\text{TaO}_x$  film deposited on a Pt-coated

SiO<sub>2</sub>/Si substrate. The Ta 4f spectrum for the as-deposited film (Figure 6.1e) shows an intense Ta 4f<sub>7/2</sub> (4f<sub>5/2</sub>) peak at 27.01 (28.93) eV and a weaker Ta 4f<sub>7/2</sub> (4f<sub>5/2</sub>) feature at 22.31 (24.23) eV, which could be attributed to Ta<sub>2</sub>O<sub>5</sub> and TaO<sub>x</sub> (1 ≤ x ≤ 2.5), respectively.<sup>102</sup> The Ta<sub>2</sub>O<sub>5</sub> layer, likely due to surface oxidation in air, is reduced, while the oxygen-deficient TaO<sub>x</sub> layer appears to increase in intensity upon sputtering for 30-60 s. Further sputtering for 300 s leads to ion-induced reduction of TaO<sub>x</sub> to metallic Ta with Ta 4f<sub>7/2</sub> (4f<sub>5/2</sub>) feature at 21.98 (23.84) eV. The intensity change in the O 1s feature at 531.45 eV is consistent with the initial removal of surface Ta<sub>2</sub>O<sub>5</sub> in the first 60 s of sputtering, followed by steady O 1s intensity after reaching the TaO<sub>x</sub> layer upon 300 s sputtering (Figure 6.1f).

### 6.3.2 Memristor Performance and Switching Mechanism

Tantalum oxide has become a popular material choice for memristors lately due to impressive performance in the areas of endurance, switching speed, and power consumption.<sup>107</sup> According to the equilibrium binary phase diagram of Ta-O, there are only two stable phases in the solid state, conducting TaO and insulating Ta<sub>2</sub>O<sub>5</sub>.<sup>202</sup> During the resistive switching of Ta<sub>2</sub>O<sub>5</sub> based memristors, the insulating Ta<sub>2</sub>O<sub>5</sub> phase transforms into the conducting TaO phase with the evolution of oxygen vacancies initiated by Joule heating at high applied bias.<sup>107,194</sup> It could, therefore, be possible to achieve the electroforming-free characteristics in the memristor devices if the Joule heating step could somehow be avoided by clever structural modification to the multilayer device structure. To accomplish this, the two preferred approaches would be (i) to create in-built oxygen vacancies in the tantalum oxide film during deposition, and (ii) to create a heterojunction multilayer structure (with different electronegativity). From our previous experience with TiO<sub>x</sub> based memristors (chapter 5), we adapt the latter approach to fabricate a heterojunction between TiO<sub>x</sub> and TaO<sub>x</sub>. The choice of metal electrode is also a crucial consideration for achieving stable memory cells, and Pt is the most suitable electrode material in this case because its work function correlates in such way that its Fermi level is almost a perfect match to the defect states of TaO<sub>x</sub>. Our heterojunction memristor therefore has three different interfaces; Pt/TiO<sub>x</sub> (top), TiO<sub>x</sub>/TaO<sub>x</sub> (middle) and TaO<sub>x</sub>/Pt (bottom), and each interface has a significant contribution to the overall resistive switching event. In its virgin state (prior to any electrical bias), the device remains in a high resistance state (HRS) (~MΩ), consistent with the oxygen vacancies uniformly distributed in the bulk of the TaO<sub>x</sub> film.<sup>90,165</sup> The virgin state of the device can be determined by applying small voltages and measuring the resistance, and then stepping up the voltage gradually to determine the set voltage.

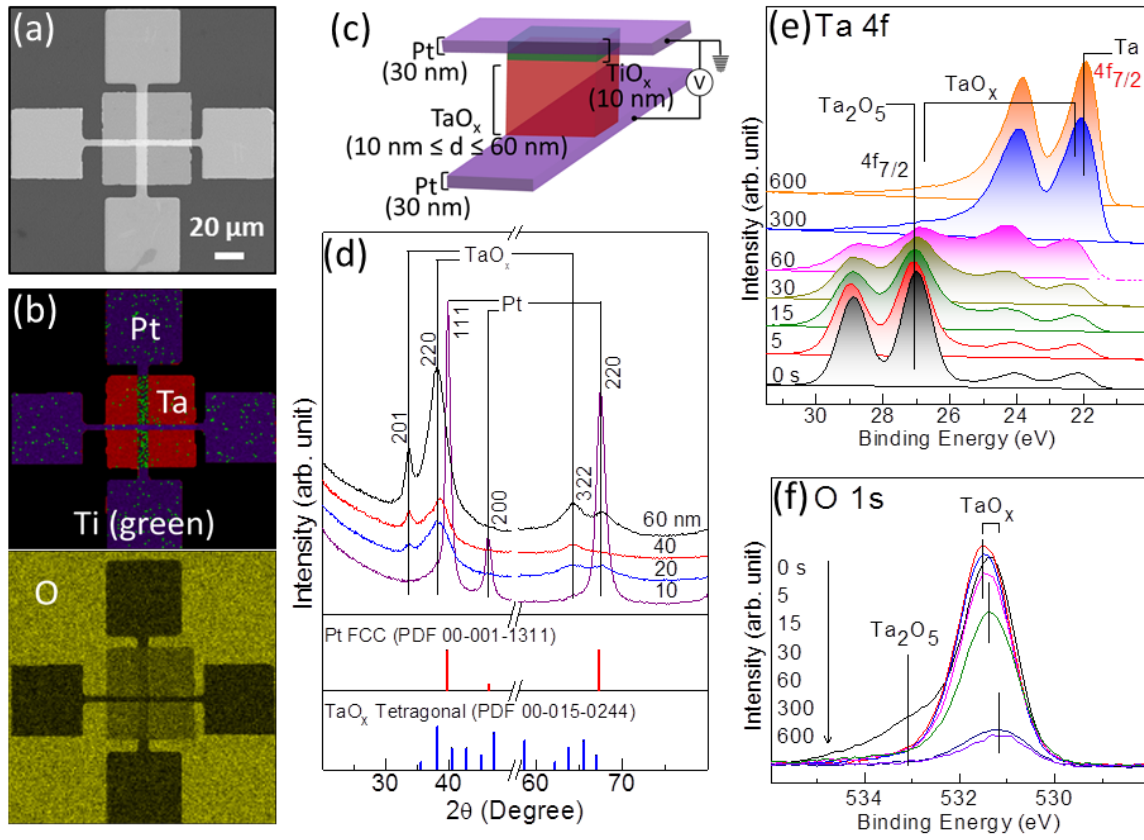


**Figure 6.1** Device schematics and physical characterization of the Pt/TiO<sub>x</sub>/TaO<sub>x</sub>/Pt heterojunction. (a) SEM images of the device with 10×10 μm<sup>2</sup> junction size along with the corresponding EDX elemental mapping (b) indicating the relative quantities of Pt, Ti, Ta, and O. (c) Schematic diagram of the multilayer architecture of the Pt/TiO<sub>x</sub>/TaO<sub>x</sub>/Pt memristor device with specified thicknesses for each layer. The thickness of the TaO<sub>x</sub> layer is varied from 10–60 nm, while keeping the TiO<sub>x</sub> thickness the same (10 nm), to observe the TaO<sub>x</sub> layer thickness dependency on the electrical behavior of the memristor devices. (d) XRD spectra of unpatterned TaO<sub>x</sub> films with four different thicknesses (10, 20, 40 and 60 nm), as deposited on the Pt coated SiO<sub>2</sub>/Si substrates (peaks are labeled with the ref. 00-015-0244 for TaO<sub>x</sub> and 00-001-1311 for Pt). It is observed that the 10 nm thick film is amorphous in nature while the other films show nanocrystalline behavior, with similar nanocrystallite size (~ 4.5 nm). (e) & (f) Depth profile with respect to Ar-ion sputtering in XPS spectra for Ta 4f and O1s for the larger area of TaO<sub>x</sub>/Pt layer deposited on SiO<sub>2</sub>/Si substrate.

In the virgin state, an intrinsic Schottky barrier exists between the Pt and the TaO<sub>x</sub> layers and the device exhibits an exponential current-voltage behavior. The resistance state can be tuned by applying bias between the metal electrodes to create an electric field that causes these positively charged oxygen vacancies to drift towards the metal electrodes. The low-bias, electroforming-free resistive switching in the TiO<sub>x</sub>/TaO<sub>x</sub> heterojunction memristor can therefore be understood in terms of drift of in-built oxygen vacancies and ions through cationic transport in the TaO<sub>x</sub> layer followed by diffusion into the TiO<sub>x</sub> layer due to the more electronegative TiO<sub>x</sub> than TaO<sub>x</sub>. Such process is often known as

valence change memory.<sup>189</sup> When a positive bias is applied to the bottom Pt electrode, the cations are pushed towards the TiO<sub>x</sub> layer and reach to the top Pt layer. In present case, the more electronegative TiO<sub>x</sub> layer can attract the vacancies efficiently even at low bias, while the leakage current remains very low because of the high- $\kappa$  nature of the TaO<sub>x</sub> layer. The process in which the device goes from HRS to LRS is called SET, with the corresponding voltage  $V_{SET}$ . Similarly, RESET is the reverse process when the device goes from LRS to HRS with voltage  $V_{RESET}$ . Figure 6.2 shows a schematic diagram for the switching mechanism based on the band structure where the oxygen vacancies are uniformly distributed in both TiO<sub>x</sub> and TaO<sub>x</sub> films in its virgin state (Figure 6.2a). The band bending in TiO<sub>x</sub> and TaO<sub>x</sub> films is due to the built-in oxygen vacancy defects. When a positive voltage is applied to the bottom Pt electrode, the Pt Fermi level is brought to coincide with the conduction band edge of the TaO<sub>x</sub> film and vacancy drift occurs. Below a certain voltage, the generated field is not sufficiently strong for the vacancies to diffuse through the TiO<sub>x</sub> layer and the device remains in the HRS (Figure 6.2b&c). When the applied voltage on the bottom Pt electrode is sufficiently high, i.e. at or above  $V_{SET}$ , the conduction band edge is further lowered to below the Pt Fermi level. In this SET process, tunneling and diffusion of oxygen vacancies occur and the vacancies could be pushed easily towards the top Pt electrode, switching the device to the LRS (Figure 6.2d). In the reverse sweep, the oxygen vacancies are pushed away from the top electrode and the device goes back to the HRS. In this RESET process, a no-vacancy zone in the TiO<sub>x</sub> layer is created and a deep trap level occurs in the TaO<sub>x</sub> layer, capturing some charge carriers for the next cycles (Figure 6.2e). After the first cycle, the SET and RESET processes could be repeated by setting the applied voltage appropriately to  $V_{SET}$  and  $V_{RESET}$ .

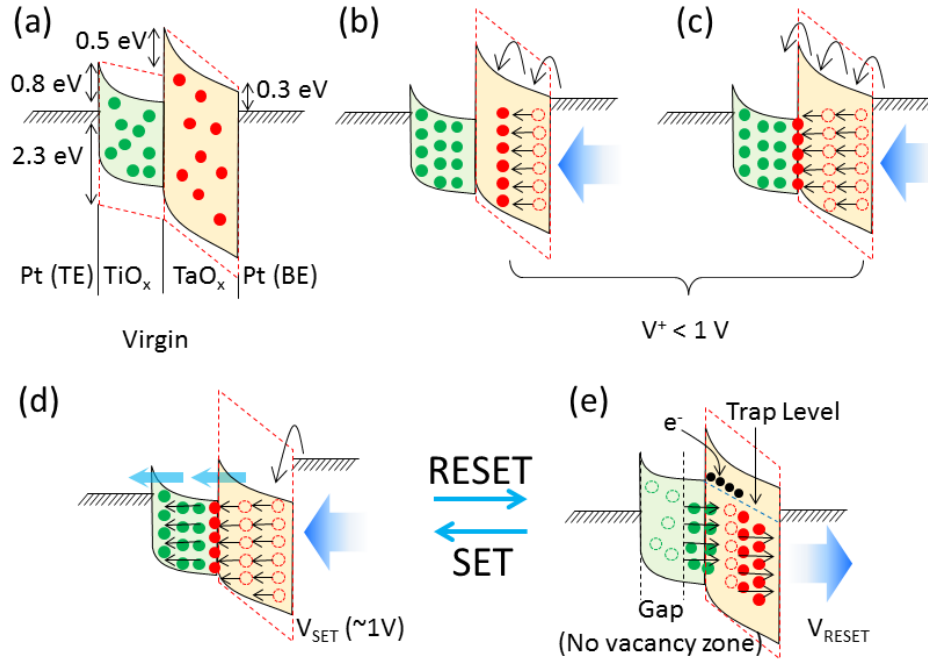


**Figure 6.2** Schematic diagrams of band structures in various states during the switching mechanism in a Pt/TiO<sub>x</sub>/TaO<sub>x</sub>/Pt heterojunction memristor for (a) Virgin state under zero bias condition: For TiO<sub>x</sub> and TaO<sub>x</sub> (solid line), band bending occurs due to smaller energy gaps of the vacancy defects in the films (Red dotted lines shows the actual band structure of pure TiO<sub>2</sub> and Ta<sub>2</sub>O<sub>5</sub>). (b) & (c) the drift of oxygen vacancies with the applied positive voltage below  $V_{SET}$  at BE. (d) At  $V_{SET}$ , the conduction band edge lowers further where oxygen vacancies may easily migrate to TE via tunneling and the device switches to LRS. (e) When the voltage is swept back, at  $V_{RESET}$ , the oxygen vacancies are pushed away from TE and the device switches back to HRS. The role of TiO<sub>x</sub> layer between TE and TaO<sub>x</sub> layer is to provide an intermediate bandgap for the vacancies flow at lower energy. During RESET, a trap level is created in the TaO<sub>x</sub> film which remains afterwards to facilitate the repeated switching cycles by trapping some charge carriers.

Typical switching  $I$ - $V$  curve of the TiO<sub>x</sub>/TaO<sub>x</sub> heterojunction device is shown in linear and semilog scale (inset) in Figure 6.3a. When a positive sweep voltage is applied on the Pt/TaO<sub>x</sub> interface side (i.e. to the bottom electrode), the device switches its resistance from HRS (low current region) to LRS (high current region) at  $V_{SET}$  (+0.8 V), i.e from a distinct binary state 0 (OFF) to a binary state 1 (ON). During the reverse sweep, the device follows the Ohmic characteristic until  $V_{RESET}$  (-2.0 V), at which the device goes to HRS with RESET. An exponential  $I$ - $V$  behavior is observed between  $V_{RESET}$  and  $V_{SET}$  (forward sweep) and a linear  $I$ - $V$  behavior between  $V_{SET}$  and  $V_{RESET}$  (reverse sweep), respectively. The resistive switching from HRS to LRS at low SET voltage, demonstrated in the present heterojunction device, is most desirable for the low power consumption, high performance COMS technology.

To evaluate the junction size effect on the resistive switching behavior, we fabricate  $\text{TiO}_x/\text{TaO}_x$  heterojunction devices with four different junction sizes. Their corresponding current density vs. voltage curves (Figure 6.3b) show that the smaller the junction size is, the larger (better) is the ON to OFF current density ratio with almost the same  $V_{SET}$ . As the dimension of the junction area becomes smaller, the oxygen vacancies are more constricted to flow vertically by the same applied electric field (due to a higher electric field density). We have also demonstrated that with the control over the compliance current, the switching from HRS to LRS can occur in the low current region ( $\sim \mu\text{A}$ ) at the programming voltage as low as 50 mV where the power consumption of the device can be lowered up to nW range. Figure 6.3c shows the ultralow bias switching with a small compliance current ( $\sim 10 \mu\text{A}$ ). Within the sweep voltage range of  $\pm 100$  mV we don't see the RESET (OFF state) because the RESET in our heterojunction device always occurs at little higher  $V_{RESET}$  than  $V_{SET}$  (Figure 6.3a for ref.)

In a separate experiment, we fabricate a  $\text{Pt}/\text{TaO}_x/\text{Pt}$  memristor device with only the  $\text{TaO}_x$  layer sandwiched between top and bottom Pt electrodes (i.e. without the  $\text{TiO}_x$  layer). Evidently, the corresponding  $I$ - $V$  curve shows that there is no clear switching onset from the HRS to LRS, at least within the sweep range of  $\pm 2.0$  V, in marked contrast to the  $\text{Pt}/\text{TiO}_x/\text{TaO}_x/\text{Pt}$  memristor that exhibits discrete ON and OFF states with  $V_{SET}$  at +0.8 V and  $V_{RESET}$  at -2.0 V.

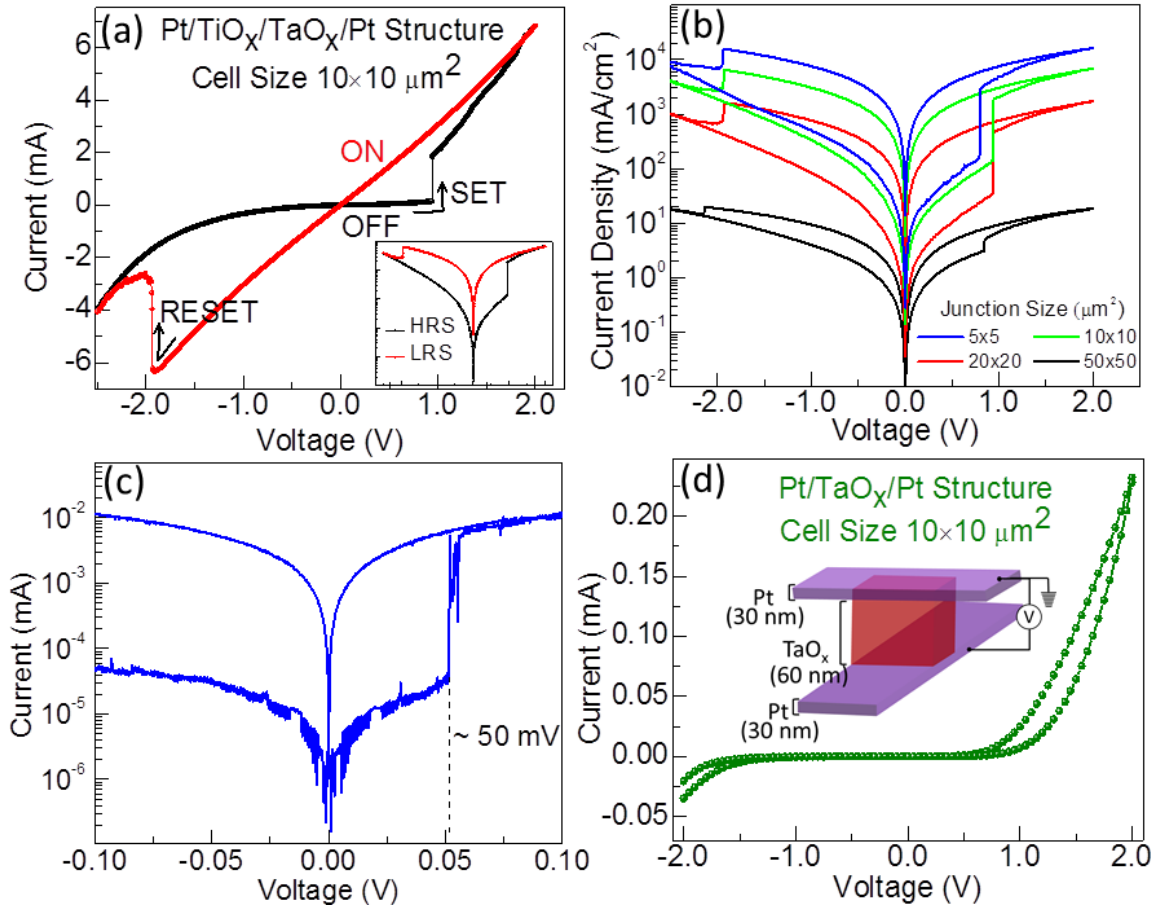


**Figure 6.3** Electrical  $I$ - $V$  characteristics of TiO<sub>x</sub>/TaO<sub>x</sub> based memory cell. (a) Electrical switching characteristics of the 5×5 μm<sup>2</sup> cell exhibiting the bipolar resistive switching with four different states, inset shows the semi-log scale. (b) Current density vs. voltage plot for demonstrating the cell-size dependency on the switching (SET) voltage. (c) The device could also be switched at ultimate low programming voltage as low as 50 mV with around 300 nW power consumption. (d) Resistive switching characteristic of the Pt/TaO<sub>x</sub>/Pt memristors for comparison with the TiO<sub>x</sub>/TaO<sub>x</sub> heterostructure based memristors. It could clearly be noticed that its  $I$ - $V$  characteristic follows the exponential (Schottky) behavior within ±2.0 V in case of TaO<sub>x</sub> based memristors while for TiO<sub>x</sub>/TaO<sub>x</sub> based memristors, the SET states is achieved at +0.8 V.

We also investigate the effects of film thickness of the TaO<sub>x</sub> base layer on the current voltage behavior of the Pt/TiO<sub>x</sub>/TaO<sub>x</sub>/Pt heterojunction device. The thickness of the base TaO<sub>x</sub> layer is varied from 10 to 60 nm by varying the sputter-deposition time. As the thickness of the switching layer exceeds a particular thickness, two different switching behaviors are evident and they appear to correlate with their different crystalline nature (Figure 6.4). The devices with the thicker TaO<sub>x</sub> nanocrystalline films (20, 40 & 60 nm) show bipolar switching with one SET step during the positive sweep and one RESET step during the negative sweep. On the other hand, the 10 nm thick TaO<sub>x</sub> film, being amorphous in nature, exhibits the complementary unipolar switching with one pair of SET and

RESET steps in each of the positive and negative sweeps (Figure 6.4a). Unlike the other thicker nanocrystalline films, the device with the 10 nm thick TaO<sub>x</sub> amorphous film does not switch and undergoes the SET process until +1.7 V. With further increase in the applied bias, the current starts to drop (at ~+2.5 V) and the device undergoes the RESET process. During the negative sweep, the device enters the SET process near -1.0 V and the drops back to RESET near -2.0 V. This behavior could be due to the depletion of conductive defects such as metallic Ta or oxygen vacancies in TaO<sub>x</sub> films below a particular thickness. During the positive sweep, these defects migrate towards the top electrode forming the conducting channel at the SET voltage, and they become depleted at high voltage. Similarly, during the reverse sweep the evolution and depletion of the channel occurs at the bottom electrode and the device goes back to its initial state. It is important to note here that each sweep cycle ends up with a RESET step and therefore the channel is always in the HRS at the end, which suppresses the leakage current in the smaller voltage range during successive operations. The device behavior can therefore be changed from bipolar to unipolar or non-polar and vice versa simply by controlling the thickness of the trapping layer which will offer advantages in further scaling. We compare the ON and OFF currents at applied bias of +0.5 V for devices with different TaO<sub>x</sub> film thickness in Figure 6.4b.

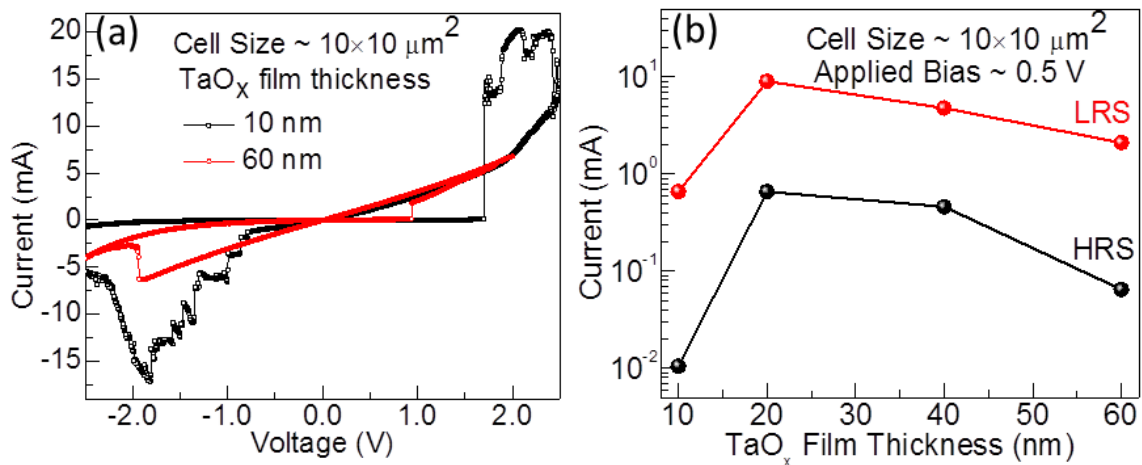


**Figure 6.4** SET and RESET states dependency on physical parameters for TiO<sub>x</sub>/TaO<sub>x</sub> memristors. (a) Two different switching mechanism for two different thicknesses of TaO<sub>x</sub> layer. (b) HRS and LRS currents vs. TaO<sub>x</sub> layer thickness for a 10×10 μm<sup>2</sup> memory cell at +0.5 V applied bias.

Based on our studies, we find that the Pt/TiO<sub>x</sub>/TaO<sub>x</sub>/Pt device with an optimized TaO<sub>x</sub> film thickness of 60 nm and junction size of 10×10 μm<sup>2</sup> provides the best (highest) ON to OFF current ratios. Using this optimized memristor device, we evaluate the device stability and endurance. Our

memristor device with a  $10 \times 10 \text{ } \mu\text{m}^2$  junction size is found to exhibit highly stable repeatability in the  $I$ - $V$  profiles, with the same SET and RESET voltages, over  $10^4$  cycles following the first switching cycle (Figure 6.5a). Out of these  $10^4$  cycles, the remarkably stable ON to OFF current ratio over  $10^3$  switching cycles at a small switching voltage of +0.5 V is shown in Figure 6.5b. As the repeated cycling between two states does not involve any further evolution of oxygen vacancies (and consequently corrosion) due to Joule heating, there is therefore no degradation in the device behavior. Since there is no difference between the  $V_{SET}$  for the first switching cycle from HRS to LRS and those for the subsequent repeated cycles, it is confirmed that no high bias electroforming step is required to initiate the device operation. The device is also found to maintain similar ON and OFF currents up to  $10^5$  s at an applied voltage of +0.5 V (Figure 6.5c). This indicates that the retention capacity of  $\text{TaO}_x$  based memristors is extremely high as compared to other metal oxides due to very low leakage current. Figure 6.5d shows the essentially the same switching voltage  $V_{SET}$  found for over 300 memristor devices with a junction size  $10 \times 10 \text{ } \mu\text{m}^2$  fabricated on the same chip, which demonstrates the high reproducibility of our accurate fabrication technique.

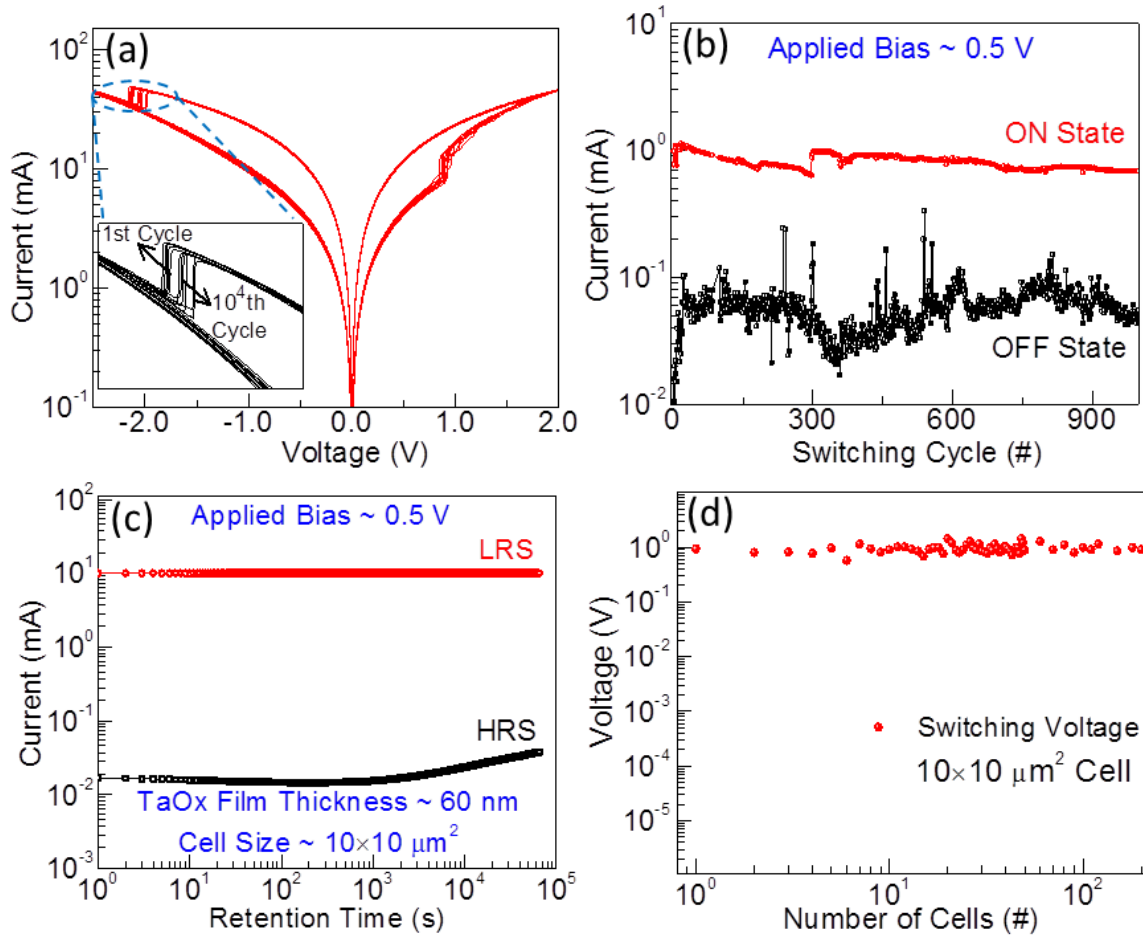


**Figure 6.5** Repeatability, endurance and retention capabilities of the  $\text{TiO}_x/\text{TaO}_x$  memristor. (a) Extremely high switching repeatability of over  $10^4$  cycles for the electroforming-free cell with junction size  $10 \times 10 \mu\text{m}^2$  and  $\text{TaO}_x$  film thickness 60 nm. (b) Plot between current vs switching cycles for HRS and LRS states showing the almost constant ON/OFF current ratio for over 1000 cycles at the applied bias +0.5 V. (c) Remarkable retention capabilities of the  $10 \times 10 \mu\text{m}^2$  cell with 60 nm  $\text{TaO}_x$  layer in HRS and LRS at a small applied voltage (+0.5 V). (d) The highly reproducible electrical behavior of the arrays of cells with same cell size, over the same chip showing the similar switching voltages.

The stopping voltage (the max limit of positive voltage during  $I$ - $V$  sweep) can be controlled to tune the SET and RESET voltages of the cell as shown in Figure 6.6a, where the SET and RESET voltages are observed to be decreased with decreasing stopping voltage. This characteristic could be important for the integration of programmable circuits, in which the behavior of the device can be programmed by simply setting the desired stopping voltages. Furthermore, binary switching with a stable ON to OFF ratio is obtained in both the virgin state and the switching state by applying a pulsed DC voltage instead of the analog DC voltage with 0.5 s intervals (Figure 6.6b). Additionally, this memristive

behavior is similar to the behavior of synaptic connections between neurons that can be made stronger or weaker through polarity, strength and duration of the chemical or electrical signals.

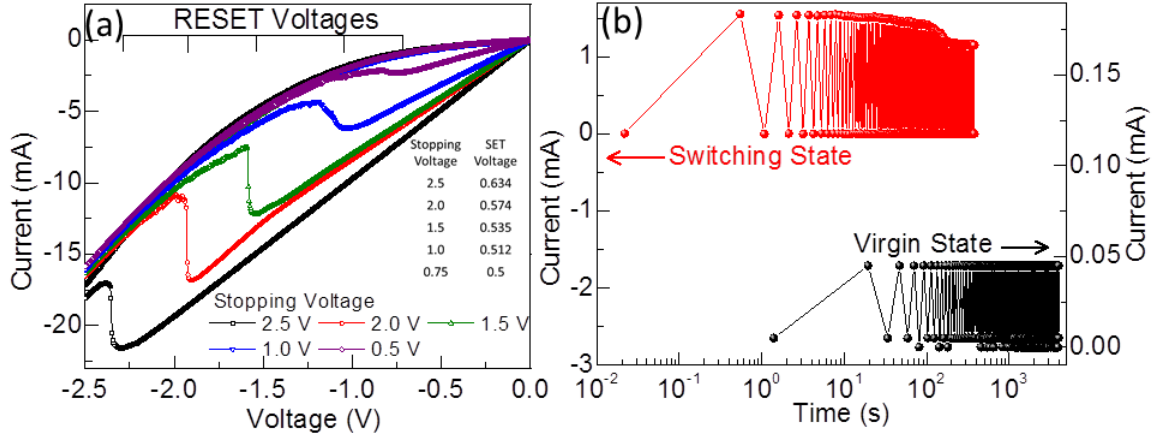


**Figure 6.6** Programmable switching modes of TiO<sub>x</sub>/TaO<sub>x</sub> memristors. (a) RESET states of the 10×10 μm<sup>2</sup> cell with 60 nm TaO<sub>x</sub> layer corresponding to different stopping voltages (+0.75-2.5 V). Inset shows the corresponding SET voltages for different stopping voltage. The SET and RESET states can be manually programmed by using different stopping voltages. (b) Binary switching in virgin state and switching state exhibiting short term potentiation at an applied voltage of +0.5 V with 0.5 s interval for 10×10 μm<sup>2</sup> cell with 60 nm thick TaO<sub>x</sub> layer.

## 6.4 Conclusion

In summary, we have presented a heterostructure based materials system for non-volatile memory, which meets the criteria of an electroforming-free low-bias memristive switching device with low power consumption. We have demonstrated the remarkable performance of employing such nanocrystalline switching matrix in the memristor device structure and account for its switching mechanism. We have further shown the low SET and RESET voltages and their junction size dependency as well as control of bipolar or unipolar switching through the fabrication parameters. The programmable switching behavior using both analog and pulsed signals by controlling the stopping voltages make them potential candidates for advanced logic components for computers and neuromorphic circuits. The fabrication of multilayer stacking using high  $\kappa$ -dielectric materials such as TaO<sub>x</sub> and its interfacial combination with higher electronegative TiO<sub>x</sub> layer and non-corrosive electrode material such as Pt makes it an exceptional memory device with extremely high repeatability/endurance, stable ON/OFF ratio and ultrafast switching speed. There remain a few challenges, such as further reducing the SET/RESET window to lower the power consumption even

further and more detailed mechanism coupled with quantitative modelling, which can be addressed by exploiting size reduction by nanoscale lithography techniques.

## Chapter 7

### Concluding Remarks and Outlook

#### 7.1 Summary

The goal of the present research is to develop size-selected nanoclusters and nanocrystalline films of transition metal and metal oxides (especially semiconducting  $\text{TiO}_2$  and  $\text{Ta}_2\text{O}_5$ ) and to exploit their applications as high-efficiency photocatalysts for photoelectrochemical water splitting and as electroforming-free active layers for resistive switching memory. Using a novel nanocluster generation source based on the gas-phase aggregation technique, we have successfully created ultrasmall ( $< 5$  nm) semiconducting oxide nanoclusters of  $\text{TiO}_2$  and  $\text{TaO}_x$  (as well as metallic nanoclusters of Pt). With precise control over such deposition parameters as aggregation zone length and Ar gas flow rate, nanoclusters with different mode sizes have been generated with a narrow size distribution. Based on their mass-to-charge ratio, precise size-selection of the as-grown nanoclusters has been performed by applying an appropriate set of AC and DC voltages on the quadrupole mass filter that is coupled with the nanocluster generation system. The resulting nearly monosized nanoclusters are then deposited on H-Si substrates. The growth mechanism, effect of various deposition parameters, materials crystallinity have been investigated by performing the extensive characterization on these supported nanoclusters. The outstanding photocatalytic properties of the resulting samples are demonstrated in the photoelectrochemical water splitting reactions (Chapters 3 and 4). In the second part of the present work, we exploit the application of ultrasmall  $\text{TiO}_x$  and  $\text{TaO}_x$  nanocrystallites (with similar size as the nanoclusters) in the form of defect-rich nanocrystalline thin films for resistive switching memristive devices. These memristors are based on a simple crossbar architecture, in which the oxide semiconducting thin film is sandwiched between a pair of metallic Pt electrodes (Chapters 5 and 6). We have greatly extended the present state-of-the-art for memristor technology by either significantly lowering the electroforming voltage or totally removing the requirement for electroforming.

Nearly monosized  $\text{TiO}_2$  nanoclusters with three different sizes (4, 6 and 8 nm) are synthesized and deposited on H-terminated Si(100), quartz and glass substrates using three different combinations of Ar flow rate and aggregation length. By controlling the ambient in the deposition chamber, it is possible to produce surface defect-rich nanoclusters. We show that these nanoclusters can be deposited with uniform distribution, with minimal aggregation, on the substrate under soft-landing condition, and that nanoclusters smaller than 8 nm (in dia.) are completely amorphous while the bigger nanoclusters have a crystalline core with an amorphous shell. As photoanode materials for the

photoelectrochemical water splitting reaction, these supported nanoclusters exhibit remarkable photocatalytic activities because of their high specific surface area and large amounts of surface defects. We show that the photoconversion efficiency increases with the decreasing nanocluster size, with the highest total photoconversion efficiency (~1%) found for the 4-nm TiO<sub>2</sub> nanoclusters at a low saturation voltage (-0.22 V vs Ag/AgCl).

Using a similar approach we deposit defect-rich, ultrasmall TaO<sub>x</sub> nanocluster photocatalysts (5 nm in dia), along with Pt nanoclusters (also 5 nm in dia) to be used as promoters. Upon soft-landing on the H-Si substrate, the as-grown TaO<sub>x</sub> nanoclusters are found to be amorphous, while Pt nanoclusters are crystalline. As the relative amount of material loading of Pt nanoclusters increases from 50% (deposition time 15 min) to 100% (30 min) with respect to the TaO<sub>x</sub> amount, the total photoconversion efficiency is found to increase dramatically (from 0.1% for TaO<sub>x</sub> NCs without Pt NC promoters to 0.4% for TaO<sub>x</sub> NCs with equal amount of Pt NC promoters). The presence of the metallic promoters therefore provides effective separation of electron and holes generated during the water splitting reaction. Interestingly, further increase of Pt NC loading to 150% decreases the efficiency, which is attributed to the blocking of photosensitive TaO<sub>x</sub> surface due to high density of Pt nanoclusters. The photoconversion efficiencies obtained for these defect-rich TiO<sub>x</sub> and TaO<sub>x</sub> NC photocatalysts (with and without Pt NC promoters) represent the best nanocluster catalysts to date. Their exceptional photocatalytic performance is especially remarkable, considering the relatively small amount of material loading on the substrate (20% coverage), These efficiencies can be enhanced at least five time by simply increasing the amount of NC loading to near a monolayer and by the use of metal promoters (as demonstrated in the TaO<sub>x</sub> work).

In the second half of this thesis, we focus on TiO<sub>x</sub> and TaO<sub>x</sub> nanocrystallites in the form of thin films for memristor application. Using a crossbar device architecture consisting of the metal oxide film sandwiched between a pair of Pt electrodes, we study the resistive switching behaviour of the defect-rich TiO<sub>x</sub> or/and TaO<sub>x</sub> nanocrystalline films. Defect-rich nanocrystalline films (with crystallite size of 4-5 nm) are deposited in a physical vapor deposition chamber using a RF magnetron sputtering technique, upon proper optimization of such deposition parameters as Ar gas flow rate, chamber pressure and deposition temperature.

In order to alleviate the requirement of high bias electroforming step during the resistive switching from the high resistance OFF state to low resistance ON state, we intentionally introduce a large amount of built-in oxygen vacancy defects in our nanocrystalline semiconducting films. In the Pt/TiO<sub>x</sub>/Pt memristor device, we observe bipolar resistive switching behavior at a low electroforming voltage of +1.5 V, which represents the smallest electroforming voltage reported to date. The device

not only exhibits remarkably high endurance and reliability, upon 250 consecutive switching cycles within  $\pm 1.0$  V, but also show a high degree of stability with similar ON/OFF current ratio and high retention capabilities ( $10^5$  s) with high switching speed ( $\sim$ ns). The quick response of the device to applied electric pulses offer potential application of such a device for simulating biological synaptic behavior.

By adding a defect-rich TaO<sub>x</sub> layer, we created a heterojunction between the TiO<sub>x</sub> and TaO<sub>x</sub> layers. In our Pt/TiO<sub>x</sub>/TaO<sub>x</sub>/Pt memristor device, we demonstrate that the oxygen-deficient TaO<sub>x</sub> layer could serve as the source of oxygen vacancies while the actual switching occurs in the TiO<sub>x</sub> layer as a result of the drift and diffusion of these oxygen vacancies induced by the applied bias. The incorporation of the TaO<sub>x</sub> layer (a high- $\kappa$  dielectric material with low leakage current) enables this Pt/TiO<sub>x</sub>/TaO<sub>x</sub>/Pt device to be electroforming-free, thus removing a major obstacle in memristor device development. More remarkable is that this device can be switched on, i.e. from the high resistance OFF state to low resistance ON state, at an even lower programming voltage of +0.8 V and switched off at -0.2 V. These switching voltages of this device are much lower than any previously reported memristors. This device also exhibits highly stable repeatability and endurance (over  $10^4$  switching cycles), and very high retention capabilities ( $10^8$  s), which makes this new device structure an even better candidate for non-volatile memory applications. We further investigate the effect of compliance current on the switching behavior of the device. By setting compliance current in  $\mu$ A range, it is possible to switch the device with an ultralow programming voltage, as low as 50 mV. This is an important result because it demonstrates the feasibility of an ultralow power consumption ( $\sim$ nW) memristor device. We also show that the thickness of the TaO<sub>x</sub> layer can be used to preselect the switching mechanism between unipolar switching for a TaO<sub>x</sub> film thinner than 10 nm and bipolar switching for a thicker TaO<sub>x</sub> film. With appropriate settings of sweep voltage range, we again can tune the SET and RESET voltages. The Pt/TiO<sub>x</sub>/TaO<sub>x</sub>/Pt heterojunction memristor therefore represents the most robust and adaptable resistive switching device constructed to date.

## 7.2 Future Work

### 7.2.1 Nanoclusters

In the present work, we utilize the size-selected nanoclusters based on TiO<sub>2</sub> and Ta<sub>2</sub>O<sub>5</sub> to exploit their application as photocatalysts in photoelectrochemical water splitting reaction. The following future work involving size-selected nanoclusters could be pursued not just to provide further improvements to their photocatalytic performance but indeed to develop other applications and better fundamental understanding of these novel nanomaterials.

1. Creating even smaller nanoclusters (below 5 nm) with controlled dimensions could offer even better size-specific photoconversion efficiencies. We have demonstrated the Nanogen source could produce TiO<sub>2</sub> nanoclusters as small as 3.5 nm using the existing parameter space. Some other possible options could be changing sputtering gas from Ar to Ne or Kr and also using He gas along with the sputtering gas to enhance the condensation process by providing low temperature nucleation seeds for cluster growth.
2. Modification of the as-grown nanoclusters by chemical post-treatment such as functionalization could be applied to enhance the surface structure of the nanoclusters, which could be potentially beneficial for specific catalytic activities.
3. Making hybrid nanoclusters, such as binary or tertiary alloys of various photoactive transition metals and transition metal oxides or creating core-shell nanoclusters could offer another revenue to performance enhancement.
4. Large-scale ab-initio quantum mechanical calculations based on Density Functional Theory not only could offer new insights to the growth mechanisms of nanoclusters but also could be used to determine to novel structural, electronic and chemical properties of these nanoclusters.
5. These size-selected ultrasmall nanoclusters can be used to decorate other nanostructured materials, including nanowires, nanotubes, and nanosheets. As these latter nanostructured materials can be used to massively increase the total surface area of the substrate when compared to a flat planar substrate such as H-Si, this combination could provide significant enhancement to their catalytic performance. As example, we show in Figure 7.1a the TiO<sub>2</sub> nanowires uniformly decorated by 5 nm Pt nanoclusters and in Figure 7.1b the CuO nanowires uniformly decorated by 3 nm Ta nanoclusters.
6. In addition to nanocatalysis, other applications of these nanoclusters, including protein immobilization, gas and chemical sensing, nanoplasmonics and quantum confinement, can be developed.

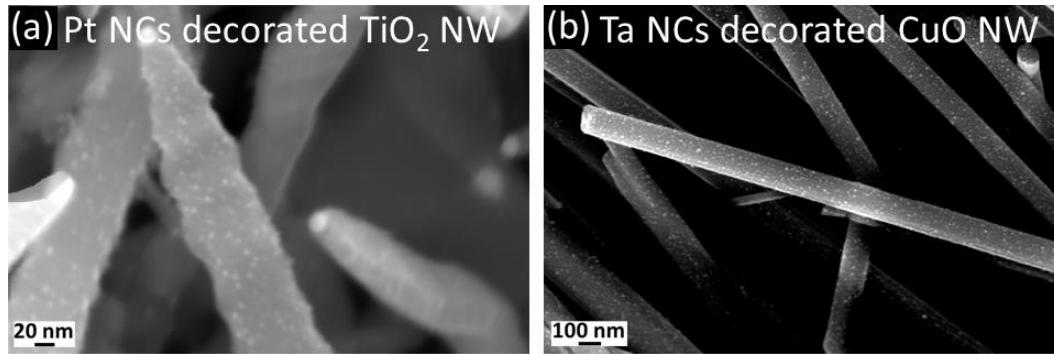


**Figure 7.1** (a) TiO<sub>2</sub> nanowires decorated by 5 nm Pt nanoclusters and (b) CuO nanowires decorated by 3 nm Ta nanoclusters.

### 7.2.2 Nanocrystalline Thin Films

In the present work, we have focussed on the use of defect-rich TiO<sub>x</sub> and TaO<sub>x</sub> nanocrystalline films deposited at room temperature for building memristor devices. Future work to improve the switching performance may include the following efforts:

1. Exploring the possibilities of achieving better switching performance by further reducing the thickness of the films (to below 10 nm). Further control over the dimensionality of the device junction size and stacking arrangements as well as reduction of the overall size to the nanoscale regime by using e-beam lithography and ion beam lithography could open up new quantum properties not observed before. This would also allow us to further evaluate the feasibility of continued miniaturization of the memristor device and of further optimization of size-dependent properties.
2. Incorporating other high- $\kappa$  dielectric materials, such as Hafnium (Hf), Vanadium (V), and Lanthanum (La), into the existing system to create different heterojunctions offers new prospect of creating more stable memristive devices with better switching performance with even smaller leakage currents.
3. Band structure engineering using different carrier dopants could modify their electronic structures, particularly their bandgaps, which would in turn affect the switching behaviour.
4. The ultrasmall nanoclusters, obtained with the Nanogen nanocluster source, can be used to provide perhaps the smallest junction size (3-5 nm) that is significantly smaller than those currently achievable with electron beam or ion beam lithographical techniques. These quantum size junctions may allow us to explore new quantum electronics not possible before.
5. The use of nanostructures such as nanowires, instead of the present planar nanocrystalline films, as the active layer could provide some insight into any possible morphology effects on

memristor properties. One possible advantage of using one dimensional structure could be the flow of oxygen vacancies restricted to one direction for better control.

6. Theoretical study of the memristive switching behavior related to specific material systems could offer further insight and better understanding of the switching mechanism and could provide useful predictions about the device characteristics and performance.

## Bibliography

- (1) Edelstein, A. S.; Murday, J. S.; Rath, B. B. Challenges in Nanomaterials Design. *Prog. Mater. Sci.* **1997**, *42*, 5–21.
- (2) Roduner, E. Size Matters: Why Nanomaterials Are Different. *Chem. Soc. Rev.* **2006**, *35*, 583–592.
- (3) Tessier, P. M.; Velev, O. D.; Kalambur, A. T.; Rabolt, J. F.; Lenhoff, A. M.; Kaler, E. W. Assembly of Gold Nanostructured Films Templated by Colloidal Crystals and Use in Surface-Enhanced Raman Spectroscopy. *J. Am. Chem. Soc.* **2000**, *122*, 9554–9555.
- (4) Zeng, S.; Baillargeat, D.; Ho, H.; Yong, K. Nanomaterials Enhanced Surface Plasmon Resonance for Biological and Chemical Sensing Applications. *Chem. Soc. Rev.* **2014**, *43*, 3426.
- (5) Zeng, S.; Yu, X.; Law, W.; Zhang, Y.; Hu, R.; Dinh, X.; Ho, H.; Yong, K. Size Dependence of Au NP-Enhanced Surface Plasmon Resonance Based on Differential Phase Measurement. *Sensors Actuators B Chem.* **2013**, *176*, 1128–1133.
- (6) Rodríguez-Lorenzo, L.; De La Rica, R.; Álvarez-Puebla, R. A.; Liz-Marzán, L. M.; Stevens, M. M. Plasmonic Nanosensors with Inverse Sensitivity by Means of Enzyme-Guided Crystal Growth. *Nat. Mater.* **2012**, *11*, 604–607.
- (7) Aluri, G. S.; Motayed, A.; Davydov, A. V.; Oleshko, V. P.; Bertness, K. A.; Sanford, N. A.; Mulpuri, R. V. Methanol, Ethanol and Hydrogen Sensing Using Metal Oxide and Metal (TiO<sub>2</sub>-Pt) Composite Nanoclusters on GaN Nanowires: A New Route towards Tailoring the Selectivity of Nanowire/nanocluster Chemical Sensors. *Nanotechnology* **2012**, *23*, 175501–175512.
- (8) Mackenzie, D. M. A.; Brown, S. A. Germanium Nano-Cluster Films as Humidity and Hydrogen Sensors. *J. Appl. Phys.* **2012**, *112*, 074514 (1–5).
- (9) Palmer, R. E.; Pratontep, S.; Boyen, H. G. Nanostructured Surfaces from Size-Selected Clusters. *Nat. Mater.* **2003**, *2*, 443–448.
- (10) Schmid, G. Nanoclusters-Building Blocks for Future Nanoelectronic Devices? *Adv. Eng. Mater.* **2001**, *3*, 737–743.
- (11) Heiz, U.; Bullock, E. L. Fundamental Aspects of Catalysis on Supported Metal Clusters. *J. Mater. Chem.* **2004**, *14*, 564.
- (12) Narayanan, R.; El-Sayed, M. A. Catalysis with Transition Metal Nanoparticles in Colloidal Solution: Nanoparticle Shape Dependence and Stability. *J. Phys. Chem. B* **2005**, *109*, 12663–12676.

- (13) Wang, J.; Sun, B.; Gao, F.; Greenham, N. C. Memristive Devices Based on Solution-Processed ZnO Nanocrystals. *Phys. Status Solidi* **2010**, *207*, 484–487.
- (14) Bruchez Jr., M. Semiconductor Nanocrystals as Fluorescent Biological Labels. *Science* **1998**, *281*, 2013–2016.
- (15) Sarkar, D.; Xie, X.; Kang, J.; Zhang, H.; Liu, W.; Navarrete, J.; Moskovits, M.; Banerjee, K. Functionalization of Transition Metal Dichalcogenides with Metallic Nanoparticles: Implications for Doping and Gas-Sensing. *Nano Lett.* **2015**, *15*, 2852–2862.
- (16) Cho, K. S.; Park, N.; Kim, T.; Kim, K.; Sung, G. Y.; Shin, J. H. High Efficiency Visible Electroluminescence from Silicon Nanocrystals Embedded in Silicon Nitride Using a Transparent Doping Layer. *Appl. Phys. Lett.* **2005**, *86*, 071909 (1–3).
- (17) Han, N.; Wang, F.; Hou, J. J.; Yip, S. P.; Lin, H.; Xiu, F.; Fang, M.; Yang, Z.; Shi, X.; Dong, G.; et al. Tunable Electronic Transport Properties of Metal-Cluster-Decorated III-V Nanowire Transistors. *Adv. Mater.* **2013**, *25*, 4445–4451.
- (18) Wei, X.; Skomski, R.; Balamurugan, B.; Sellmyer, D. J. Magnetism of Core-Shell Ti:TiO Nanoparticles. *J. Appl. Phys.* **2010**, *107*, 09B516 (1–3).
- (19) Lu, Z.; Ye, M.; Li, N.; Zhong, W.; Yin, Y. Self-Assembled TiO<sub>2</sub> Nanocrystal Clusters for Selective Enrichment of Intact Phosphorylated Proteins. *Angew. Chem. Int. Ed. Engl.* **2010**, *49*, 1862–1866.
- (20) Heiliger, C.; Czerner, M.; Klar, P. J.; Hara, S. Magnetic Sensor Devices Based on Ordered Planar Arrangements of MnAs Nanocluster. *IEEE Trans. Magn.* **2010**, *46*, 1702–1704.
- (21) Xue, X.; Ji, W.; Mao, Z.; Mao, H.; Wang, Y.; Wang, X.; Ruan, W.; Zhao, B.; Lombardi, J. R. Raman Investigation of Nanosized TiO<sub>2</sub>: Effect of Crystallite Size and Quantum Confinement. *J. Phys. Chem. C* **2012**, *116*, 8792–8797.
- (22) Luo, M.; Cheng, K.; Weng, W.; Song, C.; Du, P.; Shen, G.; Xu, G.; Han, G. Size-Dependent Ultraviolet Luminescence and Low-Field Electron Emission of TiO<sub>2</sub> Nanodots Formed by Phase-Separation-Induced Self-Assembly. *J. Phys. D: Appl. Phys.* **2009**, *42*, 105414 (1–7).
- (23) Rai, A. K.; Anh, L. T.; Gim, J.; Mathew, V.; Kang, J.; Paul, B. J.; Song, J.; Kim, J. Simple Synthesis and Particle Size Effects of TiO<sub>2</sub> Nanoparticle Anodes for Rechargeable Lithium Ion Batteries. *Electrochim. Acta* **2013**, *90*, 112–118.
- (24) van Buuren, T.; Dinh, L.; Chase, L.; Siekhaus, W.; Terminello, L. Changes in the Electronic Properties of Si Nanocrystals as a Function of Particle Size. *Phys. Rev. Lett.* **1998**, *80*, 3803–3806.
- (25) Rao, C. N. R.; Kulkarni, G. U.; Thomas, P. J.; Edwards, P. P. Size-Dependent Chemistry: Properties of Nanocrystals. *Chemistry* **2002**, *8*, 28–35.

- (26) Bromann, K.; Felix, C.; Brune, H.; Harbich, W.; Monot, R.; Buttet, J.; Kern, K. Controlled Deposition of Size-Selected Silver Nanoclusters. *Science*, 1996, *274*, 956–958.
- (27) Gracia-Pinilla, M.; Martínez, E.; Vidaurri, G. S.; Pérez-Tijerina, E. Deposition of Size-Selected Cu Nanoparticles by Inert Gas Condensation. *Nanoscale Res. Lett.* **2009**, *5*, 180–188.
- (28) Ayesh, A. I.; Qamhieh, N.; Ghamlouche, H.; Thaker, S.; El-Shaer, M. Fabrication of Size-Selected Pd Nanoclusters Using a Magnetron Plasma Sputtering Source. *J. Appl. Phys.* **2010**, *107*, 034317 (1–5).
- (29) Su, X.; Wu, Q.; Zhan, X.; Wu, J.; Wei, S.; Guo, Z. Advanced Titania Nanostructures and Composites for Lithium Ion Battery. *J. Mater. Sci.* **2011**, *47*, 2519–2534.
- (30) Park, J. Y.; Choi, S.-W.; Kim, S. S. Fabrication of a Highly Sensitive Chemical Sensor Based on ZnO Nanorod Arrays. *Nanoscale Res. Lett.* **2010**, *5*, 353–359.
- (31) Kim, S. H.; Umar, A.; Hwang, S. W. Rose-like CuO Nanostructures for Highly Sensitive Glucose Chemical Sensor Application. *Ceram. Int.* **2015**, *41*, 9468–9475.
- (32) Rahman, M. M.; Jamal, A.; Khan, S. B.; Faisal, M. Highly Sensitive Ethanol Chemical Sensor Based on Ni-Doped SnO<sub>2</sub> Nanostructure Materials. *Biosens. Bioelectron.* **2011**, *28*, 127–134.
- (33) Wang, H.; Liang, Q.; Wang, W.; An, Y.; Li, J.; Guo, L. Preparation of Flower-like SnO<sub>2</sub> Nanostructures and Their Applications in Gas-Sensing and Lithium Storage. *Cryst. Growth Des.* **2011**, *11*, 2942–2947.
- (34) Lemmon, J. P.; Polikarpov, E.; Bennett, W. D.; Kovarik, L. Thin Metal Oxide Films to Modify a Window Layer in CdTe-Based Solar Cells for Improved Performance Solar Power Conversion Efficiency in Modulated Silicon Nanowire Photonic Crystals. *Appl. Phys. Lett. J. Appl. Phys.* **2012**, *100*, 213908–274327.
- (35) Ni, M.; Leung, M. K. H.; Leung, D. Y. C.; Sumathy, K. A Review and Recent Developments in Photocatalytic Water-Splitting Using TiO<sub>2</sub> for Hydrogen Production. *Renew. Sustain. Energy Rev.* **2007**, *11*, 401–425.
- (36) Hartmann, P.; Lee, D.; Smarsly, B. M.; Janek, J. Mesoporous TiO<sub>2</sub> : Comparison of Classical Sol-Gel and Nanoparticle Based Photoelectrodes for the Water Splitting Reaction. *ACS Nano* **2010**, *4*, 3147–3154.
- (37) Yu, J.; Qi, L.; Jaroniec, M. Hydrogen Production by Photocatalytic Water Splitting over Pt/TiO<sub>2</sub> Nanosheets with Exposed (001) Facets. *J. Phys. Chem. C* **2010**, *114*, 13118–13125.
- (38) Shyjumon, I.; Gopinadhan, M.; Helm, C. A.; Smirnov, B. M.; Hippler, R. Deposition of Titanium/Titanium Oxide Clusters Produced by Magnetron Sputtering. *Thin Solid Films* **2006**, *500*, 41–51.
- (39) Pazoki, M.; Taghavinia, N.; Abdi, Y.; Tajabadi, F.; Boschloo, G.; Hagfeldt, A. CVD-Grown

- TiO<sub>2</sub> Particles as Light Scattering Structures in Dye-Sensitized Solar Cells. *RSC Adv.* **2012**, *2*, 12278–12285.
- (40) Rahman, M. A.; Bazargan, S.; Srivastava, S.; Wang, X.; Abd-Ellah, M.; Thomas, J. P.; Heinig, N. F.; Pradhan, D.; Leung, K. T. Defect-Rich Decorated TiO<sub>2</sub> Nanowires for Super-Efficient Photoelectrochemical Water Splitting Driven by Visible Light. *Energy Environ. Sci.* **2015**, *8*, 3363–3373.
- (41) Pradhan, S. K.; Reucroft, P. J.; Yang, F.; Dozier, A. Growth of TiO<sub>2</sub> Nanorods by Metalorganic Chemical Vapor Deposition. *J. Cryst. Growth* **2003**, *256*, 83–88.
- (42) Jacobs, J. F.; van de Poel, I.; Osseweijer, P. Sunscreens with Titanium Dioxide (TiO<sub>2</sub>) Nanoparticles: A Societal Experiment. *Nanoethics* **2010**, *4*, 103–113.
- (43) Lim, J. H.; Sisco, P.; Mudalige, T. K.; Sanchez-Pomales, G.; Howard, P. C.; Linder, S. W. Detection and Characterization of SiO<sub>2</sub> and TiO<sub>2</sub> Nanostructures in Dietary Supplements. *J. Agric. Food Chem.* **2015**, *63*, 3144–3152.
- (44) Carbone, R.; De Marni, M.; Zanardi, A.; Vinati, S.; Barborini, E.; Fornasari, L.; Milani, P. Characterization of Cluster-Assembled Nanostructured Titanium Oxide Coatings as Substrates for Protein Arrays. *Anal. Biochem.* **2009**, *394*, 7–12.
- (45) Austin, R. H.; Lim, S. The Sackler Colloquium on Promises and Perils in Nanotechnology for Medicine. *Proc. Natl. Acad. Sci. U. S. A.* **2008**, *105*, 17217–17221.
- (46) Yang, Y.; Peng, Z.; Wang, G.; Ruan, G.; Fan, X.; Li, L.; Fei, H.; Hauge, R. H.; Tour, J. M. Three-Dimensional Thin Film for Lithium-Ion Batteries and Supercapacitors. *ACS Nano* **2014**, *8*, 7279–7287.
- (47) Prof, F.; Royal, C.; Acadd, I. The Bakerian Lecture: Experimental Relations of Gold (and Other Metals) to Light. *Philos. Trans. R. Soc. London* **1857**, *147*, 145–181.
- (48) Turkevich, J.; Stevenson, P. C.; Hillier, J. A Study of the Nucleation and Growth Processes in the Synthesis of Colloidal Gold. *Discuss. Faraday Soc.* **1951**, *11*, 55–75.
- (49) Gu, F.; Wang, S. F.; Lü, M. K.; Zhou, G. J.; Xu, D.; Yuan, D. R. Photoluminescence Properties of SnO<sub>2</sub> Nanoparticles Synthesized by Sol–Gel Method. *J. Phys. Chem. B* **2004**, *108*, 8119–8123.
- (50) Moghimi, N.; Abdellah, M.; Thomas, J. P.; Mohapatra, M.; Leung, K. T. Bimetallic FeNi Concave Nanocubes and Nanocages. *J. Am. Chem. Soc.* **2013**, *135*, 10958–10961.
- (51) Dietz, T. G.; Duncan, M. A.; Powers, D. E.; Smalley, R. E. Laser Production of Supersonic Metal Cluster Beams. *J. Chem. Phys.* **1981**, *74*, 6511–6512.
- (52) Ribeiro, J. F.; Sousa, R.; Cunha, D. J.; Vieira, E. M. F.; Silva, M. M.; Dupont, L.; Goncalves, L. M. A Chemically Stable PVD Multilayer Encapsulation for Lithium Microbatteries. *J.*

- Phys. D. Appl. Phys.* **2015**, *48*, 395306 (1–7).
- (53) Yu, H. K.; Lee, J. L. Growth Mechanism of Metal-Oxide Nanowires Synthesized by Electron Beam Evaporation: A Self-Catalytic Vapor-Liquid-Solid Process. *Sci. Rep.* **2014**, *4*, 6589 (1–8).
- (54) Wang, P. H.; Wang, S. J.; Uang, K. M.; Chen, T. M.; Wang, T. C. Synthesis of Single-Crystal Rutile TiO<sub>2</sub> Nanowire Arrays on a Sputtered TiO<sub>2</sub> Seed Layer. In *218th ECS Meeting (The Electrochemical Society)*; 2010.
- (55) Dhara, S.; Giri, P. K. Effect of Growth Temperature on the Catalyst-Free Growth of Long Silicon Nanowires Using Radio Frequency Magnetron Sputtering. *Int. J. Nanosci.* **2011**, *10*, 13–17.
- (56) Arroyo-Hernández, M.; Alvaro, R.; Serrano, S.; Costa-Krämer, J. L. Catalytic Growth of ZnO Nanostructures by RF Magnetron Sputtering. *Nanoscale Res. Lett.* **2011**, *6*, 437 (1–6).
- (57) Gratzel, M. Photoelectrochemical Cells. *Nature* **2001**, *414*, 338–344.
- (58) Mor, G. K.; Varghese, O. K.; Paulose, M.; Shankar, K.; Grimes, C. A. A Review on Highly Ordered, Vertically Oriented TiO<sub>2</sub> Nanotube Arrays: Fabrication, Material Properties, and Solar Energy Applications. *Sol. Energy Mater. Sol. Cells* **2006**, *90*, 2011–2075.
- (59) Fujishima, A.; Honda, K. Electrochemical Photolysis of Water at a Semiconductor Electrode. *Nature* **1972**, *238*, 37–38.
- (60) Khan, S. U. M.; Al-Shahry, M.; Ingler, W. B. Efficient Photochemical Water Splitting by a Chemically Modified n-TiO<sub>2</sub>. *Science* **2002**, *297*, 2243–2245.
- (61) Shaban, Y. Visible Light Active Carbon Modified n-TiO<sub>2</sub> for Efficient Hydrogen Production by Photoelectrochemical Splitting of Water. *Int. J. Hydrogen Energy* **2008**, *33*, 1118–1126.
- (62) Park, J. H.; Kim, S.; Bard, A. J. Novel Carbon-Doped TiO<sub>2</sub> Nanotube Arrays with High Aspect Ratios for Efficient Solar Water Splitting. *Nano Lett.* **2006**, *6*, 24–28.
- (63) Kitano, M.; Takeuchi, M.; Matsuoka, M.; Thomas, J. M.; Anpo, M. Photocatalytic Water Splitting Using Pt-Loaded Visible Light-Responsive TiO<sub>2</sub> Thin Film Photocatalysts. *Catal. Today* **2007**, *120*, 133–138.
- (64) Lin, Y.; Zhou, S.; Liu, X.; Sheehan, S.; Wang, D. TiO<sub>2</sub>/TiSi<sub>2</sub> Heterostructures for High-Efficiency Photoelectrochemical H<sub>2</sub>O Splitting. *J. Am. Chem. Soc.* **2009**, *131*, 2772–2773.
- (65) Allam, N. K.; Poncheri, A. J.; El-Sayed, M. A. Vertically Oriented Ti-Pd Mixed Oxynitride Nanotube Arrays for Enhanced Photoelectrochemical Water Splitting. *ACS Nano* **2011**, *5*, 5056–5066.
- (66) Cho, I. S.; Chen, Z.; Forman, A. J.; Kim, D. R.; Rao, P. M.; Jaramillo, T. F.; Zheng, X. Branched TiO<sub>2</sub> Nanorods for Photoelectrochemical Hydrogen Production. *Nano Lett.* **2011**,

- 11, 4978–4984.
- (67) Wang, G.; Wang, H.; Ling, Y.; Tang, Y.; Yang, X.; Fitzmorris, R. C.; Wang, C.; Zhang, J. Z.; Li, Y. Hydrogen-Treated TiO<sub>2</sub> Nanowire Arrays for Photoelectrochemical Water Splitting. *Nano Lett.* **2011**, *11*, 3026–3033.
- (68) Zhang, P.; Zhang, J.; Gong, J. Tantalum-Based Semiconductors for Solar Water Splitting. *Chem. Soc. Rev.* **2014**, *43*, 4395–4422.
- (69) Zou, Z.; Ye, J.; Sayama, K.; Arakawa, H. Direct Splitting of Water under Visible Light Irradiation with an Oxide Semiconductor Photocatalyst. *Nature* **2001**, *414*, 625–627.
- (70) Strukov, D. B.; Snider, G. S.; Stewart, D. R.; Williams, R. S. The Missing Memristor Found. *Nature* **2008**, *453*, 80–83.
- (71) Chua, L. O. Memristor-The Missing Circuit Element. *IEEE Trans. Circuit Theory* **1971**, *18*, 507–519.
- (72) Seo, S.; Lee, M. J.; Seo, D. H.; Jeoung, E. J.; Suh, D. S.; Joung, Y. S.; Yoo, I. K.; Hwang, I. R.; Kim, S. H.; Byun, I. S.; et al. Reproducible Resistance Switching in Polycrystalline NiO Films. *Appl. Phys. Lett.* **2004**, *85*, 5655–5657.
- (73) Szot, K.; Speier, W.; Bihlmayer, G.; Waser, R. Switching the Electrical Resistance of Individual Dislocations in Single-Crystalline SrTiO<sub>3</sub>. *Nat. Mater.* **2006**, *5*, 312–320.
- (74) Beck, A.; Bednorz, J. G.; Gerber, C.; Rossel, C.; Widmer, D. Reproducible Switching Effect in Thin Oxide Films for Memory Applications. *Appl. Phys. Lett.* **2000**, *77*, 139–141.
- (75) Russo, U.; Kamalanathan, D.; Ielmini, D.; Lacaíta, A. L.; Kozicki, M. N. Study of Multilevel Programming in Programmable Metallization Cell (PMC) Memory. *IEEE Trans. Electron Devices* **2009**, *56*, 1040–1047.
- (76) Valov, I.; Sapezanskaia, I.; Nayak, A.; Tsuruoka, T.; Bredow, T.; Hasegawa, T.; Staikov, G.; Aono, M.; Waser, R. Atomically Controlled Electrochemical Nucleation at Superionic Solid Electrolyte Surfaces. *Nat. Mater.* **2012**, *11*, 530–535.
- (77) Wang, Z.; Griffin, P. B.; McVittie, J.; Wong, S.; McIntyre, P. C.; Nishi, Y. Resistive Switching Mechanism in Zn<sub>x</sub>Cd<sub>1-x</sub>S Nonvolatile Memory Devices. *IEEE Electron Device Lett.* **2007**, *28*, 14–16.
- (78) Shima, H.; Takano, F.; Muramatsu, H.; Akinaga, H.; Tamai, Y.; Inque, I. H.; Takagi, H. Voltage Polarity Dependent Low-Power and High-Speed Resistance Switching in CoO Resistance Random Access Memory with Ta Electrode. *Appl. Phys. Lett.* **2008**, *93*.
- (79) Lee, H. Y.; Chen, P. S.; Wu, T. Y.; Chen, Y. S.; Wang, C. C.; Tzeng, P. J.; Lin, C. H.; Chen, F.; Lien, C. H.; Tsai, M. J. Low Power and High Speed Bipolar Switching with a Thin Reactive Ti Buffer Layer in Robust HfO<sub>2</sub> Based RRAM. *Tech. Dig. Int. Electron Devices*

*Meet. IEDM 2008*, 3–6.

- (80) Yoshida, C.; Tsunoda, K.; Noshiro, H.; Sugiyama, Y. High Speed Resistive Switching in Pt/TiO<sub>2</sub>/TiN Film for Nonvolatile Memory Application. *Appl. Phys. Lett.* **2007**, *91*, 223510 (1–3).
- (81) Sun, B.; Liu, Y. X.; Liu, L. F.; Xu, N.; Wang, Y.; Liu, X. Y.; Han, R. Q.; Kang, J. F. Highly Uniform Resistive Switching Characteristics of TiN/ZrO<sub>2</sub>/Pt Memory Devices. *J. Appl. Phys.* **2009**, *105*, 061630 (1–4).
- (82) Kim, Y. M.; Lee, J. S. Reproducible Resistance Switching Characteristics of Hafnium Oxide-Based Nonvolatile Memory Devices. *J. Appl. Phys.* **2008**, *104*, 114115 (1–6).
- (83) Zhang, L.; Member, S.; Huang, R.; Member, S.; Zhu, M.; Qin, S. Unipolar TaO<sub>x</sub>-Based Resistive Change Memory Realized with Electrode Engineering. *IEEE Electron Device Lett.* **2009**, *31*, 966–968.
- (84) Shima, H.; Takano, F.; Muramatsu, H.; Akinaga, H.; Inoue, I. H.; Takagi, H. Control of Resistance Switching Voltages in Rectifying Pt/TiO<sub>x</sub>/Pt Trilayer. *Appl. Phys. Lett.* **2008**, *92*, 043510 (1–3).
- (85) Chien, W. C.; Chen, Y. C.; Lai, E. K.; Yao, Y. D.; Lin, P.; Horng, S. F.; Gong, J.; Chou, T. H.; Lin, H. M.; Chang, M. N.; et al. Unipolar Switching Behaviors of RTO WO<sub>x</sub> RRAM. *IEEE Electron Device Lett.* **2010**, *31*, 126–128.
- (86) Chang, W.-Y.; Lai, Y. C.; Wu, T. B.; Wang, S. F.; Chen, F.; Tsai, M. J. Unipolar Resistive Switching Characteristics of ZnO Thin Films for Nonvolatile Memory Applications. *Appl. Phys. Lett.* **2008**, *92*, 022110 (1–3).
- (87) Yang, J. J.; Pickett, M. D.; Li, X.; Ohlberg, D. A. A.; Stewart, D. R.; Williams, R. S. Memristive Switching Mechanism for Metal/oxide/metal Nanodevices. *Nat. Nanotechnol.* **2008**, *3*, 429–433.
- (88) Yang, J. J.; Borghetti, J.; Murphy, D.; Stewart, D. R.; Williams, R. S. A Family of Electronically Reconfigurable Nanodevices. *Adv. Mater.* **2009**, *21*, 3754–3758.
- (89) Yang, J. J.; Strukov, D. B.; Stewart, D. R. Memristive Devices for Computing. *Nat. Nanotechnol.* **2013**, *8*, 13–24.
- (90) Kwon, D. H.; Kim, K. M.; Jang, J. H.; Jeon, J. M.; Lee, M. H.; Kim, G. H.; Li, X. S.; Park, G. S.; Lee, B.; Han, S.; et al. Atomic Structure of Conducting Nanofilaments in TiO<sub>2</sub> Resistive Switching Memory. *Nat. Nanotechnol.* **2010**, *5*, 148–153.
- (91) Celano, U.; Goux, L.; Belmonte, A.; Opsomer, K.; Franquet, A.; Schulze, A.; Detavernier, C.; Richard, O.; Bender, H.; Jurczak, M.; et al. Three-Dimensional Observation of the Conductive Filament in Nanoscaled Resistive Memory Devices. *Nano Lett.* **2014**, *14*, 2401–2406.

- (92) Pickett, M. D.; Borghetti, J.; Yang, J. J.; Medeiros-Ribeiro, G.; Williams, R. S. Coexistence of Memristance and Negative Differential Resistance in a Nanoscale Metal-Oxide-Metal System. *Adv. Mater.* **2011**, *23*, 1730–1733.
- (93) Alexandrov, A. S.; Bratkovsky, A. M.; Bridle, B.; Savel'ev, S. E.; Strukov, D. B.; Stanley Williams, R. Current-Controlled Negative Differential Resistance due to Joule Heating in TiO<sub>2</sub>. *Appl. Phys. Lett.* **2011**, *99*, 202104 (1–3).
- (94) Sharma, A. A.; Noman, M.; Abdelmoula, M.; Skowronski, M.; Bain, J. A. Electronic Instabilities Leading to Electroformation of Binary Metal Oxide-Based Resistive Switches. *Adv. Funct. Mater.* **2014**, *24*, 5522–5529.
- (95) Miao, F.; Joshua Yang, J.; Borghetti, J.; Medeiros-Ribeiro, G.; Stanley Williams, R. Observation of Two Resistance Switching Modes in TiO<sub>2</sub> Memristive Devices Electroformed at Low Current. *Nanotechnology* **2011**, *22*, 254007 (1–7).
- (96) Salaoru, I.; Khiat, A.; Li, Q.; Berdan, R.; Prodromakis, T. Pulse-Induced Resistive and Capacitive Switching in TiO<sub>2</sub> Thin Film Devices. *Appl. Phys. Lett.* **2013**, *103*, 233513 (1–4).
- (97) Lee, C.; Kim, I.; Shin, H.; Kim, S.; Cho, J. Nonvolatile Memory Properties of Pt Nanoparticle-Embedded TiO<sub>2</sub> Nanocomposite Multilayers via Electrostatic Layer-by-Layer Assembly. *Nanotechnology* **2010**, *21*, 185704 (1–7).
- (98) Choi, B. J.; Torrezan, A. C.; Norris, K. J.; Miao, F.; Strachan, J. P.; Zhang, M. X.; Ohlberg, D. A. A.; Kobayashi, N. P.; Yang, J. J.; Williams, R. S. Electrical Performance and Scalability of Pt Dispersed SiO<sub>2</sub> Nanometallic Resistance Switch. *Nano Lett.* **2013**, *13*, 3213–3217.
- (99) Kim, J. D.; Baek, Y. J.; Jin Choi, Y.; Jung Kang, C.; Ho Lee, H.; Kim, H. M.; Kim, K. B.; Yoon, T. S. Investigation of Analog Memristive Switching of Iron Oxide Nanoparticle Assembly between Pt Electrodes. *J. Appl. Phys.* **2013**, *114*, 224505 (1–6).
- (100) Mickel, P. R.; Lohn, A. J.; Joon Choi, B.; Joshua Yang, J.; Zhang, M. X.; Marinella, M. J.; James, C. D.; Stanley Williams, R. A Physical Model of Switching Dynamics in Tantalum Oxide Memristive Devices. *Appl. Phys. Lett.* **2013**, *102*, 223502 (1–5).
- (101) Wei, X. Y.; Hu, M.; Zhang, K. L.; Wang, F.; Zhao, J. S.; Miao, Y. P. Analysis of the Resistive Switching Behaviors of Vanadium Oxide Thin Film. *Chinese Phys. B* **2013**, *22*, 037201 (1–5).
- (102) Yoon, J. H.; Song, S. J.; Yoo, I. H.; Seok, J. Y.; Yoon, K. J.; Kwon, D. E.; Park, T. H.; Hwang, C. S. Highly Uniform, Electroforming-Free, and Self-Rectifying Resistive Memory in the Pt/Ta<sub>2</sub>O<sub>5</sub>/HfO<sub>2-x</sub>/TiN Structure. *Adv. Funct. Mater.* **2014**, *24*, 5086–5095.
- (103) Miao, F.; Yi, W.; Goldfarb, I.; Yang, J. J.; Zhang, M. X.; Pickett, M. D.; Strachan, J. P.; Medeiros-Ribeiro, G.; Williams, R. S. Continuous Electrical Tuning of the Chemical Composition of TaO<sub>x</sub>-Based Memristors. *ACS Nano* **2012**, *6*, 2312–2318.

- (104) Kim, S.; Choi, S.; Lee, J.; Lu, W. D. Tuning Resistive Switching Characteristics of Tantalum Oxide Memristors through Si Doping. *ACS Nano* **2014**, *8*, 10262–10269.
- (105) Strachan, J. P.; Yang, J. J.; Montoro, L. A.; Ospina, C. A.; Ramirez, A. J.; Kilcoyne, A. L. D.; Medeiros-Ribeiro, G.; Williams, R. S. Characterization of Electroforming-Free Titanium Dioxide Memristors. *Beilstein J. Nanotechnol.* **2013**, *4*, 467–473.
- (106) Lee, S.; Sangle, A.; Lu, P.; Chen, A.; Zhang, W.; Lee, J. S.; Wang, H.; Jia, Q.; Macmanus-driscoll, J. L. Novel Electroforming-Free Nanoscaffold Memristor with Very High Uniformity, Tunability, and Density. *Adv. Mater.* **2014**, *26*, 6284–6289.
- (107) Lee, M. J.; Lee, C. B.; Lee, D.; Lee, S. R.; Chang, M.; Hur, J. H.; Kim, Y. B.; Kim, C. J.; Seo, D. H.; Seo, S.; et al. A Fast, High-Endurance and Scalable Non-Volatile Memory Device Made from Asymmetric Ta<sub>2</sub>O<sub>5-x</sub>/TaO<sub>2-x</sub> Bilayer Structures. *Nat. Mater.* **2011**, *10*, 625–630.
- (108) Pratontep, S.; Carroll, S. J.; Xirouchaki, C.; Streun, M.; Palmer, R. E. Size-Selected Cluster Beam Source Based on Radio Frequency Magnetron Plasma Sputtering and Gas Condensation. *Rev. Sci. Instrum.* **2005**, *76*, 045103 (1–9).
- (109) *NANOGEN SERIES NANOCLUSTER SOURCE.*
- (110) Brandon, D.; Kaplan, W. D. *Microstructural Characterization of Materials; 2nd Ed.*; 2008.
- (111) Carl Zeiss SMT Inc. Instruction Manual: SEM MERLIN Users Manual. 2013,.
- (112) Williams, D. B.; Carter, C. B. *Transmission Electron Microscopy*; Springer, 2009.
- (113) Carl Zeiss SMT Inc. *Instruction Manual: Libra 200 MC Transmission Electron Microscope*; 2009.
- (114) Haugstad, G. *Atomic Force Microscopy: Understanding Basic Modes and Advanced Applications*; Wiley & sons, 2012.
- (115) Vickerman, J. C.; Gilmore, I. S. *Surface Analysis- The Principal Techniques*; 2nd ed.; John Wiley & Sons, 2009.
- (116) TOF.SIMS 5 Brochure.
- (117) Vickerman, J. C.; Briggs, D. *TOF-SIMS: Surface Analysis by Mass Spectrometry*; 2nd ed.; IMPublications, 2013.
- (118) Warren, B. E. *X-Ray Diffraction*; Dover ed.; Dover Publications: New York, 1990.
- (119) Quack, M.; Merkt, F. *Handbook of High-Resolution Spectroscopy: Fundamental and Theory*; 1st ed.; John Wiley & Sons, 2011.
- (120) *SF-100 XPRESS Small Lines at a Great Price*; 2014.
- (121) Arshak, K.; Mihov, M.; Arshak, a; McDonagh, D.; Sutton, D. Focused Ion Beam Lithography - Overview and New Approaches. *Proc. 24th Int. Conf. Microelectron. (MIEL 2004)* **2004**, *2*, 459–462.

- (122) Technology, K. *Keysight Technologies B1500A Semiconductor Device Analyzer*; 2105.
- (123) Schmid, G.; Bäuml, M.; Geerkens, M.; Heim, I.; Osemann, C.; Sawitowski, T. Current and Future Applications of Nanoclusters. *Chem. Soc. Rev.* **1999**, *28*, 179–185.
- (124) Ott, L. S.; Finke, R. G. Transition-Metal Nanocluster Stabilization for Catalysis: A Critical Review of Ranking Methods and Putative Stabilizers. *Coord. Chem. Rev.* **2007**, *251*, 1075–1100.
- (125) Enterkin, J. A.; Poepelmeier, K. R.; Marks, L. D. Oriented Catalytic Platinum Nanoparticles on High Surface Area Strontium Titanate Nanocuboids. *Nano Lett.* **2011**, *11*, 993–997.
- (126) Habibpour, V.; Wang, Z. W.; Palmer, R. E.; Heiz, U. Size-Selected Metal Clusters: New Models for Catalysis with Atomic Precision. *J. Appl. Sci.* **2011**, *11*, 1164–1170.
- (127) Li, J.; Guo, S.; Wang, E. Recent Advances in New Luminescent Nanomaterials for Electrochemiluminescence Sensors. *RSC Adv.* **2012**, *2*, 3579–3586.
- (128) Sattler, K.; Muhlbach, J.; Recknagel, E. Generation of Metal Clusters Containing from 2 to 500 Atoms. *Phys. Rev. Lett.* **1980**, *45*, 821–824.
- (129) Heer, W. A. The Physics of Simple Metal Clusters: Experimental Aspects and Simple Models. *Rev. Mod. Phys.* **1993**, *65*, 611–676.
- (130) Valden, M.; Lai, X.; Goodman, D. W. Onset of Catalytic Activity of Gold Clusters on Titania with the Appearance of Nonmetallic Properties. *Science* **1998**, *281*, 1647–1650.
- (131) Claridge, S. A.; Castleman, A. W.; Khanna, S. N.; Murray, C. B.; Sen, A.; Weiss, P. S. Cluster-Assembled Materials. *ACS Nano* **2009**, *3*, 244–255.
- (132) In, S.; Kean, A. H.; Orlov, A.; Tikhov, M. S.; Lambert, R. M. A Versatile New Method for Synthesis and Deposition of Doped, Visible Light-Activated TiO<sub>2</sub> Thin Films. *Energy Environ. Sci.* **2009**, *2*, 1277–1279.
- (133) Haberland, H.; Karrais, M.; Mall, M. A New Type of Cluster and Cluster Ion Source. *Z. Phys. D - Atoms, Mol. Clust.* **1991**, *20*, 413–415.
- (134) Haberland, H.; Mall, M.; Moseler, M.; Qiang, Y.; Reiners, T.; Thurner, Y. Filling of Micron-Sized Contact Holes with Copper by Energetic Cluster Impact. *J. Vac. Sci. Technol. A* **1994**, *12*, 2925–2930.
- (135) Lang, S. M.; Bernhardt, T. M. Gas Phase Metal Cluster Model Systems for Heterogeneous Catalysis. *Phys. Chem. Chem. Phys.* **2012**, *14*, 9255–9269.
- (136) Thangadurai, P.; Zergioti, I.; Saranu, S.; Chandrinou, C.; Yang, Z.; Tsoukalas, D.; Kean, A.; Boukos, N. ZnO Nanoparticles Produced by Novel Reactive Physical Deposition Process. *Appl. Surf. Sci.* **2011**, *257*, 5366–5369.
- (137) Drabik, M.; Choukourov, A.; Artemenko, A.; Polonskyi, O.; Kylian, O.; Kousal, J.; Nichtova,

- L.; Cimrova, V.; Slavinska, D.; Biederman, H. Structure and Composition of Titanium Nanocluster Films Prepared by a Gas Aggregation Cluster Source. *J. Phys. Chem. C* **2011**, *115*, 20937–20944.
- (138) Marek, A.; Valter, J.; Kadlec, S.; Vyskočil, J. Gas Aggregation Nanocluster Source-Reactive Sputter Deposition of Copper and Titanium Nanoclusters. *Surf. Coatings Technol.* **2011**, *205*, S573–S576.
- (139) Drábik, M.; Choukourov, A.; Artemenko, A.; Kousal, J.; Polonskyi, O.; Solař, P.; Kylián, O.; Matoušek, J.; Pešička, J.; Matolínová, I.; et al. Morphology of Titanium Nanocluster Films Prepared by Gas Aggregation Cluster Source. *Plasma Process. Polym.* **2011**, *8*, 640–650.
- (140) Fujishima, A.; Honda, K. Electrochemical Photolysis of Water at a Semiconductor Electrode. *Nature* **1972**, *238*, 37–38.
- (141) Grätzel, M.; Gratzel, M. Photoelectrochemical Cells. *Nature* **2001**, *414*, 338–344.
- (142) Peng, Q.; Kalanyan, B.; Hoertz, P. G.; Miller, A.; Kim, D. H.; Hanson, K.; Alibabaei, L.; Liu, J.; Meyer, T. J.; Parsons, G. N.; et al. Solution-Processed, Antimony-Doped Tin Oxide Colloid Films Enable High-Performance TiO<sub>2</sub> Photoanodes for Water Splitting. *Nano Lett.* **2013**, *13*, 1481–1488.
- (143) Cowan, A. J.; Tang, J.; Leng, W.; Durrant, J. R.; Klug, D. R. Water Splitting by Nanocrystalline TiO<sub>2</sub> in a Complete Photoelectrochemical Cell Exhibits Efficiencies Limited by Charge Recombination. *J. Phys. Chem. C* **2010**, *114*, 4208–4214.
- (144) Cowan, A. J.; Barnett, C. J.; Pendlebury, S. R.; Barroso, M.; Sivula, K.; Grätzel, M.; Durrant, J. R.; Klug, D. R. Activation Energies for the Rate-Limiting Step in Water Photooxidation by Nanostructured  $\alpha$ -Fe<sub>2</sub>O<sub>3</sub> and TiO<sub>2</sub>. *J. Am. Chem. Soc.* **2011**, *133*, 10134–10140.
- (145) Nanocluster Deposition Systems [www.mantisdeposition.com](http://www.mantisdeposition.com).
- (146) Carroll, S.; Hall, S.; Palmer, R. E.; Smith, R. Energetic Impact of Size-Selected Metal Cluster Ions on Graphite. *Phys. Rev. Lett.* **1998**, *81*, 3715–3718.
- (147) Hashimoto, S.; Tanaka, A. Alteration of Ti 2p XPS Spectrum for Titanium Oxide by Low-Energy Ar Ion Bombardment. *Surf. Interface Anal.* **2002**, *34*, 262–265.
- (148) Shi, J.; Hara, Y.; Sun, C.; Anderson, M. A.; Wang, X. Three-Dimensional High-Density Hierarchical Nanowire Architecture for High-Performance Photoelectrochemical Electrodes. *Nano Lett.* **2011**, *11*, 3413–3419.
- (149) Khan, S. U. M.; Akikusa, J. Photoelectrochemical Splitting of Water at Nanocrystalline N-Fe<sub>2</sub>O<sub>3</sub> Thin-Film Electrodes. *J. Phys. Chem. B* **1999**, *103*, 7184–7189.
- (150) Pradhan, D.; Mohapatra, S. K.; Tymen, S.; Misra, M.; Leung, K. T. Morphology-Controlled ZnO Nanomaterials for Enhanced Photoelectrochemical Performance. *Mater. Express* **2011**, *1*,

- 59–67.
- (151) Sheng, W.; Sun, B.; Shi, T.; Tan, X.; Peng, Z.; Liao, G. Quantum Dot-Sensitized Hierarchical Micro/Nanowire Architecture for Photoelectrochemical Water Splitting. *ACS Nano* **2014**, *8*, 7163–7169.
- (152) Gracia-Pinilla, M. A.; Perez-Tijerina, E.; Garcia, J. A.; Tlahuice-Flores, A.; Mejia-Rosale, S.; Montejano-Carrizales, J. M.; Jose-Yacamán, M. On the Structure and Properties of Silver Nanoparticles. *J. Phys. Chem. C* **2008**, *112*, 13492–13498.
- (153) Srivastava, S.; Thomas, J. P.; Rahman, A.; Abd-ellah, M.; Mohapatra, M.; Pradhan, D.; Heinig, N. F.; Leung, K. T. Size-Selected TiO<sub>2</sub> Nanocluster Catalysts for Efficient Photoelectrochemical Water Splitting. *ACS Nano* **2014**, *8*, 11891–11898.
- (154) Momin, T.; Bhowmick, A. A New Magnetron Based Gas Aggregation Source of Metal Nanoclusters Coupled to a Double Time-of-Flight Mass Spectrometer System. *Rev. Sci. Instrum.* **2010**, *81*, 075110 (1–8).
- (155) Pérez-Tijerina, E.; Gracia Pinilla, M.; Mejía-Rosales, S.; Ortiz-Méndez, U.; Torres, A.; José-Yacamán, M. Highly Size-Controlled Synthesis of Au/Pd Nanoparticles by Inert-Gas Condensation. *Faraday Discuss.* **2008**, *138*, 353–362.
- (156) Yin, F.; Wang, Z. W.; Palmer, R. E. Ageing of Mass-Selected Cu/Au and Au/Cu Core/shell Clusters Probed with Atomic Resolution. *J. Exp. Nanosci.* **2012**, *7*, 703–710.
- (157) Liu, X.; Kuposova, E.; Offenhäusser, A.; Mourzina, Y. Self-Assembly of Platinum Nanoparticles and Coordination-Driven Assembly with Porphyrin. *RSC Adv.* **2015**, *5*, 86934–86940.
- (158) Hashimoto, S.; Tanaka, C.; Murata, A.; Sakurada, T. Formulation for XPS Spectral Change of Oxides by Ar Ion Bombardment: Application of the Formulation to Ta<sub>2</sub>O<sub>5</sub> System. *Journal of Surface Analysis*, 2006, *13*, 14–18.
- (159) Chun, W.; Ishikawa, A.; Fujisawa, H.; Takata, T.; Kondo, J. N.; Hara, M.; Kawai, M.; Matsumoto, Y.; Domen, K. Conduction and Valence Band Positions of Ta<sub>2</sub>O<sub>5</sub>, TaON, and Ta<sub>3</sub>N<sub>5</sub> by UPS and Electrochemical Methods. *J. Phys. Chem. B* **2003**, *107*, 1798–1803.
- (160) Li, Y.; Nagato, K.; Delaunay, J. J.; Kubota, J.; Domen, K. Fabrication of Highly Ordered Ta<sub>2</sub>O<sub>5</sub> and Ta<sub>3</sub>N<sub>5</sub> Nanorod Arrays by Nanoimprinting and through-Mask Anodization. *Nanotechnology* **2014**, *25*, 014013 (1–8).
- (161) Dabirian, A.; Spijker, H. V.; Van De Krol, R. Wet Ammonia Synthesis of Semiconducting N:Ta<sub>2</sub>O<sub>5</sub>, Ta<sub>3</sub>N<sub>5</sub> and β-TaON Films for Photoanode Applications. *Energy Procedia* **2011**, *22*, 15–22.
- (162) Allam, N. K.; Shaheen, B. S.; Hafez, A. M. Layered Tantalum Oxynitride Nanorod Array

- Carpets for Efficient Photoelectrochemical Conversion of Solar Energy: Experimental and DFT Insights. *ACS Appl. Mater. Interfaces* **2014**, *6*, 4609–4615.
- (163) Wang, L.; Zhou, X.; Nguyen, N. T.; Hwang, I.; Schmuki, P. Strongly Enhanced Water Splitting Performance of Ta<sub>3</sub>N<sub>5</sub> Nanotube Photoanodes with Subnitrides. *Adv. Mater.* **2016**.
- (164) Chua, L. O. Memristive Devices and Systems. *Proc. IEEE* **1976**, *64*, 209–223.
- (165) Nili, H.; Walia, S.; Balendhran, S.; Strukov, D. B.; Bhaskaran, M.; Sriram, S. Nanoscale Resistive Switching in Amorphous Perovskite Oxide ( $\alpha$ -SrTiO<sub>3</sub>) Memristors. *Adv. Funct. Mater.* **2014**, *24*, 6741–6750.
- (166) Bessonov, A. A.; Kirikova, M. N.; Petukhov, D. I.; Allen, M.; Ryhänen, T.; Bailey, M. J. A. Layered Memristive and Memcapacitive Switches for Printable Electronics. *Nat. Mater.* **2015**, *14*, 199–204.
- (167) Kim, S.; Choi, S.; Lu, W. Comprehensive Physical Model of Dynamic Resistive Switching in an Oxide Memristor. *ACS Nano* **2014**, *8*, 2369–2376.
- (168) Nili, H.; Walia, S.; Kandjani, A. E.; Ramanathan, R.; Gutruf, P.; Ahmed, T.; Balendhran, S.; Bansal, V.; Strukov, D. B.; Kavehei, O.; et al. Donor-Induced Performance Tuning of Amorphous SrTiO<sub>3</sub> Memristive Nanodevices: Multistate Resistive Switching and Mechanical Tunability. *Adv. Funct. Mater.* **2015**, *25*, 3172–3182.
- (169) Szot, K.; Rogala, M.; Speier, W.; Klusek, Z.; Besmehn, A.; Waser, R. TiO<sub>2</sub>-a Prototypical Memristive Material. *Nanotechnology* **2011**, *22*, 254001 (1–21).
- (170) Du, Y.; Pan, H.; Wang, S.; Wu, T.; Feng, Y. P.; Pan, J.; Wee, A. T. S. Symmetrical Negative Differential Resistance Behavior of a Resistive Switching Device. *ACS Nano* **2012**, *6*, 2517–2523.
- (171) Inoue, I.; Yasuda, S.; Akinaga, H.; Takagi, H. Nonpolar Resistance Switching of Metal/binary-Transition-Metal Oxides/metal Sandwiches: Homogeneous/inhomogeneous Transition of Current Distribution. *Phys. Rev. B* **2008**, *77*, 035105 (1–7).
- (172) Mickel, P. R.; Lohn, A. J.; James, C. D.; Marinella, M. J. Isothermal Switching and Detailed Filament Evolution in Memristive Systems. *Adv. Mater.* **2014**, *26*, 4486–4490.
- (173) Yang, J. J.; Zhang, M. X.; Pickett, M. D.; Miao, F.; Strachan, J. P.; Li, W. Di; Yi, W.; Ohlberg, D. A. A.; Choi, B. J.; Wu, W.; et al. Engineering Nonlinearity into Memristors for Passive Crossbar Applications. *Appl. Phys. Lett.* **2012**, *100*, 113501 (1–4).
- (174) Jo, S. H.; Kim, K. H.; Lu, W. High-Density Crossbar Arrays Based on a Si Memristive System. *Nano Lett.* **2009**, *9*, 870–874.
- (175) Chung, A.; Deen, J.; Lee, J. S.; Meyyappan, M. Nanoscale Memory Devices. *Nanotechnology* **2010**, *21*, 412001 (1–22).

- (176) Ha, S. D.; Ramanathan, S. Adaptive Oxide Electronics: A Review. *J. Appl. Phys.* **2011**, *110*, 071101 (1–20).
- (177) Sawa, A. Resistive Switching in Transition Metal Oxides. *Mater. Today* **2008**, *11*, 28–36.
- (178) Fujii, T.; Kawasaki, M.; Sawa, A.; Akoh, H.; Kawazoe, Y.; Tokura, Y. Hysteretic Current-Voltage Characteristics and Resistance Switching at an Epitaxial Oxide Schottky Junction SrRuO<sub>3</sub>/SrTi<sub>0.99</sub>Nb<sub>0.01</sub>O<sub>3</sub>. *Appl. Phys. Lett.* **2005**, *86*, 1–3.
- (179) Sawa, A.; Fujii, T.; Kawasaki, M.; Tokura, Y. Hysteretic Current-Voltage Characteristics and Resistance Switching at a Rectifying Ti/Pr<sub>0.7</sub>Ca<sub>0.3</sub>MnO<sub>3</sub> Interface. *Appl. Phys. Lett.* **2004**, *85*, 4073–4075.
- (180) Strukov, D. B.; Alibart, F.; Williams, R. S. Thermophoresis/diffusion as a Plausible Mechanism for Unipolar Resistive Switching in Metal-Oxide-Metal Memristors. *Appl. Phys. A Mater. Sci. Process.* **2012**, *107*, 509–518.
- (181) Blanc, J.; Staebler, D. L. Electrocoloration in SrTiO<sub>3</sub>: Vacancy Drift and Oxidation-Reduction of Transition Metals. *Phys. Rev. B* **1971**, *4*, 3548–3557.
- (182) Cao, X.; Li, X. M.; Gao, X. D.; Zhang, Y. W.; Liu, X. J.; Wang, Q.; Chen, L. D. Effects of the Compliance Current on the Resistive Switching Behavior of TiO<sub>2</sub> Thin Films. *Appl. Phys. A* **2009**, *97*, 883–887.
- (183) Hou, J.; Nonnenmann, S. S.; Qin, W.; Bonnell, D. A. Size Dependence of Resistive Switching at Nanoscale Metal-Oxide Interfaces. *Adv. Funct. Mater.* **2014**, *24*, 4113–4118.
- (184) Jiang, H.; Xia, Q. Effect of Voltage Polarity and Amplitude on Electroforming of TiO<sub>2</sub> Based Memristive Devices. *Nanoscale* **2013**, *5*, 3257–3261.
- (185) Yoon, K. J.; Lee, M. H.; Kim, G. H.; Song, S. J.; Seok, J. Y.; Han, S.; Yoon, J. H.; Kim, K. M.; Hwang, C. S. Memristive Tri-Stable Resistive Switching at Ruptured Conducting Filaments of a Pt/TiO<sub>2</sub>/Pt Cell. *Nanotechnology* **2012**, *23*, 185202 (1–8).
- (186) Zhu, X. J.; Shang, J.; Li, R. W. Resistive Switching Effects in Oxide Sandwiched Structures. *Front. Mater. Sci.* **2012**, *6*, 3–24.
- (187) Kim, K. M.; Park, T. H.; Hwang, C. S. Dual Conical Conducting Filament Model in Resistance Switching TiO<sub>2</sub> Thin Films. *Sci. Rep.* **2015**, *5*, 7844 (1–9).
- (188) Wedig, A.; Luebben, M.; Moors, M.; Cho, D. Y.; Skaja, K.; Hasegawa, T.; Adepalli, K. K.; Yildiz, B.; Waser, R.; Valov, I. Nanoscale Cation Motion in TaO<sub>x</sub>, HfO<sub>x</sub> and TiO<sub>x</sub> Memristive Systems. *Nat. Nanotechnol.* **2015**, *11*, 67–75.
- (189) Waser, R.; Dittmann, R.; Staikov, G.; Szot, K. Redox-Based Resistive Switching Memories - Nanoionic Mechanisms, Prospects, and Challenges. *Adv. Mater.* **2009**, *21*, 2632–2663.
- (190) Yang, J. J.; Zhang, M. X.; Strachan, J. P.; Miao, F.; Pickett, M. D.; Kelley, R. D.; Medeiros-

- Ribeiro, G.; Williams, R. S. High Switching Endurance in TaO<sub>x</sub> Memristive Devices. *Appl. Phys. Lett.* **2010**, *97*, 232102 (1–3).
- (191) Lau, C. N.; Stewart, D. R.; Williams, R. S.; Bockrath, M. Direct Observation of Nanoscale Switching Centers in Metal/Molecule/Metal Structures. *Nano Lett.* **2004**, *4*, 569–572.
- (192) Bae, Y. C.; Lee, A. R.; Lee, J. B.; Koo, J. H.; Kwon, K. C.; Park, J. G.; Im, H. S.; Hong, J. P. Oxygen Ion Drift-Induced Complementary Resistive Switching in Homo TiO<sub>x</sub>/TiO<sub>y</sub>/TiO<sub>x</sub> and Hetero TiO<sub>x</sub>/TiON/TiO<sub>x</sub> Triple Multilayer Frameworks. *Adv. Funct. Mater.* **2012**, *22*, 709–716.
- (193) Prakash, A.; Maikap, S.; Chiu, H. C.; Tien, T. C.; Lai, C. S. Enhanced Resistive Memory Characteristics and Switching Mechanism Using a Ti Nanolayer at the W/TaO<sub>x</sub> Interface. *Nanoscale Res. Lett.* **2014**, *9*, 125 (1–9).
- (194) Zhou, Q.; Zhai, J. Resistive Switching Characteristics of Pt/TaO<sub>x</sub>/HfN<sub>x</sub> Structure and Its Performance Improvement. *AIP Adv.* **2013**, *3*, 032102 (1–12).
- (195) Rahaman, S.; Maikap, S.; Tien, T. C.; Lee, H. Y.; Chen, W. S.; Chen, F. T.; Kao, M. J.; Tsai, M. J. Excellent Resistive Memory Characteristics and Switching Mechanism Using a Ti Nanolayer at the Cu/TaO<sub>x</sub> Interface. *Nanoscale Res. Lett.* **2012**, *7*, 345 (1–11).
- (196) Lee, C. T.; Chiu, Y. S. Field-Effect-Transistor-Based Calcium Ion Sensors Using Zn<sub>3</sub>Ta<sub>2</sub>O<sub>5</sub> Sensing Membrane. *Sensors Actuators B Chem.* **2014**, *203*, 790–794.
- (197) Zhu, H.; Bonevich, J. E.; Li, H.; Richter, C. A.; Yuan, H.; Kirillov, O.; Li, Q. Discrete Charge States in Nanowire Flash Memory with Multiple Ta<sub>2</sub>O<sub>5</sub> Charge-Trapping Stacks. *Appl. Phys. Lett.* **2014**, *104*, 233504 (1–5).
- (198) Liu, J. W.; Liao, M. Y.; Imura, M.; Watanabe, E.; Oosato, H.; Koide, Y. Diamond Field Effect Transistors with a High-Dielectric Constant Ta<sub>2</sub>O<sub>5</sub> as Gate Material. *J. Phys. D: Appl. Phys.* **2014**, *47*, 245102 (1–5).
- (199) Yang, Y.; Sheridan, P.; Lu, W. Complementary Resistive Switching in Tantalum Oxide-Based Resistive Memory Devices. *Appl. Phys. Lett.* **2012**, *100*, 203112 (1–5).
- (200) Strachan, J. P.; Medeiros-Ribeiro, G.; Yang, J. J.; Zhang, M.; Miao, F.; Goldfarb, I.; Holt, M.; Rose, V.; Williams, R. S. Spectromicroscopy of Tantalum Oxide Memristors. *Appl. Phys. Lett.* **2011**, *98*, 242114 (1–3).
- (201) Wang, X.; Liu, J.; Bai, W.; Kwong, D. L. A Novel MONOS-Type Nonvolatile Memory Using High-K Dielectrics for Improved Data Retention and Programming Speed. *IEEE Trans. Electron Devices* **2004**, *51*, 597–602.
- (202) Garg, S. P.; Krishnamurthy, N. Awasthi, A. The O-Ta ( Oxygen-Tantalum ) System. *J. Phase Equilibria* **1996**, *17*, 63–77.

# Appendix A

## Permissions

Ref. 40



The screenshot shows the RightsLink interface with the following details:

- Copyright Clearance Center RightsLink®** logo and navigation buttons: Home, Account Info, Help, Live Chat.
- Title:** Defect-rich decorated TiO<sub>2</sub> nanowires for super-efficient photoelectrochemical water splitting driven by visible light
- Author:** Md Anisur Rahman, Samad Bazargan, Saurabh Srivastava, Xiongyao Wang, Marwa Abd-Elilah, Joseph P. Thomas, Nina F. Heinig, Debabrata Pradhan, Kam Tong Leung
- Publication:** Energy & Environmental Science
- Publisher:** Royal Society of Chemistry
- Date:** Sep 21, 2015
- Copyright © 2015, Royal Society of Chemistry**
- Logged in as:** Saurabh Srivastava, Account #: 3001003535, with a LOGOUT button.

### Order Completed

Thank you for your order.

This Agreement between Saurabh Srivastava ("You") and Royal Society of Chemistry ("Royal Society of Chemistry") consists of your license details and the terms and conditions provided by Royal Society of Chemistry and Copyright Clearance Center.

Your confirmation email will contain your order number for future reference.

[Get the printable license.](#)

License Number	3827720825026
License date	Mar 14, 2016
Licensed Content Publisher	Royal Society of Chemistry
Licensed Content Publication	Energy & Environmental Science
Licensed Content Title	Defect-rich decorated TiO <sub>2</sub> nanowires for super-efficient photoelectrochemical water splitting driven by visible light
Licensed Content Author	Md Anisur Rahman, Samad Bazargan, Saurabh Srivastava, Xiongyao Wang, Marwa Abd-Elilah, Joseph P. Thomas, Nina F. Heinig, Debabrata Pradhan, Kam Tong Leung
Licensed Content Date	Sep 21, 2015
Licensed Content Volume	8
Licensed Content Issue	11
Type of Use	Thesis/Dissertation
Requestor type	commercial (for-profit)
Portion	figures/tables/images
Number of figures/tables /images	1
Distribution quantity	1
Format	print and electronic
Will you be translating?	no
Order reference number	None
Title of the thesis/dissertation	Defect-Rich Size-Selected Nanoclusters and Nanocrystalline Films of Titanium (IV) Oxide and Tantalum (IV) Oxide for Efficient Photocatalyst and Electroforming-Free Memristor Applications
Expected completion date	May 2016
Estimated size	160
Requestor Location	Saurabh Srivastava 702, 25-Westmount Rd. N.  Waterloo, ON N2L3G1 Canada Attn: Saurabh Srivastava
Billing Type	Invoice
Billing address	Saurabh Srivastava 702, 25-Westmount Rd. N.  Waterloo, ON N2L3G1 Canada Attn: Saurabh Srivastava
Total	0.00 USD

[ORDER MORE](#)

[CLOSE WINDOW](#)



RightsLink®

Home

Account  
Info

Help



**Title:** Photoelectrochemical cells  
**Author:** Michael Grätzel  
**Publication:** Nature  
**Publisher:** Nature Publishing Group  
**Date:** Nov 15, 2001

Copyright © 2001, Rights Managed by Nature Publishing Group

Logged in as:  
Saurabh Srivastava  
Account #:  
3001003535

[LOGOUT](#)

### Order Completed

Thank you very much for your order.

This is a License Agreement between Saurabh Srivastava ("You") and Nature Publishing Group ("Nature Publishing Group"). The license consists of your order details, the terms and conditions provided by Nature Publishing Group, and the [payment terms and conditions](#).

[Get the printable license.](#)

License Number	3827720584257
License date	Mar 14, 2016
Licensed content publisher	Nature Publishing Group
Licensed content publication	Nature
Licensed content title	Photoelectrochemical cells
Licensed content author	Michael Grätzel
Licensed content date	Nov 15, 2001
Type of Use	reuse in a dissertation / thesis
Volume number	414
Issue number	6861
Requestor type	non-commercial (non-profit)
Format	print and electronic
Portion	figures/tables/illustrations
Number of figures/tables /illustrations	2
Figures	1, 2
Author of this NPG article	no
Your reference number	None
Title of your thesis / dissertation	Defect-Rich Size-Selected Nanoclusters and Nanocrystalline Films of Titanium (IV) Oxide and Tantalum (IV) Oxide for Efficient Photocatalyst and Electroforming-Free Memristor Applications
Expected completion date	May 2016
Estimated size (number of pages)	160
Total	0.00 USD

[ORDER MORE...](#)
[CLOSE WINDOW](#)



RightsLink®

[Home](#)[Account Info](#)[Help](#)

**Title:** Branched TiO<sub>2</sub> Nanorods for Photoelectrochemical Hydrogen Production

**Author:** In Sun Cho, Zhebo Chen, Arnold J. Forman, et al

**Publication:** Nano Letters

**Publisher:** American Chemical Society

**Date:** Nov 1, 2011

Copyright © 2011, American Chemical Society

Logged in as:  
Saurabh Srivastava  
Account #:  
3001003535

[LOGOUT](#)

### PERMISSION/LICENSE IS GRANTED FOR YOUR ORDER AT NO CHARGE

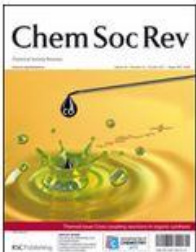
This type of permission/license, instead of the standard Terms & Conditions, is sent to you because no fee is being charged for your order. Please note the following:

- Permission is granted for your request in both print and electronic formats, and translations.
- If figures and/or tables were requested, they may be adapted or used in part.
- Please print this page for your records and send a copy of it to your publisher/graduate school.
- Appropriate credit for the requested material should be given as follows: "Reprinted (adapted) with permission from (COMPLETE REFERENCE CITATION). Copyright (YEAR) American Chemical Society." Insert appropriate information in place of the capitalized words.
- One-time permission is granted only for the use specified in your request. No additional uses are granted (such as derivative works or other editions). For any other uses, please submit a new request.

If credit is given to another source for the material you requested, permission must be obtained from that source.

[BACK](#)[CLOSE WINDOW](#)

Copyright Clearance Center **RightsLink®** Home Account Info Help Live Chat



**Title:** Tantalum-based semiconductors for solar water splitting  
**Author:** Peng Zhang, Jijie Zhang, Jinlong Gong  
**Publication:** Chemical Society Reviews  
**Publisher:** Royal Society of Chemistry  
**Date:** Mar 25, 2014  
 Copyright © 2014, Royal Society of Chemistry

Logged in as:  
 Saurabh Srivastava  
 Account #: 3001003535  
 LOGOUT

**Order Completed**

Thank you for your order.

This Agreement between Saurabh Srivastava ("You") and Royal Society of Chemistry ("Royal Society of Chemistry") consists of your license details and the terms and conditions provided by Royal Society of Chemistry and Copyright Clearance Center.

Your confirmation email will contain your order number for future reference.

[Get the printable license.](#)

License Number	3827721001516
License date	Mar 14, 2016
Licensed Content Publisher	Royal Society of Chemistry
Licensed Content Publication	Chemical Society Reviews
Licensed Content Title	Tantalum-based semiconductors for solar water splitting
Licensed Content Author	Peng Zhang, Jijie Zhang, Jinlong Gong
Licensed Content Date	Mar 25, 2014
Licensed Content Volume	43
Licensed Content Issue	13
Type of Use	Thesis/Dissertation
Requestor type	non-commercial (non-profit)
Portion	figures/tables/images
Number of figures/tables/images	1
Distribution quantity	1
Format	print and electronic
Will you be translating?	no
Order reference number	None
Title of the thesis/dissertation	Defect-Rich Size-Selected Nanoclusters and Nanocrystalline Films of Titanium (IV) Oxide and Tantalum (IV) Oxide for Efficient Photocatalyst and Electroforming-Free Memristor Applications
Expected completion date	May 2016
Estimated size	160
Requestor Location	Saurabh Srivastava 702, 25-Westmount Rd. N.  Waterloo, ON N2L3G1 Canada Attn: Saurabh Srivastava
Billing Type	Invoice
Billing address	Saurabh Srivastava 702, 25-Westmount Rd. N.  Waterloo, ON N2L3G1 Canada Attn: Saurabh Srivastava
Total	0.00 USD

ORDER MORE

CLOSE WINDOW



Home

Account Info

Help



**Title:** The missing memristor found  
**Author:** Dmitri B. Strukov, Gregory S. Snider, Duncan R. Stewart and R. Stanley Williams  
**Publication:** Nature  
**Publisher:** Nature Publishing Group  
**Date:** May 1, 2008

Logged in as:  
 Saurabh Srivastava  
 Account #:  
 3001003535  
[LOGOUT](#)

Copyright © 2008, Rights Managed by Nature Publishing Group

**Order Completed**

Thank you very much for your order.

This is a License Agreement between Saurabh Srivastava ("You") and Nature Publishing Group ("Nature Publishing Group"). The license consists of your order details, the terms and conditions provided by Nature Publishing Group, and the [payment terms and conditions](#).

[Get the printable license.](#)

License Number	3827721099522
License date	Mar 14, 2016
Licensed content publisher	Nature Publishing Group
Licensed content publication	Nature
Licensed content title	The missing memristor found
Licensed content author	Dmitri B. Strukov, Gregory S. Snider, Duncan R. Stewart and R. Stanley Williams
Licensed content date	May 1, 2008
Type of Use	reuse in a dissertation / thesis
Volume number	453
Issue number	7191
Requestor type	non-commercial (non-profit)
Format	print and electronic
Portion	figures/tables/illustrations
Number of figures/tables /illustrations	2
High-res required	no
Figures	1, 2
Author of this NPG article	no
Your reference number	None
Title of your thesis / dissertation	Defect-Rich Size-Selected Nanoclusters and Nanocrystalline Films of Titanium (IV) Oxide and Tantalum (IV) Oxide for Efficient Photocatalyst and Electroforming-Free Memristor Applications
Expected completion date	May 2016
Estimated size (number of pages)	160
Total	0.00 USD

[ORDER MORE...](#)

[CLOSE WINDOW](#)



- [Home](#)
- [Account Info](#)
- [Help](#)



**Title:** Memristive switching mechanism for metal/oxide /metal nanodevices  
**Author:** J. Joshua Yang, Matthew D. Pickett, Xuema Li, Douglas A. A. Ohlberg, Duncan R. Stewart et al.

Logged in as:  
 Saurabh Srivastava  
 Account #:  
 3001003535  
[LOGOUT](#)

**Publication:** Nature Nanotechnology  
**Publisher:** Nature Publishing Group  
**Date:** Jun 15, 2008

Copyright © 2008, Rights Managed by Nature Publishing Group

**Order Completed**

Thank you very much for your order.

This is a License Agreement between Saurabh Srivastava ("You") and Nature Publishing Group ("Nature Publishing Group"). The license consists of your order details, the terms and conditions provided by Nature Publishing Group, and the [payment terms and conditions](#).

[Get the printable license.](#)

License Number	3827721360168
License date	Mar 14, 2016
Licensed content publisher	Nature Publishing Group
Licensed content publication	Nature Nanotechnology
Licensed content title	Memristive switching mechanism for metal/oxide/metal nanodevices
Licensed content author	J. Joshua Yang, Matthew D. Pickett, Xuema Li, Douglas A. A. Ohlberg, Duncan R. Stewart et al.
Licensed content date	Jun 15, 2008
Type of Use	reuse in a dissertation / thesis
Volume number	3
Issue number	7
Requestor type	non-commercial (non-profit)
Format	print and electronic
Portion	figures/tables/illustrations
Number of figures/tables /illustrations	1
High-res required	no
Figures	1
Author of this NPG article	no
Your reference number	None
Title of your thesis / dissertation	Defect-Rich Size-Selected Nanoclusters and Nanocrystalline Films of Titanium (IV) Oxide and Tantalum (IV) Oxide for Efficient Photocatalyst and Electroforming-Free Memristor Applications
Expected completion date	May 2016
Estimated size (number of pages)	160
Total	0.00 USD

- [ORDER MORE...](#)
- [CLOSE WINDOW](#)



# RightsLink®

[Home](#)
[Account Info](#)
[Help](#)



Live Chat



**Title:** A Family of Electronically Reconfigurable Nanodevices

**Author:** J. Joshua Yang, Julien Borghetti, David Murphy, Duncan R. Stewart, R. Stanley Williams

**Publication:** Advanced Materials

**Publisher:** John Wiley and Sons

**Date:** Jun 2, 2009

Copyright © 2009 WILEY-VCH Verlag GmbH & Co. KGaA, Weinheim

Logged in as:  
Saurabh Srivastava

Account #:  
3001003535

LOGOUT

### Order Completed

Thank you for your order.

This Agreement between Saurabh Srivastava ("You") and John Wiley and Sons ("John Wiley and Sons") consists of your license details and the terms and conditions provided by John Wiley and Sons and Copyright Clearance Center.

Your confirmation email will contain your order number for future reference.

[Get the printable license.](#)

License Number	3827721244378
License date	Mar 14, 2016
Licensed Content Publisher	John Wiley and Sons
Licensed Content Publication	Advanced Materials
Licensed Content Title	A Family of Electronically Reconfigurable Nanodevices
Licensed Content Author	J. Joshua Yang, Julien Borghetti, David Murphy, Duncan R. Stewart, R. Stanley Williams
Licensed Content Date	Jun 2, 2009
Licensed Content Pages	5
Type of use	Dissertation/Thesis
Requestor type	University/Academic
Format	Print and electronic
Portion	Figure/table
Number of figures/tables	1
Original Wiley figure/table number(s)	1
Will you be translating?	No
Title of your thesis / dissertation	Defect-Rich Size-Selected Nanoclusters and Nanocrystalline Films of Titanium (IV) Oxide and Tantalum (IV) Oxide for Efficient Photocatalyst and Electroforming-Free Memristor Applications
Expected completion date	May 2016
Expected size (number of pages)	160
Requestor Location	Saurabh Srivastava 702, 25-Westmount Rd. N.  Waterloo, ON N2L3G1 Canada Attn: Saurabh Srivastava
Billing Type	Invoice
Billing address	Saurabh Srivastava 702, 25-Westmount Rd. N.  Waterloo, ON N2L3G1 Canada Attn: Saurabh Srivastava
Total	0.00 USD



**Title:** Memristive devices for computing  
**Author:** J. Joshua Yang, Dmitri B. Strukov, Duncan R. Stewart  
**Publication:** Nature Nanotechnology  
**Publisher:** Nature Publishing Group  
**Date:** Dec 27, 2012

Copyright © 2012, Rights Managed by Nature Publishing Group

Logged in as:  
 Saurabh Srivastava  
 Account #:  
 3001003535

LOGOUT

### Order Completed

Thank you very much for your order.

This is a License Agreement between Saurabh Srivastava ("You") and Nature Publishing Group ("Nature Publishing Group"). The license consists of your order details, the terms and conditions provided by Nature Publishing Group, and the [payment terms and conditions](#).

[Get the printable license.](#)

License Number	3827721448234
License date	Mar 14, 2016
Licensed content publisher	Nature Publishing Group
Licensed content publication	Nature Nanotechnology
Licensed content title	Memristive devices for computing
Licensed content author	J. Joshua Yang, Dmitri B. Strukov, Duncan R. Stewart
Licensed content date	Dec 27, 2012
Type of Use	reuse in a dissertation / thesis
Volume number	8
Issue number	1
Requestor type	non-commercial (non-profit)
Format	print and electronic
Portion	figures/tables/illustrations
Number of figures/tables/illustrations	1
High-res required	no
Figures	1
Author of this NPG article	no
Your reference number	None
Title of your thesis / dissertation	Defect-Rich Size-Selected Nanoclusters and Nanocrystalline Films of Titanium (IV) Oxide and Tantalum (IV) Oxide for Efficient Photocatalyst and Electroforming-Free Memristor Applications
Expected completion date	May 2016
Estimated size (number of pages)	160
Total	0.00 USD

ORDER MORE...

CLOSE WINDOW



RightsLink®

Home

Account  
Info

Help



ACS Publications  
Most Trusted. Most Cited. Most Read.

**Title:** Three-Dimensional  
Observation of the Conductive  
Filament in Nanoscaled  
Resistive Memory Devices

**Author:** Umberto Celano, Ludovic  
Goux, Attilio Belmonte, et al

**Publication:** Nano Letters

**Publisher:** American Chemical Society

**Date:** May 1, 2014

Copyright © 2014, American Chemical Society

Logged in as:  
Saurabh Srivastava

LOGOUT

### PERMISSION/LICENSE IS GRANTED FOR YOUR ORDER AT NO CHARGE

This type of permission/license, instead of the standard Terms & Conditions, is sent to you because no fee is being charged for your order. Please note the following:

- Permission is granted for your request in both print and electronic formats, and translations.
- If figures and/or tables were requested, they may be adapted or used in part.
- Please print this page for your records and send a copy of it to your publisher/graduate school.
- Appropriate credit for the requested material should be given as follows: "Reprinted (adapted) with permission from (COMPLETE REFERENCE CITATION). Copyright (YEAR) American Chemical Society." Insert appropriate information in place of the capitalized words.
- One-time permission is granted only for the use specified in your request. No additional uses are granted (such as derivative works or other editions). For any other uses, please submit a new request.

If credit is given to another source for the material you requested, permission must be obtained from that source.



Home Account Info Help



**Title:** A fast, high-endurance and scalable non-volatile memory device made from asymmetric Ta<sub>2</sub>O<sub>5-x</sub>/TaO<sub>2-x</sub> bilayer structures

**Author:** Myoung-Jae Lee, Chang Bum Lee, Dongsoo Lee, Seung Ryul Lee, Man Chang, Ji Hyun Hur

**Publication:** Nature Materials

**Publisher:** Nature Publishing Group

**Date:** Jul 10, 2011

Copyright © 2011, Rights Managed by Nature Publishing Group

Logged in as:  
Saurabh Srivastava  
Account #:  
3001003535

LOGOUT

**Order Completed**

Thank you very much for your order.

This is a License Agreement between Saurabh Srivastava ("You") and Nature Publishing Group ("Nature Publishing Group"). The license consists of your order details, the terms and conditions provided by Nature Publishing Group, and the [payment terms and conditions](#).

[Get the printable license.](#)

License Number	3827730161137
License date	Mar 14, 2016
Licensed content publisher	Nature Publishing Group
Licensed content publication	Nature Materials
Licensed content title	A fast, high-endurance and scalable non-volatile memory device made from asymmetric Ta <sub>2</sub> O <sub>5-x</sub> /TaO <sub>2-x</sub> bilayer structures
Licensed content author	Myoung-Jae Lee, Chang Bum Lee, Dongsoo Lee, Seung Ryul Lee, Man Chang, Ji Hyun Hur
Licensed content date	Jul 10, 2011
Type of Use	reuse in a dissertation / thesis
Volume number	10
Issue number	8
Requestor type	non-commercial (non-profit)
Format	print and electronic
Portion	figures/tables/illustrations
Number of figures/tables/illustrations	1
High-res required	no
Figures	1
Author of this NPG article	no
Your reference number	None
Title of your thesis / dissertation	Defect-Rich Size-Selected Nanoclusters and Nanocrystalline Films of Titanium (IV) Oxide and Tantalum (IV) Oxide for Efficient Photocatalyst and Electroforming-Free Memristor Applications
Expected completion date	May 2016
Estimated size (number of pages)	160
Total	0.00 USD

ORDER MORE...

CLOSE WINDOW



RightsLink®

Home

Account  
Info

Help



ACS Publications  
Most Trusted. Most Cited. Most Read.

**Title:** Size-Selected TiO<sub>2</sub>  
Nanocluster Catalysts for  
Efficient Photoelectrochemical  
Water Splitting

**Author:** Saurabh Srivastava, Joseph  
Palathinkal Thomas, Md.  
Anisur Rahman, et al

**Publication:** ACS Nano

**Publisher:** American Chemical Society

**Date:** Nov 1, 2014

Copyright © 2014, American Chemical Society

Logged in as:

Saurabh Srivastava

LOGOUT

#### PERMISSION/LICENSE IS GRANTED FOR YOUR ORDER AT NO CHARGE

This type of permission/license, instead of the standard Terms & Conditions, is sent to you because no fee is being charged for your order. Please note the following:

- Permission is granted for your request in both print and electronic formats, and translations.
- If figures and/or tables were requested, they may be adapted or used in part.
- Please print this page for your records and send a copy of it to your publisher/graduate school.
- Appropriate credit for the requested material should be given as follows: "Reprinted (adapted) with permission from (COMPLETE REFERENCE CITATION). Copyright (YEAR) American Chemical Society." Insert appropriate information in place of the capitalized words.
- One-time permission is granted only for the use specified in your request. No additional uses are granted (such as derivative works or other editions). For any other uses, please submit a new request.